SHOCKS IN THE INTERSTELLAR MEDIUM

Dissertation
zur
Erlangung des Doktorgrades (Dr. rer. nat)
der
Mathematisch-Naturwissenschaftlichen Fakultät
der
Rheinischen Friedrich-Wilhelms-Universität Bonn

vorgelegt von
Sibylle Anderl
aus
Oldenburg (Oldb.)

Bonn, September 2013

Angefertigt mit Genehmigung der Mathematisch-Naturwissenschaftlichen Fakultät der
Rheinischen Friedrich-Wilhelms-Universität Bonn

1. Gutachter:	Prof. Dr. Frank Bertoldi
2. Gutachter:	Prof. Dr. Peter Schilke

Tag der Promotion: 11. Dezember 2013

Erscheinungsjahr: 2014

Diese Dissertation ist auf dem Hochschulschriftenserver der ULB Bonn unter
`http://hss.ulb.uni-bonn.de/diss_online/` elektronisch publiziert.

SUMMARY

Shocks are ubiquitous in the interstellar medium (ISM), occurring whenever large pressure gradients lead to fluid-dynamical disturbances that move at a velocity that exceeds the local sound speed. As shocks dissipate kinetic energy into heat, they give rise to strong cooling radiation that constitutes excellent diagnostics for the study of the conditions in the shocked gas. The interpretation of this radiation requires the application of detailed numerical shock models.

Grain-grain processing has been shown to be an indispensable ingredient of shock modelling in high-density environments. However, an analysis of the effects of shattering and vaporization on molecular line emission had remained open. I have developed a new method for implementing grain-grain processing into a 2-fluid magnetohydrodynamic (MHD) shock model, which includes a self-consistent treatment of the molecular line transfer. Using this combined model, it was shown that shattering has a strong influence on continuous MHD shocks ("C-type shocks") for a broad range of shock parameters: the shocks become hotter and thinner. Predictions were made for the emission of H_2, CO, OH and H_2O. The main focus of the study lay on SiO, which is a prominent indicator of shock processing in dense clouds and is released into the gas-phase by the vaporization of grain cores. The release by vaporization already early in the shock changes the excitation characteristics of the SiO line radiation, although it does not change the width of SiO rotational lines. This study has significantly improved our understanding of shock emission in high-density environments. The method that was developed will make it possible to easily implement the effect of grain-grain processing in other numerical shock models.

MHD shock models were applied in the interpretation of observations of supernova remnants (SNRs) interacting with molecular clouds. New CO rotational line observations with the APEX telescope from shocked regions in two of these SNRs, W28 and W44, were presented. Towards W28, data was also taken with the SOFIA telescope. The integrated CO intensities observed towards positions of shock interaction were compared with a large grid of MHD shock models. Towards W28, it was found that only stationary C-type shock models were compatible with the observed emission. These shocks could satisfactorily account for the pure rotational H_2 emission as observed with Spitzer. In W44, however, only models of much younger, non-stationary shocks could reproduce the observations. The preshock densities found in both SNRs were too low for grain-grain processing to be significant. Based on our modelling, we were able to constrain the physical and chemical conditions in the shocked regions, give predictions for H_2O and the full ladder of CO rotational transitions, and quantify the momentum and energy injection of the SNR into the ISM. The results are important for a proper understanding of the local characteristics of SNR-cloud interactions, as well as for the study of the global energetics and dynamics of the ISM and the study of cosmic rays. The developed method enables a systematic comparison of a large grid of detailed MHD shock models with observations of shocked molecular gas and will be further applied in future studies.

I conclude with a critical reflection of research on astrophysical shocks within the framework of recent discussions in the philosophy of science.

PUBLICATIONS

Chapter 5 was published as:

"Shocks in dense clouds – IV. Effects of grain-grain processing on molecular line emission", **Anderl, S.**, Guillet, V., Pineau des Forêts, G., & Flower, D. R. 2013, A&A, 556, 69

Chapter 9 was published as:

"Probing magnetohydrodynamic shocks with high-*J* CO observations: W28F", Gusdorf, A., **Anderl, S.**, Güsten, R., Stutzki, J., Hübers, H.-W., Hartogh, P., Heymick, S., & Okada, Y. 2012, A&A, 542, L19

Chapter 12 will be submitted to A&A as:

"APEX observations of supernova remnants – I. Non-stationary magnetohydrodynamic shocks in W44", **Anderl, S.**, Gusdorf, A., & Güsten, R.

Additional publications that were not incorporated into this thesis:

"Star-forming Dense Cloud Cores in the TeV Gamma-ray SNR RX J1713.7-3946", Sano, H., ..., **Anderl, S.** et al. 2010, ApJ, 724, 59

"PACS and SPIRE photometer maps of M 33: First results of the HERschel M 33 Extended Survey (HERM33ES)", Kramer, C., ..., **Anderl, S.** et al. 2010, A&A, 518, 67

"Cool and warm dust emission from M33 (HerM33es)", Xilouris, M., ..., **Anderl, S.** et al. 2012, A&A, 543, 74

"Magnetic fields in old supernova remnants", Gusdorf, A., Hezareh, T., **Anderl, S.**, Wiesemeyer, H., 2013, SF2A-2013: Proceedings of the Annual meeting of the French Society of Astronomy and Astrophysics, 399

PREFACE

This thesis is concerned with shocks in the interstellar medium, with a specific focus on shocks in dense molecular clouds. Shocks occur when matter moves into a medium at a velocity that exceeds the local sound speed - a condition that is easily met in many different astrophysical contexts. Therefore, shocks are ubiquitously found in the interstellar medium. They dissipate kinetic energy into heat and their passage modifies the physical and chemical conditions in the gas.

Shocks are therefore relevant for the studies of diverse environments and phenomena. They underlie the energetic feedback of supernovae, stellar winds, cloud-cloud collisions, or expanding H II regions. They have a major impact on the chemistry of the interstellar medium, and through the bright emission of shock-heated gas they provide excellent diagnostics for the chemical and physical conditions in the interstellar medium.

The theoretical understanding of shocks is complex because it comprises the description not only of the kinematics and multi-fluid magnetohydrodynamics (MHD) of gas and dust, but also of gas-phase and dust-surface chemistry in a large regime of temperatures and densities, of dust processing, of heating and cooling processes, and of radiation transport.

This complexity makes numerical shock models inevitable tools for the interpretation of observations of shocks, and in fact, of the emission from most of the dynamic ISM where kinetic energy is dissipated in weak shocks. These numerical models have been in constant evolution – assumptions get questioned, the effects of simplifications are critically examined or replaced by more accurate descriptions, and idealizations are progressively abandoned.

I have joined this modelling-enterprise in the first main project of my thesis, where I have implemented the numerical treatment of grain-grain processing into an existing MHD shock model. Such grain-grain processing was shown to be highly relevant in high-density environments by earlier studies. This implementation in a comprehensive MHD shock model code enabled me to investigate the observational consequences of this more accurate description of the dust evolution in magnetohydrodynamic shocks.

While the modelling of astrophysical phenomena requires an application of physical theories to particular astrophysical conditions and situations, it also relies on a comparison of model predictions with actual observations. Such a comparison is crucial for a proper understanding of the observed cosmic phenomenon, and at the same time it provides important clues for the adequacy and shortcomings of the models. It is this close interplay of modelling and observations that governs the progress of astrophysical research, and being involved in both activities has been a leading motivation during my doctoral studies.

Accordingly the second main project of my thesis is dedicated to the applications of numerical MHD shock models to astronomical observations. We observed regions in the interstellar medium where supernova remnants (SNRs) interact with molecular clouds. Such regions provide excellent case studies for the application of MHD shock models, yielding valuable information on the SNR's environment and its impact on the interstellar medium. Two SNRs that are known to interact with

ambient molecular clouds were investigated in this project. One was observed in various rotational transitions of CO with the APEX and SOFIA observatories. In addition, existing Spitzer observations of rotational H_2 emission were used in the analysis. The more detailed study of the other remnant, W44, was solely based on APEX observations of CO spectral line emission.

In summary, one may describe astrophysics as the endeavour to understand the nature of cosmic phenomena using models in the interpretation of astronomical observations. This understanding of astrophysical research is mirrored in the structure of my thesis. It starts with an introductory description of the phenomena under study: shocks, interstellar dust, and supernova remnants (Part I "Phenomena", Chapters 1–3). The second part is concerned with the numerical modelling of shocks with a focus on grain-grain processing (Part II "Models", Chapters 4–7), and the third part of this thesis is primarily based on astronomical observations of shocks produced in the interaction of supernova remnants with molecular clouds (Part III "Data", Chapters 8–14). The term "astronomical observation" abbreviates the complex processes of data generation, selection, processing and analysis. Therefore, observational research first of all means working with observational data, rather than directly investigating the observed phenomena.

The (philosophical) distinction between data and phenomena will be further motivated in the final part of my thesis (Part IV "Philosophy", Chapter 15), which contains philosophical reflections on astrophysics in general and on my own research in particular. They were motivated by an interdisciplinary research project of philosophers, historians and sociologists of science together with astrophysicists that I have helped to intiate in recent years.

CONTENTS

Part I

PHENOMENA

Phenomena [. . .] are not idiosyncratic to specific experimental contexts. We expect phenomena to have stable, repeatable characteristics which will be detectable by means of a variety of different procedures, which may yield quite different kinds of data.

James Bogen & James Woodward 1988

1

SHOCKS

In this chapter, we will give an introduction to the theory of shock waves. Depending on whether a magnetic field is relevant for the shock dynamics, hydrodynamic and magnetohydrodynamic shocks can be distinguished (Sect. 1.1 and 1.2, respectively). The general theoretical description of shocks typically relies on simplifying assumptions, such as stationarity, the magnetic field being oriented perpendicular to the shock direction, and the possibility of a one-dimensional treatment of the shock. The consequences of these assumptions being renounced are summarized in Sect. 1.3. Finally, Sect. 1.4 introduces the properties of shocks in the interstellar medium. This introduction is mainly based on the corresponding chapters of Draine (2010), Guillet (2008), Lequeux (2005), Tielens (2005), and Stahler & Palla (2004), and further publications as indicated in the text.

1.1 HYDRODYNAMIC SHOCKS

1.1.1 *J-type shocks*

Shock waves are common phenomena also in non-astrophysical contexts. For example, they are associated with sonic booms originating from airplanes travelling supersonically, or with supersonic pressure waves caused by explosions such as can be frequently seen in action movies. Based on these situations, we already have some basic intuition about the nature of shocks: they are related to matter moving at very high velocities, they cause an irreversible change in the medium, and this change happens faster than the shocked medium can react. The more formal definition of shock waves comprises these features: "A shock wave is a pressure-driven disturbance propagating faster than the signal speed for compressive waves, resulting in an irreversible change (i.e., an increase in entropy)" (Draine 2010). More specifically, shock waves lead to a compression, heating, and acceleration of the medium and thereby contribute to the dissipation of kinetic energy.

If the shock is faster than any signal-bearing speed in the medium, the preshock medium cannot receive any "warning" of the approaching disturbance. Therefore, the changes in the fluid properties (density, temperature, and velocity) occur so suddenly that they can be described as discontinuities in the fluid variables: the shock front, where the entropy is generated, is much thinner than the postshock relaxation layer. Shocks of this character are termed "Jump shocks" or "J-type shocks", accordingly.

1.1.2 *From sound waves to shocks*

Pressure perturbations propagate in a medium at the speed of sound. In an ideal gas the sound waves are adiabatic and reversible and their speed is given as

$$c_\mathrm{s} = \sqrt{\left(\frac{\partial P}{\partial \rho}\right)_\mathrm{s}} = \sqrt{\frac{\gamma P}{\rho}} = \sqrt{\left(\frac{\gamma k T}{\mu}\right)}, \tag{1}$$

where P is the gas pressure, ρ the density, k the Boltzmann constant, T the gas temperature, γ the ratio between the specific heats at constant pressure and at constant volume respectively (γ is $5/3$ for an atomic and $7/5$ for a diatomic gas), μ the molecular weight (about $1.5{\cdot}m_{\rm H}$ for atomic, $2.7{\cdot}m_{\rm H}$ for molecular, and $0.7{\cdot}m_{\rm H}$ for fully ionized gas, with $m_{\rm H}$ being the hydrogen mass). The speed of sound is proportional to the square root of the temperature but independent of pressure or density for an ideal gas. On earth this speed in dry air at 20°C is approximately 330 m s^{-1}, in a molecular gas at 10 K it is ~240 m s^{-1}, and in a highly ionized plasma at 10^7 K it is ~370 km s^{-1}.

If an obstacle is placed into a flowing gas, sound waves can propagate the information about the obstacle upstream and let the flow adapt, as long as the flow is subsonic. If the velocity of the flow approaches the speed of sound, the upstream fluid cannot receive this information in advance. The flow will then undergo a sudden transition from super- to subsonic in a discontinuous shock front. Correspondingly, when an object (e.g. an airplane) is moving through gas, sound waves are sent out and affect the medium ahead as long as the object's velocity is subsonic. If the object accelerates, the wave fronts ahead of the object cluster. When the velocity exceeds the speed of sound, a shock front and a so-called Mach cone, is created. This Mach cone separates the region reachable by sound waves from the region cut off from advance information.

Thus, the characteristic quantity to describe situations where shocks occur is the ratio of the disturbance velocity and the sound speed. This quantity is called the Mach number: $M = v/c_{\rm s}$. For $M < 1$ the flow is subsonic, while for $M > 1$ it is supersonic.

1.1.3 *The Rankine-Hugoniot relations*

The centrepiece in the physical description of J-type shocks is the description of the sharp change in fluid properties that occurs in the shock front. In order to simplify the problem, it is convenient to consider a steady, plane-parallel shock. If the x-coordinate denotes the direction normal to the shock front, this condition is equivalent to: $\partial/\partial t = 0$, $\partial/\partial y = 0$, and $\partial/\partial z = 0$. Furthermore, it is useful to treat the problem in the frame of reference moving with the shock. Accordingly, the shock front will be fixed in space and the upfront material is approaching the shock front at the shock velocity, where it is then suddenly decelerated. The motion of a hydrodynamic fluid is governed by the conservation of mass, momentum, and energy. Given our approximations, these reduce to (see e.g. Landau & Lifshitz 1987; Lequeux 2005; Draine 2010)

$$\frac{\partial}{\partial x}(\rho v_x) = 0\,, \tag{2}$$

$$\frac{\partial}{\partial x}(\rho v_x^2 + p - \sigma_{xx}) = -\rho\,\frac{\partial \Psi_{\rm grav}}{\partial x}\,, \tag{3}$$

and

$$\frac{\partial}{\partial x}\left(\frac{1}{2}\rho v_x v^2 + U v_x + p v_x - v_j\,\sigma_{jx} - \kappa\frac{{\rm d}T}{{\rm d}x} + \rho v_x \Psi_{\rm grav}\right) = \Gamma - \Lambda\,, \tag{4}$$

where σ_{xx} is the viscous stress tensor, $\Psi_{\rm grav}$ the gravitational potential, $U = p/(\gamma - 1)$ the internal energy per unit volume, κ the conductivity, Γ the heating and Λ the cooling rate per volume. To obtain

the jump conditions these equations are integrated across the shock front. The integration boundaries x_1 (preshock) and x_2 (postshock) are chosen just outside the shock transition layer, such that the viscous stress tensor, which is only large within the transition layer, is vanishing at these locations. Because the shock front is very thin, the gravitational potential is assumed to be the same in locations x_1 and x_2, such that the corresponding terms cancel out in the integration. For the same reason, the integrated net heating rate and radiative losses can be neglected. If heat conduction is also assumed to be negligible and the frame of reference is chosen such that $v_y = v_z = 0$ in the preshock gas, the Rankine-Hugoniot jump conditions can be written as

$$\rho_1 v_1 = \rho_2 v_2 \,, \tag{5}$$

$$\rho_1 v_1^2 + p_1 = \rho_2 v_2^2 + p_2 \,, \tag{6}$$

$$v_1\left(\frac{\rho_1 v_1^2}{2} + \frac{\gamma}{\gamma-1}p_1\right) = v_2\left(\frac{\rho_2 v_2^2}{2} + \frac{\gamma}{\gamma-1}p_2\right) . \tag{7}$$

With the preshock conditions being known, these three equations, (5), (6), and (7), contain three unknowns. The system of equations has two solutions. The first one is the trivial solution where all physical variables stay constant across the shock front. The second solution describes the transition between the supersonic and the subsonic medium. The fluid variables and Mach numbers can then be expressed as functions of values of the pre- and postshock pressure p_1 and p_2 (Guillet 2008). One obtains

$$\frac{\rho_2}{\rho_1} = \frac{v_1}{v_2} = \frac{(\gamma-1)p_1 + (\gamma+1)p_2}{(\gamma+1)p_1 + (\gamma-1)p_2} \,, \tag{8}$$

$$\frac{T_2}{T_1} = \frac{\mu_2}{\mu_1}\,\frac{p_2}{p_1}\left(\frac{(\gamma+1)p_1 + (\gamma-1)p_2}{(\gamma-1)p_1 + (\gamma+1)p_2}\right) , \tag{9}$$

$$v_1 = \sqrt{\frac{(\gamma-1)p_1 + (\gamma+1)p_2}{2\,\rho_1}} = V_\mathrm{s} \,, \tag{10}$$

$$v_2 = \frac{(\gamma+1)\,p_1 + (\gamma-1)\,p_2}{\sqrt{2\rho_1[(\gamma-1)\,p_1 + (\gamma+1)\,p_2]}} \,, \tag{11}$$

$$M_\mathrm{s} = \sqrt{\frac{(\gamma-1)p_1 + (\gamma+1)p_2}{2\gamma p_1}} = M_1 \,, \tag{12}$$

$$M_2 = \sqrt{\frac{(\gamma+1)p_1 + (\gamma-1)p_2}{2\gamma p_2}} = M_1 \,, \tag{13}$$

where V_s is the shock velocity and M_s the adiabatic shock Mach number.

1.1.4 *Strong shocks*

For a strong shock ($M_\mathrm{s} \gg 1$ or equivalently $p_2 \gg p_1$) the Rankine-Hugoniot relations derived in the previous section can be further simplified to (Guillet 2008)

$$\rho_2 = \left(\frac{\gamma+1}{\gamma-1}\right)\rho_1 \tag{14}$$

$$= 4\,\rho_1 \quad \text{for} \quad \gamma = 5/3\,, \tag{15}$$

$$V_\mathrm{s} = \sqrt{\frac{(\gamma+1)p_2}{2\,\rho_1}} = v_1\,, \tag{16}$$

$$v_2 = \left(\frac{\gamma-1}{\gamma+1}\right)V_\mathrm{s} = \sqrt{\frac{(\gamma-1)^2\,p_2}{2\,(\gamma+1)\,\rho_1}} \tag{17}$$

$$= \frac{1}{4}V_\mathrm{s} \quad \text{for} \quad \gamma = 5/3\,, \tag{18}$$

$$T_2 = \frac{\gamma-1}{\gamma+1}\,\frac{p_2}{p_1}\,\frac{\mu_2}{\mu_1}\,T_1 = \frac{2\,(\gamma-1)\,\mu_2 V_\mathrm{s}^2}{(\gamma+1)^2\,k} \tag{19}$$

$$= \frac{3}{16}\,\frac{\mu_2 V_\mathrm{s}^2}{k} \quad \text{for} \quad \gamma = 5/3\,, \tag{20}$$

$$p_2 = \frac{2\gamma}{\gamma+1}M_\mathrm{s}^2 p_1 \tag{21}$$

$$= \frac{5}{4}M_\mathrm{s}^2 p_1 \quad \text{for} \quad \gamma = 5/3\,. \tag{22}$$

Accordingly, for an atomic gas with $\gamma = 5/3$ the preshock gas is decelerated to $1/4$ of its previous velocity across the shock transition in a strong J-type shock (or, in the preshock gas reference frame, accelerated to $3/4\ V_\mathrm{s}$) and is compressed by a factor of 4. The expression for the postshock temperature can immediately be derived from energy conservation in the shocked fluid frame, where the upstream kinetic energy per particle, $1/2\,\mu_2(V_\mathrm{s}-v_2)^2$, must equal the thermal energy per particle, $3/2\,kT_2$, in the postshock gas (McKee & Hollenbach 1980). The decrease in ordered kinetic energy leads to a strong increase of the internal energy per unit mass of the postshock medium, given by

$$u = \frac{1}{\gamma-1}\,\frac{p_2}{\rho_2} = \frac{9}{32}\,V_\mathrm{s}^2\,. \tag{23}$$

The dissipated kinetic energy that is not converted into thermal energy is consumed by compression forces that keep the decelerated gas in pressure equilibrium with the postshock gas. This illustrates that, more precisely, it is not the energy $\rho(u+v^2/2)$, which is conserved across the shock discontinuity but the enthalpy $\rho(h+v^2/2)$, see Guillet (2008). We note that the postshock temperature depends on the molecular weight μ. For neutral H I we have $\mu = 1.273\,m_\mathrm{H}$ and $\mu = 0.609\,m_\mathrm{H}$ for fully ionized gas (Draine 2010).

1.1.5 *Radiative shocks*

Behind the shock transition the hot gas can cool by emitting radiation[1]. A strong radiative shock can be schematized as consisting of four different zones (Draine & McKee 1993): In the preshock gas a "radiative precursor" is formed where the upfront gas is irradiated, heated, and partly ionized by photons emitted from the shocked gas. In the "shock transition", where the ordered kinetic energy

1 If the postshock gas is very hot and tenuous, however, radiative cooling will be inefficient and the shock will be non-radiative, see e.g. Subsect. 3.2.2

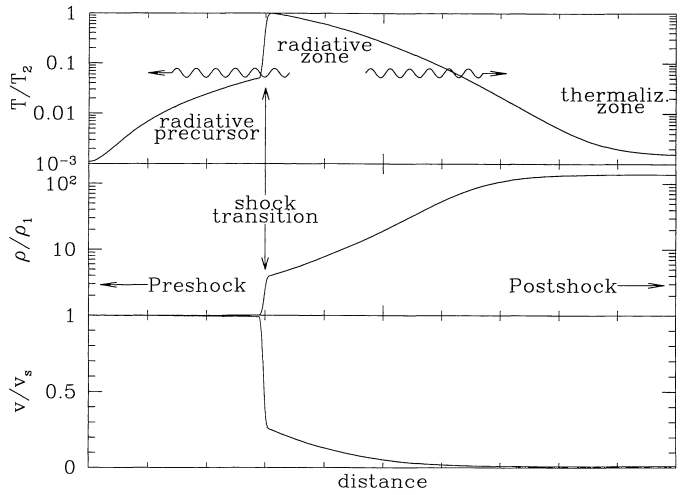

Figure 1: Schematic structure of a strong hydrodynamic shock wave: temperature, density and velocity relative to the values ρ_1, V_s, and T_2 just behind the shock transition. Extracted from Draine & McKee (1993).

is dissipated into heat, the preshock gas is then decelerated and compressed. The hot postshock gas subsequently cools by radiating its energy and is further compressed in this "radiative zone". Finally, far downstream in the "thermalization zone" the shocked gas reaches a near-equilibrium between heating and cooling. These different zones are sketched in Fig. 1.

Shocks in which the gas finally cools to a temperature T_3 that equals the preshock temperature T_1 are called "isothermal". To determine the fluid variables at that point far downstream the Rankine-Hugoniot relations can be used. However, the assumption that radiative losses can be neglected is obviously not justified anymore and the equation stemming from conservation of energy has to be replaced by $T_3 = T_1$. For this case one obtains

$$\rho_1 v_1 = \rho_3 v_3 \,, \tag{24}$$

$$\rho_1 v_1^2 + p_1 = \rho_3 v_3^2 + p_3 \,, \tag{25}$$

$$\frac{p_1}{\rho_1} = \frac{p_3}{\rho_3} \qquad (T_1 = T_3) \,. \tag{26}$$

Equations (24), (25), and (26) show that an isothermal shock leads to a strong compression of the postshock gas compared to the value of 4 taking place in the shock transition. One obtains

$$\frac{\rho_3}{\rho_1} = \frac{v_1}{v_3} = \frac{\rho_1 V_s^2}{p_1} = M_{\rm iso}^2 \,, \tag{27}$$

with $M_{\rm iso}$ being the isothermal Mach number defined as the ratio of the shock speed and the isothermal sound speed. However, it is important to note that this strong compression is also a consequence of the one-dimensional nature of the equations: it prevents the gas from its natural relaxation and from reaching a state of pressure equilibrium with its surrounding medium. Furthermore, the existence of a transverse magnetic field in the preshock gas would create an additional pressure term counteracting the compression, as will be shown in Sect. 1.2. The ratio of the pressure values is the same as the ratio of the densities, given as

$$\frac{p_3}{p_1} = M_{\rm iso}^2 \,. \tag{28}$$

Compared to the increase in pressure within the shock transition (see Eq. (22)) the radiative cooling leads to an increase in pressure of only a factor $1/3$ relative to the pressure immediately behind the shock transition. The postshock gas can therefore be considered as isobaric.

1.2 MAGNETOHYDRODYNAMIC SHOCKS

While in some aspects the equations developed in Sect. 1.1 are only slightly modified by the presence of a magnetic field, magnetohydrodynamic (MHD) fluids give rise to additional wave modes within the magnetized medium that allow for the existence of an additional class of shocks. These shocks are named "C-type" shocks and differ quite radically from the already discussed J-type shocks. This kind of shocks will be described in Subsect. 1.2.4 after the general description of MHD fluids has been introduced.

1.2.1 *Rankine-Hugoniot relations*

The presence of a magnetic field affects the conservation of momentum and energy by adding magnetic pressure and energy to the fluid. This yields

$$\frac{\partial}{\partial x}\left(\rho v_x^2 + p + \frac{(B_y^2 + B_z^2)}{8\pi} - \sigma_{xx}\right) = -\rho\frac{\partial \Psi_{\rm grav}}{\partial x} \ , \tag{29}$$

and

$$\frac{\partial}{\partial x}\left(\frac{1}{2}\rho v_x v^2 + U v_x + p v_x + \frac{(B_y^2 + B_z^2)}{8\pi} v_x - \frac{B_x B_y v_y}{4\pi} \right.$$
$$\left. - \frac{B_x B_z v_x}{4\pi} - v_j\,\sigma_{jx} - \kappa\frac{{\rm d}T}{{\rm d}x} + \rho v_x \Psi_{\rm grav}\right) = \Gamma - \Lambda \ , \tag{30}$$

where all symbols have the same physical meaning as in equations (2) – (4), and where B denotes the magnetic field strength. Furthermore, the presence of a magnetic field adds an equation of conservation of magnetic flux, given as

$$\frac{\partial \boldsymbol{B}}{\partial t} = \nabla \times (\boldsymbol{v} \times \boldsymbol{B}) \ . \tag{31}$$

The electric field vanishes in the frame co-moving with the plasma because the plasma is assumed to be a perfect conductor. Furthermore, it is assumed that the magnetic field is "frozen" into the fluid, a situation that is known under the label "frozen field" assumption. The flux-freezing condition is expressed as $\boldsymbol{E} + (\boldsymbol{v}/c) \times \boldsymbol{B} = 0$ (McKee & Hollenbach 1980).

For a transverse magnetic case with $B_x = B_z = 0$ with the same assumptions as adopted in Subsect. 1.1.3 the Rankine-Hugoniot relations become (see e.g. McKee & Hollenbach 1980)

$$\rho_1 v_1 = \rho_2 v_2 \,, \tag{32}$$

$$\rho_1 v_1^2 + p_1 + \frac{B_1^2}{8\pi} = \rho_2 v_2^2 + p_2 + \frac{B_2^2}{8\pi} \,, \tag{33}$$

$$v_1\left(\frac{\rho_1 v_1^2}{2} + \frac{\gamma}{\gamma-1}p_1 + \frac{B_1^2}{8\pi}\right) = v_2\left(\frac{\rho_2 v_2^2}{2} + \frac{\gamma}{\gamma-1}p_2 + \frac{B_2^2}{8\pi}\right) . \tag{34}$$

$$v_1 B_1 = v_2 B_2 \,. \tag{35}$$

Equations (33) and (35) show that in a one-dimensional, one-fluid, transverse shock the magnetic field follows the fluid compression as

$$B_2 = B_1 \frac{\rho_1}{\rho_2} \,. \tag{36}$$

This system of equations can be solved for the compression of the gas (Draine 2010). One obtains

$$\frac{\rho_2}{\rho_1} = \frac{2(\gamma+1)}{D + \sqrt{D^2 + 4(\gamma+1)(2-\gamma)M_{\rm A}^{-2}}} \,, \tag{37}$$

$$D \equiv (\gamma-1) + 2M_{\rm s}^{-2} + \gamma M_{\rm A}^{-2} \,, \tag{38}$$

$$M_{\rm A} \equiv \frac{V_{\rm s}}{B_1/\sqrt{4\pi\rho_1}} \,, \tag{39}$$

with $M_{\rm A}$ being the Alfvén Mach number. Compressive solutions exist if the following conditon is fullfilled

$$V_{\rm s} > V_{\rm ms} \equiv \sqrt{\frac{\gamma p_1}{\rho_1} + \frac{B_1^2}{4\pi\rho_1}} \,. \tag{40}$$

The physical meaning of this equation will be discussed in Subsect. 1.2.3. For a strong adiabatic shock with $M \equiv V_{\rm s}/V_{\rm ms} \gg 1$ the jump conditions in an atomic gas with $\gamma = 5/3$ yield the same relations between the values across the shock transition in the co-moving shock frame as in the hydrodynamic case: the gas is compressed by a factor 4, decelerated to $1/4$ of its velocity, and the temperature is raised to a value equivalent to $3/16$ of the shock kinetic energy.

1.2.2 *Isothermal MHD shocks*

In the treatment of isothermal shocks , where the temperature in the postshock gas T_3 finally returns to its preshock value T_1, the influence of the magnetic field is to counteract the compression of the gas. This can be seen if equations (38) and (39) are evaluated for an isothermal shock with $\gamma = 1$. For this case one obtains

$$\frac{\rho_3}{\rho_1} = \frac{4}{2M_{\rm iso}^{-2} + M_{\rm A}^{-2} + \sqrt{\left(2M_{\rm iso}^{-2} + M_{\rm A}^{-2}\right)^2 + 8M_{\rm A}^{-2}}} \,. \tag{41}$$

In the limit of a very strong magnetic field, the Alfén Mach number is much smaller than the isothermal Mach number, but according to equation (40) still larger than 1. Evaluation of equation (41) with $(1 < M_{\rm A} \ll M_{\rm iso})$ then yields

$$\frac{\rho_3}{\rho_1} = \sqrt{2} M_{\rm A} \ll M_{\rm iso}^2 \,. \tag{42}$$

Compared to the case of non-magnetic isothermal shocks, where the compression equals $M_{\rm iso}^2$, the compression for isothermal MHD-shocks is much weaker because it is dominated by the magnetic pressure.

1.2.3 *MHD wave modes*

The definition of the Alfén Mach number as well as condition (40) already hinted at the existence of additional wave modes in an MHD fluid. In fact, there are compressive "slow" and "fast", and non-compressive "intermediate" waves with the following speeds (Draine & McKee 1993)

$$v_{\rm F} = \frac{1}{\sqrt{2}}\sqrt{\left(v_{\rm A}^2 + c_{\rm s}^2\right) + \sqrt{v_{\rm A}^4 + c_{\rm s}^4 - 2v_{\rm A}^2 c_{\rm s}^2 \cos 2\theta}}\,, \tag{43}$$

$$v_{\rm I} = v_{\rm A}\cos\theta\,, \tag{44}$$

$$v_{\rm S} = \frac{1}{\sqrt{2}}\sqrt{\left(v_{\rm A}^2 + c_{\rm s}^2\right) - \sqrt{v_{\rm A}^4 + c_{\rm s}^4 - 2v_{\rm A}^2 c_{\rm s}^2 \cos 2\theta}}\,, \tag{45}$$

$$\tag{46}$$

with $v_{\rm A}$ being the Alfvén speed

$$v_{\rm A} \equiv \frac{B}{\sqrt{4\pi\rho}}\,, \tag{47}$$

θ the angle between the direction of wave propagation and $\boldsymbol{B}$, and ρ the density of matter coupled to the magnetic field. Alfén waves travel parallel to the magnetic field lines and distort these lines without changing the magnitude of the field. They are, however, able to change the polarization of the field. For oblique incidence relative to the magnetic field these waves correspond to the intermediate wave modes. The compressive fast and slow wave modes behave similar to a hydrodynamic sound wave and change the magnitude of the field but not its plane of polarization. Because they are subject to the thermal and the magnetic pressure their velocity is higher than for hydrodynamic sound waves. The slow wave modes (as well as the intermediate modes) are not able to propagate perpendicular to the magnetic field. Thus, for $\theta = \pi/2$ only fast modes exist (other cases are discussed in Subsec. 1.3.2) , then called "magnetosonic waves", which travel at a speed of

$$v_{\rm ms} = \sqrt{c_{\rm s}^2 + v_{\rm A}^2}\,. \tag{48}$$

Getting back to equation (40), we can now see that compressive, perpendicular shocks satisfying the Rankine-Hugoniot relations are only allowed if the shock speed exceeds the speed of magnetosonic waves. However, as the magnetosonic speed $v_{\rm ms}$ is higher than the adiabatic sound speed the possibility of supersonic shocks slower than the magnetosonic waves arises. From equation (47) it follows that the magnetosonic speed is indeed much larger than the sound speed for strong magnetic fields and a low density of matter coupled to the magnetic field. These conditions are often met in interstellar clouds with low fractional ionization where the charged fluid component, coupled to the magnetic field, decouples from the neutral fluid component. In this case, there is a broad range of shock velocities lower than the magnetosonic speed. These shocks, which are not described by the jump conditions, give rise to a new class of shocks, the so-called C-type shocks.

1.2.4 *C-type shocks*

In 1971, D. J. Mullan pointed out that for predominantly neutral gas with a low fraction of ionization in shocked magnetized clouds it is not enough to simply add magnetic terms to the Rankine-Hugoniot relations in order to understand the compression of the magnetic field. Precisely, the problem is how the kinetic energy of mostly neutral gas can be converted into magnetic field energy if the classical "frozen field" assumption is not valid anymore. In a partially ionized gas, the passage of a shock leads to a decoupling of ions and neutrals and a difference in the corresponding fluid temperatures. In order to amplify the magnetic field, occasional collisions between ions and neutrals have to induce a drift of the ions along the shock direction. However, due to the low ionization the length scale of field amplification is much larger than the atom-atom mean free path, which defines the width of the shock transition in a single-fluid shock. Mullan supposed that for slow shocks with strong magnetic fields the supersonic flow can lead to an increase of the magnetic field without an increase in entropy and therefore to a continuous shock transition. For faster shocks, a discontinuity remains in the neutral fluid while the electron and ion fluids change their variables continuously. In any case, Mullan (1971) questioned the assumption of an infinitesimally narrow shock transition as it had been the standard in the shock literature by then.

Draine (1980) followed this route of a multi-fluid shock description and discussed transverse MHD shocks with magnetic precursors. As announced in the previous section, these shocks are slower than the magnetosonic speed, so that magnetosonic waves are able to travel ahead of the shock front and a "magnetic precursor" arises. Therefore, the ions are able to adapt to the arrival of the shock already before the shock front arrives, and the fluid variables of the ion fluid change in a continuous way. Due to ion-neutral scattering the discontinuity in the neutral fluid can then disappear as well. These shocks, where all fluid variables change continuously, are termed "C-type shocks" (Draine 1980)[2]. In these shocks the entropy is generated over a broad region, such that heating and cooling take place simultaneously. Accordingly, C-type shocks are less hot than J-type shocks and molecules are at most partially dissociated. Therefore, a characteristic feature of C-type shocks is therefore strong H_2 emission (e.g. Wilgenbus et al. 2000). This made them very attractive in the interpretation of observations of regions of star formation in the Orion molecular cloud OMC-1, where the molecular gas was observed to move at high velocities, emitting strongly in ro-vibrational lines of molecular hydrogen (Draine et al. 1983). J-type shock models, which predict H_2 to be completely dissociated already for moderate shock velocities, were not able to explain these observations. Furthermore, the ion-neutral streaming is able to drive endothermic chemical ion-neutral reactions, which yield a very characteristic, rich chemistry in C-type shocks.

1.2.5 *Multi-fluid equations*

In order to describe the decoupling of the neutral and the ion fluid for shocks in media with low fractional ionization and a magnetic field, the magnetohydrodynamic equations have to be evaluated for each fluid separately and complemented by exchange terms of mass, momentum and energy between

2 It is interesting that Mullan (1971) already talked about "C-shocks". However, in his case the "C" does not stand for "continuous", but for "carbon" and denotes shocks that solely contain carbon ions.

the different fluids (Draine 1980; Draine et al. 1983; Flower et al. 1986; Draine 1986). The three flow components considered are neutrals, ions, and electrons (subscript n, i, and e, respectively). Electrons and ions are assumed to move at the same velocity, as otherwise electric fields would outbalance the velocity difference. Again, a steady, one-dimensional flow (along the z-direction) is considered, with the electric field vanishing in the co-moving shock frame of reference in the absence of viscosity and thermal conduction. This yields the following fluid equations from conservation of particle number density, mass, momentum, and energy (Draine 1980; Flower et al. 1985)

$$\frac{\mathrm{d}}{\mathrm{d}z}\left(\frac{\rho_\mathrm{n} v_\mathrm{n}}{\mu_\mathrm{n}}\right) = N_\mathrm{n}\,, \tag{49}$$

$$\frac{\mathrm{d}}{\mathrm{d}z}\left(\frac{\rho_\mathrm{i} v_\mathrm{i}}{\mu_\mathrm{i}}\right) = N_\mathrm{i}\,, \tag{50}$$

$$\frac{\mathrm{d}}{\mathrm{d}z}\left(\rho_\mathrm{n} v_\mathrm{n}\right) = S_\mathrm{n}\,, \tag{51}$$

$$\frac{\mathrm{d}}{\mathrm{d}z}\left(\rho_\mathrm{i} v_\mathrm{i}\right) = -S_\mathrm{n}\,, \tag{52}$$

$$\frac{\mathrm{d}}{\mathrm{d}z}\left(\rho_\mathrm{n} v_\mathrm{n}^2 + \rho_\mathrm{n}\frac{kT_\mathrm{n}}{\mu_\mathrm{n}}\right) = A_\mathrm{n}\,, \tag{53}$$

$$\frac{\mathrm{d}}{\mathrm{d}z}\left(\rho_\mathrm{i} v_\mathrm{i}^2 + \rho_\mathrm{i}\frac{k\left(T_\mathrm{i}+T_\mathrm{e}\right)}{\mu_\mathrm{i}} + \left(\frac{V_\mathrm{s}}{v_\mathrm{i}}\right)^2\left(\frac{B_0^2}{8\pi}\right)\right) = -A_\mathrm{n}\,, \tag{54}$$

$$\frac{\mathrm{d}}{\mathrm{d}z}\left(\frac{1}{2}\rho_\mathrm{n} v_\mathrm{n}^3 + \frac{\rho_\mathrm{n} v_\mathrm{n}}{\mu_\mathrm{n}}\left(\frac{5}{2}kT_\mathrm{n} + u_\mathrm{n}\right)\right) = B_\mathrm{n}\,, \tag{55}$$

$$\frac{\mathrm{d}}{\mathrm{d}z}\left(\frac{1}{2}\rho_\mathrm{i} v_\mathrm{i}^3 + \frac{5}{2}\rho_\mathrm{i} v_\mathrm{i}\frac{k\left(T_\mathrm{i}+T_\mathrm{e}\right)}{\mu_\mathrm{i}} + v_\mathrm{i}\left(\frac{V_\mathrm{s}}{v_\mathrm{i}}\right)^2\left(\frac{B_0^2}{4\pi}\right)\right) = B_\mathrm{i}\,, \tag{56}$$

$$\frac{\mathrm{d}}{\mathrm{d}z}\left(\frac{5}{2}\rho_\mathrm{i} v_\mathrm{i}\frac{k\left(T_\mathrm{i}-T_\mathrm{e}\right)}{\mu_\mathrm{i}}\right) = B_\mathrm{e}\,, \tag{57}$$

where the magnetic field is compressed with the ion fluid as

$$B = B_0\left(\frac{V_\mathrm{s}}{v_\mathrm{i}}\right)\,. \tag{58}$$

The source terms are defined as follows: N_n and N_i are the numbers of neutral particles and ions created per unit volume and time; S_n is the mass source term describing how much ion-electron mass is converted into neutral mass per unit volume and time; A_n gives the momentum transferred from the ion-electron fluid to the neutral fluid per unit volume and time; B_n, B_i, and B_e are energy source terms for the neutral, ion and electron fluid, respectively, and u_n is the mean internal energy per neutral particle. In addition, the abundances of all atomic and molecular species are to be calculated using

$$\frac{\mathrm{d}}{\mathrm{d}z}\left(n_\alpha v_\alpha\right) = C_\alpha\,, \tag{59}$$

with C_α being the rate at which the species α is formed through chemical reactions per unit volume and time.

So, while for J-type shocks the most crucial information about the shock can be obtained by evaluating the jump conditions across the shock front, for C-type shocks it is necessary to integrate the full set of differential equations for the fluid variables and the chemical abundances including heating and cooling processes for all fluid components across the whole shock.

1.3 BEYOND THE "STANDARD" SHOCKS

In the previous sections some common assumptions were applied in the derivation of the shock equations. While some of them, such as the neglect of thermal conduction or viscosity outside the shock transition, can be justified in most situations, others are more difficult to motivate. Most prominently, the adoption of stationarity, of a one-dimensional geometry, and of a purely transverse magnetic field is problematic in many applications. Correspondingly, the consequences of these assumptions have to be evaluated. The following sections will give a short review on modelling efforts taking time-dependence and more realistic geometries into account.

1.3.1 *Non-stationary shocks*

The question whether the assumption of a stationary shock structure is justified is a crucial one, particularly for C-type shocks in which the ion-neutral coupling, the central process determining the shock structure, is very slow. Chieze et al. (1998) explored the time-dependent structure of shocks in dark and diffuse interstellar clouds. For J-type shocks, the relevant time-scale to attain a steady state is set by the postshock cooling. They found that for a slow shock at a velocity of 10 km s^{-1} propagating into a dark cloud with a density of 10^3 cm^{-3} a stationary state is attained after 2000 years. In contrast, the time for C-type shocks to reach a stationary state in a dark cloud is much longer; with the same preshock density and shock velocity as before but for a magnetic field strength of $B = 10\mu$G Chieze et al. (1998) found the necessary time to be more than 10^5 years. For times $t \leq 10^4$ years, they found a discontinuity remaining in the neutral flow, while for larger times the stationary solution is delineated by the time-dependent calculation. This behaviour was found for a range of magnetic field strengths typical for the interstellar medium. For shocks in diffuse clouds (preshock density $n_H = 25$ cm^{-3}, $B = 5\mu$G, and $V_s = 10$ km s^{-1}) direct photoreactions are possible. Thus, the degree of ionization is higher than in dark clouds and the coupling between the ion and the neutral fluid is enhanced. Accordingly, the time to reach a stationary state is less than in dark clouds. At the same time, the neutral fluid reaches higher temperatures due to the enhanced coupling, the sound speed becomes higher, and discontinuities in the flow of the neutral fluid remain, also after a stationary state has been reached.

In order to avoid a computation of the fully time-dependent shock equations, the structure of these time-dependent shocks can approximately be modelled by means of truncated stationary shocks for non-dissociative velocities (Lesaffre et al. 2004b, based on Lesaffre et al. 2004a). This semi-analytical approach relies on the finding that stable solutions of the time-dependent shock simulation are in a quasi-steady state. A similar idea had already been applied earlier in the interpretation of shocks in supernova remnants (Raymond et al. 1988). The temporal evolution of non-dissociative C-type shocks reveals a shock structure consisting of a magnetic precursor in a quasi-steady state, followed by a non-dissociative adiabatic front and a relaxation layer. A snapshot of this structure can then be approximated by a combination of a truncated J- and a truncated C-type shock, where the entrance parameters and lengths auf both shock components have to be determined as described in Lesaffre et al. (2004b).

1.3.2 *Oblique shocks*

In Subsect. 1.2.3 we have seen that for shocks propagating in a direction not perpendicular to the magnetic field three MHD wave modes are possible parallel to the direction of shock propagation: slow, fast, and intermediate waves. Assuming a strongly ionized plasma where no decoupling between charged and neutral particles occurs, one has to distinguish different classes of shocks, depending on the relation between the shock velocity and these different wave velocities (Draine & McKee 1993). Accordingly, "fast" shocks are faster than the fast wave modes in the preshock gas and slower than these in the postshock gas, "slow" shocks have velocities lying between the ones of intermediate and slow wave modes in the preshock gas and are slower than the slow wave modes in the postshock, and finally "intermediate" shocks make a transition from super-intermediate to sub-intermediate velocities. In fast shocks, the magnitude of the magnetic field is enhanced but its direction is not changed. The latter is also true for slow shocks, while here the magnetic field strength is decreased in magnitude. Only intermediate shocks can both change the magnitude of the magnetic field and change its direction. If the magnetic field is parallel to the shock front, there exist "switch-on" solutions, in which the postshock flow acquires a transverse magnetic field. The nature and existence of these different classes of shocks is still under debate.

The multi-fluid MHD equations for the case of oblique shocks were developed by Chernoff (1987) and Wardle & Draine (1987). Chernoff (1987) found that in astrophysical environments super-Alfvénic shocks are rarely intermediate but rather C- or strong J-type shocks. Wardle & Draine (1987) studied oblique shocks in diffuse molecular clouds, where the structure of C-type shocks turned out to be only weakly dependent on the angle θ between the direction of shock propagation and the direction of the magnetic field. Focusing on a more realistic modelling of grains in oblique shocks, (Pilipp & Hartquist 1994) brought about another feature of oblique shocks in dark molecular clouds: large grains in high-density environments introduce a Hall resistivity and create a current occurring parallel to the magnetic field component transverse to the shock propagation. This current induces a rotation of the transverse magnetic field around the direction of shock propagation. This effect was shown to be strongest for single-sized grains and small angles of θ (Van Loo et al. 2009). However, it mostly disappeared when small grains were also included.

Furthermore, recent work combining dust processing with an oblique multi-fluid model (Van Loo et al. 2012) shows that the destruction of dust, or more precisely the sputtering, also depends on the angle between the magnetic field and the shock normal. However, compared with models of perpendicular shocks the fraction of sputtered material still exhibits the same order of magnitude. One might conclude that, although the work done so far on oblique shocks has shown deviations from the perpendicular cases, perpendicular shocks seem to provide a satisfying approach to the shock physics.

1.3.3 *More-dimensional shocks*

Although shocks are frequently approximated as plane-parallel structures, which can be described within a one-dimensional framework, the geometry of shocks is of course more complex. Observations often reveal shocks as bow-shaped structures, with the ambient material being compressed

and pushed aside. The effect of a bow shock geometry can be schematically understood as a three-dimensional superposition of one-dimensional shocks. The bow shock will have its strongest effect at its apex, which often may correspond to dissociative J-type shocks (e.g. Smith & Brand 1990; Smith et al. 2003). Accordingly, this apex will be visible in optical and ultraviolet emission. Because the shock speed is locally given as the component of the bow speed transverse to the bow's surface it can be described as $V_\mathrm{s} = v_\perp = v_\mathrm{bow} \sin\alpha$, where α is the angle between the surface element and the shock direction and v_bow is the velocity of the bow structure. This means that down the bow wings the shocks become C-type and are hence mostly visible in rotational molecular and atomic fine-structure emission. Because the gas is decelerated perpendicular to the bow surface while its parallel component is preserved the postshock gas will nearly move along the sides of the curved shock front. Therefore, the bow shock geometry has consequences for the resulting spectroscopic line profiles (e.g. Brand et al. 1989). Depending on the orientation of the bow-shock relative to the line-of-sight, the profile is significantly broadened and might obtain a double-peaked shape, the latter stemming from the strong radiation at the apex on the one hand and the large emission-area of the bow wings (Stahler & Palla 2004).

Full more-dimensional grid computations of shocks require strong simplifications on the part of the ingoing microphysics (see e.g. Fragile et al. 2005). In order to keep a high level of detail with respect to the ingoing physics, an alternative to more-dimensional grid-calculations is the construction of a more-dimensional shock structure out of one-dimensional plane parallel shock models (Kristensen et al. 2008; Gustafsson et al. 2010). However, such a construction requires the determination of additional new parameters, such as the velocity-, density-, and magnetic field strength profiles along the bow shock's surface, together with the explicit shape of that surface (Kristensen 2007).

1.4 SHOCKS IN THE INTERSTELLAR MEDIUM

Shocks are ubiquitous events in the interstellar medium. They are caused by strong stellar winds, the radiation of young massive stars creating expanding H II regions, colliding clouds, jets and outflows in the context of star formation, by large scale galactic spiral density waves and by supernova explosions (e.g. McKee & Hollenbach 1980). They play a central role for the energy budget of the interstellar medium because they convert bulk kinetic energy into heat and turbulence. The shocks penetrating the interstellar medium as supernova remnants are responsible for the hot and tenuous "third" phase of the interstellar medium (McKee & Ostriker 1977). Thereby, they determine the pressure of the interstellar medium and influence the transition of gas between different interstellar phases: cold clouds evaporate and are converted into diffuse gas, while diffuse gas is swept up by supernova blast waves and compressed in high-pressure shells of radiative supernova remnants. The understanding of shocks is therefore closely related not only to the understanding of particular local phenomena, but also to the understanding of the evolution of the entire galaxy.

1.4.1 *J-type shocks in the interstellar medium*

The heating and compression of the interstellar medium in J-type shocks leads to a considerable change in the chemistry of the postshock gas. Fast shocks cause collisional dissociation of molecular

hydrogen up to a degree that depends on the shock speed and the preshock density. The atomic hydrogen can then chemically attack other molecules (Tielens 2005) and give rise to their dissociation. The high temperatures obtained in shocks enable endothermic chemical reactions among neutral species. A rich carbon and oxygen chemistry is therefore encouraged by the warm postshock temperatures if molecular hydrogen is present (e.g. Hollenbach & McKee 1989). In this case, atomic oxygen is converted into OH, H_2O, and O_2. After the gas has cooled sufficiently, molecules are reformed and the ion-molecule chemistry typical for dark clouds becomes relevant.

The temperature structure of the postshock gas in J-type shocks is characterized by a two-plateau-appearance: The first plateau at a temperature of $\sim 10^4$ K can be attributed to the temperature sensitivity of H I excitation due to electron collisions, which arises because electrons at lower thermal velocities are not able to excite the electronic levels of hydrogen. The second plateau, further in the postshock gas at a temperature of ~500 K, arises when the formation of H_2 on grain surfaces is heating the gas due to the vibrational excitation of newly formed H_2 (e.g. Stahler & Palla 2004).

1.4.2 *Cooling of J-type shocks*

The radiation emitted by J-type shocks obviously depends on the shock velocity. For very fast J-type shocks, as found in young supernova remnants, the postshock temperature can be higher than 10^6 K, such that X-rays are emitted. Slower, but still fast, shocks will radiate mostly in ultraviolet (UV) and optical wavelengths. The excitation in the postshock gas will be dominated by inelastic electron collisions that excite electronic levels within ions or atoms of abundant metals and permitted lines of neutral H, if present. Photons stemming from the latter process are resonantly scattered until they can escape as Lyα emission. Excitation due to proton collisions is important for the excitation of neutral atomic fine-structure lines. The UV radiation created in the hot postshock gas causes a radiative precursor in the preshock gas that leads to photodissociation and ionization in that gas.

Finally, recombination of hydrogen starts in the cooling postshock gas, giving rise to corresponding optical recombination lines. As the temperature is not high enough anymore to allow for permitted transitions within the metal atoms, the excitation of metastable states becomes relevant for the cooling. At low temperatures ($T < 5000$ K), the cooling is dominated by fine-structure lines of neutral atoms or ions. Finally, molecules are reformed that contribute to the shock cooling in the far-infrared and millimetre regime due to rotational emission (e.g. McKee & Hollenbach 1980; Hollenbach & McKee 1989; Stahler & Palla 2004; Lequeux 2005; Tielens 2005).

Shocks can be distinguished from photoionized gas in the optical regime as they also exhibit strong lines from low excitation species, because the recombination zone is much more extended than the zone of complete ionization. Thus, line ratios such as [S II]λ6717,6731/Hα and [O I]λ6300/Hα are much higher in shocks (Lequeux 2005). Also, lines of [Fe II] can be used as shock tracer because iron in H II regions is mostly present in higher ionisation states. Furthermore, the entropy generation in fast shocks is able to create higher temperatures than obtained from photoionization. The discrimination from photodissociation regions in the infrared is more difficult. The lack of PAH emission in shocks, characteristic for gas illuminated by far-ultraviolet photons, can be used as a discriminator (Tielens 2005). In addition, the [O I]λ63μm/[C II]λ158μm ratio is often cited as being much higher in shocks than in photodissociation regions (the quoted value deciding between both phenomena is

~10), because high postshock temperatures and densities in shocks favour [O I] while C^+ is rapidly converted to CO (Hollenbach & McKee 1989). The most uncontroversial chemical tracers of shocks, however, stem from the processing of dust grains that results in a strong enhancement of otherwise strongly depleted species, such as silicon and silicon-bearing species.

1.4.3 *C-type shocks in the interstellar medium*

While C-type shocks do not reach the high temperatures of J-type shocks, they are still warm enough to lead to a rich molecular chemistry that produces large amounts of OH and H_2O. Furthermore, ambipolar diffusion between ions and neutrals allows for endothermic ion-neutral reactions. The latter effect has been utilized in order to understand the formation of CH^+ (e.g. Pineau des Forêts et al. 1986). As for J-type shocks, dust processing is very important in C-type shocks (see Chapter 5) and enriches the gas-phase chemistry with species that are otherwise heavily depleted by dust in quiescent dark molecular clouds. These species, like SiO, can be used as clear shock tracers.

1.4.4 *Cooling of C-type shocks*

C-type shocks predominantly emit at infrared and sub-mm wavelengths. Because they are too slow to substantially dissociate molecular hydrogen, rotational lines of H_2 contribute strongly to the cooling. Furthermore, they strongly emit in atomic fine-structure lines, such as [O I] (63 and 146 μm), [C I] (370 and 610 μm), or [S I] (25 μm) and in molecular rotational lines. The latter stem from abundant molecules such as CO, H_2O, OH, CH_3OH, or NH_3. Particularly prominent shock tracing lines, enhanced by the effect of dust processing, originate from rotational transitions in SiO molecules. The chemistry and cooling of C-type shocks is subject of Chapter 5 and will be further elaborated there.

2

INTERSTELLAR DUST

Approximately 1% of the gas mass in the interstellar medium is contained in dust grains. Although this might not sound much, interstellar dust plays an important role in astrophysics for several reasons. It attenuates starlight by absorption and scattering and gives rise to thermal emission, predominantly in infrared and sub-millimetre wavelengths. It furthermore plays an important role for the chemistry of the interstellar medium because it provides a chemical reaction surface, notably controlling the formation of molecular hydrogen this way. The gas phase abundances of elements are regulated by dust as it locks up a large fraction of heavy elements in its cores and in icy mantles and releases them again in the course of dust processing. Moreover, it is also an important heating agent due to the process of photoelectric heating. In this chapter, some key properties of interstellar dust are introduced, i.e., its size distribution (Sect. 2.1), its composition (Sect. 2.2), its possible destruction processes (Sect. 2.3), and its dynamics (Sect. 2.4). The following chapter is mainly based on the corresponding chapters of Draine (2010) and Tielens (2005), and further publications as indicated in the text.

2.1 SIZE DISTRIBUTION

The size distribution of interstellar grains can be inferred from their interaction with stellar radiation as displayed in the so-called extinction curve, which shows the attenuation of the starlight by dust as a function of wavelength. Mathis et al. (1977) fittet the observed interstellar extinction for wavelengths between 0.11 μm and 0.1 μm using a dust model with uncoated, spherical particles consisting of graphite, enstatite, olivine, silicon carbide, iron, and magnetite. They found a variety of mixtures to yield satisfying fits, but these mixtures always included graphite to create the observed feature of the extinction curve at $\lambda 2160$. The particle size distribution they derived follows a power-law with an exponent between -3.3 and -3.6. This distribution is referred to as "MRN" (named after the authors Mathis, Rumpl & Nordsieck) distribution, given as

$$\frac{\mathrm{d}n_{\mathrm{g}}(a)}{\mathrm{d}a} \propto a^{-3.5} \,, \tag{60}$$

where $n_{\mathrm{g}}(a)$ is the dust size distribution and a the dust radius. Mathis et al. (1977) adopted grain sizes of the graphite grains between 0.005 μm and 1 μm and of olivine grains between 0.005 μm and 0.25 μm. It is noteworthy that in this distribution the large grains contain most of the mass, while the small grains have most of the surface.

More recent observations revealed a variation of the interstellar extinction depending on different interstellar environments. This variation can be characterized by a dimensionless parameter $R_V \equiv A_V/(A_B - A_V)$, where A_B and A_V are the extinctions measured in the B (4405Å) and V (5470Å) photometric bands. On average the value of this parameter is approximately 3.1 in the diffuse medium, but values of $R_V = 2.1$ and 5.7 have also been observed (Cardelli et al. 1989; Fitzpatrick 1999).

Extinction curves corresponding to higher values of R_V, as observed for dense clouds, are reproduced by models with significantly fewer small grains and a modest increase of the distribution at larger sizes (Weingartner & Draine 2001). This lack of small grains might hint at coagulation taking place in dense environments. Lower values of R_V, on the other hand, suggest the presence of many small grains, probably being the product of shattering of larger grains. Given the frequent occurrence of shocks leading to the disruption of large grains, it remains an open question how an efficient reformation of large grains can be explained, although it seems clear that the bulk of interstellar dust must have been grown in the ISM (Draine 2009).

Furthermore, observed IR emission features of HII regions, reflection nebulae, diffuse interstellar clouds, and surfaces of dark clouds suggest a population of large molecules, which bridge the grain population towards the molecular domain. These IR emission features are due to vibrational relaxation and have helped to identify this population as polycyclic aromatic hydrocarbons (PAHs), containing some 50 C atoms. The population of PAHs seems to be quite abundant: 10% of the elemental carbon is believed to be locked up in these species.

2.2 COMPOSITION OF INTERSTELLAR DUST

The question of the composition of dust is somewhat difficult and its answer still widely uncertain, because the absorption by dust in the optical and UV appears as a continuum and the observed spectral features are broad and hard to identify. One way to identify the constituents of dust grains is via abundance constraints. Assuming the elemental abundances in the solar photosphere to be representative for the interstellar medium, one can compare the observed gas-phase abundances with the solar values and take the difference as the contribution of heavy elements to the dust mass. Draine (2010) presents such an analysis towards ζOph and arrives at ∼28% of the dust mass being composed of carbon, and ∼72% of species like Mg, Al, Si, Ca, Fe, Ni and O, probably contained in silicates. On this basis, spectral features present in the interstellar extinction curves can be attributed to certain materials. One very prominent feature is found at $\lambda = 2175$ Å (already described in the paper of Mathis et al. 1977 as lying at 2160 Å), which is attributed to small graphite grains, either 200 Å graphite spheres or graphite prolate spheroids with a size of 30 Å (Tielens 2005). Furthermore there are broad features at 9.7 and 18 μm due to Si-O stretching and bending modes in amorphous silicate grains. Another feature is found at 3.4 μm, which is probably due to the C-H stretching mode in hydrocarbons. There are some more features, referred to as diffuse interstellar bands, which cannot be absorption lines of atoms, ions or small molecules due to their broad line width. Their identification is still largely uncertain, although they could be due to free-flying, possibly ionized, molecules (Draine 2010). Furthermore, there is strong evidence for large amounts of silicate material, as traced by emission features of radiation-heated dust near 10 μm. Based on the interstellar absorption it seems like the silicate material is rather amorphous than crystalline. The fraction of crystalline silicates is less than 5×10^{-3} (Tielens 2005). However, crystalline silicates can be abundant in certain environments especially close to stars. In dense molecular clouds dust grains attain icy mantles, containing various molecules such as H_2O, CO_2, NH_3, or CH_3OH, as observed by absorption features in the infrared spectra of irradiated dense clouds.

2.3 DUST PROCESSING

Variations in the assumed grain size distribution among different environments in the interstellar medium hint at the occurrence of dust processing, for example in interstellar shocks. There are processes changing the dust-to-mass ratio and processes conserving this ratio. Accretion, sputtering and vaporisation belong to the former group, shattering and coagulation to the latter.

The accretion of gas-phase species increases the radii of the dust grains. Because the rate of adsorption is to a first order proportional to the grain cross-section, the thickness of the accreted grain mantle will be the same for all different grain sizes. Therefore, most of the mantle material is found on the smallest grains and lets them basically disappear. For the refractory elements, accretion can still occur at dust temperatures as high as 1000 K, while icy mantle formation requires lower temperatures of ≈100 K (Guillet et al. 2008). The growth of mantles is counteracted by desorption processes, such as photodesorption and cosmic ray induced desorption.

Sputtering of dust grains is caused by atoms or ions impinging on the dust surface and eroding that surface. There are two types of sputtering, one that is due to high temperatures of the gas, thus termed thermal sputtering, and one due to relative motions of the dust relative to the gas, termed inertial sputtering. Thermal sputtering is only relevant for temperatures higher than 10^5 K (Draine & Salpeter 1979). The sputtering yields depend on the impact energy, mass and charge of the projectile, and on the chemical composition of the target. Thermal sputtering removes a layer of equal thickness for all dust grain sizes. Therefore, it leads to a preferred destruction of small grains. Inertial sputtering, on the other hand, requires impact velocities of ≃30–40 km s^{-1} (Tielens et al. 1994). The effect of inertial sputtering depends on the dust dynamics and therefore on the grain size. Vaporization of grains also releases grain material into the gas phase. It occurs when grains collide with impact velocities of more than ≃20 km s^{-1} (see Chapter 5).

Collisions of dust grains also lead to the shattering of grains into smaller fragments. This can already happen at velocities of a few km s^{-1}. This process obviously has a central influence on the dust size distribution. However, its theoretical description is very involved because it requires detailed knowledge of the dust dynamics. Guillet et al. (2007); Guillet et al. (2009) and Guillet et al. (2011) have undertaken a multi-fluid modelling approach for the dust dynamics, following the detailed size and charge distribution of grains, in order to study the impact of shattering on shocks. Chapter 5 includes subsequent work on this problem and presents the influence of shattering and vaporization on the molecular line emission of C-type shocks.

Finally, coagulation is believed to be responsible for the formation of larger grains in dense molecular clouds. If grains collide at low velocities, the exact value depending on the dust composition and the radius, dust grains can stick together. Chokshi et al. (1993) report that micron-sized quartz particles can coagulate at collision velocities less than 10^2 cm s^{-1}, while centimetre-sized grains require velocities below 10^{-2} cm s^{-1}. The presence of an icy mantle promotes the possibility of grains sticking together.

Dust processing in shocks is the topic of Chapter 5 and a more detailed description of, in particular, vaporization and shattering will be found therein.

2.4 GRAIN DYNAMICS

The charging of dust is a significant parameter for the understanding of the grain dynamics due to the ubiquitous presence of magnetic fields. It is set by a balance of different processes such as positive ion and electron attachment, photo-electric emission induced by the radiation field, charge transfer between grains and ions, atoms, or molecules, and at high densities secondary electron emission due to collisions with ions or energetic electrons. The grain charge is typically negative and proportional to the grain radius and the electron-ion temperature (McKee et al. 1987; Draine & Sutin 1987). In C-type shocks in dense clouds, photo-induced processes can be ignored as well as secondary electron emission, which requires high electron/ion impact energies. Therefore, the charge in C-type shocks in dense clouds is set by the interplay of electron attachment and ion recombination (Guillet et al. 2011).

The motion of interstellar grains is mainly determined by magnetic forces and gas drag. The magnetic field leads to a gyration of dust grains around the magnetic field lines, experiencing a force $\boldsymbol{F_B} = m_{\rm gr}\, \boldsymbol{v} \times \boldsymbol{\omega}_B$, with $m_{\rm gr}$ being the grain mass and $\boldsymbol{\omega}_B \equiv q\boldsymbol{B}/m_{\rm gr}$ being the cyclotron frequency (with grain charge q and the magnetic field $\boldsymbol{B}$). For an increasing magnetic field, as can be found in postshock regions, dust grains can undergo betatron acceleration due to conservation of their magnetic moment $\mu_{\rm gr} = m_{\rm gr} v^2/(2B)$.

Drag forces, on the other hand, are generated by colliding atoms or ions and therefore tend to damp the grain gyration: $F_{\rm drag} \propto \rho_{\rm gr} v_{\rm gyr}^2 a^2$, where $v_{\rm gyr}$ is the gyration velocity, $\rho_{\rm gr}$ the grain mass density and a the grain radius. The force per mass acting on grains due to drag forces is therefore anti-proportional to the grain radius, and thus stronger for small dust grains. A more detailed description of the multi-fluid grain dynamics in J- and C-type shocks is found in Guillet et al. (2007); Guillet et al. (2009); Guillet et al. (2011).

For our study of shattering and vaporization, the interplay between gas drag and magnetic forces on dust grains is a central element because it determines the degree of dust processing due to grain-grain processing (Guillet et al. 2011). In particular, it explains the catastrophic self-enhancement of shattering in high-density environments.

With respect to the dust dynamics in shocks, one has to distinguish between large grains (≥ 100Å) and small grains (≤ 100Å). The dynamics of the large grains is not affected by charge fluctuations. After they have entered a C-type shock, their gyration is rapidly damped by gas drag and they basically follow the motion of the ions. For small grains, on the other hand, charge fluctuations lead to stochastic dynamics. Due to their small inertia, gyration can be ignored and depending on their charge they follow the neutral or the ion fluid.

If fragmentation occurs, small grains cause a drastic depletion of electrons from the gas phase. The ionisation of the gas becomes extremely low and dust grains become the dominant charge carrier. As a result of this lack of electrons in the gas phase, the large grains cannot sustain their high negative charge anymore and they finally become positive. The largest grains are affected first by this effect due to their highest cross-section. As the charge of these grains goes through zero, their coupling to the magnetic field weakens and is overcome by gas drag. They are decoupled from the magnetic field and start gyrating again when they attain high positive charge. This gyration gets damped again by gas drag, but this phase subjects the large grains to high-velocity grain-grain collisions and subsequent

shattering. At the same time, the lack of electrons in the gas phase increases the lifetimes of small neutral grains, such that they have enough time to couple to the neutral gas and are able to crater the surfaces of larger grains that are moving with the charged fluid. The large effect of grain-grain processing in high-density environments is a result of these feedback effects, that only end when the ions and neutrals move at a common speed again and the shock is over.

3

SUPERNOVA REMNANTS

This chapter introduces the phenomenon of supernova explosions (Sect. 3.1) and their subsequent evolution (Sect. 3.2). The great importance of these explosions for the interstellar medium is illustrated within the three phase model of the interstellar medium (Sect. 3.3). Finally, we will focus on the effect of an inhomogeneos medium on the evolution of supernova remnants (Sect. 3.4), and the ability of these remnants to accelerate cosmic ray particles. This introduction is mainly based on the corresponding chapters of Draine (2010), Lequeux (2005), and Tielens (2005), and further publications as indicated in the text.

3.1 SUPERNOVA EXPLOSIONS

Supernova explosions (SNe) constitute the most luminous and violent events in the interstellar medium. They occur when massive stars ($M > 8\ M_{Sun}$) end their lives in an explosion due to gravitational core-collapse or when white dwarfs reignite nuclear fusion after accretion of matter from a binary companion. In each case, substantial fractions of the stellar mass are ejected into the surrounding medium. The last supernova observed in the Milky Way was Kepler's Supernova in 1604. The closest observed supernova explosion since then took place in the Large Magellanic Cloud as SN1987A. The Galactic rate of supernova explosions is assumed to be one event every 40 ± 10 yr (Tammann et al. 1994).

Different types of supernovae are distinguished. Historically, the first classification was introduced between SNe of Type II, which show hydrogen lines in their spectra, and SNe of Type I, which do not. This broad classification has been refined since then. While Type Ia supernovae constitute the "classical" Type I SNe, another Type Ib has been introduced that lacks the SiII λ6355 Å blueshifted feature at λ6150 Å (Weiler & Sramek 1988). This latter class is less luminous than Type Ia and shows lines of helium. SNe lacking the silicon feature as well as clear helium lines are classified as Type Ic. Type Ia supernovae correspond to a scenario where a substantial fraction of a white dwarf's matter undergoes nuclear fusion. Because this mechanism depends on the mass of the white dwarf, the peak luminosity of these explosions is very uniform and makes them excellent standard candles for distance determination. Type II SNe correspond to the explosion of massive stars. These stars would have already influenced the surrounding interstellar medium by ejecting matter in stellar winds. When they finally undergo a core-collapse because at some point nuclear fusion is not able to counteract the gravitational pressure anymore, the ejecta from this explosion first encounter the matter previously ejected in winds. If the exploding star is in a late Wolf-Rayet stage where hydrogen has disappeared, the explosion following core collapse will belong to Type Ib. In both cases, the matter that is not ejected ends up as a black hole or a neutron star, depending on the star's initial mass. A remnant pulsar can emit high-energy particles of which the electrons will give rise to synchrotron radiation. The class of Type II SNe has also been further separated. Type II-L and Type II-B SNe

are distinguished depending on whether they show or show not a temporary flattening in their light curves between one to three months after their maximum (Weiler & Sramek 1988). Type II SNe are usually fainter than Type Ia SNe. The kinetic energy that is ejected is of the order of $\sim 10^{51}$ ergs for all supernovae.

3.2 EVOLUTIONARY PHASES

The evolution of supernova remnants can be described as passing through several phases (e.g. Woltjer 1972). In the classic description of these phases, it is assumed that the supernova explosion forms a spherical shell and that the remnant expands isotropically into a homogeneous medium. Although this condition is not met in the interstellar medium, it is useful in order to understand the main characteristics of the different phases.

3.2.1 *The free expansion phase*

The initial velocity of the ejecta is quite high. Depending on the mass of the ejecta (1.4 M_{Sun} for Type Ia SNe and up to 20 M_{Sun} for Type II SNe), the mean velocity is of the order of several tens of thousands km s^{-1}. Because the density of the ejecta is much higher than that of the surrounding medium, the expansion occurs at nearly constant velocity. However, the density of the ejecta drops and so does the thermal pressure. When it becomes less than the pressure of the surrounding interstellar medium, a reverse shock is formed travelling through the ejecta and shock-heats them. The free expansion phase ends when the mass of the swept-up interstellar material is of the same order as the ejected mass. This is the case after some 100 years, depending on the ejected mass, energy, and the density of the surrounding medium. The radius of the supernova remnant is about 2 pc then (Draine 2010).

3.2.2 *The Sedov-Taylor Phase*

When the free expansion phase is over, the reverse shock has heated the interior of the SNR to very high temperatures ($\sim 10^8$ K). The high temperatures and low densities prevent the gas from efficiently radiating away its energy, and the further evolution can be described as being adiabatic. The pressure of the SNR is much higher again than that of the surrounding medium and is driving the expansion, which can be approximately described as a point explosion. This yields a self-similar solution for the temporal evolution of the spatial density, velocity, and pressure distribution of the remnant (Sedov 1993). Combining this ansatz with the Rankine-Hugoniot relations as boundary conditions, the so-called Sedov-Taylor solution can be obtained. The temperature in the remnant increases towards the centre while the density falls steeply. The mass of the ejecta is highly concentrated towards the outer shell: 50% of the mass is found in the outer 6.1% of the remnant's radius (Draine 2010). Within this solution thermal conduction is neglected, an assumption that has been questioned in recent modelling approaches (e.g. Cox et al. 1999; Kawasaki et al. 2005). The general effect of thermal conduction is to level out temperature gradients. However, this effect is strongly reduced perpendicular to the field

lines of a magnetic field. The Sedov-Taylor phase ends when the post-shock temperature has fallen to about 10^6 K such that radiative losses become important. Typically, this is the case after some ten thousands of years at a radius of about 20 pc when the shock velocity has fallen to about 200 km s^{-1}.

3.2.3 *The radiative phase*

When the temperatures allow the nuclei of abundant metals to recombine with electrons, these ions can be collisionally excited by electrons and efficiently contribute to the cooling of the gas. The overpressure of the SNR's interior relative to the surrounding medium still drives the expansion but the hot interior gas is now enclosed by a dense shell of gas that cools radiatively. The mass of the shell increases as it sweeps up the ambient gas, the radiative phase is therefore also called "snowplow phase". Depending on whether the internal pressure of the hot interior is accounted for or not, the radial momentum of the cool shell is either assumed to increase or to be constant. The former, more realistic, approach is referred to as pressure-modified snowplow phase. In this case, ignoring the external pressure, the evolution can again be described in a self-similar way. The radiative phase ends when the shock velocity approaches the sound speed of the interstellar medium and turns into a sound wave. The hot gas of the remnant's interior will then spread out into the interstellar medium where it contributes to the hot phase of the medium. This will typically be the case after some 10^6 years when the remnant's size is about 40 pc.

3.3 THE THREE PHASE MODEL OF THE ISM

The interstellar medium can be described as containing different phases. These phases can be characterized by different temperatures, densities, and ionization fractions. Considering the atomic interstellar medium, these different phases can be understood in terms of stable configurations in pressure equilibrium, as arising from different heating and cooling processes. While for the cold atomic gas the cooling is dominated by forbidden lines (predominantly the [CII]λ158μm line), for the warm gas several cooling mechanisms, such as visible electronic transitions of oxygen and HI Lyα radiation, become important. These cooling mechanisms keep the gas temperature at about 100 K and 5000 K, respectively. Pressure equilibrium then sets the densities of these phases as about 30 cm^{-3} for the cold neutral medium (CNM) and 0.6 cm^{-3} for the warm neutral medium (WNM). Molecular clouds condense out of the cold neutral medium if this becomes gravitationally unstable. Typically, they are not counted as "phase" of the interstellar medium because their existence is not based on thermal equilibrium but rather on the predominance of self-gravity. Their cooling is dominated by rotational transitions of molecules. Furthermore, a warm, low-density, ionized component is observed and can be attributed to the photoionization by OB stars. This classic two-phase model (cold and warm atomic gas) of the interstellar medium dates back to the late 1960s (Field et al. 1969). However, observations have revealed a large amount of hot, low-density gas in the interstellar medium originating from supernova explosions. Therefore, the simple two-phase model of the interstellar medium cannot be complete. Accordingly, McKee & Ostriker (1977) suggested a three-phase model of the interstellar medium. Supernova explosions in a cloudy medium cause the evaporation of cold clouds and lead to the formation of dense shells. This mass balance together with the energy balance between super-

nova shock input and radiative losses determines the density and the temperature of this additional phase, the hot intercloud medium (with an estimated density of $n = 10^{-2.5}$ cm^{-3} and a temperature of $T = 10^6$ K). The supernova remnant will expand in the low-density intercloud gas. Estimations based on the two-phase model of the ISM show (e.g. Draine 2010) that supernova remnants will finally overlap with other supernova remnants, filling a large volume of the ISM with hot gas. Thus, the pressure of the ISM is maintained by supernova remnants. Its value can be estimated based on the kinetic energy per supernova explosion, the mean density of the ISM, the galactic supernova rate per volume, and the condition of overlapping SNRs (see e.g. Draine 2010). The understanding of the interstellar medium is therefore closely linked to that of supernovae and supernova remnants.

3.4 EXPANSION IN AN INHOMOGENEOUS MEDIUM

Contrary to the assumption of an homogeneous interstellar environment applied in Sect. 3.2, supernova remnants will encounter clouds or filaments during their expansion. This situation was studied by Cox & Smith (1974) or McKee & Ostriker (1977). If the interstellar medium is seen as consisting of cool clouds being embedded in a hot phase, the supernova remnant will expand into that tenuous gas, passing around the dense clouds. The blast wave then applies a pressure on the cloud surface, given by the density of the intercloud medium ρ_{ICM} and the shock speed v_{s}, and drives a shock wave into the cloud. If the shocked material is roughly in pressure equilibrium with the surrounding medium, the velocity v_{cs} of this internal shock is given as

$$v_{\mathrm{cs}} = \sqrt{\frac{\rho_{\mathrm{ICM}}}{\rho_{\mathrm{c}}}}\, v_{\mathrm{s}} \,, \tag{61}$$

where ρ_{c} is the density of the cloud (see e.g. Lequeux 2005; Draine 2010). As the density contrast between the intercloud medium and the clouds can amount to a factor of a few thousands, the difference in the shock velocities will approximately correspond to a factor of 100. The resulting velocities of the shocks within the molecular clouds will then typically be intermediate velocity J- and C-type shocks, which give rise to strong radiation in the IR and sub-mm regime. Depending on the magnetic field of the clouds and their mass, the shock creates velocity gradients within the cloud and might cause instabilities, which can destroy the clouds. After the passage of the shock, the clouds are immersed in very hot gas. Thermal conduction will transport heat into the cloud and leads to evaporation. Thereby, the mass density of the intercloud medium is increased and its temperature drops. Large clouds, however, will be able to cool radiatively and can gain material by the condensation of the hot medium (McKee & Ostriker 1977).

3.5 COSMIC RAY ACCELERATION

Supernova remnants are believed to be sites of particle acceleration and the origin of high-energy galactic cosmic rays. The composition of cosmic rays is dominated by protons, but they also contain relativistic electrons, He, and nuclei of heavier elements. In the 1970s (e.g. Axford et al. 1977; Krymskii 1977), it was shown that cosmic rays could be created in shocks by first order Fermi acceleration. Particles can be scattered by electromagnetic fluctuation back and forth between the pre-

and postshock medium. In each round trip, the particle gains energy. The particle can be imagined as being trapped in between two converging mirrors, one moving at the preshock velocity and the other at the velocity of the postshock fluid (Draine 2010). It can be shown that this process leads to a power-law distribution of particle momenta in steady state, where the power-law index depends on the acceleration time and the escape time. The observed value of this power-law index is $\alpha \approx 2.65$ for $10 \leq E/\mathrm{GeV} \leq 10^7$ (Draine 2010). It still remains unclear, however, how particles enter the acceleration process with enough energy, such that they are not quickly thermalized by Coulomb scattering. This problem is referred to as "injection problem". This problem could be related to first-order Fermi acceleration of dust grains where subsequent grain processing would be able to insert high-velocity atoms into the plasma (Slavin et al. 2004; Guillet et al. 2009).

Cosmic rays can be most directly observed by synchrotron emission of relativistic electrons. Furthermore cosmic rays give rise to γ-ray emission when they interact with nuclei in gas or dust. This radiation comprises different components: relativistic electrons create bremsstrahlung and they upscatter photons via the inverse Compton effect. Proton-proton collisions, on the other hand, create neutral pions, which then decay into γ-rays. Emission of the leptonic component dominates for energies less than 150 MeV while the hadronic component dominates for higher energies.

Part II

MODELS

In physics it is usual to give alternative theoretical treatments of the same phenomenon. We construct different models for different purposes, with different equations to describe them. Which is the right model, which the 'true' set of equations? The question is a mistake. One model brings out some aspects of the phenomenon; a different model brings out others. Some equations give a rougher estimate for a quantity of interest, but are easier to solve. No single model serves all purposes best.

Nancy Cartwright 1983

4

INTRODUCTION

4.1 GRAIN-GRAIN PROCESSING IN C-TYPE SHOCKS

Guillet et al. (2007, 2009, 2011) have demonstrated that shattering and the accompanying vaporisations are indispensable ingredients of shock modelling. For preshock densities higher than $\sim 10^5$ cm^{-3}, shattering becomes dramatically self-enhanced and yields a severe change of the shock structure due to a strong increase of the total geometrical grain cross-section. The shocks become much hotter and thinner and vaporization releases depleted species into the gas phase. In order to model these consequences of shattering and vaporization, Guillet et al. (2007, 2009, 2011) applied a multi-fluid appproach to the dust dynamics together with a detailed calculation of the grain charge distribution. Their studies left open a series of issues. In particular, they covered only a very limited range of shock parameters and did not examine the effect of a variation in the magnetic field strength. They also did not study the consequences of shattering and vaporization for the molecular line emission. These questions are however crucial for the use of these modelling results in the interpretation of actual astronomical observations. In our study, which is presented in Chapter 5, we aimed at addressing these questions by implementing the effects of shattering and vaporization into the "standard" 2-fluid shock model, as it has been developed in the groups of Guillaume Pineau des Forêts and David Flower since the 1980s.

4.2 THE SHOCK MODEL

The shock model we have used is a one-dimensional, steady-state, 2-fluid model of plane-parallel C-type shocks. At its heart, it solves the magnetohydrodynamical equations as presented in Sect. 1.2.5 in parallel with a large chemical network (more than 100 species and approximately 1000 reactions). This network includes ion-neutral reactions, neutral-neutral reactions, charge transfer, radiative and dissociative recombination. The populations of the H_2 ro-vibrational levels are computed at each integration step. This is possible without the need of a detailed treatment of the radiative transfer because the radiation of H_2 is optically thin. In addition, the cooling lines of the most abundant atomic metals and their ions are computed in detail.

The model is also able to calculate the stationary chemical state of the preshock medium before the actual shock calculation is performed. The fractional elemental abundances of gas-phase species and species contained in grain cores and mantles as well as the fractional abundances of the chemical species composing the grain mantles can be found in Tables 1 and 2 of Flower & Pineau des Forêts (2003). Main input parameters of the model are the number of fluids, the preshock magnetic field strength, the preshock hydrogen density, and the shock velocity. It is furthermore possible to specify the initial H_2 ortho/para ratio (we used a value of 3), the initial gas temperature (we used a value of

10 K), the initial grain temperature (we used a value of 15 K), and the cosmic ray ionization rate (we used a value of 10^{-17} s^{-1}).

4.3 GRAIN-GRAIN PROCESSING IN THE 2-FLUID MODEL

Figure 2 shows a schematic flow chart of the dust treatment in the basic shock model as described by Flower & Pineau des Forêts (2003). As will be shown in the subsequent chapter, the most prominent consequence of dust shattering is the enhanced exchange of energy and momentum between the ion and the neutral fluid due to the increase of the total grain cross-section (red box in Fig. 2). The momentum exchange due to elastic scattering between charged grains and the neutral fluid without the influence of grain-grain processing is described by a corresponding source term (in g cm^{-2} s^{-2})

$$A_{\mathrm{grain,n}} = \rho_{\mathrm{n}} n_{\mathrm{grain}} \pi \langle r_{\mathrm{grain}} \rangle^2 |v_{\mathrm{i}} - v_{\mathrm{n}}| (v_{\mathrm{i}} - v_{\mathrm{n}}) \frac{n_{\mathrm{G-}} + n_{\mathrm{G+}}}{n_{\mathrm{G-}} + n_{\mathrm{G+}} + n_{\mathrm{G0}}}, \tag{62}$$

with ρ_{n} being the neutral mass density, n_{grain} the total grain number density, $\langle r_{\mathrm{grain}} \rangle$ the mean radius of grains and $n_{\mathrm{G-}}$, $n_{\mathrm{G+}}$, and n_{G0} the number densities of the negatively and positively charged, and of the neutral grains. If the effect of shattering is included in the model, this source term needs to grow through the shock wave in accord with the calculations presented in Guillet et al. (2011). In order to achieve this growth we have multiplied $A_{\mathrm{grain,n}}$ by an additional factor that varies with the spatial coordinate, z, through the shock wave. This factor is introduced in Appendix A of the following chapter. As can be seen from Fig. 2, the rate of energy exchange between neutrals and grains due to elastic diffusion is derived from $A_{\mathrm{grain,n}}$ and therefore adapted automatically, while the rate of energy exchange between neutrals and grains through thermalization with grains needs to be multiplied with the same factor as $A_{\mathrm{grain,n}}$. The change of these source terms gives the major contribution to the narrowing of shock temperature profiles as presented in Fig. 4.

The increase in the total grain cross-section also influences the chemistry, especially the formation of H_2 and HD on grains (green box in Fig. 2). Grain processing originating from interactions between grains and gas is treated with the use of pseudo-chemical reactions in the shock code. These grain processing reactions have to be adapted to the change in the total grain cross-section as well. These processes are cosmic ray induced desorption from grains, sputtering of grain mantles, erosion of grain cores, and adsorption of gas-phase species on grains. All these processes are displayed in Fig. 2 in yellow boxes.

However, the consequences of shattering for energy- and momentum exchange, for the chemistry, and for gas-grain interactions are only indirect results of the most direct consequence of shattering: the change in the dust size distribution. Therefore shattering first of all changes the total grain particle density (in the flow chart labelled "Dens_GRAIN"), the mean radius, area, volume and mantle thickness of the grains. The computation of all these mean grain properties relies on the total grain particle density, which is assumed to follow the compression of the ions as

$$n_{\mathrm{grain}} = n_{\mathrm{grain,init}} \frac{V_{\mathrm{s}}}{v_{\mathrm{i}}}, \tag{63}$$

if shattering is neglected. Therefore, if this grain particle density is influenced such that it leads to the desired increase in the total grain cross section, the other mean properties of the grains (displayed in blue in Fig. 2) are adapted automatically[1].

The modelling of dust in the shock code differentiates numerically between different aspects of the dust physics: mean dust properties rely on the total grain particle density n_{grain} while the chemical aspects of gas-grain interactions are described using chemical core- and mantle species that are treated in parallel to the gas-phase species. If it comes to the physics of grain charging, there are yet three additional chemical species: G_+, G_-, and G_0 (the three different representations of the dust particle density are displayed in orange in Fig. 2). The particle density of these species is determined by charge transfer processes, such as electron attachment and electron detachment by the radiation field as well as attachment of and neutralization by positive ions. If the total grain particle density is increased as a consequence of shattering, this has to be consistent with the sum of the particle densities of the charged and neutral species. Therefore, we introduced additional shattering source terms in the differential equations governing the number densities of neutral, positively, and negatively charged grains, as described in Appendix A of the subsequent chapter. The process of vaporization, the release of gas-phase species as a by-product of grain shattering, is introduced as another pseudo-chemical reaction, numerically parallel to the other pseudo-chemical reactions describing changes in the dust-to-gas ratio.

All different influences of grain shattering on the different parts of the code were tested separately in the development of the approximations in order to guarantee the consistency of the description of grain physics within the shock model. By implementing the effects of shattering and vaporization into a version of the shock code including a large velocity gradient (LVG) treatment of the radiative transfer, we were able to study the effects of grain-grain processing on molecular line emission. This study is presented in the subsequent chapter.

1 Their values also rely on the mass densities of the chemical species bond in grain mantles and cores, the particle densities of which are integrated together with the densities of the gas-phase species (upper right part of Fig. 2).

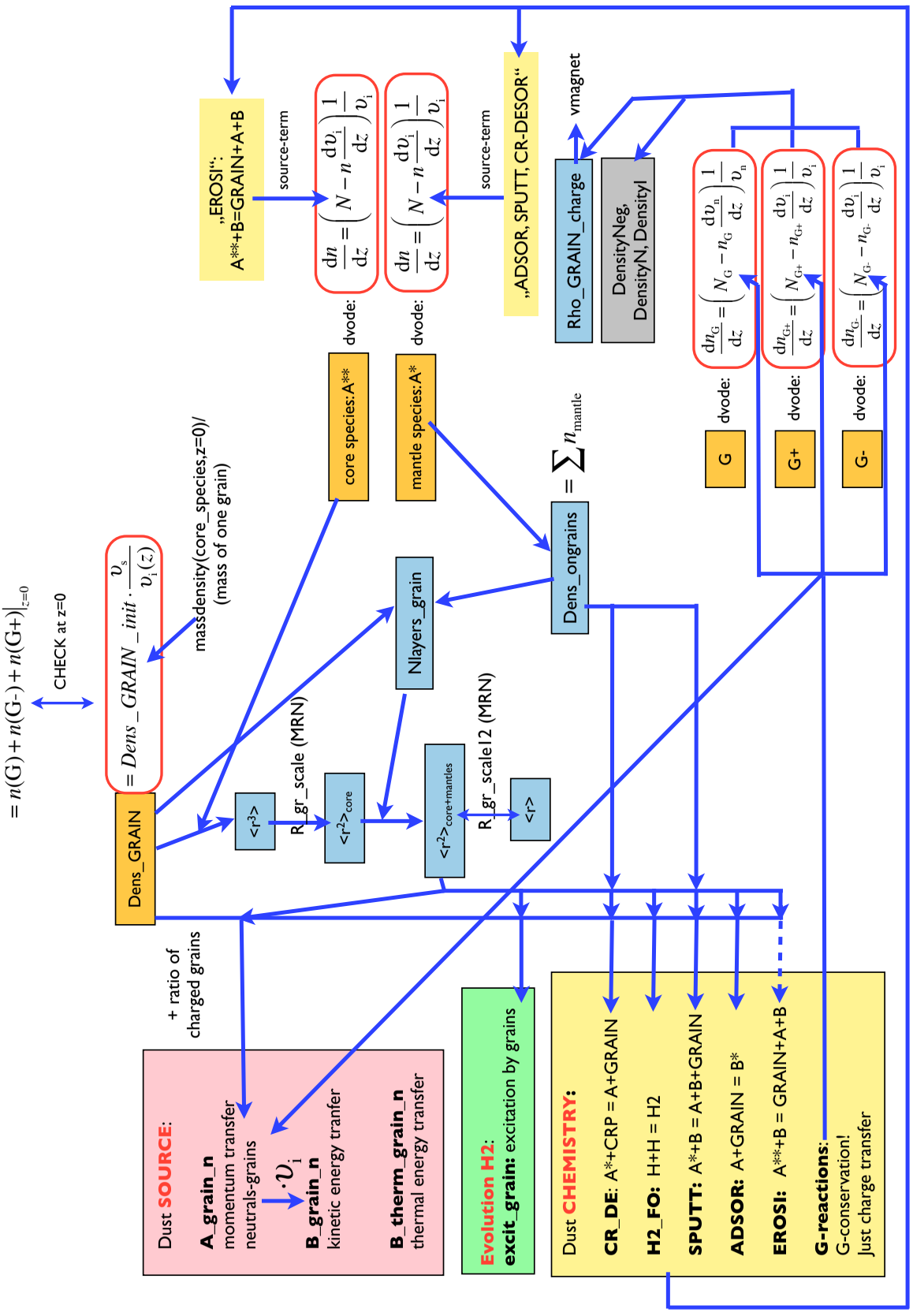

Figure 2: Flow diagram illustrating the implementation of dust physics in the shock model as described in Flower & Pineau des Forêts (2003).

5

SHOCKS IN DENSE CLOUDS[1] – IV. EFFECTS OF GRAIN-GRAIN PROCESSING ON MOLECULAR LINE EMISSION

5.1 ABSTRACT

Contex: Grain-grain processing has been shown to be an indispensable ingredient of shock modelling in high density environments. For densities higher than $\sim 10^5$ cm^{-3}, shattering becomes a self-enhanced process that imposes severe chemical and dynamical consequences on the shock characteristics. Shattering is accompanied by the vaporization of grains, which can, in addition to sputtering, directly release SiO to the gas phase. Given that SiO rotational line radiation is used as a major tracer of shocks in dense clouds, it is crucial to understand the influence of vaporization on SiO line emission.

Aims: We extend our study of the impact of grain-grain processing on C-type shocks in dense clouds. Various values of the magnetic field are explored. We study the corresponding consequences for molecular line emission and, in particular, investigate the influence of shattering and related vaporization on the rotational line emission of SiO.

Methods: We have developed a recipe for implementing the effects of shattering and vaporization into a 2-fluid shock model, resulting in a reduction of computation time by a factor ~ 100 compared to a multi-fluid modelling approach. This implementation was combined with an LVG-based modelling of molecular line radiation transport. Using this combined model we calculated grids of shock models to explore the consequences of different dust-processing scenarios.

Results: Grain-grain processing is shown to have a strong influence on C-type shocks for a broad range of magnetic fields: the shocks become hotter and thinner. The reduction in column density of shocked gas lowers the intensity of molecular lines, at the same time as higher peak temperatures increase the intensity of highly excited transitions compared to shocks without grain-grain processing. For OH the net effect is an increase in line intensities, while for CO and H_2O it is the contrary. The intensity of H_2 emission is decreased in low transitions and increased for highly excited lines. For all molecules, the highly excited lines become sensitive to the value of the magnetic field. Although vaporization increases the intensity of SiO rotational lines, this effect is weakened by the reduced shock width. The release of SiO early in the hot shock changes the excitation characteristics of SiO radiation, although it does not yield an increase in width for the line profiles. To significantly increase the intensity and width of SiO rotational lines, SiO needs to be present in grain mantles.

5.2 INTRODUCTION

Shocks are ubiquitous in the interstellar medium, occurring when matter moves into a more rarefied medium at a velocity that exceeds the local sound speed. Depending on the value of the local magne-

1 This chapter has been published as Anderl, S., et al. (2013).

tosonic speed, different types of shocks can be distinguished. The classical shocks are faster than any signal speed in the shocked medium, so the preshock medium is not able to dynamically respond to the shockwave before it arrives. This type of shock is called "J-type" (see e.g. Hollenbach & McKee (1979); McKee & Hollenbach (1980)). A different situation can occur if a low degree of ionization and the presence of a magnetic field allow magnetosonic waves to precede the shock. Ions then decouple from the neutrals and are already accelerated in the preshock gas, so that there is no longer a discontinuity in the flow of the ion fluid. In the preshock gas, the ions heat and accelerate the neutrals and broaden the heating region, so that heating and cooling take place simultaneously. The shock transition can then become continuous in the neutral fluid ("C-type shocks") also. Shocks of this type are thicker and less hot than J-type shocks (see Draine 1980; Draine & McKee 1993). Observations often reveal shocks as bow-shaped structures, with the ambient material being compressed and pushed aside (e.g. Nissen et al. 2007; Davis et al. 2009).

Shocks play an important role in the energy budget of the interstellar medium by determining the energetic feedback of events such as supernovae, stellar winds, cloud-cloud collisions, or expanding H II regions. On the other hand, shocks have a major influence on the chemistry of the interstellar medium. Among the most characteristic chemical tracers of shock waves are species that are typically heavily depleted on dust grains, such as Fe, Mg, or Si. Dust processing occurring in the violent environment of shocked media is able to release these species into the gas phase (e.g. Liffman & Clayton 1989; O'Donnell & Mathis 1997). The understanding of dust processing in shocks is therefore intimately linked with the theoretical interpretation of characteristic emission lines in environments where shocks occur.

The processing of dust in shocks can have two different consequences. It either changes the dust-to-gas mass ratio or alters the dust size distribution. The former occurs in the processes of sputtering and vaporization, while the latter is also found with shattering. Sputtering denotes energetic impacts of gas particles on grains that can release species from the grain surfaces into the gas phase. This can happen either at very high temperatures (thermal sputtering) or at high relative gas–grain velocities (inertial sputtering). Sputtering of dust grains has been the subject of many theoretical studies (Barlow 1978; Tielens et al. 1994; Jones et al. 1994; May et al. 2000; Van Loo et al. 2012) and has become an established ingredient of shock models. Shattering, which is the fragmentation of grains due to grain-grain collisions, has been identified as a crucial process for determining the grain-size spectrum of interstellar grains (Biermann & Harwit 1980; Borkowski & Dwek 1995). Together with vaporization, which describes the return of grain material to the gas phase following grain-grain collisions, shattering needs to be included in order to account for UV extinction curves (Seab & Shull 1983). Moreover, recent infrared and sub-mm observations hint at an overabundance of small dust grains relative to the expected size-distribution in parts of the interstellar medium and thereby stress the importance of dust processing (Andersen et al. 2011; Planck Collaboration 2011), which has also been associated with MHD turbulence acceleration of dust grains or charge-fluctuation induced acceleration (e.g. Ivlev et al. 2010; Hirashita 2010).

A rigorous theoretical description of grain-grain collisions requires a detailed description of shock waves in solids, which had not been undertaken before the work of Tielens et al. (1994), earlier studies having relied on much simplified models (e.g. Seab & Shull 1983). The effect of the microphysics of grain shattering and its effects on the grain size distribution in J-type shocks in the warm intercloud

medium was studied by Jones et al. (1996). Slavin et al. (2004) extended this work by explicitly following individual trajectories of the grains, considered as test particles.

In a series of papers, Guillet et al. (2007, 2009, 2011, hereafter Papers I, II and III) have shown that a multi-fluid approach to the dust dynamics, together with a detailed calculation of the grain charge distribution, shows shattering and the accompanying vaporization to be indispensable ingredients of shock models. For C-type shocks at preshock densities higher than $\sim 10^5$ cm^{-3}, shattering becomes dramatically self-enhanced, due to feedback processes: electrons are heavily depleted on to small grain fragments, and the lack of electrons in the gas phase affects the grain dynamics, resulting in even more shattering and production of small grains. Owing to the increase of the total geometrical grain cross-section, these shocks become much hotter and narrower, and vaporization becomes important for the release of depleted species into the gas phase. Both the dynamical and the chemical consequences of shattering affect the predicted observational characteristics, compared with models in which shattering and vaporization are neglected. Given that conditions favoring C-shocks are frequently found in dense clouds and Bok globules, it is necessary to evaluate the observational consequences of shock models including grain-grain processing for a proper understanding of massive star formation and interactions of supernova remnants with molecular cloud cores (Cabrit et al. 2012).

The aforementioned studies leave open a series of issues that we aim to address in this paper. The three main questions are:

- How do the effects of shattering and vaporization change if the magnetic field strength is varied?
- What are the consequences of shattering for molecular line emission?
- How do shattering and associated vaporization of SiO and C influence the SiO and atomic carbon line emission?

In order to answer the last two questions, it is necessary to introduce a detailed treatment of radiative transport. However, due to the numerical complexity of the multifluid treatment of Papers I–III, a self-consistent merging of this multifluid model with an LVG treatment of molecular line emission would be technically difficult. It would also prevent the resulting model from being a practical analysis tool whenever large grids of models are required. Therefore, we have developed a method for implementing the effects of shattering and vaporization into a 2-fluid shock model that is sufficiently general to be applied to any similar model. We incorporated the main features, neglecting all the minor details of grain-grain processing; the resulting saving in computation time amounts to a factor of $\sim$100. With this model, the consequences of shattering and vaporization on the molecular line emission of C-type shocks can be studied in detail, using a self-consistent treatment of the line transfer (Flower & Pineau des Forêts 2010). In the context of the emission of SiO from C-type shocks (Schilke et al. 1997; Gusdorf et al. 2008b; Gusdorf et al. 2008a), the inclusion of grain shattering and vaporization, along with the line transfer, should improve significantly our ability to interpret the observations correctly.

Our paper is structured as follows. In Sect. 5.3, we introduce our model, which extends the work of Flower & Pineau des Forêts (2010) by including the shattering and vaporization of grains and molecular line transfer. We use this model to demonstrate the effect of shattering on the shock structure for

different values of the magnetic field in the preshock gas (Sect. 5.4). In Sect. 5.5, we consider observational diagnostics, with the main emphasis being on the rotational line emission of SiO. In addition, we investigate the influence of vaporization on the [C I] emission lines. The results are discussed and summarized in Sect. 5.6.

5.3 OUR MODEL

In order to study the effect of shattering and vaporization on molecular line emission, we have built on the findings of Papers I–III, where shattering and vaporization are described within a multi-fluid formalism for the dust grains. These results needed to be transferred to a 2-fluid formulation, as used in the model of Flower & Pineau des Forêts 2010 (hereafter FPdF10), whose model includes a detailed treatment of molecular line radiative transfer, in the presence of the cosmic microwave background radiation. In the present Section, we first describe the treatment of dust in the model of FPdF10 and then summarize the multi-fluid treatment of dust and its implications, finally outlining how we introduced the effects of shattering and vaporization into the model of FPdF10.

5.3.1 *Two-fluid treatment of dust*

The way in which dust is treated in the LVG-model of FPdF10 derives from the work of Flower & Pineau des Forêts 2003 (hereafter FPdF03). This one-dimensional, steady-state, 2-fluid model[2] of plane–parallel C-type shocks solves the magneto-hydrodynamical equations in parallel with a large chemical network, comprising more than 100 species and approximately 1000 reactions, including ion-neutral and neutral-neutral reactions, charge transfer, radiative and dissociative recombination. Furthermore the populations of the H_2 ro-vibrational levels are computed at each integration step, along with the populations of the rotational levels of other important coolants, such as CO, OH and H_2O. In these cases, the molecular line transfer is treated by means of the large velocity gradient approximation (see also Sect. 5.5). 'Dust' is included in the forms of polycyclic aromatic hydrocarbons (PAHs), represented by $C_{54}H_{18}$, and large grains from bulk carbonaceous material and silicates (specifically olivine, $MgFeSiO_4$). The large grains are assumed to have a power law size distribution, $\mathrm{d}n_\mathrm{g}(a)/\mathrm{d}a \propto a^{-3.5}$ (Mathis et al. 1977), and radii in the range 100 to 3000 Å (0.3 μm). In the preshock medium, the grain cores are covered by ice mantles, consisting of the chemical species listed in Table 2 of FPdF03 and including H_2O, CO and CO_2. Both PAHs and large grains exist as neutral, singly positively and singly negatively charged species. The physical treatment of dust comprises:

- determination of the grain charge distribution, limited to $Z = -1, 0, 1$;
- sputtering of grain cores and mantles due to grain-gas collisions;
- removal of mantles by cosmic ray desorption;
- build-up of mantles by adsorption of gas-phase species in the postshock gas.

2 Although electrons and ions are treated as one dynamical fluid, their temperatures are calculated separately.

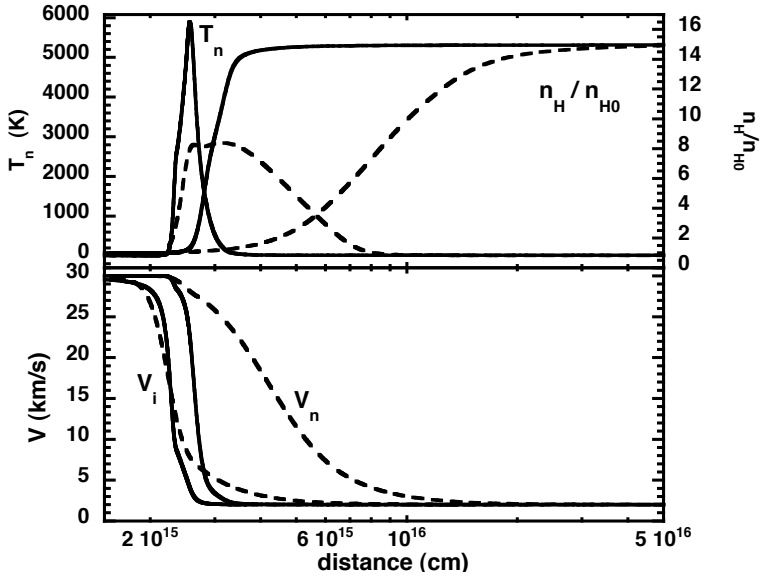

Figure 3: Temperature and density (upper panel) and velocity profiles in the shock frame (lower panel) for a 30 km s^{-1} C-type shock with a magnetic field parameter $b = 1.5$ and a preshock density of $n_{\rm H} = 10^5$ cm^{-3}. The full curves show the results obtained when grain-grain processing is treated as in Paper III; the broken curves are obtained by following the approach of FPdF03.

5.3.2 *Multi-fluid treatment of dust*

To properly account for the effects of grain-grain collisions in shocks, it is necessary to introduce a multi-fluid description of the dust dynamics, in which dust grains are treated as test particles. In Papers I–III the dust size distribution was modeled by the use of discrete bins, with grain sizes ranging from 5 to 3000 Å. PAHs were not included as separate species, distinct from the dust grains (as in the two-fluid model), but were incorporated into the dust size distribution. The equations describing the 2-D grain dynamics and complete charge distribution were integrated for each individual bin size, independently for silicate and carbon grains.

While the shock structure is not much affected by this more accurate treatment of the grain dynamics and charging (Paper I, Appendix D[3]), the introduction of dust shattering in grain-grain collisions and the corresponding changes to the grain size distribution have major effects on shocks in dense clouds with a low degree of ionization (Paper III). When grains collide with a velocity greater than 1.2 km s^{-1} (carbon grains) or 2.7 km s^{-1} (silicate grains), a fraction of their mass, which increases with velocity, is shattered into smaller fragments. At higher velocities, another fraction is vaporized and released into the gas phase (the numerical treatment follows the models of Tielens et al. (1994) and Jones et al. (1996), where the vaporization threshold is ∼19 km s^{-1}).

Paper III demonstrated that there is a marked shift of the dust size distribution towards smaller grains when the grain dynamics, charging and evolution are coupled self-consistently with the shock dynamics and chemistry. The most dramatic consequence is an increase of the total geometrical grain

3 Although changes to the re-accretion of mantle species in the multi-fluid treatment give rise to a slightly different temperature profile in the postshock gas.

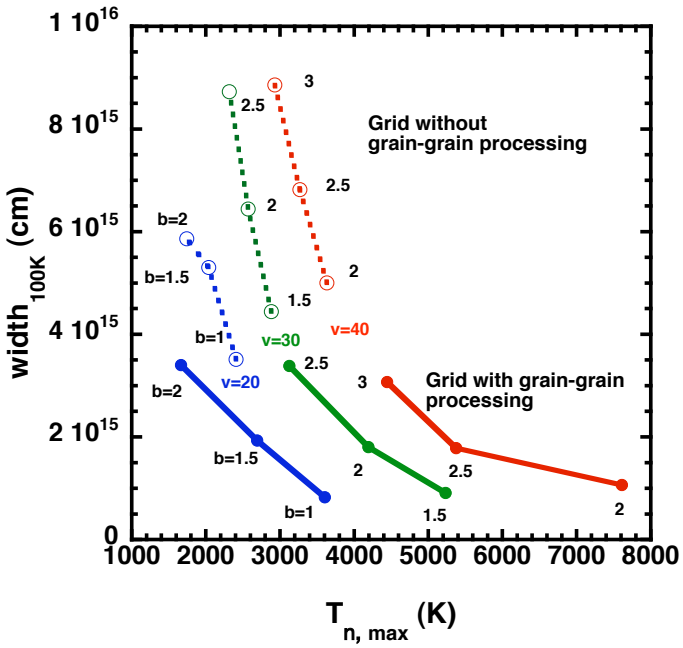

Figure 4: Peak temperature of the neutral fluid and the shock width (in cm), to $T = 100$ K in the cooling flow, for the grid of models without (broken lines) and with (full lines) grain-grain processing. The preshock density is 10^5 cm^{-3}, and the shock velocities are 20 km s^{-1} (blue), 30 km s^{-1} (green) and 40 km s^{-1} (red) for various values of the magnetic field parameter, b, in $B(\mu\mathrm{G}) = b\sqrt{n_\mathrm{H}(\mathrm{cm}^{-3})}$.

cross-section – which governs the coupling between the neutral and charged fluids – by a factor[4] of ~10. The shock becomes narrower by a factor of ~4, and the peak temperature increases by a factor of 1.5–2 (see Fig. 3). The small grain fragments deplete ions and electrons from the gas until grains become the dominant charge carriers, a situation known as a *dusty plasma* (Fortov et al. 2005). The strong effect of shattering, for preshock densities of 10^5 cm^{-3} and higher, can be understood in terms of the feedback processes described in Paper III. At these high preshock densities, it turns out that vaporization related to shattering becomes important, if not dominant, compared to sputtering.

5.3.3 *Implementation of shattering*

As described in Sect. 5.3.2, there are two ways in which shattering affects the shock wave: first it increases the collisional dust cross-section, and second it lowers the degree of ionization of the gas. In the model of FPdF10, dust as a dynamical species and dust as a chemically reacting species were treated separately. Our implementation and validation of shattering in the FPdF10 model are described in Appendix A.1. Here we only summarize our basic approach.

- The dynamical effects of shattering can be simulated by incorporating the change in the total grain cross section $\langle n\sigma \rangle$, computed with the model of Paper III; this is done by multiplying $\langle n\sigma \rangle$ by an additional factor that varies with the spatial coordinate, z, through the shock wave.

4 This factor refers to the total cross-section of grain cores. The re-accretion of grain mantles in the postshock gas leads to a much larger increase in the total cross-section, by a factor of ~100 (see. Fig. 12). However, this large increase is irrelevant to the shock dynamics, as it happens where the momentum transfer between the ionized and the neutral fluids is almost complete (T ~100 K).

This factor is modelled as an implicit function of the compression of the ionized fluid; its value is 1 in the preshock gas, and its maximum value – derived from the multi-fluid model – is attained when shattering is completed. It is possible to use linear fits of the parameters that are required.

- The chemical effects of shattering, i.e. the consequences for grains as charged species, as determined by grain-charging reactions, need to be considered separately. In order to model the influence of shattering on the abundances of charged grains, a shattering source-term is introduced, whose value is consistent with $\langle n\sigma \rangle$.

5.3.4 *Implementation of vaporization*

Grain-grain collisions lead not only to shattering of grains, and consequent changes in the shock structure and degree of ionization, but also to their vaporization, when the impact velocity is higher than the vaporization threshold of ~19 km s^{-1}. We assume that the silicon released through vaporization is in the form of SiO (Nagahara & Ozawa 1996; Wang et al. 1999). We have implemented the effect of SiO vaporization in a similar way as for shattering[5]; the details are given in Appendix A.2. Our procedure involves introducing an additional term in the rate of creation of gas-phase SiO from Si and O in the grain cores. Thus, vaporization is incorporated as a new type of pseudo-chemical reaction. The rate of creation of SiO through vaporization is determined by parameterizing the results of the multi-fluid models.

Another modification of the FPdF10 model concerns the mantle thickness, which is now calculated as described in Paper I, Appendix B. Our simplified, but self-consistent, treatment of shattering and vaporization reduces the computation time by a factor of more than 100.

5.4 THE INFLUENCE OF GRAIN-GRAIN PROCESSING ON THE SHOCK STRUCTURE

5.4.1 *The grid of models*

Having implemented shattering and vaporization in the model of FPdF10, we first study the dependence of grain-grain processing and feedback on the strength of the transverse magnetic field. The analysis of Paper III was restricted to shocks propagating at the critical velocity, which defines the fastest possible C-type shock for a given magnetic field (or, conversely, the lowest value of the magnetic field possible for a given shock velocity). This critical velocity is determined by the condition that the shock velocity should be only slightly smaller than the velocity of magnetosonic waves,

$$V_{\rm ms} = \frac{B}{\sqrt{4\pi\rho_{\rm c}}}$$

where $\rho_{\rm c}$ is the mass density of matter that is strongly coupled to the magnetic field. We assumed that the magnetic field strength, B, in dense clouds scales with the total proton density, $n_{\rm H}$, as

5 We emphasize the effects of SiO vaporization because the fine-structure lines of atomic carbon are optically thin and do not require an LVG treatment.

$B(\mu\mathrm{G}) = b\sqrt{n_\mathrm{H}(\mathrm{cm}^{-3})}$ (Crutcher 1999), which implies that the magnetic energy density is proportional to n_H. The assumed power-law exponent of 0.5 is somewhat lower than the more recent value of 0.65±0.05, given by Crutcher (2012), but is probably consistent with the uncertainties associated with its deduction from measurements of Zeeman splitting. The restriction to critical shocks was justified in Paper III by the fact that the observations will be dominated by the fastest shocks, if present. However, to assess the importance of shattering in the dense interstellar medium, it is necessary to establish whether shattering is still a relevant factor when the magnetic field is higher and the (charged) grains are better protected by their coupling to the magnetic field. Shattering is sensitive to the preshock density because the drag force becomes more important, relative to the Lorentz force, as the density increases. At high densities, large grains decouple from the magnetic field and exhibit a large velocity dispersion in the initial part of the shock wave, where they undergo destruction. Furthermore, the degree of ionization is lower in higher density gas, so the feedback due to the depletion of electrons is enhanced.

We have studied shocks with a preshock density of 10^5 cm^{-3}. We consider only this value because, on the one hand, it was shown that the change in the grain size distribution due to shattering is negligible for a preshock density of 10^4 cm^{-3}, and, on the other hand, the strength of the feedback from shattering at higher densities prevents the multi-fluid model of Paper III from converging at a preshock density of 10^6 cm^{-3}, and hence there are no results with which to compare at this density. We have restricted our calculations to shocks that do not fully dissociate H_2 (shock velocity $V_\mathrm{s} \leq 50$ km s^{-1}), in practice to 20, 30 and 40 km s^{-1}.

The values of the magnetic field that we considered were determined by two considerations. First, in order to study critical shocks, we adopted the corresponding (minimum) values of b (see Paper III); and, second, we varied b for a given shock velocity in order to study the influence of variations in the magnetic field strength. Thus, we consider three values of the b parameter for each velocity, in steps of 0.5, where the lowest value is close to that for a critical shock; the lowest values are $b = 1.0$ for 20 km s^{-1}, $b = 1.5$ for 30 km s^{-1}, and $b = 2.0$ for 40 km s^{-1}. The corresponding grid of nine models is summarized in Table 1. We note that a comparison of models with different shock velocities and the same magnetic field is possible for the case $b = 2.0$.

5.4.2 *Hotter and thinner*

The most dramatic effect of shattering is the change in the overall shock structure, owing to the increase in the collision cross-section of the dust and the corresponding increase in the coupling between the neutral and charged fluids. Figure 4 shows the peak temperature of the neutral fluid and the shock width (up to the point at which the temperature has fallen to 100 K) for our grid of nine models, as compared with the results obtained without grain-grain processing.

The peak temperature of the models that include shattering increases by a factor of 1.5–2 for the shocks closest to the critical velocity, as in Paper III. Our models show that this increase is smaller for slower shocks, and for shocks with higher magnetic field strengths, because the charged grains are more strongly bound to and protected by the magnetic field. Thus, shocks with $V_\mathrm{s} = 20$ km s^{-1} and $b = 2$ have a peak temperature comparable to that found without grain-grain processing. However, the shock width, as determined at the point in the cooling flow at which the gas temperature has fallen

Table 1: Parameters defining our grid of models.

V_s [km s^{-1}]	b	B [μG]	n_H [cm^{-3}]
20	1.0	316	10^5
20	1.5	474	10^5
20	2.0	632	10^5
30	1.5	474	10^5
30	2.0	632	10^5
30	2.5	791	10^5
40	2.0	632	10^5
40	2.5	791	10^5
40	3.0	949	10^5

to 100 K, is always much smaller for models in which grain-grain processing is included. For the shocks closest to the critical velocity, the width is reduced by a factor of 4–5. The trend is the same as for the peak temperature: the shock widths, as computed with and without grain-grain processing, are most similar for lower velocities and higher magnetic fields, differing by a factor of only 1.7 for $V_s = 20$ km s^{-1} and $b = 2$.

It is interesting to see the dependence of the shock structure on the transverse magnetic field strength. In models that neglect grain-grain processing, a change in the magnetic field modifies the shock width at almost constant peak temperature, whereas, when grain-grain processing is included, a variation in the magnetic field has a strong affect on the peak temperature. We return to this point in Sect. 5.5, where we consider the differences between the spectra predicted by these two categories of model; but it is already clear that shattering is significant, even for non-critical shocks, and should be included in steady-state C-type shock models with high preshock densities ($n_H \geq 10^5$ cm^{-3}).

5.5 OBSERVATIONAL CONSEQUENCES

In our model, the molecular line transfer is treated using the large velocity gradient (LVG) approximation (e.g. Surdej 1977), allowing for self-absorption via the escape probability formalism. The LVG method is well adapted to the conditions of shocks, where flow velocities change rapidly. The computation of the molecular energy level populations is performed in parallel with the integration of the chemical and dynamical rate equations, as introduced for CO by Flower & Gusdorf (2009). The molecular line transfer of H_2O, CH_3OH, NH_3, OH and SiO has since been added (Flower & Pineau des Forêts 2010; Flower et al. 2010; Flower & Pineau des Forêts 2012).

The modelling of interstellar shock waves requires many molecular energy levels to be considered. As described in FPdF10, we include levels of H_2O up to an energy of approximately 2000 K above ground. Although this is less than the maximum temperatures that are attained, the high values of the radiative (electric dipole) transition probabilities ensure that the populations of higher, neglected levels remain small, and hence the associated errors in the computed line intensities are modest. Above

the maximum temperatures for which the rotational de-excitation coefficients have been calculated, their values are assumed to remain constant (cf. Flower & Pineau des Forêts 2012, Appendix A). Rate coefficients for excitation are obtained from the detailed balance relation.

The consequences of grain-grain processes for the molecular line radiation of H_2, H_2O and OH for representative shocks of $V_s = 30$ km s^{-1} are briefly discussed in Sect. 5.5.1 and in more detail in Appendix B. In Sect. 5.5.2, we consider the rotational line emission of SiO and, in Sect. 5.5.3, the vaporization of carbon.

5.5.1 *Molecular line emission*

We have seen that including grain-grain processing leads to an increase in the peak shock temperature; this affects the chemistry and gives rise to higher fractional abundances of molecules in excited states. The intensities of lines emitted by highly excited states are thereby enhanced. At the same time, the column density of shocked gas decreases, which tends to reduce the intensity of molecular line emission. The net effect depends on the chemical and spectroscopic properties of the individual molecules.

In Appendix B, we show that the intensities of all transitions of OH increase in shocks faster than 30 km s^{-1} that incorporate grain-grain processing; this is due to the temperature sensitivity of OH formation. On the other hand, the intensities of the emission lines of H_2, CO, and H_2O decrease because of the reduction in the column density of shocked material. Furthermore, the inclusion of grain-grain processing introduces a dependence of the intensities of lines from highly excited states on the magnetic field, owing to the variation of the peak shock temperature with the field strength (see Sect. 5.4.2 and Fig. 4).

5.5.2 *The effect of vaporization on SiO emission*

SiO is a prominent indicator of shock processing in dense clouds associated with jets and molecular outflows (e.g. Bachiller et al. 1991; Martin-Pintado et al. 1992; Gueth et al. 1998; Nisini et al. 2007; Cabrit et al. 2007). The first chemically adequate theoretical study of SiO production by sputtering in C-type shocks was conducted by Schilke et al. (1997); this work was pursued subsequently by Gusdorf et al. (2008a); Gusdorf et al. (2008b). These studies considered the release, by sputtering, of Si from grain cores and SiO from grain mantles, but not the process of vaporization, which could modify the predicted SiO rotational line profiles. We note that Cabrit et al. (2012) found that, in the protostellar jet HH212, at least 10% of elemental Si could be present as gas-phase SiO, if the wind is dusty. To explain such a high value, they hint at the possible importance of grain-grain processing and the release of SiO by vaporization. The sputtering of Si from the grain cores seems unable to account for the observations in this case, as the dynamical timescale of 25 yr is too short for the chemical conversion, in the gas phase, of the sputtered Si into SiO.

The influence of grain-grain processing on the SiO line emission is twofold. On the one hand, vaporization strongly increases the amount of SiO released from grain cores, at sufficiently high shock speeds. On the other hand, as the process of vaporization is necessarily related to shattering of dust grains, shocks with grain-grain processing have a different structure (cf. Sect. 5.4.2). The

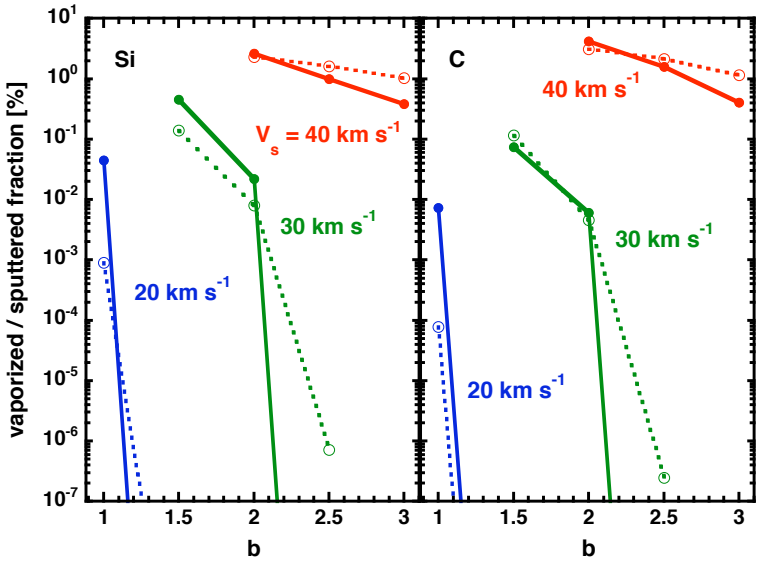

Figure 5: The fractions of Si (left panel) and C (right panel) released from grain cores in model M1 of Table 2 by vaporization (full lines) and sputtering (broken lines), for $V_s = 20$ km s^{-1} (blue), $V_s = 30$ km s^{-1} (green), and $V_s = 40$ km s^{-1} (red), as functions of the magnetic field parameter, b, in $B(\mu\mathrm{G}) = b\sqrt{n_\mathrm{H}(\mathrm{cm}^{-3})}$.

Table 2: Summary of the three dust processing scenarios investigated in order to study the release of SiO into the gas phase. The percentage refers to elemental silicon in the form of SiO in the mantles.

Scenario	Si in cores	SiO in mantles	Grain-grain processing
M1	yes	no	yes
M2	yes	no	no
M3	yes	10%	no

consequences of the latter effect for the emission by molecules whose abundances are not directly influenced by vaporization are summarized in Sect. 5.5.1.

In order to address the question of how the related effects of shattering and vaporization affect the emission of SiO in C-type shocks, we compare results of shock models, obtained including and excluding grain-grain processing, for three different scenarios, summarized in Table 2. Models corresponding to scenario 1 (M1) were calculated using the implementation of shattering and vaporization described in Sect. 5.3.3 and 5.3.4 with the parameters of Table 3. Models corresponding to scenario 2 (M2) do not include grain-grain processing, but Si is still released by the sputtering of grain cores. Scenario 3 (M3) differs from M2 in that 10% of the elemental Si is assumed to be in the form of SiO in the grain mantles. In total, there are $9 \times 3 = 27$ individual models to be computed.

5.5.2.1 *The release of SiO through dust processing*

In order to compare the relative importance of vaporization and sputtering, we investigate the release of the Si in grain cores into the gas phase by each of these processes during the passage of a shock wave. The left-hand panel of Figure 5 shows the fraction of Si eroded from grain cores through sputtering and vaporization in model M1. There is negligible sputtering for $V_s \leq 20\ \mathrm{km\,s^{-1}}$, because the adopted sputtering threshold for refractory grain material is $\sim$25 $\mathrm{km\,s^{-1}}$ (May et al. 2000). Both the sputtering of Si and the vaporization of SiO are inhibited by the magnetic field. In the case of sputtering, the maximum ion-neutral drift velocity decreases with increasing field strength, whereas, for vaporization, the charged grains are more strongly coupled to the field and hence to the charged fluid (we assume that the magnetic field is 'frozen' in the charged fluid). For models M3 (SiO in mantles) with velocities sufficient for mantle sputtering, all the SiO initially in the mantles is released into the gas phase. The rotational line emission of SiO depends not only on the amount of silicon released from the grains but also on the location of its release and the physical conditions prevailing where SiO is present within the shock wave.

The upper panel of Figure 6 shows the fractional abundance of SiO in the gas phase, for dust models M1–3 of Table 2 and three different values of the shock speed. In model M1, vaporization releases SiO directly into the gas phase in the region where the temperature of the neutral fluid is rising steeply. The higher the shock speed, the more SiO is produced. The large increase in the total grain cross section in the postshock gas enhances the rate of formation of mantles and removes SiO from the gas phase.

The variation of the fractional abundance of SiO is very different if only the sputtering of grain cores is considered (M2), because the Si that is released by sputtering has to be transformed into SiO by gas-phase chemical reactions, predominantly oxidation by O_2 and OH. The corresponding reactions are

$$\mathrm{Si} + \mathrm{O_2} \longrightarrow \mathrm{SiO} + \mathrm{O} \tag{64}$$

and

$$\mathrm{Si} + \mathrm{OH} \longrightarrow \mathrm{SiO} + \mathrm{H}\,. \tag{65}$$

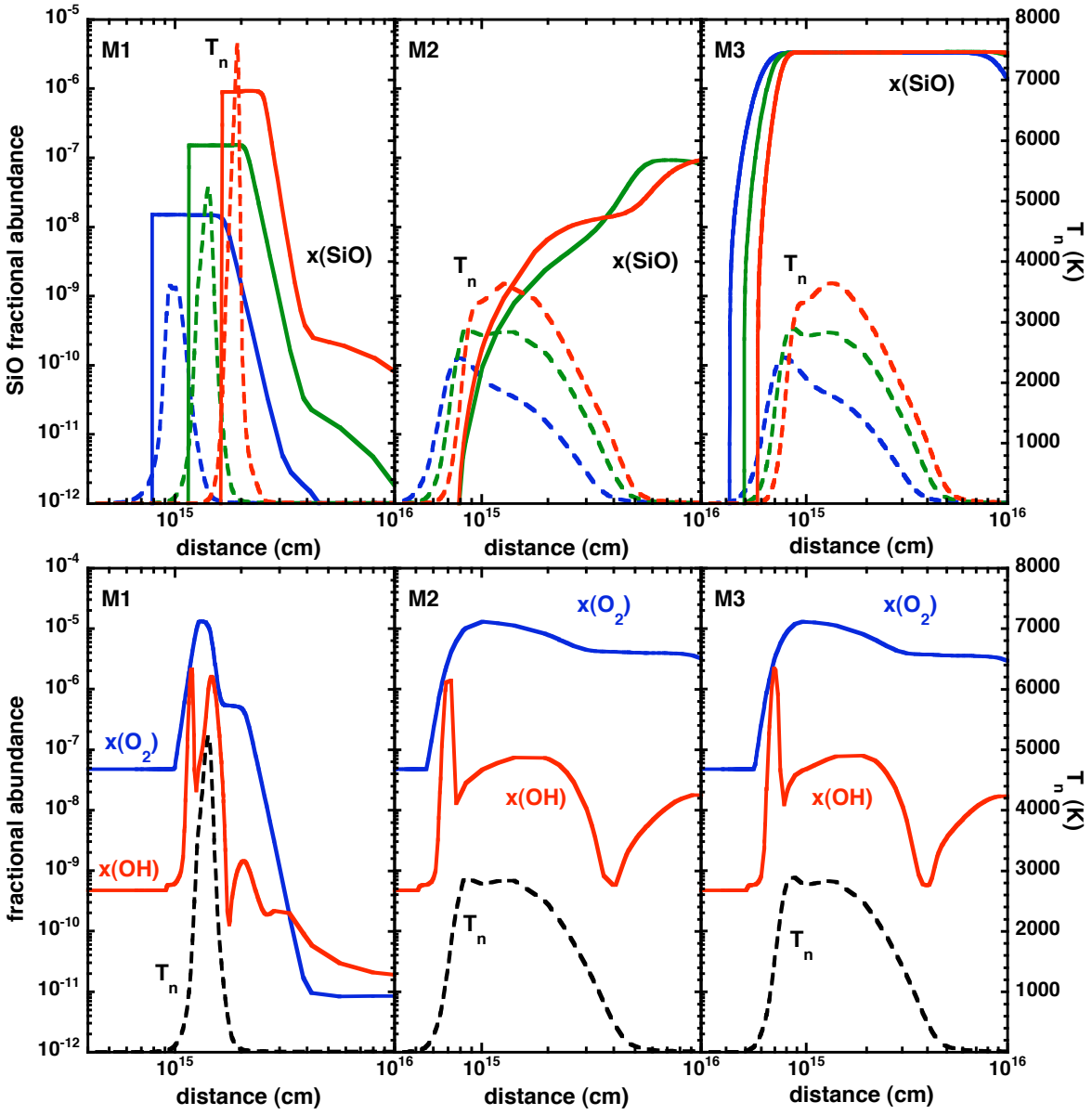

Figure 6: Upper panel: Evolution of the fractional abundance of SiO in the gas phase (left ordinate, full curves) and temperature of the neutral fluid (right ordinate, broken curves). From left to right: dust modelling scenarios M1, M2, and M3. The models shown in all three panels are for $V_s = 20$ km s^{-1} with $b = 1.0$ (blue), $V_s = 30$ km s^{-1} with $b = 1.5$ (green), and $V_s = 40$ km s^{-1} with $b = 2.0$ (red). The fractional abundance of SiO in the gas phase is negligible for $V_s = 20$ km s^{-1} with $b = 1.0$ in scenario M2. Lower panel: Variation through the shock wave of the gas-phase fractional abundances of O_2 (left ordinate, full blue curves) and OH (left ordinate, full red curves), together with the temperature of the neutral fluid (right ordinate, black broken curves), for $V_s = 30$ km s^{-1} and $b = 1.5$ and each of the dust models M1, M2 and M3 (from left to right).

For reaction (64) the rate coefficient ($cm^3\ s^{-1}$)

$$k = 1.72 \times 10^{-10} (T/300)^{-0.53} \exp(-17/T)$$

was measured by Le Picard et al. (2001). The rate coefficient for reaction (65), which is not measured, was adopted to be the same.

Thus, the fractional abundance of SiO in the gas phase depends not only on the amount of Si sputtered from the grain cores but also on the abundances of O_2 and OH, displayed in the lower panel of Fig. 6. The chemical delay in SiO production is apparent in the upper panel of Fig. 6; the abundance of SiO peaks in the cool and dense postshock region. If SiO is initially in the grain mantles (M3), its release is rapid and complete even before the temperature of the neutral fluid rises significantly.[6] For the shock models considered, all the SiO in the mantles is released into the gas phase. We have assumed that 10% of elemental silicon is initially in the form SiO in the mantles; this is the largest of the values considered by Gusdorf et al. (2008b). If the same fraction of silicon is initially in the form of SiH_4 in the mantles, there occurs the same chemical delay in the production of SiO in the gas phase as in models M2.

5.5.2.2 *Excitation of the SiO rotational lines*

The differences in the SiO abundance profiles in the three cases M1–3 – specifically, whether SiO is already present in the hot gas, early in the shock wave, or only in the cold postshock gas – have consequences for the relative intensities of the SiO rotational lines. To illustrate this point, we compare, in Fig. 7, the peak temperatures of the rotational lines of SiO, relative to the $J = 5$–4 transition, calculated for each of these three cases. The results in Fig. 7 may be better understood by referring to the line profiles, shown for the $V_s = 30\ km\ s^{-1}$ shock in Fig. 9.

The first thing to note is the similarity of the relative peak line temperatures for the $V_s = 30\ km\ s^{-1}$ and $V_s = 40\ km\ s^{-1}$ models with only core sputtering (M2); this can be ascribed to the chemical delay in SiO formation. The rotational lines up to the 8–9 transition in these models mostly stem from the cold postshock gas, where almost maximum compression is reached. Therefore, the lines have large optical depths and near-LTE excitation conditions, which makes the relative peak temperatures of the transitions displayed independent of the shock velocity. The models with vaporization (M1), on the other hand, show a clear variation of excitation conditions with shock speed. The lines are formed mainly in the cooling flow, where the temperature of the neutral fluid is a few hundred K (the case for $V_s = 30\ km\ s^{-1}$, $J_{up} > 4$ and for $V_s = 40\ km\ s^{-1}$, $J_{up} > 2$), and are sensitive to the velocity dependence of both the temperature in the cooling flow and the amount of SiO that is produced by vaporization.

For the models with SiO in the mantles (M3), the differences in the relative peak line temperatures are much less between shocks of different velocities than is the case for models with vaporization. The same amount of SiO is released for both velocities and the column density of the cooling gas is greater than in models that include vaporization. Most of the radiation arises in the cooling flow, where the temperature profiles are very similar and the optical depths are large: for model M2, with $V_s = 30\ km\ s^{-1}$ and $b = 1.5$, the transitions up to $J = 7$–6 become optically thick, with optical depths at the line centres reaching $1 \lesssim \tau \lesssim 6$, depending on the transition. We conclude that clear variations

6 The threshold velocity for sputtering of the mantles is $\sim 10\mu^{-\frac{1}{2}}\ km\ s^{-1}$, where μ is the reduced mass of the colliding species, relative to atomic hydrogen (Barlow 1978).

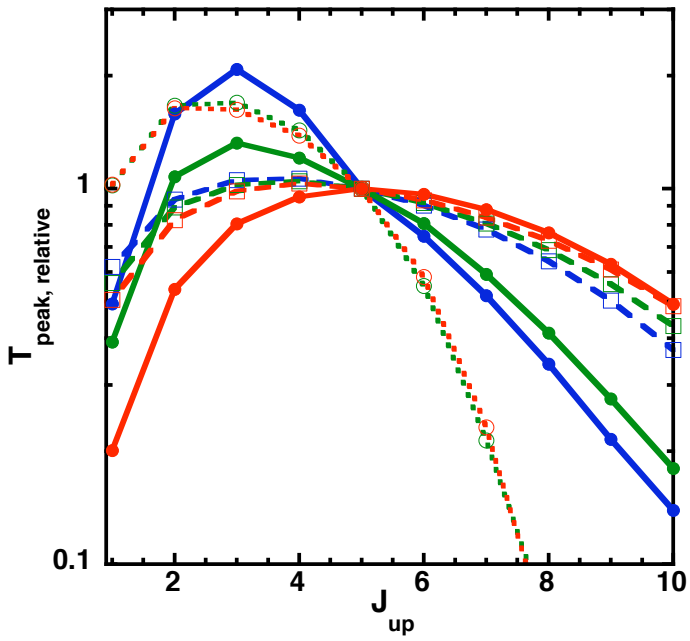

Figure 7: The peak temperatures (K) of the rotational emission lines of SiO, relative to the $J = 5$–4 transition, as functions of the rotational quantum number of the upper level of the transition $J_{\rm up}$. Displayed are the shock models in our grid that are most strongly influenced by vaporization, i.e. $V_{\rm s} = 20$ km s^{-1} with $b = 1$ (blue), $V_{\rm s} = 30$ km s^{-1} with $b = 1.5$ (green), and $V_{\rm s} = 40$ km s^{-1} with $b = 2$ (red). Full lines: M1; dotted lines: M2; broken lines: M3.

of the relative line intensities with the shock velocity are characteristic of those models in which grain vaporization occurs.

5.5.2.3 *SiO rotational line profiles*

Given that the excitation conditions of the SiO lines differ in the three scenarios M1–3, we expect the SiO spectral line profiles differ also, with respect to line width, location of the peak, and integrated flux. Line profiles for $V_{\rm s} = 30$ km s^{-1}, divided by the peak temperature of the $J = 5$–4 transition (except for the 5–4 transition itself), are shown in Fig. 8. Model M1 predicts narrower lines for low-J transitions, but similar widths for high-J transitions, as model M2, and much narrower lines than model M3. There is a weak variation with $J_{\rm up}$ of the location of the line peak in models M1 and M2. For M1, the peak in the profile of the lowest transition occurs in the cold posthock gas, where the neutral fluid is moving at a velocity $V_{\rm n}$ ~3 km s^{-1}, whereas, for higher transitions, the peak moves to hotter gas, at $V_{\rm n}$ ~4 km s^{-1}. A similar trend is seen for model M2, but, in this case, it is only the highest (and very weak) transitions that peak earlier in the shock wave. In contrast, the line peaks for model M3 are always located at the same velocity of $V_{\rm n}$ ~24 km s^{-1}. Thus, the differences in shock structure and spatial distribution of SiO between models M1 and M2 do not have a strong effect on the SiO rotational line profiles. *In particular, the release of SiO through vaporization early in the shock wave does not lead to significant broadening of the lines*. However, the lines are strongly broadened if SiO is present in the grain mantles (scenario M3), and this seems to be the only way of accounting for observed line widths of several tens of km s^{-1} if they are to be explained by one single shock. Alternatively, broad SiO lines can be explained by the existence of several shocks inside the

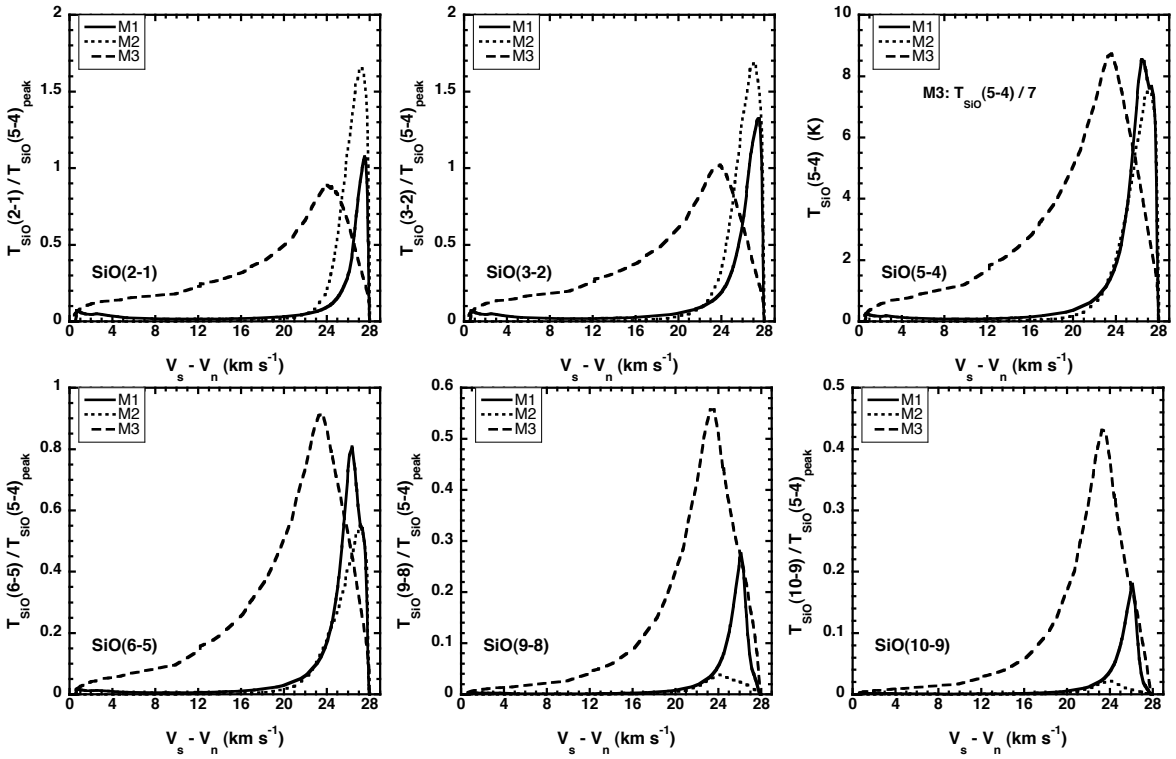

Figure 8: Profiles of the SiO rotational transitions (2–1), (3–2), (5–4), (6–5), (9–8), and (10–9), for $V_s = 30$ km s^{-1} and $b = 1.5$. The line temperatures have been divided by the peak temperature of the (5–4) transition, except for the (5–4) transition itself, for which the absolute line profiles are given (for models M1 and M2; for model M3, the line temperature has been divided by a factor of 7 for the purposes of presentation). Full lines: M1; dotted lines: M2; broken lines: M3.

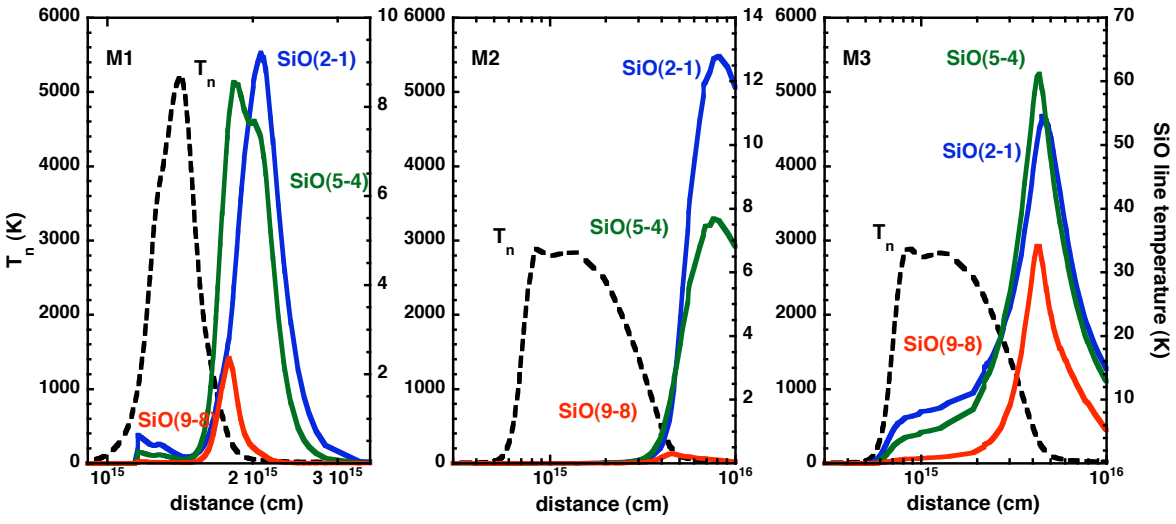

Figure 9: Temperature profiles of the neutral fluid (left ordinate, broken curves) and SiO line temperatures (right ordinate, full curves) of the rotational transitions $J = 2$–1 (blue), 5–4 (green), and 9–8 (red) for $V_s = 30$ km s^{-1} , $b = 1.5$; models M1 (left panel), M2 (centre panel), and M3 (right panel). The abscissa is the distance through the shock wave.

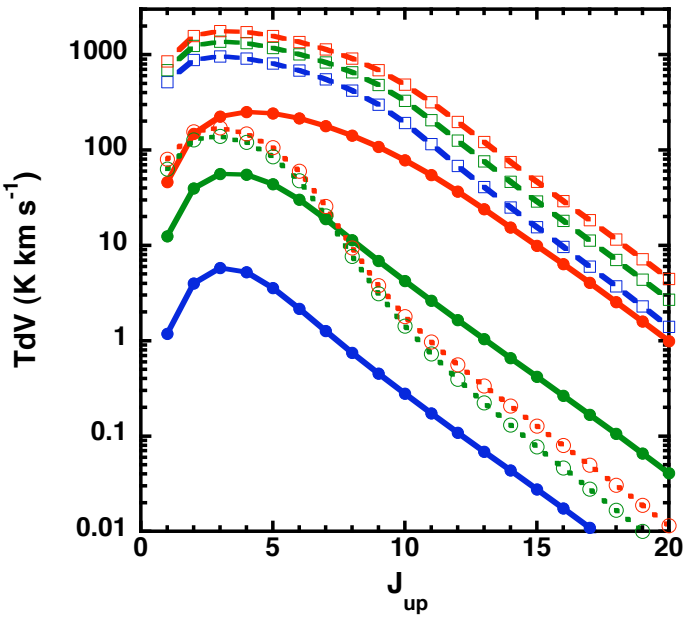

Figure 10: Integrated intensities of the rotational transitions $J_{\rm up} \rightarrow J_{\rm up} - 1$ of SiO for shocks with $V_{\rm s} = 20$ km s^{-1}, $b = 1$ (blue), $V_{\rm s} = 30$ km s^{-1}, $b = 1.5$ (green), and $V_{\rm s} = 40$ km s^{-1}, $b = 2$ (red). Full lines: model M1; dotted lines: model M2; broken lines: model M3.

telescope beam, such that the individual narrow line profiles appear spread out in radial velocity due to different velocities and inclination angles, in the observer's frame. Similarly, the lines would be broadened by the velocity profile associated with a bow shock (e.g. Brand et al. 1989).

5.5.2.4 *Integrated SiO rotational line intensities*

An interesting question is whether the release of SiO due to vaporization significantly increases the integrated (along the z-direction) SiO rotational line intensities. Fig. 10 shows, that indeed there is an increase in the intensities of the highly excited transitions. Furthermore, the slope of the integrated intensity curves differs between models M1 and M2 for transitions $3 \leq J_{\rm up} \leq 10$.

The integrated intensities of the lowest transitions – up to $J_{\rm up} \sim 7$ – are dependent on the timescale for accretion of gas-phase species on to grains in the cooling flow; this timescale depends on the (uncertain) accretion rates. In addition, 1-dimensional models tend to overestimate the compression of the postshock gas. Previous studies (Gusdorf et al. 2008a) have found the accretion timescale to be unimportant for the molecular line emission. However, owing to the large increase in the total grain cross-section, induced by vaporization, we see, for the first time, an observational consequence that may be related to this timescale.

Independent of the accretion timescale, the integrated intensities of, in particular, the lowest transitions increase significantly for model M3; but we recall that the amount of SiO in the mantles is treated as a free parameter, and the absolute intensities can be varied accordingly. The intensity curves corresponding to model M3 have similar slopes to the curves of model M1, for transitions from $J_{\rm up} \gtrsim 10$; they peak at $J_{\rm up} = 3$. On the other hand, the peak of the curve corresponding to model M1 at $V_{\rm s} = 40$ km s^{-1} is displaced to $J_{\rm up} = 4$, owing to the higher maximum temperature. As may be

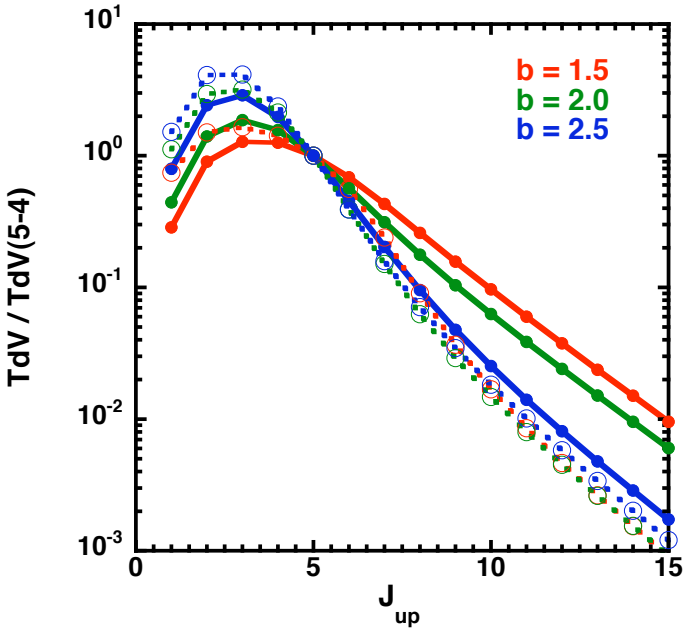

Figure 11: Integrated intensities of the rotational transitions $J_{\rm up} \rightarrow J_{\rm up} - 1$ of SiO, relative to the intensity of the transition with $J_{up} = 5$. The shock velocity is $V_{\rm s} = 30$ km s^{-1}, with values of the magnetic field parameter $b = 1.5$ (red), $b = 2.0$ (green) and $b = 2.5$ (blue). Full curves denote model M1, dotted curves model M2.

seen from Fig. 10, the integrated line intensities decrease by a factor ∼100 between $5 \leq J_{\rm up} \leq 10$ for model M2, which sets it apart from models M1 and M3.

Fig. 11 shows the effect of variations in the magnetic field on the integrated SiO rotational line intensities. In this Figure, the integrated intensities are expressed relative to the 5–4 transition, in order to focus attention on the excitation conditions, rather than the release of SiO into the gas phase. For model M1, there is a clear variation with magnetic field strength, which is not present for model M2. This difference can be understood from Fig. 4, which shows that the maximum temperature of the neutral fluid hardly varies with the magnetic field strength for model M2, whereas the maximum value changes for model M1. Thus, Fig. 11 demonstrates that the excitation conditions vary with the strength of the magnetic field when the effects of grain-grain collisions are incorporated.

5.5.3 *The effect of vaporization on [C I] emission*

Our model, and the models of Papers I–III, includes two different populations of dust grains: silicate and carbon grains. While emission of SiO could be used as a tracer of vaporization in shocks because of the strong depletion of Si and SiO in quiescent gas, the effects of vaporization on [C I] emission will not be seen as clearly. Nonetheless, the vaporization of graphite grains modifies the emission of atomic carbon. In order to predict the magnitude of this effect, we have used the multi-fluid model of Paper III.

Fig. 5 (right-hand panel) shows the fraction of carbon released from grain cores by sputtering (M2) and vaporization (M1). At low velocities, the destruction of carbon grains is less than for silicates because the gyration of large carbon grains is damped more rapidly, owing to their lower specific

density. At higher velocities, for which small grains also contribute significantly to vaporization, the fraction of carbon released from graphite grains is higher than the fraction of silicon from silicates; graphite grains are more strongly affected by shattering. Table B.1 shows the intensities of two [C I] forbidden lines, at 609.8 μm and 370.4 μm. The values in these Tables confirm that the effect of vaporization on the [C I] lines is less than on the SiO rotational transitions.

5.6 CONCLUDING REMARKS

In this series of papers, the consequences of grain-grain collisions in shock waves have been investigated; such processes had been ignored in previous studies of C-type shocks. Shattering is a key factor in the production of the large populations of very small grains (mostly carbonaceous: see, for example, Li & Draine 2001) in the turbulent ISM (Hirashita 2010). It has been shown, in earlier papers in the series, that C-type shock waves provide similar dynamical conditions to turbulence, and so shattering needs to be included in shock models.

Our study relies on the shattering model that was developed in Paper III, and our results inherit the dependence of this model on parameters such as the size of the smallest fragments (5Å in Paper III), the slope of the size distribution of the fragments, their charge distribution, and the composition of the dust grains. Whilst shattering almost certainly occurs in the ISM, as a direct consequence of the weak coupling of large grains to the magnetic field in high density clouds, the threshold density at which shattering starts to have a significant effect on the shock dynamics is more uncertain.

In our model, the processes of shattering and vaporization are linked, so that the threshold density for shattering applies also to vaporization. The parameters of the shattering model in Paper III were chosen to minimize the amount of shattering and thereby yield a conservative estimate of the threshold density. It was shown that strong feedback on the shock dynamics was expected only for densities higher than $\sim 10^5$ cm^{-3}. The results of the present paper include some observational predictions that should help to constrain the grain-shattering model. The main conclusions of our study are as follows:

1. The influence of grain-grain processing on the overall shock structure was found to be significant for the full range of magnetic field strengths that we studied. The maximum temperature increases by a factor of 1.5–2, and the shock width is reduced by a factor 4–5. The inclusion of grain-grain processing changes the dependence of the shock structure on the magnetic field strength. While for shocks without grain-grain processing there is only a weak dependence of the peak temperature on the magnetic field, the peak temperature becomes strongly dependent on the magnetic field when grain-shattering and vaporization are incorporated. Consequently, the intensities of, in particular, highly excited molecular transitions become dependent on the strength of the magnetic field. While shattering is shown to be important for all models of our grid, the vaporization of SiO from silicate grain cores is significant only for fast shocks and low magnetic fields.

2. There are two consequences of grain-grain processing for the molecular line emission: the reduced shock width results in a lower column density of shock-heated gas, whereas the higher peak temperature can modify the chemistry and enhance the fractional abundances of molecules in highly excited states. Which of these tendencies prevails is decided by the chemical and phys-

ical properties of the individual molecules and their transitions. The intensities of all lines of OH increase in shocks with velocities greater than 30 $\mathrm{km\,s^{-1}}$, when grain-grain processing is included, owing to the temperature sensitivity of OH formation. On the other hand, the intensities of the emission of CO and H_2O decrease because of the reduced column density of shocked material. In the case of H_2, the intensities of highly-excited transitions increase, whilst the intensities of lines of lower excitation decrease.

3. The release of SiO through collisional vaporization of silicate grain cores enhances the integrated intensities of SiO rotational lines, mainly from highly-excited levels. However, this effect is counteracted by the reduction in shock width. To obtain significantly higher line intensities, it is necessary to introduce SiO into the grain mantles. The situation is similar with respect to the widths of the SiO rotational lines. Although vaporizations releases SiO early, in the hot part of the shock wave, the reduction in the shock width prevents the lines from becoming significantly broader than in models that neglect grain-grain processing. Therefore, vaporization alone cannot account for broad lines if only one single shock is considered. To obtain broad profiles, it seems necessary that SiO should be present in the grain mantles, such that mantle sputtering releases SiO, also in the early part of the shock wave. It is essential that SiO is released directly, thereby eliminating the chemical delay that would be associated with its production, in gas-phase reactions, from Si or SiH_4.

   Due to the fact, that most of the SiO emission stems from the early part of the shock, where the temperature profile depends on the shock velocity, the SiO rotational line ratios vary with the shock velocity; this variation is not present if vaporization is ignored. The effect of vaporization on [C I] emission lines was found to be less than for the SiO rotational lines.

ACKNOWLEDGEMENTS. We are grateful to an anonymous referee for useful comments that helped to strengthen the paper. S. Anderl acknowledges support by the DFG SFB 956, the International Max Planck Research School (IMPRS) for Astronomy and Astrophysics, and the Bonn-Cologne Graduate School of Physics and Astronomy.

5.7 APPENDIX A: SHATTERING AND VAPORIZATION: THEIR IMPLEMENTATION AND VALIDATION

5.7.1 *Shattering*

5.7.1.1 *Dynamical effects of shattering*

The dynamical effects of shattering on the shock structure can be simulated by ensuring that the total grain cross section, $\langle n\sigma \rangle$, changes in accord with the results of Paper III. We found that it is possible to model the increase of $\langle n\sigma \rangle$ due to shattering by multiplying the total grain cross section, in the absence of grain-grain processing, by an additional factor, which varies with the spatial coordinate, z, through the shock wave. This factor is modelled as an intrinsic function of the compression of the ion fluid, normalized to the theoretical postshock compression at infinity, as predicted by the Rankine-Hugoniot relations. This normalized ion compression parameter constitutes a function, $\eta(z)$, varying from 0 in the preshock to 1 in the postshock medium.

The preshock (medium 1) and postshock (medium 2) kinetic temperatures are approximately equal in the C-type shock models of our grid. Thus, the Rankine-Hugoniot continuity relations may be applied across the shock wave, replacing the relation of conservation of energy flux by the isothermal condition, $T_1 = T_2$. Then, setting the ratio of specific heats $\gamma = 1$, the expression for the compression ratio, ρ_2/ρ_1, across the shock wave may be derived (cf. Draine & McKee 1993). Under the conditions of our models, which are such that $\mathrm{M_s} = V_\mathrm{s}/c_1 \gg \mathrm{M_A} = V_\mathrm{s}/V_\mathrm{A} \gg 1$, where $\mathrm{M_s}$ is the sonic Mach number of the flow, evaluated in the preshock gas, c_1 is the sound speed, and $\mathrm{M_A}$ is the Alfvénic Mach number, also in the preshock gas, the compression ratio reduces to $\rho_2/\rho_1 \approx \sqrt{2}\mathrm{M_A}$, whence

$$V_\mathrm{postshock} = \frac{V_\mathrm{A}}{\sqrt{2}} = \frac{B}{\sqrt{2 \times 4\pi\ 1.4\ m_\mathrm{H} n_\mathrm{H}}}\ , \tag{66}$$

where $V_\mathrm{postshock}$ is the flow speed in the postshock gas, m_H the proton mass and $n_\mathrm{H} = n(\mathrm{H}) + 2\,n(\mathrm{H_2})$ the proton density in the preshock gas. Using

$$\eta(z) = \frac{V_\mathrm{s}/V_\mathrm{i}(z) - 1}{V_\mathrm{s}/V_\mathrm{postshock} - 1} \tag{67}$$

(where V_s is the shock velocity and V_i the velocity of the ion fluid in the shock frame, respectively), the factor by which the total grain cross section is enhanced is given by

$$\Sigma(z) = \eta(z) \cdot (\Sigma_\mathrm{max} - 1) + 1\ . \tag{68}$$

The extent of the increase of $\langle n\sigma \rangle$ due to shattering is given by the final value of the shattering-factor, Σ_max. This value depends on the shock velocity and the magnetic field and is an external parameter, which needs to be extracted from the multi-fluid models. However, this simple functional form did not reproduce satisfactorily the onset of shattering in the shock. We therefore propose the following refined expression

$$\Sigma = \left(\eta^\beta - \frac{\sin\left(2\pi\,\eta^\beta\right)}{2\pi}\right) \cdot \left(\Sigma_{max} - 1\right) + 1 \tag{69}$$

that introduces another parameter, β, which needs to be extracted from the corresponding multi-fluid model. β describes the delay in the shattering feedback, relative to the ion compression, and is only weakly dependent on the shock velocity. The parameters, β and Σ_max, which correspond to the grid of models introduced in Section 5.4.1, are listed in Table 3. Linear fits in the shock velocity V_s and the magnetic field parameter b are

$$\Sigma_{max} = 9.5 + 0.4 \cdot V_\mathrm{s} - 4.6 \cdot b \tag{70}$$

and

$$\beta = 0.95 - 0.025 \cdot V_\mathrm{s} + 0.4 \cdot b\ . \tag{71}$$

The increase of the total grain collisional cross-section needs to be consistent with the mean square radius of the grains and with their total number density, following the compression of the ions. Analyzing the multi-fluid computations corresponding to Paper III, we find a reasonable approximation

Table 3: Parameters relating to the modification by shattering of the total grain cross-section, $\langle n\sigma \rangle$ and to SiO vaporization, for the grid of multi-fluid models introduced in Section 5.4.1.

V_s [km s^{-1}]	b	B [μG]	Σ_{max}	β	$x(SiO_{peak})$
20	1.0	316	11.7	0.8	$1.53 \cdot 10^{-8}$
20	1.5	474	10.5	1.1	$1.99 \cdot 10^{-17}$
20	2.0	632	8.5	2.0	$2.16 \cdot 10^{-19}$
30	1.5	474	14.2	0.8	$1.55 \cdot 10^{-7}$
30	2.0	632	11.7	0.9	$7.92 \cdot 10^{-9}$
30	2.5	791	10.5	1.2	$5.63 \cdot 10^{-13}$
40	2.0	632	18.4	0.8	$9.13 \cdot 10^{-7}$
40	2.5	791	13.7	0.9	$3.43 \cdot 10^{-7}$
40	3.0	949	11.4	1.1	$1.34 \cdot 10^{-7}$

to the behaviour of the total grain number density, n_G, and the mean square radius, $\langle \sigma \rangle_G$: the former increases as Σ^4, the latter decreases as Σ^{-3}, relative to the corresponding values without shattering. These changes affect the rates of grain-catalyzed reactions, adsorption to the grain mantles, excitation of H_2 in collisions with grains, and transfer of momentum and thermal and kinetic energy between the neutral and the charged fluids.

Figure 12 shows a comparison between the multi-fluid model of Paper III and our current model[7] for a representative shock for which $n_H = 10^5$ cm^{-3}, $V_s = 30$ km s^{-1} and $b = 1.5$. The temperature profiles of the neutral fluid agree well. Furthermore, the variation of the total grain-core cross-section is reproduced by our simulation, as may be seen from the lower panel of Figure 12. The total grain cross-section (including mantles) increases somewhat later in our current model, due to small differences – independent of grain shattering –with the model of Paper III. The discrepancy in the value of the grain cross-section in the postshock medium arises because our simplified treatment of shattering tends to underestimate the final number density of small grains. However, this simplification introduces only small deviations in the hydrodynamic parameters, such that the values of both the peak temperature of the neutral fluid and the shock width (up to 100 K in the cooling flow) agree to within $\pm \sim 15$ % for the entire grid of models incorporating shattering.

5.7.1.2 *Chemical effect of shattering*

The change in the total grain cross-section, $\langle n\sigma \rangle$, owing to shattering, has consequences for the rates of grain-charging reactions. In order to model the effect of shattering on the abundances of charged grains, the corresponding chemical source term needs to be introduced.

The charge distribution of the fragments is essentially unknown and cannot be numerically integrated separately from that of grains already present in the medium. In the present paper[8], the charge

7 In order to make a direct comparison with the results of Paper III, it is necessary to disable the LVG treatment of molecular line transfer in our current model.

8 The situation was more complicated in Paper III, which dealt with a full grain size distribution. Fragments were allocated to the size bins corresponding to their individual mass, while the corresponding mass was removed from the projectile and

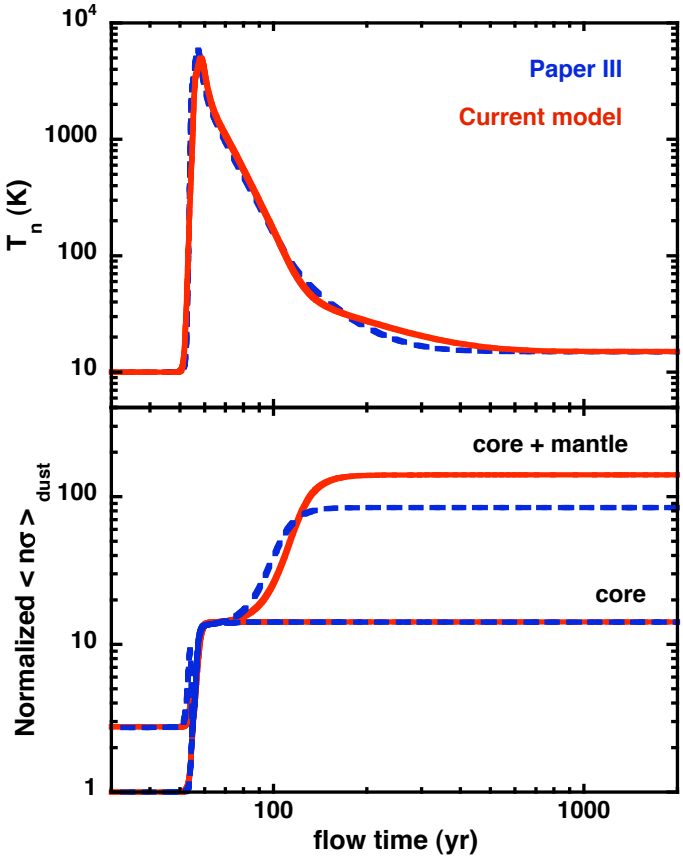

Figure 12: Upper panel: Temperature profiles of the neutral fluid for a shock with $n_{\rm H} = 10^5$ cm^{-3}, $V_{\rm s} = 30$ km s^{-1} and $b = 1.5$ corresponding to Paper III (in blue) and our current model (in red). Lower panel: Evolution of the total grain cross section, $\langle n\sigma \rangle$, for the same shock models, with and without taking into account the grain mantles and normalized to the preshock values of $\langle n\sigma \rangle$.

distribution of fragments is designed to ensure charge conservation. We fitted the fragment charge distribution by aligning the shock widths (see Fig. 12, upper panel). This procedure yielded a charge distribution in which 1/2 of the fragments were neutral, and 1/4 were positively and 1/4 negatively charged, following shattering. Subsequently, the grain charge distribution evolved on a timescale that can be long – of the order of the flow time through the shock wave when the mean grain size becomes very small.

The source term for the creation of grains through shattering can be derived from the equation of conservation of the total flux of grains, in the absence of shattering,

$$\sum_{j\,\in\{\mathrm{G0,G+,G-}\}} n_j \cdot V_j \cdot \Sigma^{-4}(z) = \text{constant} \tag{72}$$

where n_{G0} is the number density of neutral grains, $n_{\mathrm{G+,G-}}$ are the number densities of positively and negatively charged grains, respectively, $V_{\mathrm{G0}} = V_{\mathrm{n}}$ is the velocity of the neutral grains, in the shock frame, and $V_{\mathrm{G+,G-}} = V_{\mathrm{i}}$ is the velocity of the charged grains, in the shock frame. Differentiation of (72), subject to the charge distribution of the fragments, then yields

$$\left.\frac{\mathrm{d}n_{\mathrm{G0}}}{\mathrm{d}z}\right|_{\mathrm{shat}} = \frac{1}{2}\cdot 4 \cdot n_{\mathrm{G,preshock}} \frac{V_{\mathrm{s}}}{V_{\mathrm{n}}} \cdot \Sigma^3 \cdot \frac{\mathrm{d}\Sigma}{\mathrm{d}z} \tag{73}$$

for the neutral grains, and

$$\left.\frac{\mathrm{d}n_{\mathrm{G+,G-}}}{\mathrm{d}z}\right|_{\mathrm{shat}} = \frac{1}{4}\cdot 4 \cdot n_{\mathrm{G,preshock}} \frac{V_{\mathrm{s}}}{V_{\mathrm{i}}} \cdot \Sigma^3 \cdot \frac{\mathrm{d}\Sigma}{\mathrm{d}z} \tag{74}$$

for the charged grains, where $n_{\mathrm{G,preshock}}$ is the total (charged and neutral) number density of grains in the preshock gas. The derivative of Σ is given by

$$\frac{\mathrm{d}\Sigma}{\mathrm{d}z} = \left(\frac{\mathrm{d}}{\mathrm{d}z}\eta^{\beta} - \cos\left(2\pi\eta^{\beta}\right)\frac{\mathrm{d}}{\mathrm{d}z}\eta^{\beta}\right)\left(\Sigma_{\max} - 1\right) \tag{75}$$

where

$$\frac{\mathrm{d}}{\mathrm{d}z}\eta^{\beta} = \beta\,\eta^{(\beta-1)}\frac{\mathrm{d}\eta}{\mathrm{d}z} \tag{76}$$

and

$$\frac{\mathrm{d}\eta}{\mathrm{d}z} = -\frac{1}{\left(V_{\mathrm{s}}/V_{\mathrm{postshock}} - 1\right)}\frac{V_{\mathrm{s}}}{V_{\mathrm{i}}^2}\frac{\mathrm{d}V_{\mathrm{i}}}{\mathrm{d}z}. \tag{77}$$

With these parameters, our model is able to reproduce the main effects of the increase in the grain cross section, reported in Paper III: the effective rate of recombination of electrons and ions is enhanced; the fractional abundance of free electrons falls by three orders of magnitude; and dust grains become the dominant charge carriers, with equal numbers of positively and negatively charged grains being produced.

---

target size bins. This procedure does not allow for charge conservation, because small grains carry much more (negative) charge per unit mass than large grains. To compensate for this charge excess, the charge distributions of all grain sizes was shifted infinitesimally at each shattering event to ensure charge conservation.

5.7.2 *Vaporization*

The effect of vaporization is modelled as an additional term in the creation rate of gas-phase SiO, from Si and O in grain cores (denoted by **), corresponding to a new type of pseudo-chemical reaction:

```
Si** + O** = SiO + GRAIN
```

Because vaporization sets in suddenly, when the vaporization threshold is reached, the function

$$\Omega(z) = \frac{1}{1 + \exp\left(-10^3 \cdot \left(V_\mathrm{s}/V_\mathrm{i}(z) - V_\mathrm{s}/6V_\mathrm{postshock}\right)\right)} \tag{78}$$

can be used to approximate the rate of creation of SiO. The function $\Omega(z)$ is centred at the point where the compression of the charged fluid reaches $1/6$ of its final value, as determined by our fitting procedure. Similarly, the factor 10^3 in the exponent, which determines the steepness of the function, derives from a fit to the numerical results of Paper III. Using this function, the creation rate ($\mathrm{cm^{-3}\ s^{-1}}$) can be expressed as

$$\left.\frac{\mathrm{d}n(\mathrm{SiO})}{\mathrm{d}t}\right|_\mathrm{vapo} = \frac{\mathrm{d}\Omega(z)}{\mathrm{d}t} \cdot n_\mathrm{H} \cdot x(\mathrm{SiO})_\mathrm{peak} \tag{79}$$

$$= \frac{\mathrm{d}\Omega(z)}{\mathrm{d}z} \cdot V_\mathrm{n} \cdot n_\mathrm{H} \cdot x(\mathrm{SiO})_\mathrm{peak} \tag{80}$$

$$= \frac{\mathrm{d}\Omega(z)}{\mathrm{d}z} \cdot V_\mathrm{s} \cdot n_\mathrm{H,preshock} \cdot x(\mathrm{SiO})_\mathrm{peak}\ , \tag{81}$$

where use is made of the conservation of the flux of n_H, and where

$$\frac{\mathrm{d}}{\mathrm{d}z}\Omega(z) = -\Omega(z) \cdot \left(1 - \Omega(z)\right) \cdot 10^3 \frac{V_\mathrm{s}}{V_\mathrm{i}^2} \cdot \frac{\mathrm{d}V_\mathrm{i}}{\mathrm{d}z}\ . \tag{82}$$

The spatial change in number density of SiO, owing to vaporization, is then given by

$$\left.\frac{\mathrm{d}n(\mathrm{SiO})}{\mathrm{d}z}\right|_\mathrm{vapo} = \left(\left.\frac{\mathrm{d}n(\mathrm{SiO})}{\mathrm{d}t}\right|_\mathrm{vapo} - n(\mathrm{SiO})\frac{\mathrm{d}V_\mathrm{n}}{\mathrm{d}z}\right)\frac{1}{V_\mathrm{n}} \tag{83}$$

The peak fractional abundance $x(\mathrm{SiO})_\mathrm{peak}$ needs to be computed with the multi-fluid model and constitutes a free parameter, given in Table 3 for our grid of models. As can be seen in Table 3, vaporization of SiO is relevant only for the shocks with high velocity and low magnetic field; it can be neglected for the shocks with $V_\mathrm{s} = 20\ \mathrm{km\,s^{-1}}$ and $b = 1.5$, $b = 2$, as well as for the model with $V_\mathrm{s} = 30\ \mathrm{km\,s^{-1}}$ and $b = 2.5$.

Figure 13 shows the result of our implementation of vaporization. We assume that, initially (in the preshock medium), there are no Si-bearing species, either in the gas phase or in the grain mantles; all the Si is contained in olivine ($\mathrm{MgFeSiO_4}$) grain cores. This Figure compares the fractional abundance of SiO, as computed with our current model (incorporating grain-grain processing) and as predicted by the multi-fluid model of Paper III. By construction, the peaks of the fractional abundance of SiO agree, whereas the timescale for its accretion on to grains differs between the two models, as is visible in the plot; this discrepancy relates to the imperfect agreement of the total cross-section, $\langle n\sigma \rangle$, in the postshock medium (see Fig. 12). However, we have verified that the timescale for SiO accretion is not critical to our analysis: the complete neglect of accretion on to grains leads to increases in the integrated intensities of the lowest rotational transitions of SiO and CO, by factors of $\sim$2 and $\sim$3, respectively. We note that the intensities of these transitions are, in any case, affected by the foreground emission of ambient, non-shocked gas.

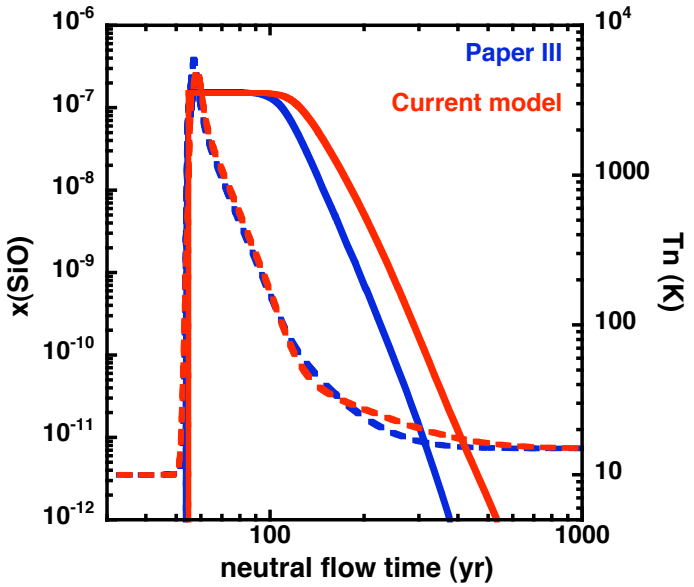

Figure 13: The fractional abundance of SiO (full curves), as determined when including grain-grain processing, using the present model (in red) and the multi-fluid model of Paper III (in blue); the shock parameters are $n_{\rm H} = 10^5$ cm^{-3}, $V_{\rm s} = 30$ km s^{-1} and $b = 1.5$. The temperature of the neutral fluid is shown also (broken curves; right-hand ordinate).

5.8 APPENDIX B: MOLECULAR LINE EMISSION

The introduction of shattering leads to a reduction of the shock width, and hence to lower column densities of shocked material, and to higher peak temperatures, which affect the chemistry and enhance the fractional abundances of molecules in excited states. Which of these effects prevails is determined by the chemical and spectroscopic properties of the individual molecular species.

5.8.1 H_2

The intensities of pure rotational and ro-vibrational lines of H_2 contain key information on the structure of C-type shock waves, as was demonstrated, for example, by Wilgenbus et al. (2000). These lines are optically thin, and their intensities are integrated in parallel with the shock structure, neglecting radiative transfer.

As may be seen from Fig. 14, the introduction of shattering leads to a reduction in the computed column densities of the lowest rotational levels of H_2, by approximately an order of magnitude. With increasing energy of the emitting level, the effect of the decrease in the shock width is compensated by the higher peak temperature, and the column densities predicted by the models that include shattering eventually exceed those calculated neglecting shattering. The change-over occurs at energies of the emitting level of $\gtrsim 6000$ K for $V_{\rm s} = 20$ km s^{-1}, $\gtrsim 7000$ K for $V_{\rm s} = 30$ km s^{-1}, and $\gtrsim 10{,}000$ K for $V_{\rm s} = 40$ km s^{-1}, with the exact values depending on the magnetic field strength. The computed intensities of selected lines of H_2 are given in Table 4, together with the intensities of forbidden lines of atomic oxygen (63 μm and 147 μm), of atomic sulfur (25 μm) and of [C I] (610 μm and 370 μm).

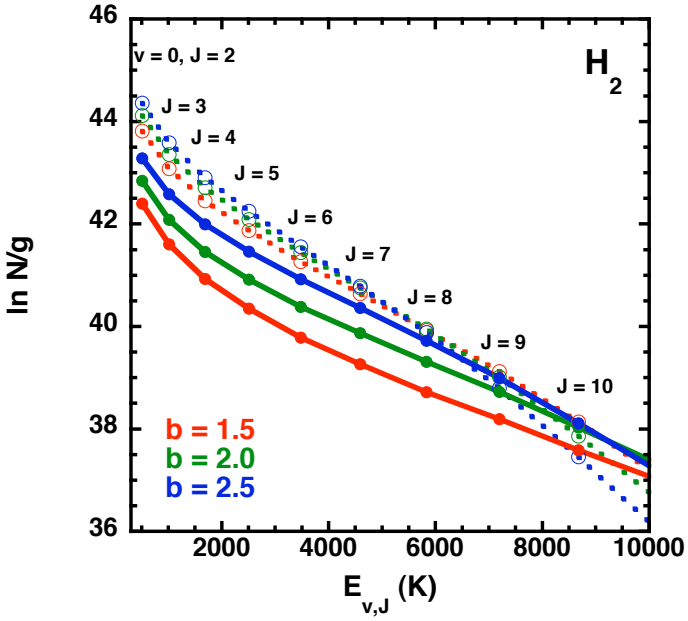

Figure 14: Computed H_2 excitation diagrams for rovibrational levels with energies $E_{v,J} \leq 10\,000$ K and for shocks with $n_H = 10^5$ cm^{-3}, $V_s = 30$ km s^{-1} and $b = 1.5$ (red), $b = 2.0$ (green) and $b = 2.5$ (blue). Full lines: model M1; dotted lines: model M2.

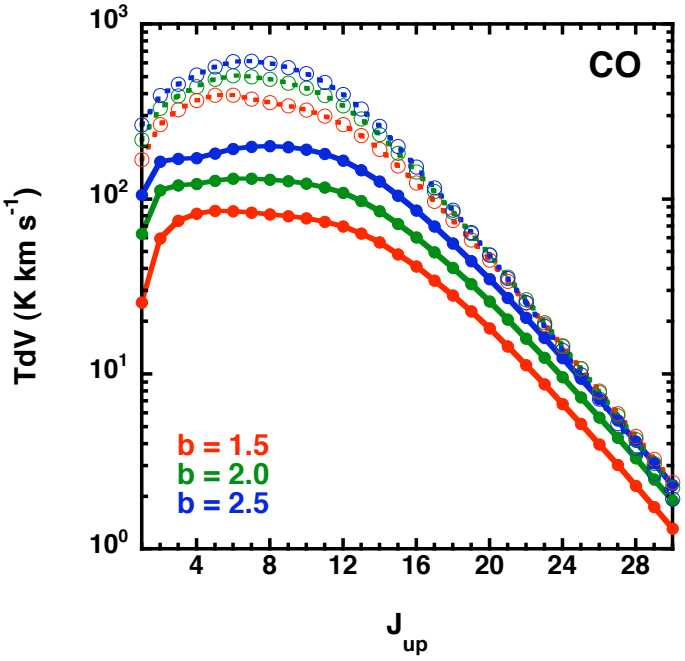

Figure 15: Integrated intensities of the rotational transitions $J_{up} \rightarrow J_{up} - 1$ of CO for shocks with $n_H = 10^5$ cm^{-3}, $V_s = 30$ km s^{-1} and $b = 1.5$ (red), $b = 2.0$ (green) and $b = 2.5$ (blue). Full lines: model M1; dotted lines: model M2.

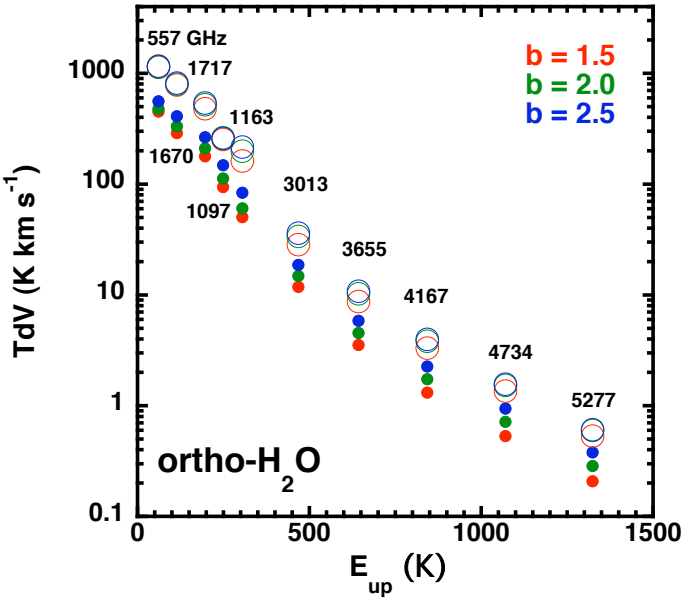

Figure 16: Integrated intensities of selected rotational transitions of ortho-H_2O plotted against the excitation energy of the emitting level, expressed relative to the energy of the $J = 0 = K$ ground state of para-H_2O. Results are shown for shocks with $n_H = 10^5$ cm^{-3}, $V_s = 30$ km s^{-1} and $b = 1.5$ (red), $b = 2.0$ (green) and $b = 2.5$ (blue). Full circles: model M1; open circles: model M2.

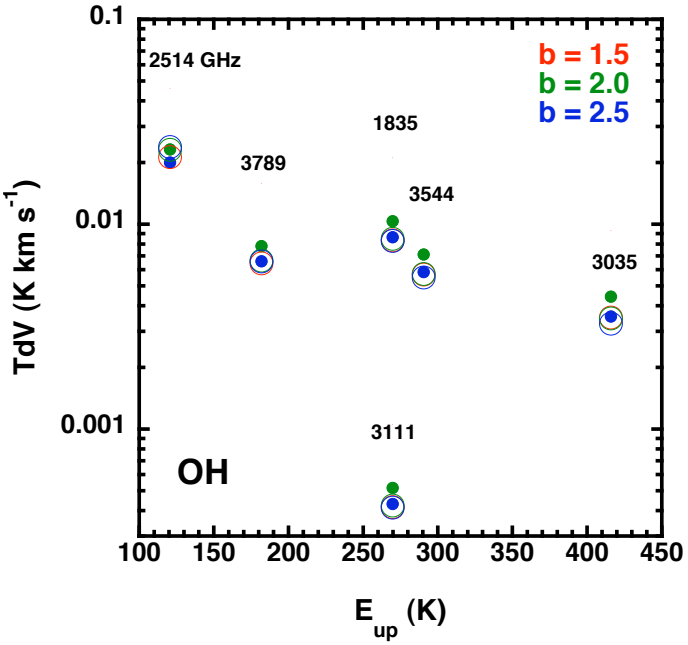

Figure 17: Integrated intensities of the rotational transitions of OH for emitting levels of negative parity, plotted against the excitation energy of the upper level. Results are shown for shocks with $V_s = 30$ km s^{-1} and $b = 1.5$ (red), $b = 2.0$ (green) and $b = 2.5$ (blue). Full circles: model M1; open circles: model M2.

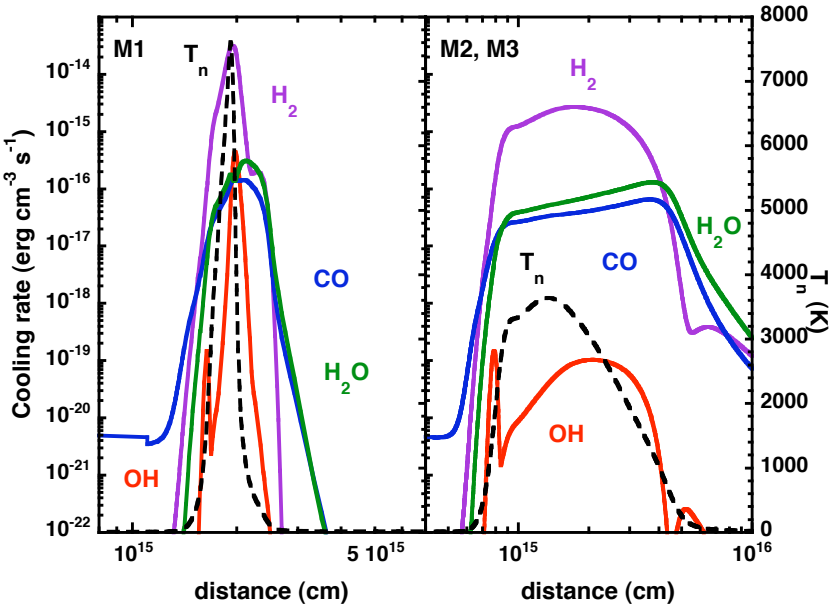

Figure 18: The rate of cooling by the principal molecular coolants, H_2 (mauve), H_2O (green), CO (blue) and OH (red) for $V_s = 40$ km s^{-1} and $b = 2$ for model M1 (left panel) and M2/M3 (right panel), which are shown together because the presence of SiO in grain mantles does not affect the cooling of the shock wave. Note the different distance intervals on the x-axes.

5.8.2 *CO, H_2O and OH*

Figure 15 shows the integrated line intensities, TdV, of the rotational transitions of CO, plotted against the rotational quantum number, J, of the emitting level for shocks with $n_H = 10^5$ cm^{-3} and $V_s = 30$ km s^{-1}. The line intensities, which are listed in Tables 5–7, are lower when shattering is included, owing to the reduction in the shock width; this effect is most pronounced at low magnetic field strengths. While the intensities computed with models M2 peak at around $J_{up} = 7$, those of models M1 peak at higher values of J_{up} and exhibit a plateau extending to $J_{up} \approx 12$. These differences reflect the corresponding excitation conditions. As in the case of SiO (see Sect. 5.5.2), the peak temperature shows a stronger dependence on the strength of the magnetic field in models that include grain-grain processing. Accordingly, the integrated intensities of highly excited transitions vary with b for models M1.

Similarly to CO, the intensities of lines of H_2O also become weaker when shattering is included, owing to the reduced shock width. Figure 16 shows the computed intensities of the lines of ortho-H_2O as a function of the excitation energy of the emitting level. The intensities of all the lines of ortho- and para-H_2O that fall in the Herschel/PACS/HIFI bands are listed in Tables 9–14.

Contrary to the behaviour of CO and H_2O, the line intensities of OH become stronger for the 30 km s^{-1} and 40 km s^{-1} shocks when shattering is included, as may be seen for $V_s = 30$ km s^{-1} in Figure 17. The lines displayed fall within the Herschel/PACS band; their emitting levels have negative parity. The intensities of all transitions of OH observable with Herschel are listed in Table 8. The increase in the integrated intensities in models M1 is due to the higher peak temperatures, which favour the conversion of the gas-phase oxygen that is not bound in CO into OH. Again, we see a

variation of the integrated line intensities with the magnetic field strength in models M1, associated with the temperature-dependent rate of OH formation.

On the basis of these findings, it is interesting to ask how the allowance for grain-grain processing affects the radiative cooling of the medium. Although the narrower shock width, and hence larger velocity gradients, in scenario M1 might be expected to modify the optical thickness of the lines, and thereby their rate of cooling, we do not detect such an effect in our models, as is demonstrated by Fig. 18. Instead, we see an increase in the contribution of OH to the rate of cooling, owing to the enhanced abundance of gas-phase OH in the hot shocked medium (see the lower panel of Fig. 6).

Table 4: Selected H_2, [OI], [CI], and [SI] line intensities (erg cm^{-2} s^{-1} sr^{-1}), for shocks with velocities V_s = 20 km s^{-1} (top), V_s = 30 km s^{-1} (middle), and V_s = 40 km s^{-1} (bottom) and the magnetic field strengths listed in Table 1. Results are given for models M1, which include grain-grain processing, and M2 (in parentheses), which neglect grain-grain processing. The preshock density is $n_H = 10^5$ cm^{-3}.

Transition	λ (μm)	v20b1, M1	(v20b1, M2)	v20b1.5, M1	(v20b1.5, M2)	v20b2, M1	(v20b2, M2)
H_2 0-0 S(0)	28.22	1.87e-06	(6.80e-06)	3.33e-06	(9.44e-06)	5.98e-06	(1.01e-05)
H_2 0-0 S(1)	17.04	9.59e-05	(3.48e-04)	1.74e-04	(4.50e-04)	3.31e-04	(4.84e-04)
H_2 0-0 S(2)	12.28	1.69e-04	(5.85e-04)	3.06e-04	(6.96e-04)	5.88e-04	(7.45e-04)
H_2 0-0 S(3)	9.66	1.55e-03	(4.79e-03)	2.73e-03	(5.17e-03)	4.92e-03	(5.46e-03)
H_2 0-0 S(4)	8.02	1.11e-03	(2.89e-03)	1.85e-03	(2.79e-03)	2.93e-03	(2.85e-03)
H_2 0-0 S(5)	6.91	5.64e-03	(1.14e-02)	8.48e-03	(9.63e-03)	1.07e-02	(9.23e-03)
H_2 0-0 S(6)	6.11	2.57e-03	(3.65e-03)	3.33e-03	(2.66e-03)	2.97e-03	(2.26e-03)
H_2 0-0 S(7)	5.51	8.75e-03	(7.71e-03)	9.09e-03	(4.78e-03)	4.90e-03	(3.35e-03)
H_2 1-0 S(1)	2.12	1.02e-03	(2.17e-04)	4.12e-04	(1.00e-04)	8.82e-05	(5.43e-05)
OI $2p^4\ ^3P_1 \rightarrow 2p^4\ ^3P_2$	63.1	3.72e-06	(3.93e-06)	1.03e-05	(7.57e-06)	2.02e-05	(1.27e-05)
OI $2p^4\ ^3P_0 \rightarrow 2p^4\ ^3P_1$	145.5	2.66e-07	(2.74e-07)	7.44e-07	(5.32e-07)	1.45e-06	(9.06e-07)
CI $^3P_1 \rightarrow\ ^3P_0$	609.75	4.84e-11	(1.11e-10)	2.21e-10	(3.36e-10)	4.68e-10	(6.45e-10)
CI $^3P_2 \rightarrow\ ^3P_1$	370.37	4.05e-11	(3.40e-10)	1.23e-10	(7.04e-10)	3.12e-10	(1.24e-09)
SI 3P J=1 → 3P J=2	25.25	2.81e-05	(7.03e-05)	3.71e-05	(9.61e-05)	8.44e-05	(1.21e-04)

Transition	λ (μm)	v30b1.5, M1	(v30b1.5, M2)	v30b2, M1	(v30b2, M2)	v30b2.5, M1	(v30b2.5, M2)
H_2 0-0 S(0)	28.22	2.13e-06	(8.83e-06)	3.34e-06	(1.19e-05)	5.19e-06	(1.52e-05)
H_2 0-0 S(1)	17.04	1.08e-04	(4.77e-04)	1.76e-04	(6.31e-04)	2.90e-04	(7.91e-04)
H_2 0-0 S(2)	12.28	1.90e-04	(8.79e-04)	3.24e-04	(1.13e-03)	5.54e-04	(1.38e-03)
H_2 0-0 S(3)	9.66	1.77e-03	(8.14e-03)	3.13e-03	(1.01e-02)	5.43e-03	(1.19e-02)
H_2 0-0 S(4)	8.02	1.29e-03	(5.68e-03)	2.34e-03	(6.78e-03)	4.03e-03	(7.57e-03)
H_2 0-0 S(5)	6.91	6.87e-03	(2.71e-02)	1.26e-02	(3.04e-02)	2.06e-02	(3.15e-02)
H_2 0-0 S(6)	6.11	3.31e-03	(1.10e-02)	5.96e-03	(1.13e-02)	8.99e-03	(1.06e-02)
H_2 0-0 S(7)	5.51	1.27e-02	(3.20e-02)	2.15e-02	(2.88e-02)	2.83e-02	(2.32e-02)
H_2 1-0 S(1)	2.12	6.92e-03	(3.42e-03)	4.82e-03	(2.32e-03)	2.93e-03	(1.40e-03)
OI $2p^4\ ^3P_1 \rightarrow 2p^4\ ^3P_2$	63.1	4.00e-06	(4.40e-06)	8.05e-06	(7.18e-06)	1.40e-05	(1.13e-05)
OI $2p^4\ ^3P_0 \rightarrow 2p^4\ ^3P_1$	145.5	2.87e-07	(2.79e-07)	5.76e-07	(4.67e-07)	1.01e-06	(7.37e-07)
CI $^3P_1 \rightarrow\ ^3P_0$	609.75	1.88e-10	(1.24e-10)	1.85e-10	(3.04e-10)	3.66e-10	(5.24e-10)
CI $^3P_2 \rightarrow\ ^3P_1$	370.37	1.18e-09	(3.98e-10)	1.09e-10	(6.58e-10)	2.01e-10	(9.67e-10)
SI 3P J=1 → 3P J=2	25.25	3.93e-04	(6.10e-04)	2.56e-04	(7.34e-04)	1.56e-04	(8.24e-04)

Transition	λ (μm)	v40b2, M1	(v40b2, M2)	v40b2.5, M1	(v40b2.5, M2)	v40b3, M1	(v40b3, M2)
H_2 0-0 S(0)	28.22	3.54e-06	(1.08e-05)	3.60e-06	(1.35e-05)	5.02e-06	(1.65e-05)
H_2 0-0 S(1)	17.04	1.46e-04	(5.81e-04)	1.81e-04	(7.26e-04)	2.73e-04	(8.79e-04)
H_2 0-0 S(2)	12.28	2.03e-04	(1.07e-03)	3.21e-04	(1.34e-03)	5.21e-04	(1.62e-03)
H_2 0-0 S(3)	9.66	1.59e-03	(1.02e-02)	3.04e-03	(1.27e-02)	5.21e-04	(1.51e-02)
H_2 0-0 S(4)	8.02	1.09e-03	(7.27e-03)	2.25e-03	(9.10e-03)	4.00e-03	(1.07e-02)
H_2 0-0 S(5)	6.91	5.78e-03	(3.65e-02)	1.23e-02	(4.54e-02)	2.20e-02	(5.19e-02)
H_2 0-0 S(6)	6.11	2.97e-03	(1.59e-02)	6.03e-03	(1.95e-02)	1.06e-02	(2.14e-02)
H_2 0-0 S(7)	5.51	1.24e-02	(5.21e-02)	2.36e-02	(6.15e-02)	3.92e-02	(6.35e-02)
H_2 1-0 S(1)	2.12	1.34e-02	(1.58e-02)	1.59e-02	(1.15e-02)	1.31e-02	(8.75e-03)
OI $2p^4\ ^3P_1 \rightarrow 2p^4\ ^3P_2$	63.1	3.72e-05	(3.48e-06)	7.41e-06	(5.98e-06)	1.17e-05	(9.20e-06)
OI $2p^4\ ^3P_0 \rightarrow 2p^4\ ^3P_1$	145.5	1.36e-06	(2.44e-07)	5.34e-07	(3.96e-07)	8.42e-07	(5.97e-07)
CI $^3P_1 \rightarrow\ ^3P_0$	609.75	5.50e-08	(6.66e-10)	1.04e-08	(4.27e-10)	5.34e-10	(5.95e-10)
CI $^3P_2 \rightarrow\ ^3P_1$	370.37	4.73e-07	(2.26e-09)	8.16e-08	(1.04e-09)	1.83e-09	(1.27e-09)
SI 3P J=1 $\rightarrow$ 3P J=2	25.25	1.35e-03	(1.43e-03)	7.07e-04	(1.37e-03)	5.97e-04	(1.40e-03)

Table 5: Intensities of CO lines (erg cm^{-2} s^{-1} sr^{-1}) for shocks with velocity V_s = 20 km s^{-1} and the magnetic field strengths listed in Table 1. Results are given for models M1, which include grain-grain processing, and M2 (in parentheses), which neglect grain-grain processing. The preshock density is n_H = 10^5 cm^{-3}.

Transition	Freq. (GHz)	λ (μm)	v20b1, M1	(v20b1, M2)	v20b1.5, M1	(v20b1.5, M2)	v20b2, M1	(v20b2, M2)
CO (1–0)	115.27	2600.7	3.47e-08	(1.85e-07)	9.49e-08	(2.63e-07)	1.47e-07	(2.69e-07)
CO (2–1)	230.54	1300.4	6.39e-07	(2.41e-06)	1.28e-06	(3.23e-06)	1.76e-06	(3.14e-06)
CO (3–2)	345.80	866.96	2.72e-06	(1.01e-05)	4.69e-06	(1.30e-05)	6.33e-06	(1.22e-05)
CO (4–3)	461.04	650.25	7.01e-06	(2.73e-05)	1.15e-05	(3.50e-05)	1.57e-05	(3.24e-05)
CO (5–4)	576.27	520.23	1.41e-05	(5.78e-05)	2.36e-05	(7.55e-05)	3.40e-05	(7.07e-05)
CO (6–5)	691.47	433.55	2.42e-05	(1.00e-04)	4.22e-05	(1.36e-04)	6.46e-05	(1.30e-04)
CO (7–6)	806.65	371.65	3.76e-05	(1.51e-04)	6.71e-05	(2.09e-04)	1.09e-04	(2.06e-04)
CO (8–7)	921.80	325.22	5.51e-05	(2.13e-04)	9.84e-05	(2.91e-04)	1.66e-04	(2.94e-04)
CO (9–8)	1036.9	289.12	7.68e-05	(2.83e-04)	1.36e-04	(3.76e-04)	2.32e-04	(3.86e-04)
CO (10–9)	1152.0	260.24	1.02e-04	(3.54e-04)	1.76e-04	(4.52e-04)	3.01e-04	(4.70e-04)
CO (11–10)	1267.0	236.61	1.29e-04	(4.16e-04)	2.17e-04	(5.09e-04)	3.63e-04	(5.31e-04)
CO (12–11)	1382.0	216.93	1.56e-04	(4.57e-04)	2.52e-04	(5.38e-04)	4.09e-04	(5.62e-04)
CO (13–12)	1496.9	200.27	1.78e-04	(4.72e-04)	2.75e-04	(5.33e-04)	4.32e-04	(5.58e-04)
CO (14–13)	1611.8	186.00	1.94e-04	(4.64e-04)	2.87e-04	(5.03e-04)	4.34e-04	(5.25e-04)
CO (15–14)	1726.6	173.63	2.00e-04	(4.29e-04)	2.83e-04	(4.47e-04)	4.11e-04	(4.65e-04)
CO (16–15)	1841.3	162.81	2.02e-04	(3.94e-04)	2.75e-04	(3.95e-04)	3.84e-04	(4.10e-04)
CO (17–16)	1956.0	153.27	1.98e-04	(3.52e-04)	2.59e-04	(3.42e-04)	3.49e-04	(3.52e-04)
CO (18–17)	2070.6	144.78	1.89e-04	(3.09e-04)	2.39e-04	(2.91e-04)	3.09e-04	(2.97e-04)
CO (19–18)	2185.1	137.20	1.78e-04	(2.67e-04)	2.17e-04	(2.44e-04)	2.70e-04	(2.48e-04)
CO (20–19)	2299.6	130.37	1.64e-04	(2.28e-04)	1.94e-04	(2.03e-04)	2.32e-04	(2.04e-04)
CO (21–20)	2413.9	124.19	1.47e-04	(1.91e-04)	1.70e-04	(1.66e-04)	1.96e-04	(1.65e-04)
CO (22–21)	2528.2	118.58	1.31e-04	(1.59e-04)	1.47e-04	(1.34e-04)	1.63e-04	(1.33e-04)
CO (23–22)	2642.3	113.46	1.15e-04	(1.31e-04)	1.26e-04	(1.08e-04)	1.34e-04	(1.06e-04)
CO (24–23)	2756.4	108.76	9.98e-05	(1.07e-04)	1.07e-04	(8.63e-05)	1.09e-04	(8.34e-05)
CO (25–24)	2870.3	104.44	8.58e-05	(8.66e-05)	8.98e-05	(6.85e-05)	8.83e-05	(6.54e-05)
CO (26–25)	2984.2	100.46	7.32e-05	(6.98e-05)	7.50e-05	(5.41e-05)	7.08e-05	(5.10e-05)
CO (27–26)	3097.9	96.772	6.20e-05	(5.60e-05)	6.23e-05	(4.25e-05)	5.63e-05	(3.95e-05)
CO (28–27)	3211.5	93.348	5.21e-05	(4.46e-05)	5.13e-05	(3.32e-05)	4.44e-05	(3.04e-05)
CO (29–28)	3325.0	90.162	4.35e-05	(3.53e-05)	4.20e-05	(2.58e-05)	3.48e-05	(2.33e-05)
CO (30–29)	3438.4	87.190	3.59e-05	(2.78e-05)	3.40e-05	(1.99e-05)	2.70e-05	(1.77e-05)
CO (31–30)	3551.6	84.410	2.95e-05	(2.17e-05)	2.74e-05	(1.52e-05)	2.08e-05	(1.33e-05)
CO (32–31)	3664.7	81.805	2.40e-05	(1.68e-05)	2.19e-05	(1.16e-05)	1.58e-05	(9.96e-06)
CO (33–32)	3777.6	79.359	1.92e-05	(1.29e-05)	1.72e-05	(8.71e-06)	1.19e-05	(7.37e-06)
CO (34–33)	3890.4	77.058	1.52e-05	(9.72e-06)	1.34e-05	(6.48e-06)	8.87e-06	(5.39e-06)
CO (35–34)	4003.1	74.889	1.18e-05	(7.21e-06)	1.02e-05	(4.73e-06)	6.46e-06	(3.87e-06)
CO (36–35)	4115.6	72.842	8.96e-06	(5.22e-06)	7.60e-06	(3.37e-06)	4.60e-06	(2.71e-06)
CO (37–36)	4228.0	70.907	6.52e-06	(3.64e-06)	5.43e-06	(2.32e-06)	3.15e-06	(1.84e-06)
CO (38–37)	4340.1	69.074	4.46e-06	(2.39e-06)	3.65e-06	(1.50e-06)	2.03e-06	(1.17e-06)
CO (39–38)	4452.2	67.336	2.72e-06	(1.41e-06)	2.19e-06	(8.72e-07)	1.17e-06	(6.69e-07)
CO (40–39)	4564.0	65.686	1.25e-06	(6.22e-07)	9.89e-07	(3.81e-07)	5.10e-07	(2.88e-07)

Table 6: Intensities of CO lines (erg cm^{-2} s^{-1} sr^{-1}) for shocks with velocity V_s = 30 km s^{-1} and the magnetic field strengths listed in Table 1. Results are given for models M1, which include grain-grain processing, and M2 (in parentheses), which neglect grain-grain processing. The preshock density is n_H = 10^5 cm^{-3}.

Transition	Freq. (GHz)	λ (μm)	v30b1.5, M1	(v30b1.5, M2)	v30b2, M1	(v30b2, M2)	v30b2.5, M1	(v30b2.5, M2)
CO (1–0)	115.27	2600.7	4.01e-08	(2.64e-07)	9.93e-08	(3.42e-07)	1.65e-07	(4.14e-07)
CO (2–1)	230.54	1300.4	7.45e-07	(3.35e-06)	1.41e-06	(4.14e-06)	2.05e-06	(4.88e-06)
CO (3–2)	345.80	866.96	3.19e-06	(1.37e-05)	5.06e-06	(1.65e-05)	7.19e-06	(1.92e-05)
CO (4–3)	461.04	650.25	8.29e-06	(3.68e-05)	1.22e-05	(4.39e-05)	1.72e-05	(5.12e-05)
CO (5–4)	576.27	520.23	1.68e-05	(7.71e-05)	2.49e-05	(9.47e-05)	3.57e-05	(1.12e-04)
CO (6–5)	691.47	433.55	2.89e-05	(1.33e-04)	4.42e-05	(1.71e-04)	6.54e-05	(2.07e-04)
CO (7–6)	806.65	371.65	4.49e-05	(2.01e-04)	7.03e-05	(2.69e-04)	1.07e-04	(3.30e-04)
CO (8–7)	921.80	325.22	6.56e-05	(2.86e-04)	1.04e-04	(3.88e-04)	1.61e-04	(4.79e-04)
CO (9–8)	1036.9	289.12	9.13e-05	(3.90e-04)	1.44e-04	(5.26e-04)	2.26e-04	(6.46e-04)
CO (10–9)	1152.0	260.24	1.22e-04	(5.06e-04)	1.92e-04	(6.74e-04)	3.00e-04	(8.15e-04)
CO (11–10)	1267.0	236.61	1.55e-04	(6.22e-04)	2.43e-04	(8.13e-04)	3.77e-04	(9.65e-04)
CO (12–11)	1382.0	216.93	1.88e-04	(7.22e-04)	2.93e-04	(9.23e-04)	4.48e-04	(1.07e-03)
CO (13–12)	1496.9	200.27	2.18e-04	(7.91e-04)	3.35e-04	(9.86e-04)	5.03e-04	(1.12e-03)
CO (14–13)	1611.8	186.00	2.42e-04	(8.26e-04)	3.66e-04	(1.00e-03)	5.40e-04	(1.12e-03)
CO (15–14)	1726.6	173.63	2.55e-04	(8.14e-04)	3.80e-04	(9.65e-04)	5.50e-04	(1.05e-03)
CO (16–15)	1841.3	162.81	2.63e-04	(7.89e-04)	3.86e-04	(9.15e-04)	5.49e-04	(9.77e-04)
CO (17–16)	1956.0	153.27	2.62e-04	(7.45e-04)	3.81e-04	(8.46e-04)	5.34e-04	(8.86e-04)
CO (18–17)	2070.6	144.78	2.55e-04	(6.87e-04)	3.68e-04	(7.65e-04)	5.07e-04	(7.87e-04)
CO (19–18)	2185.1	137.20	2.43e-04	(6.23e-04)	3.48e-04	(6.81e-04)	4.73e-04	(6.89e-04)
CO (20–19)	2299.6	130.37	2.27e-04	(5.57e-04)	3.24e-04	(5.98e-04)	4.35e-04	(5.96e-04)
CO (21–20)	2413.9	124.19	2.07e-04	(4.88e-04)	2.94e-04	(5.16e-04)	3.91e-04	(5.06e-04)
CO (22–21)	2528.2	118.58	1.86e-04	(4.23e-04)	2.64e-04	(4.40e-04)	3.47e-04	(4.25e-04)
CO (23–22)	2642.3	113.46	1.65e-04	(3.62e-04)	2.34e-04	(3.72e-04)	3.05e-04	(3.54e-04)
CO (24–23)	2756.4	108.76	1.45e-04	(3.08e-04)	2.05e-04	(3.11e-04)	2.65e-04	(2.93e-04)
CO (25–24)	2870.3	104.44	1.25e-04	(2.60e-04)	1.78e-04	(2.59e-04)	2.28e-04	(2.40e-04)
CO (26–25)	2984.2	100.46	1.08e-04	(2.18e-04)	1.54e-04	(2.14e-04)	1.95e-04	(1.96e-04)
CO (27–26)	3097.9	96.772	9.19e-05	(1.81e-04)	1.32e-04	(1.76e-04)	1.66e-04	(1.58e-04)
CO (28–27)	3211.5	93.348	7.78e-05	(1.50e-04)	1.12e-04	(1.43e-04)	1.39e-04	(1.27e-04)
CO (29–28)	3325.0	90.162	6.53e-05	(1.23e-04)	9.40e-05	(1.16e-04)	1.17e-04	(1.02e-04)
CO (30–29)	3438.4	87.190	5.43e-05	(1.00e-04)	7.85e-05	(9.33e-05)	9.66e-05	(8.07e-05)
CO (31–30)	3551.6	84.410	4.49e-05	(8.08e-05)	6.51e-05	(7.44e-05)	7.94e-05	(6.35e-05)
CO (32–31)	3664.7	81.805	3.67e-05	(6.47e-05)	5.34e-05	(5.89e-05)	6.46e-05	(4.95e-05)
CO (33–32)	3777.6	79.359	2.97e-05	(5.12e-05)	4.33e-05	(4.60e-05)	5.19e-05	(3.81e-05)
CO (34–33)	3890.4	77.058	2.37e-05	(4.00e-05)	3.45e-05	(3.55e-05)	4.11e-05	(2.90e-05)
CO (35–34)	4003.1	74.889	1.85e-05	(3.06e-05)	2.70e-05	(2.68e-05)	3.19e-05	(2.16e-05)
CO (36–35)	4115.6	72.842	1.41e-05	(2.29e-05)	2.06e-05	(1.98e-05)	2.42e-05	(1.57e-05)
CO (37–36)	4228.0	70.907	1.03e-05	(1.64e-05)	1.51e-05	(1.40e-05)	1.76e-05	(1.10e-05)
CO (38–37)	4340.1	69.074	7.11e-06	(1.11e-05)	1.04e-05	(9.36e-06)	1.20e-05	(7.26e-06)
CO (39–38)	4452.2	67.336	4.37e-06	(6.68e-06)	6.39e-06	(5.58e-06)	7.31e-06	(4.27e-06)
CO (40–39)	4564.0	65.686	2.02e-06	(3.03e-06)	2.95e-06	(2.50e-06)	3.35e-06	(1.89e-06)

Table 7: Intensities of CO lines (erg cm^{-2} s^{-1} sr^{-1}) for shocks with velocity V_s = 40 km s^{-1} and the magnetic field strengths listed in Table 1. Results are given for models M1, which include grain-grain processing, and M2 (in parentheses), which neglect grain-grain processing. The preshock density is n_H = 10^5 cm^{-3}.

Transition	Freq. (GHz)	λ (μm)	v40b2, M1	(v40b2, M2)	v40b2.5, M1	(v40b2.5, M2)	v40b3, M1	(v40b3, M2)
CO (1–0)	115.27	2600.7	3.42e-08	(3.41e-07)	1.00e-07	(4.18e-07)	1.73e-07	(4.86e-07)
CO (2–1)	230.54	1300.4	6.14e-07	(4.33e-06)	1.45e-06	(5.02e-06)	2.22e-06	(5.69e-06)
CO (3–2)	345.80	866.96	2.73e-06	(1.76e-05)	5.30e-06	(1.98e-05)	7.52e-06	(2.21e-05)
CO (4–3)	461.04	650.25	7.90e-06	(4.67e-05)	1.30e-05	(5.22e-05)	1.76e-05	(5.82e-05)
CO (5–4)	576.27	520.23	1.81e-05	(9.75e-05)	2.68e-05	(1.11e-04)	3.63e-05	(1.25e-04)
CO (6–5)	691.47	433.55	3.51e-05	(1.68e-04)	4.79e-05	(1.99e-04)	6.58e-05	(2.30e-04)
CO (7–6)	806.65	371.65	6.04e-05	(2.53e-04)	7.70e-05	(3.11e-04)	1.07e-04	(3.66e-04)
CO (8–7)	921.80	325.22	9.53e-05	(3.58e-04)	1.14e-04	(4.49e-04)	1.61e-04	(5.35e-04)
CO (9–8)	1036.9	289.12	1.40e-04	(4.91e-04)	1.59e-04	(6.17e-04)	2.27e-04	(7.36e-04)
CO (10–9)	1152.0	260.24	1.93e-04	(6.46e-04)	2.11e-04	(8.08e-04)	3.03e-04	(9.57e-04)
CO (11–10)	1267.0	236.61	2.51e-04	(8.09e-04)	2.67e-04	(1.00e-03)	3.84e-04	(1.18e-03)
CO (12–11)	1382.0	216.93	3.11e-04	(9.61e-04)	3.23e-04	(1.18e-03)	4.64e-04	(1.37e-03)
CO (13–12)	1496.9	200.27	3.66e-04	(1.08e-03)	3.71e-04	(1.31e-03)	5.32e-04	(1.50e-03)
CO (14–13)	1611.8	186.00	4.12e-04	(1.15e-03)	4.09e-04	(1.38e-03)	5.84e-04	(1.56e-03)
CO (15–14)	1726.6	173.63	4.39e-04	(1.17e-03)	4.29e-04	(1.38e-03)	6.09e-04	(1.54e-03)
CO (16–15)	1841.3	162.81	4.57e-04	(1.16e-03)	4.40e-04	(1.36e-03)	6.22e-04	(1.50e-03)
CO (17–16)	1956.0	153.27	4.61e-04	(1.11e-03)	4.39e-04	(1.30e-03)	6.17e-04	(1.42e-03)
CO (18–17)	2070.6	144.78	4.52e-04	(1.04e-03)	4.26e-04	(1.21e-03)	5.98e-04	(1.31e-03)
CO (19–18)	2185.1	137.20	4.33e-04	(9.61e-04)	4.05e-04	(1.11e-03)	5.68e-04	(1.19e-03)
CO (20–19)	2299.6	130.37	4.07e-04	(8.71e-04)	3.79e-04	(1.00e-03)	5.31e-04	(1.07e-03)
CO (21–20)	2413.9	124.19	3.74e-04	(7.73e-04)	3.46e-04	(8.86e-04)	4.85e-04	(9.36e-04)
CO (22–21)	2528.2	118.58	3.37e-04	(6.76e-04)	3.11e-04	(7.74e-04)	4.37e-04	(8.13e-04)
CO (23–22)	2642.3	113.46	3.01e-04	(5.86e-04)	2.76e-04	(6.69e-04)	3.89e-04	(6.99e-04)
CO (24–23)	2756.4	108.76	2.65e-04	(5.02e-04)	2.42e-04	(5.74e-04)	3.43e-04	(5.96e-04)
CO (25–24)	2870.3	104.44	2.30e-04	(4.27e-04)	2.11e-04	(4.88e-04)	2.99e-04	(5.04e-04)
CO (26–25)	2984.2	100.46	1.99e-04	(3.61e-04)	1.82e-04	(4.12e-04)	2.59e-04	(4.23e-04)
CO (27–26)	3097.9	96.772	1.70e-04	(3.03e-04)	1.56e-04	(3.45e-04)	2.23e-04	(3.53e-04)
CO (28–27)	3211.5	93.348	1.45e-04	(2.52e-04)	1.32e-04	(2.88e-04)	1.90e-04	(2.93e-04)
CO (29–28)	3325.0	90.162	1.22e-04	(2.08e-04)	1.11e-04	(2.38e-04)	1.61e-04	(2.41e-04)
CO (30–29)	3438.4	87.190	1.03e-04	(1.71e-04)	9.31e-05	(1.95e-04)	1.35e-04	(1.97e-04)
CO (31–30)	3551.6	84.410	8.53e-05	(1.39e-04)	7.72e-05	(1.59e-04)	1.12e-04	(1.60e-04)
CO (32–31)	3664.7	81.805	7.03e-05	(1.12e-04)	6.34e-05	(1.28e-04)	9.22e-05	(1.28e-04)
CO (33–32)	3777.6	79.359	5.73e-05	(8.96e-05)	5.15e-05	(1.02e-04)	7.50e-05	(1.02e-04)
CO (34–33)	3890.4	77.058	4.61e-05	(7.05e-05)	4.12e-05	(8.06e-05)	6.01e-05	(7.99e-05)
CO (35–34)	4003.1	74.889	3.63e-05	(5.44e-05)	3.23e-05	(6.22e-05)	4.72e-05	(6.13e-05)
CO (36–35)	4115.6	72.842	2.79e-05	(4.09e-05)	2.47e-05	(4.68e-05)	3.61e-05	(4.59e-05)
CO (37–36)	4228.0	70.907	2.06e-05	(2.96e-05)	1.82e-05	(3.38e-05)	2.66e-05	(3.31e-05)
CO (38–37)	4340.1	69.074	1.43e-05	(2.02e-05)	1.26e-05	(2.30e-05)	1.84e-05	(2.24e-05)
CO (39–38)	4452.2	67.336	8.88e-06	(1.22e-05)	7.73e-06	(1.40e-05)	1.13e-05	(1.35e-05)
CO (40–39)	4564.0	65.686	4.13e-06	(5.58e-06)	3.58e-06	(6.36e-06)	5.22e-06	(6.14e-06)

Table 8: Intensities of OH lines (erg cm^{-2} s^{-1} sr^{-1}) observable with the PACS instrument on the Herschel Space Observatory, for shocks with velocities V_s = 20 km s^{-1} (top), V_s = 30 km s^{-1} (middle), and V_s = 40 km s^{-1} (bottom) and the magnetic field strengths listed in Table 1. Results are given for models M1, which include grain-grain processing, and M2 (in parentheses), which neglect grain-grain processing. The preshock density is $n_H = 10^5$ cm^{-3}.

Transition	λ (μm)	E_{up} (K)	v20b1, M1	(v20b1, M2)	v20b1.5, M1	(v20b1.5, M2)	v20b2, M1	(v20b2, M2)
1834.8 GHz	163.39	269.8	1.65e-08	(1.76e-08)	2.58e-08	(2.51e-08)	3.92e-08	(3.03e-08)
1839.0 GHz	163.01	270.2	2.42e-08	(2.54e-08)	3.75e-08	(3.58e-08)	5.65e-08	(4.35e-08)
2510.0 GHz	119.44	120.5	1.79e-07	(2.71e-07)	2.88e-07	(4.89e-07)	4.38e-07	(4.20e-07)
2514.0 GHz	119.23	120.7	9.78e-08	(1.65e-07)	1.60e-07	(3.14e-07)	2.44e-07	(2.50e-07)
3035.0 GHz	98.76	415.9	3.11e-08	(3.08e-08)	4.61e-08	(4.01e-08)	6.78e-08	(5.11e-08)
3036.0 GHz	98.74	415.5	1.00e-08	(1.00e-08)	1.50e-08	(1.31e-08)	2.22e-08	(1.68e-08)
3111.0 GHz	96.36	269.8	4.01e-09	(4.28e-09)	6.28e-09	(6.11e-09)	9.54e-09	(7.36e-09)
3114.0 GHz	96.27	270.2	5.86e-09	(6.16e-09)	9.07e-09	(8.67e-09)	1.37e-08	(1.05e-08)
3544.0 GHz	84.60	290.5	8.10e-08	(8.30e-08)	1.24e-07	(1.13e-07)	1.86e-07	(1.41e-07)
3551.0 GHz	84.42	291.2	1.94e-08	(2.01e-08)	3.00e-08	(2.76e-08)	4.52e-08	(3.44e-08)
3786.0 GHz	79.18	181.7	1.01e-07	(1.19e-07)	1.61e-07	(1.88e-07)	2.47e-07	(2.03e-07)
3789.0 GHz	79.12	181.9	1.11e-07	(1.27e-07)	1.76e-07	(1.96e-07)	2.68e-07	(2.17e-07)
4210.0 GHz	71.22	617.9	1.51e-08	(1.45e-08)	2.13e-08	(1.81e-08)	3.04e-08	(2.31e-08)
4212.0 GHz	71.17	617.6	2.92e-09	(2.81e-09)	4.17e-09	(3.53e-09)	5.96e-09	(4.52e-09)
4592.0 GHz	65.28	510.9	2.78e-08	(2.71e-08)	4.05e-08	(3.46e-08)	5.87e-08	(4.43e-08)
4603.0 GHz	65.13	512.1	4.03e-09	(3.94e-09)	5.90e-09	(5.05e-09)	8.58e-09	(6.47e-09)

Transition	λ (μm)	E_{up} (K)	v30b1.5, M1	(v30b1.5, M2)	v30b2, M1	(v30b2, M2)	v30b2.5, M1	(v30b2.5, M2)
1834.8 GHz	163.39	269.8	1.33e-07	(5.28e-08)	6.54e-08	(5.38e-08)	5.46e-08	(5.24e-08)
1839.0 GHz	163.01	270.2	1.98e-07	(7.76e-08)	9.67e-08	(7.86e-08)	8.00e-08	(7.62e-08)
2510.0 GHz	119.44	120.5	4.38e-07	(6.17e-07)	6.95e-07	(6.58e-07)	5.94e-07	(6.68e-07)
2514.0 GHz	119.23	120.7	7.47e-07	(3.46e-07)	3.77e-07	(3.76e-07)	3.26e-07	(3.88e-07)
3035.0 GHz	98.76	415.9	2.66e-07	(1.00e-07)	1.27e-07	(9.94e-08)	1.02e-07	(9.38e-08)
3036.0 GHz	98.74	415.5	8.54e-08	(3.23e-08)	4.08e-08	(3.21e-08)	3.28e-08	(3.04e-08)
3111.0 GHz	96.36	269.8	3.24e-08	(1.28e-08)	1.59e-08	(1.31e-08)	1.34e-08	(1.27e-08)
3114.0 GHz	96.27	270.2	4.80e-08	(1.88e-08)	2.34e-08	(1.90e-08)	1.94e-08	(1.84e-08)
3544.0 GHz	84.60	290.5	6.69e-07	(2.59e-07)	3.24e-07	(2.61e-07)	2.66e-07	(2.50e-07)
3551.0 GHz	84.42	291.2	1.59e-07	(6.20e-08)	7.73e-08	(6.26e-08)	6.38e-08	(6.04e-08)
3786.0 GHz	79.18	181.7	7.87e-07	(3.27e-07)	3.93e-07	(3.40e-07)	3.34e-07	(3.39e-07)
3789.0 GHz	79.12	181.9	8.78e-07	(3.59e-07)	4.36e-07	(3.71e-07)	3.67e-07	(3.67e-07)
4210.0 GHz	71.22	617.9	1.37e-07	(4.97e-08)	6.34e-08	(4.83e-08)	4.89e-08	(4.45e-08)
4212.0 GHz	71.17	617.6	2.64e-08	(9.61e-09)	1.22e-08	(9.35e-09)	9.50e-09	(8.65e-09)
4592.0 GHz	65.28	510.9	2.45e-07	(9.07e-08)	1.15e-07	(8.90e-08)	9.07e-08	(8.31e-08)
4603.0 GHz	65.13	512.1	3.53e-08	(1.31e-08)	1.66e-08	(1.29e-08)	1.31e-08	(1.21e-08)

Transition	λ (μm)	E_{up} (K)	v40b2, M1	(v40b2, M2)	v40b2.5, M1	(v40b2.5, M2)	v40b3, M1	(v40b3, M2)
1834.8 GHz	163.39	269.8	6.25e-06	(2.49e-07)	4.66e-07	(1.67e-07)	2.05e-07	(1.36e-07)
1839.0 GHz	163.01	270.2	9.23e-06	(3.69e-07)	6.95e-07	(2.47e-07)	3.05e-07	(2.01e-07)
2510.0 GHz	119.44	120.5	6.49e-05	(2.67e-06)	4.84e-06	(1.86e-06)	2.15e-06	(1.58e-06)
2514.0 GHz	119.23	120.7	3.68e-05	(1.45e-06)	2.60e-06	(1.02e-06)	1.16e-06	(8.84e-07)
3035.0 GHz	98.76	415.9	1.23e-05	(4.90e-07)	9.37e-07	(3.25e-07)	4.06e-07	(2.60e-07)
3036.0 GHz	98.74	415.5	4.21e-06	(1.57e-07)	3.01e-07	(1.04e-07)	1.30e-07	(8.37e-08)
3111.0 GHz	96.36	269.8	1.52e-06	(6.06e-08)	1.13e-07	(4.07e-08)	4.99e-08	(3.32e-08)
3114.0 GHz	96.27	270.2	2.24e-06	(8.94e-08)	1.68e-07	(5.99e-08)	7.38e-08	(4.87e-08)
3544.0 GHz	84.60	290.5	3.11e-05	(1.24e-06)	2.35e-06	(8.30e-07)	1.03e-06	(6.70e-07)
3551.0 GHz	84.42	291.2	7.93e-06	(2.96e-07)	5.59e-07	(1.98e-07)	2.44e-07	(1.60e-07)
3786.0 GHz	79.18	181.7	3.54e-05	(1.49e-06)	2.74e-06	(1.02e-06)	1.22e-06	(8.42e-07)
3789.0 GHz	79.12	181.9	3.90e-05	(1.66e-06)	3.06e-06	(1.12e-06)	1.36e-06	(9.26e-07)
4210.0 GHz	71.22	617.9	6.52e-06	(2.48e-07)	4.85-07	(1.63e-07)	2.07e-07	(1.29e-07)
4212.0 GHz	71.17	617.6	1.29e-06	(4.79e-08)	9.34e-08	(3.15e-08)	4.00e-08	(2.50e-08)
4592.0 GHz	65.28	510.9	1.18e-05	(4.79e-08)	8.66e-07	(2.96e-07)	3.73e-07	(2.36e-07)
4603.0 GHz	65.13	512.1	1.79e-06	(6.46e-08)	1.25e-07	(4.27e-08)	5.37e-08	(3.40e-08)

Table 9: Intensities of ortho-H_2O lines (erg cm^{-2} s^{-1} sr^{-1}) observable with the PACS (top) and HIFI (bottom) instruments on the Herschel Space Observatory, for shocks with velocity V_s = 20 km s^{-1} and the magnetic field strengths listed in Table 1. Results are given for models M1, which include grain-grain processing, and M2 (in parentheses), which neglect grain-grain processing. The preshock density is $n_H = 10^5$ cm^{-3}.

Transition	λ (μm)	E_{up} (K)	v20b1, M1	(v20b1, M2)	v20b1.5, M1	(v20b1.5, M2)	v20b2, M1	(v20b2, M2)
5500.1 GHz	54.506	732.1	1.31e-06	(2.25e-06)	1.56e-06	(2.12e-06)	1.38e-06	(1.44e-06)
5437.8 GHz	55.131	1274.	5.49e-06	(8.49e-06)	6.44e-06	(7.07e-06)	5.49e-06	(4.75e-06)
5276.5 GHz	56.816	1324	1.97e-05	(3.03e-05)	2.30e-05	(2.43e-05)	1.95e-05	(1.64e-05)
5107.3 GHz	58.699	550.4	1.10e-04	(1.98e-04)	1.29e-04	(1.94e-04)	1.16e-04	(1.33e-04)
4764.0 GHz	62.928	1553	2.74e-07	(4.08e-07)	3.20e-07	(3.36e-07)	2.67e-07	(2.24e-07)
4734.3 GHz	63.323	1071	3.62e-05	(5.86e-05)	4.26e-05	(4.87e-05)	3.72e-05	(3.32e-05)
4600.4 GHz	65.166	795.5	2.57e-05	(4.19e-05)	3.03e-05	(3.89e-05)	2.61e-05	(2.61e-05)
4535.9 GHz	66.092	1013	9.11e-06	(1.44e-05)	1.07e-05	(1.29e-05)	9.17e-06	(8.64e-06)
4512.4 GHz	66.437	410.7	1.54e-04	(2.99e-04)	1.76e-04	(2.47e-04)	1.74e-04	(1.85e-04)
4456.6 GHz	67.268	410.7	7.77e-06	(1.24e-05)	1.08e-05	(2.21e-05)	6.45e-06	(1.24e-05)
4240.2 GHz	70.702	1274	7.40e-07	(1.14e-06)	8.68e-07	(9.53e-07)	7.39e-07	(6.40e-07)
4166.9 GHz	71.946	843.5	6.01e-05	(9.94e-05)	7.09e-05	(8.79e-05)	6.23e-05	(5.96e-05)
4000.2 GHz	74.944	1126	2.34e-06	(3.70e-06)	2.75e-06	(3.13e-06)	2.36e-06	(2.11e-06)
3977.0 GHz	75.380	305.3	2.90e-04	(4.45e-04)	3.37e-04	(4.79e-04)	2.63e-04	(3.07e-04)
3971.0 GHz	75.495	1806	3.32e-07	(4.91e-07)	3.83e-07	(3.59e-07)	3.20e-07	(2.45e-07)
3807.3 GHz	78.742	432.2	1.30e-04	(2.33e-04)	1.53e-04	(2.21e-04)	1.36e-04	(1.53e-04)
3654.6 GHz	82.031	643.5	1.07e-04	(1.81e-04)	1.26e-04	(1.70e-04)	1.11e-04	(1.15e-04)
3536.7 GHz	84.766	1013	1.61e-06	(2.56e-06)	1.90e-06	(2.29e-06)	1.62e-06	(1.53e-06)
3167.6 GHz	94.643	795.5	3.28e-06	(5.34e-06)	3.87e-06	(4.97e-06)	3.34e-06	(3.33e-06)
3165.5 GHz	94.704	702.3	1.26e-06	(2.24e-06)	1.51e-06	(2.23e-06)	1.34e-06	(1.50e-06)
3013.2 GHz	99.492	468.1	1.97e-04	(3.45e-04)	2.33e-04	(3.41e-04)	2.04e-04	(2.31e-04)
2970.8 GHz	100.91	574.7	2.80e-05	(4.71e-05)	3.32e-05	(4.70e-05)	2.84e-05	(3.13e-05)
2774.0 GHz	108.07	194.1	6.17e-04	(1.30e-03)	7.25e-04	(1.52e-03)	6.04e-04	(1.00e-03)
2664.6 GHz	112.51	1340	3.64e-07	(5.72e-07)	4.24e-07	(4.42e-07)	3.66e-07	(3.04e-07)
2640.5 GHz	113.54	323.5	4.32e-04	(7.79e-04)	5.14e-04	(8.34e-04)	4.39e-04	(5.55e-04)
2462.9 GHz	121.72	550.4	5.88e-06	(9.46e-06)	7.77e-06	(1.16e-05)	5.79e-06	(7.11e-06)
2344.3 GHz	127.88	1126	7.24e-07	(1.14e-06)	8.51e-07	(9.68e-07)	7.30e-07	(6.52e-07)
2264.1 GHz	132.41	432.2	2.81e-05	(4.18e-05)	3.53e-05	(6.21e-05)	2.45e-05	(3.65e-05)
2221.8 GHz	134.93	574.7	1.01e-05	(1.70e-05)	1.20e-05	(1.70e-05)	1.03e-05	(1.13e-05)
2196.3 GHz	136.49	410.7	2.79e-05	(4.79e-05)	3.62e-05	(8.13e-05)	2.36e-05	(4.71e-05)
1918.5 GHz	156.26	642.4	6.92e-07	(1.17e-06)	8.33e-07	(1.13e-06)	7.12e-07	(7.49e-07)
1867.7 GHz	160.51	732.1	9.50e-07	(1.63e-06)	1.13e-06	(1.54e-06)	9.99e-07	(1.04e-06)
1716.8 GHz	174.62	196.8	6.14e-04	(1.34e-03)	7.21e-04	(1.31e-03)	6.77e-04	(9.16e-04)
1669.9 GHz	179.53	114.4	9.57e-04	(2.22e-03)	1.09e-03	(2.06e-03)	1.05e-03	(1.49e-03)
1661.0 GHz	180.49	194.1	1.93e-04	(4.63e-04)	2.30e-04	(5.06e-04)	2.03e-04	(3.41e-04)
1162.9 GHz	257.79	305.3	5.65e-05	(1.39e-04)	7.12e-05	(1.64e-04)	6.68e-05	(1.11e-04)
1153.1 GHz	259.98	249.4	1.22e-04	(2.54e-04)	1.49e-04	(3.43e-04)	1.12e-04	(2.17e-04)
1097.4 GHz	273.19	249.4	8.72e-05	(1.96e-04)	1.04e-04	(1.71e-04)	1.07e-04	(1.25e-04)
556.94 GHz	538.28	61.0	5.61e-05	(1.32e-04)	6.01e-05	(1.21e-04)	5.73e-05	(8.89e-05)

Table 10: Intensities of ortho-H_2O lines (erg cm^{-2} s^{-1} sr^{-1}) observable with the PACS (top) and HIFI (bottom) instruments on the Herschel Space Observatory, for shocks with velocity V_s = 30 km s^{-1} and the magnetic field strengths listed in Table 1. Results are given for models M1, which include grain-grain processing, and M2 (in parentheses), which neglect grain-grain processing. The preshock density is $n_H = 10^5$ cm^{-3}.

Transition	λ (μm)	E_{up} (K)	v30b1.5, M1	(v30b1.5, M2)	v30b2, M1	(v30b2, M2)	v30b2.5, M1	(v30b2.5, M2)
5500.1 GHz	54.506	732.1	2.16e-06	(5.36e-06)	2.80e-06	(6.34e-06)	3.60e-06	(6.74e-06)
5437.8 GHz	55.131	1274	8.87e-06	(2.26e-05)	1.21e-05	(2.60e-05)	1.60e-05	(2.68e-05)
5276.5 GHz	56.816	1324	3.13e-05	(8.00e-05)	4.30e-05	(8.99e-05)	5.69e-05	(9.14e-05)
5107.3 GHz	58.699	550.4	1.75e-04	(4.39e-04)	2.13e-04	(4.97e-04)	2.72e-04	(5.15e-04)
4764.0 GHz	62.928	1553	4.44e-07	(1.13e-06)	6.15e-07	(1.32e-06)	8.16e-07	(1.36e-06)
4734.3 GHz	63.323	1071	5.78e-05	(1.47e-04)	7.78e-05	(1.66e-04)	1.02e-04	(1.70e-04)
4600.4 GHz	65.166	795.5	4.28e-05	(1.05e-04)	5.60e-05	(1.25e-04)	7.23e-05	(1.33e-04)
4535.9 GHz	66.092	1013	1.50e-05	(3.76e-05)	2.00e-05	(4.43e-05)	2.62e-05	(4.65e-05)
4512.4 GHz	66.437	410.7	2.35e-04	(5.69e-04)	2.82e-04	(5.97e-04)	3.60e-04	(5.97e-04)
4456.6 GHz	67.268	410.7	1.89e-05	(3.95e-05)	2.66e-05	(6.85e-05)	3.09e-05	(8.70e-05)
4240.2 GHz	70.702	1274	1.20e-06	(3.04e-06)	1.64e-06	(3.51e-06)	2.16e-06	(3.62e-06)
4166.9 GHz	71.946	843.5	9.74e-05	(2.45e-04)	1.29e-04	(2.83e-04)	1.68e-04	(2.95e-04)
4000.2 GHz	74.944	1126	3.76e-06	(9.59e-06)	5.09e-06	(1.10e-05)	6.71e-06	(1.13e-05)
3977.0 GHz	75.380	305.3	5.48e-04	(1.11e-03)	6.56e-04	(1.35e-03)	7.45e-04	(1.49e-03)
3971.0 GHz	75.495	1806	5.24e-07	(1.32e-06)	7.29e-07	(1.42e-06)	9.63e-07	(1.41e-06)
3807.3 GHz	78.742	432.2	2.22e-04	(5.14e-04)	2.80e-04	(6.19e-04)	3.49e-04	(6.68e-04)
3654.6 GHz	82.031	643.5	1.76e-04	(4.35e-04)	2.27e-04	(5.11e-04)	2.92e-04	(5.41e-04)
3536.7 GHz	84.766	1013	2.65e-06	(6.66e-06)	3.55e-06	(7.86e-06)	4.64e-06	(8.23e-06)
3167.6 GHz	94.643	795.5	5.47e-06	(1.35e-05)	7.15e-06	(1.60e-05)	9.23e-06	(1.69e-05)
3165.5 GHz	94.704	702.3	2.11e-06	(5.21e-06)	2.69e-06	(6.29e-06)	3.43e-06	(6.79e-06)
3013.2 GHz	99.492	468.1	3.31e-04	(7.96e-04)	4.16e-04	(9.46e-04)	5.23e-04	(1.01e-03)
2970.8 GHz	100.91	574.7	4.87e-05	(1.14e-04)	6.22e-05	(1.40e-04)	7.79e-05	(1.52e-04)
2774.0 GHz	108.07	194.1	1.01e-03	(2.62e-03)	1.15e-03	(3.14e-03)	1.39e-03	(3.42e-03)
2664.6 GHz	112.51	1340	5.73e-07	(1.46e-06)	7.81e-07	(1.58e-06)	1.03e-06	(1.58e-06)
2640.5 GHz	113.54	323.5	7.37e-04	(1.76e-03)	8.96e-04	(2.12e-03)	1.11e-03	(2.29e-03)
2462.9 GHz	121.72	550.4	1.30e-05	(2.68e-05)	1.89e-05	(4.43e-05)	2.29e-05	(5.58e-05)
2344.3 GHz	127.88	1126	1.16e-06	(2.96e-06)	1.57e-06	(3.39e-06)	2.07e-06	(3.49e-06)
2264.1 GHz	132.41	432.2	5.71e-05	(1.27e-04)	7.08e-05	(1.80e-04)	8.42e-05	(2.07e-04)
2221.8 GHz	134.93	574.7	1.76e-05	(4.13e-05)	2.24e-05	(5.05e-05)	2.81e-05	(5.47e-05)
2196.3 GHz	136.49	410.7	5.57e-05	(1.36e-04)	6.77e-05	(1.98e-04)	7.99e-05	(2.33e-04)
1918.5 GHz	156.26	642.4	1.23e-06	(2.87e-06)	1.66e-06	(3.67e-06)	2.08e-06	(4.13e-06)
1867.7 GHz	160.51	732.1	1.57e-06	(3.89e-06)	2.03e-06	(4.60e-06)	2.62e-06	(4.90e-06)
1716.8 GHz	174.62	196.8	9.24e-04	(2.48e-03)	1.09e-03	(2.70e-03)	1.37e-03	(2.79e-03)
1669.9 GHz	179.53	114.4	1.38e-03	(3.73e-03)	1.58e-03	(3.81e-03)	1.96e-03	(3.89e-03)
1661.0 GHz	180.49	194.1	2.93e-04	(8.45e-04)	3.41e-04	(9.58e-04)	4.19e-04	(1.03e-03)
1162.9 GHz	257.79	305.3	8.11e-05	(2.61e-04)	9.72e-05	(3.20e-04)	1.35e-04	(3.48e-04)
1153.1 GHz	259.98	249.4	2.09e-04	(5.63e-04)	2.44e-04	(7.36e-04)	2.97e-04	(8.35e-04)
1097.4 GHz	273.19	249.4	1.27e-04	(3.43e-04)	1.52e-04	(3.55e-04)	2.00e-04	(3.50e-04)
556.94 GHz	538.28	61.0	7.98e-05	(2.06e-04)	8.45e-05	(2.00e-04)	9.89e-05	(2.04e-04)

Table 11: Intensities of ortho-H_2O lines (erg cm^{-2} s^{-1} sr^{-1}) observable with the PACS (top) and HIFI (bottom) instruments on the Herschel Space Observatory, for shocks with velocity V_s = 40 km s^{-1} and the magnetic field strengths listed in Table 1. Results are given for models M1, which include grain-grain processing, and M2 (in parentheses), which neglect grain-grain processing. The preshock density is $n_H = 10^5$ cm^{-3}.

Transition	λ (μm)	E_{up} (K)	v40b2, M1	(v40b2, M2)	v40b2.5, M1	(v40b2.5, M2)	v40b3, M1	(v40b3, M2)
5500.1 GHz	54.506	732.1	5.58e-06	(9.15e-06)	3.78e-06	(1.08e-05)	4.89e-06	(1.19e-05)
5437.8 GHz	55.131	1274	1.47e-05	(3.87e-05)	1.53e-05	(4.56e-05)	2.14e-05	(4.94e-05)
5276.5 GHz	56.816	1324	4.82e-05	(1.35e-04)	5.37e-05	(1.56e-04)	7.51e-05	(1.67e-04)
5107.3 GHz	58.699	550.4	3.39e-04	(7.11e-04)	2.75e-04	(7.70e-04)	3.44e-04	(8.04e-04)
4764.0 GHz	62.928	1553	7.07e-07	(1.96e-06)	7.73e-07	(2.35e-06)	1.09e-06	(2.55e-06)
4734.3 GHz	63.323	1071	9.55e-05	(2.46e-04)	9.84e-05	(2.83e-04)	1.35e-04	(3.03e-04)
4600.4 GHz	65.166	795.5	9.22e-05	(1.83e-04)	7.40e-05	(2.17e-04)	9.76e-05	(2.37e-04)
4535.9 GHz	66.092	1013	2.84e-05	(6.51e-05)	2.59e-05	(7.73e-05)	3.51e-05	(8.41e-05)
4512.4 GHz	66.437	410.7	5.35e-04	(8.84e-04)	3.80e-04	(9.42e-04)	4.63e-04	(9.85e-04)
4456.6 GHz	67.268	410.7	1.27e-04	(8.96e-05)	4.90e-05	(1.41e-04)	5.51e-05	(1.74e-04)
4240.2 GHz	70.702	1274	1.98e-06	(5.21e-06)	2.07e-06	(6.15e-06)	2.88e-06	(6.65e-06)
4166.9 GHz	71.946	843.5	1.83e-04	(4.15e-04)	1.66e-04	(4.81e-04)	2.22e-04	(5.19e-04)
4000.2 GHz	74.944	1126	6.26e-06	(1.62e-05)	6.44e-06	(1.89e-05)	8.87e-06	(2.03e-05)
3977.0 GHz	75.380	305.3	1.64e-03	(2.05e-03)	9.85e-04	(2.40e-03)	1.10e-03	(2.62e-03)
3971.0 GHz	75.495	1806	7.12e-07	(2.20e-06)	8.98e-07	(2.48e-06)	1.27e-06	(2.62e-06)
3807.3 GHz	78.742	432.2	6.95e-04	(8.97e-04)	4.06e-04	(1.09e-03)	4.95e-04	(1.21e-03)
3654.6 GHz	82.031	643.5	3.82e-04	(7.41e-04)	3.01e-04	(8.65e-04)	3.90e-04	(9.37e-04)
3536.7 GHz	84.766	1013	5.03e-06	(1.15e-05)	4.58e-06	(1.37e-05)	6.22e-06	(1.49e-05)
3167.6 GHz	94.643	795.5	1.18e-05	(2.34e-05)	9.46e-06	(2.78e-05)	1.25e-05	(3.02e-05)
3165.5 GHz	94.704	702.3	5.90e-06	(8.94e-06)	3.70e-06	(1.07e-05)	4.67e-06	(1.18e-05)
3013.2 GHz	99.492	468.1	8.28e-04	(1.36e-03)	5.70e-04	(1.59e-03)	7.08e-04	(1.73e-03)
2970.8 GHz	100.91	574.7	1.47e-04	(2.03e-04)	8.82e-05	(2.48e-04)	1.10e-04	(2.76e-04)
2774.0 GHz	108.07	194.1	2.17e-03	(4.21e-03)	1.56e-03	(4.71e-03)	1.79e-03	(5.06e-03)
2664.6 GHz	112.51	1340	8.39e-07	(2.40e-06)	9.72e-07	(2.69e-06)	1.35e-06	(2.85e-06)
2640.5 GHz	113.54	323.5	1.78e-03	(3.00e-03)	1.24e-03	(3.45e-03)	1.48e-03	(3.73e-03)
2462.9 GHz	121.72	550.4	7.19e-05	(6.04e-05)	3.27e-05	(9.70e-05)	3.95e-05	(1.21e-04)
2344.3 GHz	127.88	1126	1.94e-06	(5.02e-06)	1.99e-06	(5.84e-06)	2.74e-06	(6.28e-06)
2264.1 GHz	132.41	432.2	1.94e-04	(2.46e-04)	1.06e-04	(3.13e-04)	1.23e-04	(3.53e-04)
2221.8 GHz	134.93	574.7	5.05e-05	(7.31e-05)	3.16e-05	(8.86e-05)	3.94e-05	(9.80e-05)
2196.3 GHz	136.49	410.7	1.60e-04	(2.56e-04)	9.58e-05	(3.20e-04)	1.10e-04	(3.57e-04)
1918.5 GHz	156.26	642.4	5.16e-06	(5.30e-06)	2.55e-06	(7.21e-06)	3.22e-06	(8.64e-06)
1867.7 GHz	160.51	732.1	4.07e-06	(6.64e-06)	2.75e-06	(7.87e-06)	3.55e-06	(8.66e-06)
1716.8 GHz	174.62	196.8	1.62e-03	(3.74e-03)	1.39e-03	(3.94e-03)	1.69e-03	(4.10e-03)
1669.9 GHz	179.53	114.4	2.15e-03	(5.35e-03)	1.98e-03	(5.35e-03)	2.38e-03	(5.47e-03)
1661.0 GHz	180.49	194.1	5.39e-04	(1.28e-03)	4.43e-04	(1.37e-03)	5.20e-04	(1.45e-03)
1162.9 GHz	257.79	305.3	1.37e-04	(3.89e-04)	1.20e-04	(4.39e-04)	1.52e-04	(4.74e-04)
1153.1 GHz	259.98	249.4	5.07e-04	(9.47e-04)	3.38e-04	(1.12e-03)	3.89e-04	(1.24e-03)
1097.4 GHz	273.19	249.4	2.20e-04	(5.04e-04)	1.97e-04	(5.22e-04)	2.42e-04	(5.29e-04)
556.94 GHz	538.28	61.0	1.14e-04	(2.84e-04)	1.06e-04	(2.71e-04)	1.20e-04	(2.74e-04)

Table 12: Intensities of para-H_2O lines (erg cm^{-2} s^{-1} sr^{-1}) observable with the PACS (top) and HIFI (bottom) instruments on the Herschel Space Observatory, for shocks with velocity V_s = 20 km s^{-1} and the magnetic field strengths listed in Table 1. Results are given for models M1, which include grain-grain processing, and M2 (in parentheses), which neglect grain-grain processing. The preshock density is $n_H = 10^5$ cm^{-3}.

Transition	λ (μm)	E_{up} (K)	v20b1, M1	(v20b1, M2)	v20b1.5, M1	(v20b1.5, M2)	v20b2, M1	(v20b2, M2)
5322.5 GHz	56.325	552.3	2.46e-05	(4.10e-05)	2.91e-05	(4.81e-05)	2.37e-05	(3.10e-05)
5280.7 GHz	56.771	1324	4.69e-06	(7.15e-06)	5.49e-06	(5.91e-06)	4.63e-06	(3.96e-06)
5201.4 GHz	57.636	454.3	6.05e-05	(1.10e-04)	7.08e-05	(1.04e-04)	6.41e-05	(7.16e-05)
5194.9 GHz	57.709	1270	9.33e-07	(1.41e-06)	1.09e-06	(1.25e-06)	9.06e-07	(8.23e-07)
4997.6 GHz	59.987	1021	1.76e-06	(2.71e-06)	2.06e-06	(2.59e-06)	1.71e-06	(1.69e-06)
4850.3 GHz	61.808	552.3	3.85e-07	(6.35e-07)	4.60e-07	(7.56e-07)	3.68e-07	(4.84e-07)
4724.0 GHz	63.457	1070	8.78e-06	(1.40e-05)	1.03e-05	(1.18e-05)	8.87e-06	(8.00e-06)
4468.6 GHz	67.089	410.4	6.05e-05	(1.16e-04)	7.04e-05	(1.13e-04)	6.54e-05	(7.90e-05)
4218.4 GHz	71.067	598.8	1.54e-05	(2.56e-05)	1.82e-05	(2.67e-05)	1.54e-05	(1.76e-05)
4190.6 GHz	71.539	843.8	1.76e-05	(2.95e-05)	2.08e-05	(2.53e-05)	1.85e-05	(1.73e-05)
3798.3 GHz	78.928	781.1	3.35e-06	(5.31e-06)	3.95e-06	(5.66e-06)	3.27e-06	(3.66e-06)
3691.3 GHz	81.215	1021	2.36e-07	(3.63e-07)	2.77e-07	(3.48e-07)	2.29e-07	(2.27e-07)
3599.6 GHz	83.283	642.7	3.16e-05	(5.37e-05)	3.74e-05	(5.04e-05)	3.29e-05	(3.40e-05)
3331.5 GHz	89.988	296.8	5.73e-05	(9.59e-05)	6.85e-05	(1.03e-04)	5.74e-05	(6.87e-05)
3182.2 GHz	94.209	877.8	2.05e-07	(3.32e-07)	2.44e-07	(3.57e-07)	2.05e-07	(2.32e-07)
3135.0 GHz	95.626	469.9	5.68e-05	(9.94e-05)	6.73e-05	(1.01e-04)	5.86e-05	(6.75e-05)
2968.7 GHz	100.98	195.9	1.86e-04	(3.60e-04)	2.14e-04	(4.13e-04)	1.68e-04	(2.66e-04)
2884.3 GHz	103.94	781.1	7.63e-07	(1.21e-06)	9.01e-07	(1.29e-06)	7.45e-07	(8.34e-07)
2685.6 GHz	111.63	598.8	1.77e-06	(2.94e-06)	2.09e-06	(3.08e-06)	1.77e-06	(2.02e-06)
2631.0 GHz	113.95	725.1	1.35e-06	(2.40e-06)	1.60e-06	(1.98e-06)	1.47e-06	(1.40e-06)
2391.6 GHz	125.35	319.5	1.12e-04	(2.04e-04)	1.33e-04	(2.18e-04)	1.14e-04	(1.46e-04)
2365.9 GHz	126.71	410.4	3.25e-06	(5.59e-06)	4.66e-06	(8.41e-06)	3.33e-06	(4.95e-06)
2164.1 GHz	138.53	204.7	2.83e-04	(5.69e-04)	3.36e-04	(6.40e-04)	2.82e-04	(4.21e-04)
2074.4 GHz	144.52	396.4	1.10e-05	(1.84e-05)	1.31e-05	(2.17e-05)	1.04e-05	(1.39e-05)
2040.5 GHz	146.92	552.3	5.41e-07	(8.92e-07)	6.47e-07	(1.06e-06)	5.18e-07	(6.80e-07)
1919.4 GHz	156.19	296.8	2.97e-05	(5.47e-05)	3.59e-05	(7.92e-05)	2.50e-05	(4.86e-05)
1794.8 GHz	167.03	867.3	1.81e-07	(3.03e-07)	2.16e-07	(3.08e-07)	1.87e-07	(2.04e-07)
1602.2 GHz	187.11	396.4	9.43e-06	(1.59e-05)	1.12e-05	(1.86e-05)	8.99e-06	(1.20e-05)
1228.8 GHz	243.97	195.9	3.48e-05	(9.50e-05)	4.45e-05	(9.36e-05)	4.62e-05	(6.63e-05)
1113.3 GHz	269.27	53.4	2.64e-04	(6.40e-04)	2.97e-04	(5.82e-04)	2.89e-04	(4.25e-04)
987.93 GHz	303.45	100.8	2.10e-04	(5.15e-04)	2.42e-04	(4.97e-04)	2.33e-04	(3.55e-04)
752.03 GHz	398.64	136.9	6.59e-05	(1.75e-04)	7.72e-05	(1.71e-04)	7.54e-05	(1.21e-04)

Table 13: Intensities of para-H_2O lines (erg cm^{-2} s^{-1} sr^{-1}) observable with the PACS (top) and HIFI (bottom) instruments on the Herschel Space Observatory, for shocks with velocity V_s = 30 km s^{-1} and the magnetic field strengths listed in Table 1. Results are given for models M1, which include grain-grain processing, and M2 (in parentheses), which neglect grain-grain processing. The preshock density is $n_H = 10^5$ cm^{-3}.

Transition	λ (μm)	E_{up} (K)	v30b1.5, M1	(v30b1.5, M2)	v30b2, M1	(v30b2, M2)	v30b2.5, M1	(v30b2.5, M2)
5322.5 GHz	56.325	552.30	4.33e-05	(1.03e-04)	5.31e-05	(1.34e-04)	6.64e-05	(1.48e-04)
5280.7 GHz	56.771	1324.0	7.51e-06	(1.93e-05)	1.03e-05	(2.21e-05)	1.38e-05	(2.26e-05)
5201.4 GHz	57.636	454.30	9.73e-05	(2.39e-04)	1.19e-04	(2.65e-04)	1.50e-04	(2.74e-04)
5194.9 GHz	57.709	1270.3	1.54e-06	(3.88e-06)	2.08e-06	(4.62e-06)	2.74e-06	(4.84e-06)
4997.6 GHz	59.987	1021.0	2.97e-06	(7.39e-06)	3.94e-06	(9.09e-06)	5.15e-06	(9.70e-06)
4850.3 GHz	61.808	552.30	7.05e-07	(1.62e-06)	8.95e-07	(2.20e-06)	1.11e-06	(2.51e-06)
4724.0 GHz	63.457	1070.0	1.41e-05	(3.60e-05)	1.90e-05	(4.10e-05)	2.51e-05	(4.21e-05)
4468.6 GHz	67.089	410.40	9.46e-05	(2.37e-04)	1.12e-04	(2.61e-04)	1.42e-04	(2.70e-04)
4218.4 GHz	71.067	598.80	2.62e-05	(6.37e-05)	3.32e-05	(7.92e-05)	4.23e-05	(8.59e-05)
4190.6 GHz	71.539	843.80	2.82e-05	(7.16e-05)	3.73e-05	(8.08e-05)	4.87e-05	(8.35e-05)
3798.3 GHz	78.928	781.10	5.73e-06	(1.41e-05)	7.39e-06	(1.81e-05)	9.56e-06	(1.97e-05)
3691.3 GHz	81.215	1021.0	3.98e-07	(9.91e-07)	5.29e-07	(1.22e-06)	6.91e-07	(1.30e-06)
3599.6 GHz	83.283	642.70	5.17e-05	(1.29e-04)	6.68e-05	(1.51e-04)	8.63e-05	(1.60e-04)
3331.5 GHz	89.988	296.80	1.09e-04	(2.28e-04)	1.33e-04	(2.99e-04)	1.60e-04	(3.30e-04)
3182.2 GHz	94.209	877.80	3.47e-07	(8.74e-07)	4.48e-07	(1.12e-06)	5.89e-07	(1.22e-06)
3135.0 GHz	95.626	469.90	9.47e-05	(2.32e-04)	1.19e-04	(2.78e-04)	1.51e-04	(2.99e-04)
2968.7 GHz	100.98	195.90	3.21e-04	(7.66e-04)	3.69e-04	(8.96e-04)	4.19e-04	(9.80e-04)
2884.3 GHz	103.94	781.10	1.31e-06	(3.23e-06)	1.69e-06	(4.12e-06)	2.18e-06	(4.49e-06)
2685.6 GHz	111.63	598.80	3.02e-06	(7.33e-06)	3.83e-06	(9.14e-06)	4.87e-06	(9.91e-06)
2631.0 GHz	113.95	725.10	2.11e-06	(5.34e-06)	2.74e-06	(5.74e-06)	3.55e-06	(5.85e-06)
2391.6 GHz	125.35	319.50	1.92e-04	(4.57e-04)	2.34e-04	(5.55e-04)	2.89e-04	(6.03e-04)
2365.9 GHz	126.71	410.40	7.21e-06	(1.60e-05)	1.03e-05	(2.66e-05)	1.25e-05	(3.32e-05)
2164.1 GHz	138.53	204.70	4.71e-04	(1.19e-03)	5.54e-04	(1.42e-03)	6.74e-04	(1.54e-03)
2074.4 GHz	144.52	396.40	2.05e-05	(4.55e-05)	2.57e-05	(6.10e-05)	3.10e-05	(6.94e-05)
2040.5 GHz	146.92	552.30	9.90e-07	(2.28e-06)	1.26e-06	(3.10e-06)	1.56e-06	(3.54e-06)
1919.4 GHz	156.19	296.80	5.46e-05	(1.33e-04)	6.41e-05	(1.80e-04)	7.51e-05	(2.08e-04)
1794.8 GHz	167.03	867.30	3.01e-07	(7.63e-07)	3.89e-07	(9.46e-07)	5.08e-07	(1.02e-06)
1602.2 GHz	187.11	396.40	1.72e-05	(3.89e-05)	2.11e-05	(5.08e-05)	2.56e-05	(5.67e-05)
1228.8 GHz	243.97	195.90	4.90e-05	(1.61e-04)	5.99e-05	(1.80e-04)	8.46e-05	(1.84e-04)
1113.3 GHz	269.27	53.400	3.72e-04	(1.03e-03)	4.20e-04	(1.01e-03)	5.13e-04	(1.02e-03)
987.93 GHz	303.45	100.80	2.97e-04	(8.56e-04)	3.40e-04	(8.95e-04)	4.31e-04	(9.18e-04)
752.03 GHz	398.64	136.90	9.10e-05	(2.81e-04)	1.03e-04	(2.98e-04)	1.35e-04	(3.04e-04)

Table 14: Intensities of para-H_2O lines (erg cm^{-2} s^{-1} sr^{-1}) observable with the PACS (top) and HIFI (bottom) instruments on the Herschel Space Observatory, for shocks with velocity V_s = 40 km s^{-1} and the magnetic field strengths listed in Table 1. Results are given for models M1, which include grain-grain processing, and M2 (in parentheses), which neglect grain-grain processing. The preshock density is $n_H = 10^5$ cm^{-3}.

Transition	λ (μm)	E_{up} (K)	v40b2, M1	(v40b2, M2)	v40b2.5, M1	(v40b2.5, M2)	v40b3, M1	(v40b3, M2)
5322.5 GHz	56.325	552.30	1.19e-04	(1.86e-04)	7.42e-05	(2.27e-04)	9.05e-05	(2.50e-04)
5280.7 GHz	56.771	1324.0	1.25e-05	(3.28e-05)	1.30e-05	(3.84e-05)	1.82e-05	(4.14e-05)
5201.4 GHz	57.636	454.30	1.94e-04	(3.86e-04)	1.55e-04	(4.16e-04)	1.93e-04	(4.33e-04)
5194.9 GHz	57.709	1270.3	2.91e-06	(6.81e-06)	2.67e-06	(8.18e-06)	3.68e-06	(8.93e-06)
4997.6 GHz	59.987	1021.0	6.42e-06	(1.32e-05)	5.17e-06	(1.61e-05)	6.97e-06	(1.77e-05)
4850.3 GHz	61.808	552.30	3.27e-06	(3.06e-06)	1.40e-06	(4.07e-06)	1.68e-06	(4.80e-06)
4724.0 GHz	63.457	1070.0	2.47e-05	(6.05e-05)	2.40e-05	(7.00e-05)	3.29e-05	(7.51e-05)
4468.6 GHz	67.089	410.40	1.96e-04	(3.74e-04)	1.46e-04	(3.99e-04)	1.79e-04	(4.15e-04)
4218.4 GHz	71.067	598.80	6.55e-05	(1.12e-04)	4.51e-05	(1.35e-04)	5.73e-05	(1.49e-04)
4190.6 GHz	71.539	843.80	5.10e-05	(1.19e-04)	4.78e-05	(1.36e-04)	6.40e-05	(1.46e-04)
3798.3 GHz	78.928	781.10	1.37e-05	(2.56e-05)	9.94e-06	(3.15e-05)	1.30e-05	(3.48e-05)
3691.3 GHz	81.215	1021.0	8.61e-07	(1.77e-06)	6.94e-07	(2.16e-06)	9.36e-07	(2.38e-06)
3599.6 GHz	83.283	642.70	1.07e-04	(2.19e-04)	8.77e-05	(2.54e-04)	1.14e-04	(2.75e-04)
3331.5 GHz	89.988	296.80	4.09e-04	(4.30e-04)	2.10e-04	(5.44e-04)	2.38e-04	(6.11e-04)
3182.2 GHz	94.209	877.80	8.47e-07	(1.57e-06)	5.99e-07	(1.93e-06)	7.86e-07	(2.14e-06)
3135.0 GHz	95.626	469.90	2.28e-04	(3.96e-04)	1.61e-04	(4.63e-04)	2.02e-04	(5.04e-04)
2968.7 GHz	100.98	195.90	7.60e-04	(1.28e-03)	5.30e-04	(1.41e-03)	5.83e-04	(1.52e-03)
2884.3 GHz	103.94	781.10	3.14e-06	(5.83e-06)	2.27e-06	(7.18e-06)	2.96e-06	(7.95e-06)
2685.6 GHz	111.63	598.80	7.73e-06	(1.30e-05)	5.23e-06	(1.57e-05)	6.63e-06	(1.72e-05)
2631.0 GHz	113.95	725.10	3.67e-06	(8.53e-06)	3.51e-06	(9.32e-06)	4.60e-06	(9.83e-06)
2391.6 GHz	125.35	319.50	5.05e-04	(7.82e-04)	3.29e-04	(9.15e-04)	3.92e-04	(9.97e-04)
2365.9 GHz	126.71	410.40	3.46e-05	(3.41e-05)	1.72e-05	(5.11e-05)	2.00e-05	(6.20e-05)
2164.1 GHz	138.53	204.70	1.05e-03	(1.96e-03)	7.60e-04	(2.20e-03)	8.84e-04	(2.36e-03)
2074.4 GHz	144.52	396.40	8.42e-05	(8.54e-05)	4.01e-05	(1.11e-04)	4.69e-05	(1.29e-04)
2040.5 GHz	146.92	552.30	4.64e-06	(4.30e-06)	1.96e-06	(5.72e-06)	2.37e-06	(6.76e-06)
1919.4 GHz	156.19	296.80	1.61e-04	(2.38e-04)	9.42e-05	(2.91e-04)	1.05e-04	(3.26e-04)
1794.8 GHz	167.03	867.30	6.52e-07	(1.33e-06)	5.12e-07	(1.60e-06)	6.72e-07	(1.75e-06)
1602.2 GHz	187.11	396.40	5.10e-05	(7.11e-05)	3.06e-05	(8.73e-05)	3.60e-05	(9.67e-05)
1228.8 GHz	243.97	195.90	8.03e-05	(2.34e-04)	7.51e-05	(2.53e-04)	9.65e-05	(2.63e-04)
1113.3 GHz	269.27	53.400	5.30e-04	(1.43e-03)	5.21e-04	(1.39e-03)	6.21e-04	(1.40e-03)
987.93 GHz	303.45	100.80	4.52e-04	(1.22e-03)	4.20e-04	(1.24e-03)	5.10e-04	(1.27e-03)
752.03 GHz	398.64	136.90	1.37e-04	(3.95e-04)	1.26e-04	(4.05e-04)	1.54e-04	(4.15e-04)

6

ADDITIONAL MATERIAL

In this chapter, we present some additional material that also resulted from the calculations presented in the previous chapter but has not been published before. More precisely, we add information on the optical thickness of molecular line emission in Sect. 6.1, describe the emission of NH_3 in Sect. 6.2, and supplement the previous chapter with tables on the emission of ortho- and para-NH_3 and SiO in Sect. 6.3.

6.1 OPTICAL THICKNESS EFFECTS

For a full understanding of molecular line emission, it is important to have information on the optical thickness of the lines. One simple way to investigate the optical thickness is to evaluate the column densities $N_{\rm up}$ of the molecules in excited states, on the one hand as obtained by the corresponding particle densities $n_{\rm up}$ integrated through the shock, given by

$$N_{\rm up,dens}\,(\mathrm{cm}^{-2}) = \int n_{\rm up}\left(\mathrm{cm}^{-3}\right) dz\,, \tag{84}$$

and on the other hand based on the resulting line intensities I as

$$N_{\rm up,int}\,(\mathrm{cm}^{-2}) = 1.894\times10^{18}\,\frac{I\,(\mathrm{erg\,cm^{-2}\,s^{-1}\,sr^{-1}})}{A_{ij}\cdot\nu\,(\mathrm{GHz})}\,, \tag{85}$$

with A_{ij} being the transition probability and ν the transition frequency. Equation (85) directly follows from the assumption of optically thin radiation, where the intensity is given as $I = \frac{h\nu}{4\pi}A_{ij}N_{\rm up}$. The column densities divided by the molecular weight for the upper energy levels of the transitions listed in Tables 5–14, calculated with these equations, are shown in Fig. 19. The column densities are shown for a shock with $V_{\rm s} = 30$ km s^{-1} and $b = 1.5$ computed with model M1 (including grain-grain processing). The level $J_{\rm up} = 20$ for CO corresponds to an upper level energy of 1160 K.

While for the water emission lines an effect of the optical thickness is seen for energy levels up to ~500 K, only the lowest transitions of OH ($E_{\rm up} \sim 121$ K) show a clear difference between the column densities as based on the densities and as based on the line emission. For CO, only the lowest six transitions suffer from optical thickness effects. Fig 20 shows the excitation diagram of SiO (left panel) and the values of the optical depths through the shock (right panel), calculated with the same shock model as used in Fig. 19. As can be seen in the right panel, the lowest transitions become optically thick in the cold postshock gas where maximum compression is reached. The transitions up to J = 7–6 become optically thick and attain values of the optical depth of $1 \le \tau \le 6$.

The optical depth of the lowest transitions is enhanced in the models without grain-grain processing (not shown here) for CO and SiO. It practically remains the same for the water and OH transitions.

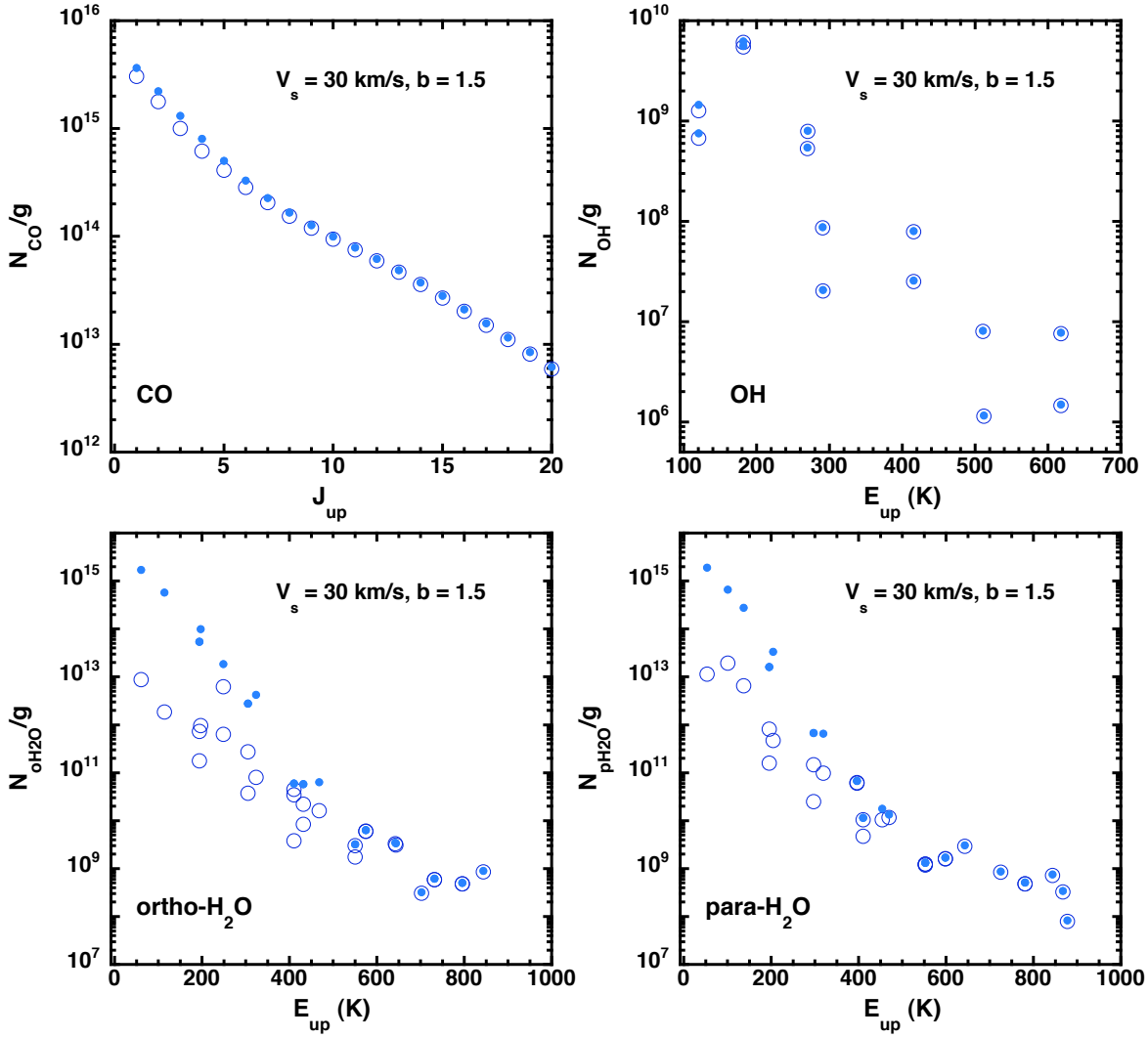

Figure 19: Excitation diagrams of the lowest rotational levels of the molecules discussed in Sect. 5.8.2: CO (top, left), OH (top, right), ortho-H_2O (bottom, right), and para-H_2O (bottom, right). Displayed are the column densities divided by the molecular weight for upper energy levels of the transitions listed in Tables 5–14, computed with model M1 (including grain-grain processing) for a shock with $V_s = 30$ km s^{-1} and $b = 1.5$. Full circles show column densities calculated with Eq. (84), while open circles show column densities calculated with Eq. (85).

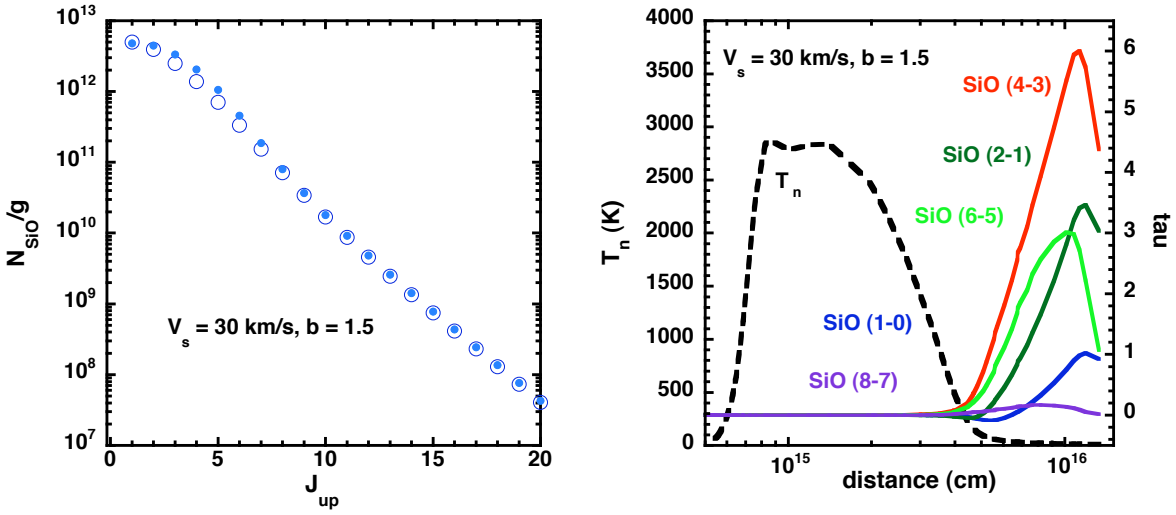

Figure 20: Left: Excitation diagram of the lowest 20 rotational levels of SiO. Displayed are the column densities divided by the molecular weight for upper energy levels computed with model M1 (including grain-grain processing) for a shock with $V_s = 30$ km s^{-1} and $b = 1.5$. Full circles show column densities calculated with Eq. (84), while open circles show column densities calculated with Eq. (85). Right: Temperature profile (black, left ordinate) and optical depths (right ordinate) of SiO (1–0) (blue), (2–1) (dark green), (4–3) (red), (6–5) (light green), and (8–7) (violett) across the shock wave.

6.2 NH3

Ammonia is one of the first molecules detected in space (Cheung et al. 1968). Since its discovery in 1968, it has proven to be a very useful tool in the study of higher-density molecular clouds because it has a high critical density. Due to its complex set of transitions, it is very sensitive to the cloud conditions, and the relative intensities of its emission lines can serve as a reliable thermometer (Ho & Townes 1983). The molecule consists of a nitrogen atom on top of an equilateral triangle out of hydrogen atoms. Therefore, it is a three-dimensional rotator that can be described as a symmetric top molecule, where two of its principal axes have identical moments of inertia.

Ammonia exists in two distinct species: ortho- and para-NH_3, where the first species has an angular momentum component along the symmetry axis attaining values of $K = 3n$, while for the latter these values obey $K \neq 3n$. These two species arise from different relative orientations of the three hydrogen spins. In statistical equilibrium, the ortho-to-para ratio is expected to have a value of 1.0. This value is attained when the NH_3 molecule is formed in gas-phase or grain surface reactions because its formation releases large excess energies compared to the energy difference between the lowest para and ortho states. The ortho-to-para ratio might be changed if NH_3 molecules are adsorbed and subsequently desorbed from grain surfaces because the excess energy in that case is comparable to the energy difference between the lowest ortho and para levels. Ammonia transitions higher than (J,K) = (3,3) are hardly excited in dark clouds and therefore serve as tracers of gas heated by shocks. Its abundance seems to be enhanced in shock heated gas. As ammonia is one of the main constituents of grain mantles in dense clouds, this enhancement points to a release of NH_3 into the gas-phase due to dust destruction during the passage of a shock (e.g. Tafalla & Bachiller 1995).

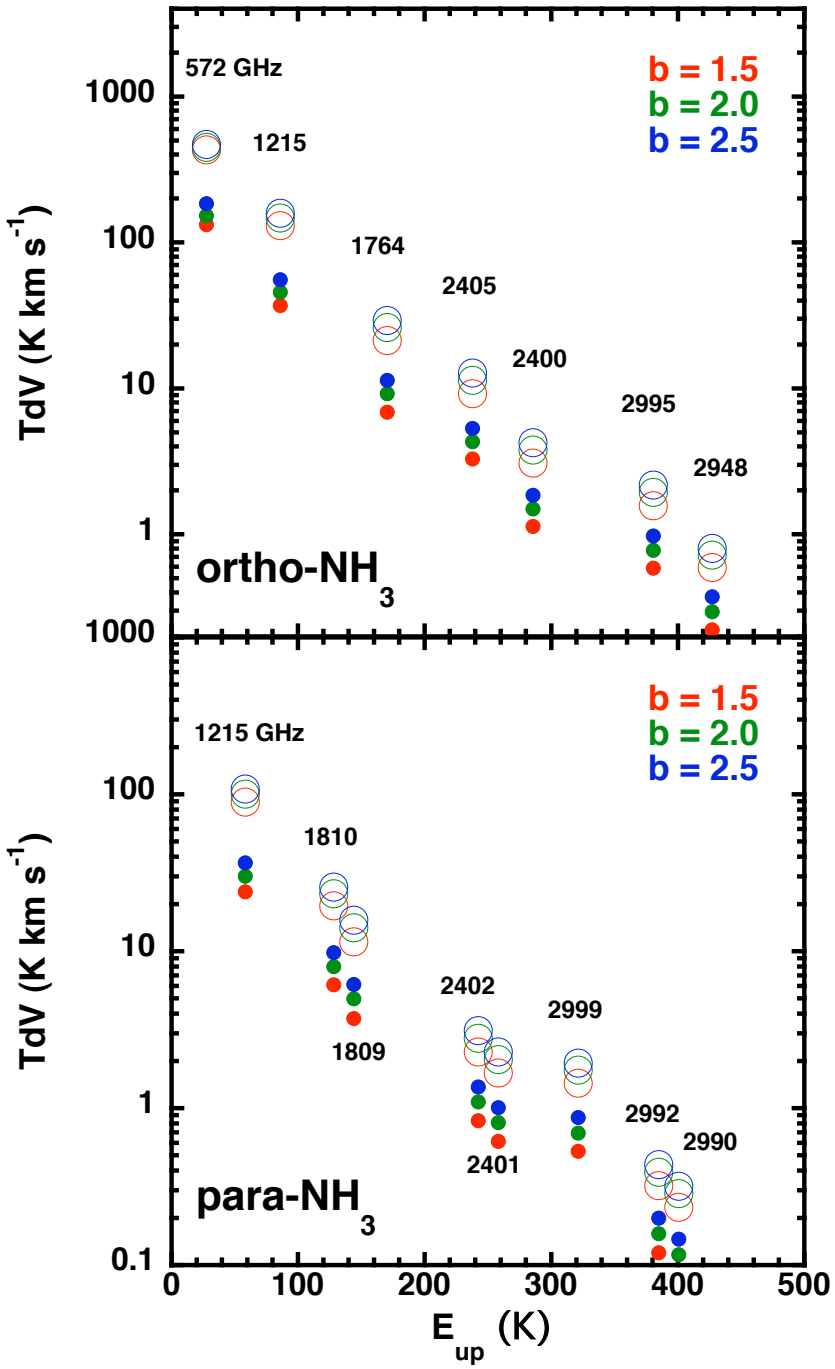

Figure 21: Integrated intensities of rotational transitions of ortho- and para-NH_3 for emitting levels of odd parity, plotted against the excitation energy of the emitting level, expressed relative to the energy of the $J = 0 = K$ ground state of ortho. Results are shown for shocks with $n_H = 10^5$ cm^{-3}, V_s = 30 km s^{-1} and b = 1.5 (red), b = 2.0 (green) and b = 2.5 (blue). Full circles: model M1; open circles: model M2.

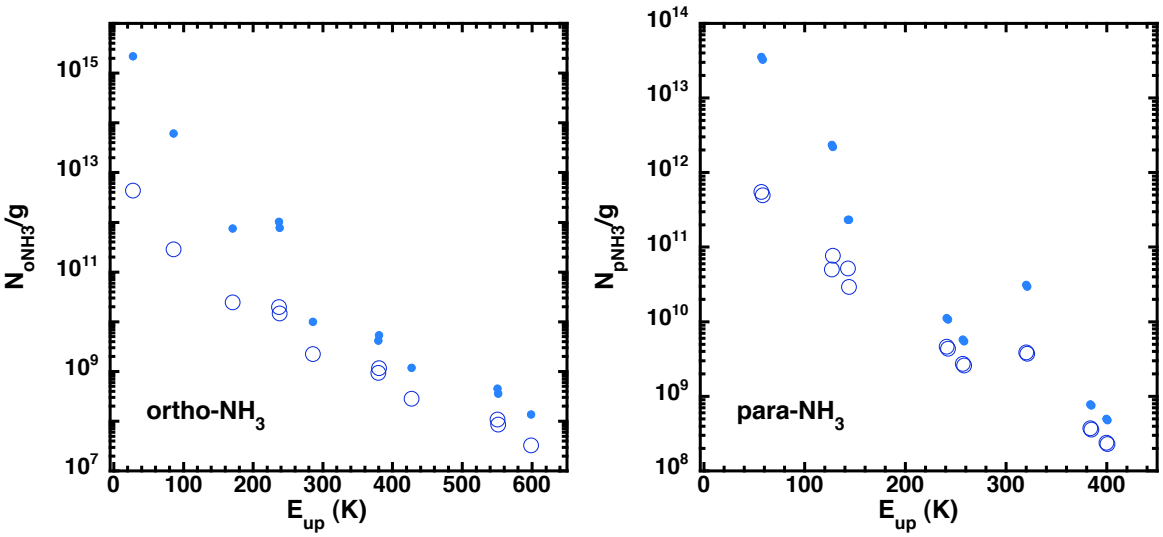

Figure 22: Excitation diagram for the upper energy levels of the transition of ortho- (left) and para-NH_3 (right) listed in Tables 15 and 16. Displayed are the column densities divided by the molecular weight for upper energy levels computed with model M1 (including grain-grain processing) for a shock with $V_s = 30$ km s^{-1} and $b = 1.5$. Full circles show column densities calculated with Eq. (84), while open circles show column densities calculated with Eq. (85).

Our shock model calculates the radiative transfer of para- and ortho-NH_3 for the first 24 rotational levels of para- and the first 17 levels of ortho-NH_3. The ortho-to-para ratio is assumed to have its statistical equilibrium value of 1.0.

Figure 21 shows the integrated line intensities, $T\mathrm{d}V$, of the rotational transitions of ortho- and para-NH_3 for emitting levels of odd parity, plotted against the excitation energy of the emitting level for a shock with $n_H = 10^5$ cm^{-3} and $V_s = 30$ km s^{-1}. As for water and CO, the line intensities for NH_3 are also lower when shattering is included due to the reduced shock width. Different than for the other molecules, the integrated intensities do not vary more strongly with the strength of the magnetic field if grain-grain processing is included. This demonstrates that the temperature dependence is not particularly strong for the displayed lines. Figure 22 shows the excitation diagrams for the upper energy levels of the transitions listed in Tables 15 and 16 for a shock with $V_s = 30$ km s^{-1} and $b = 1.5$. The lines become optically thick in the warm postshock gas. The optical thickness behaviour is similar for the models with and without grain-grain processing.

6.3 ADDITIONAL TABLES

In this section we list the unpublished intensities of rotational lines of ortho- and para-NH_3 (Tables 15–16) together with the rotational lines of SiO (Tables 17–19). For SiO, we only show the results for models M1 and M2, but not for models M3. This is because the amount of elemental Si assumed to be in the form of SiO in the grain mantles is a free parameter. Accordingly, the intensity values for the particular value of 10% for this free parameter, that we applied in models M3 in our paper, are not as meaningful as the ones for models M1 and M2.

We recall that the transformation of the integrated intensities obtained by the integration of the line temperature $T\mathrm{d}V$ (in K km s^{-1}) and the intensities I (in erg cm^{-2} s^{-1} sr^{-1}) is given as

$$I\left(\mathrm{erg\,cm^{-2}\,s^{-1}\,sr^{-1}}\right) = 27.61\frac{T\mathrm{d}V\left(\mathrm{K\,km\,s^{-1}}\right)}{\left(\lambda(\mu\mathrm{m})\right)^3}\,, \tag{86}$$

based on the Rayleigh-Jeans law, $I = \frac{2k\nu^2}{c^2}T$, and the Doppler relation, $\frac{\Delta v}{c} = \frac{\Delta\nu}{\nu_0}$, between the differential frequency ν and the differential velocity v, where ν_0 is the transition frequency at rest.

Table 15: Intensities of ortho-NH_3 lines (erg cm^{-2} s^{-1} sr^{-1}) for shocks with velocity V_s = 20 km s^{-1} (top), V_s = 30 km s^{-1} (middle),and V_s = 40 km s^{-1} (bottom) and the magnetic field strengths listed in Table 1. Results are given for models M1, which include grain-grain processing, and M2 (in parentheses), which neglect grain-grain processing. The preshock density is $n_H = 10^5$ cm^{-3}.

Transition	λ (μm)	E_{up} (K)	v20b1, M1	(v20b1, M2)	v20b1.5, M1	(v20b1.5, M2)	v20b2, M1	(v20b2, M2)
572.5 GHz	523.66	27.5	2.08e-05	(5.62e-05)	2.30e-05	(5.78e-05)	2.59e-05	(4.95e-05)
1214.9 GHz	246.77	85.8	5.31e-05	(1.51e-04)	6.26e-05	(1.71e-04)	7.01e-05	(1.52e-04)
1763.5 GHz	170.00	170.4	2.90e-05	(6.93e-05)	3.58e-05	(8.39e-05)	4.36e-05	(8.24e-05)
2358.6 GHz	127.11	236.7	4.51e-05	(9.86e-05)	5.38e-05	(1.13e-04)	6.77e-05	(1.12e-04)
2400.0 GHz	124.91	285.6	1.23e-05	(2.56e-05)	1.48e-05	(3.01e-05)	1.90e-05	(3.09e-05)
2405.1 GHz	124.65	237.8	3.56e-05	(7.67e-05)	4.29e-05	(9.20e-05)	5.41e-05	(9.34e-05)
2948.4 GHz	101.68	427.1	4.53e-06	(9.15e-06)	5.44e-06	(1.04e-05)	7.13e-06	(1.07e-05)
2950.8 GHz	101.60	379.4	9.45e-06	(1.90e-05)	1.14e-05	(2.22e-05)	1.48e-05	(2.30e-05)
2994.8 GHz	100.10	380.5	1.25e-05	(2.53e-05)	1.50e-05	(2.97e-05)	1.95e-05	(3.08e-05)
3540.3 GHz	84.680	550.4	3.22e-06	(6.39e-06)	3.87e-06	(7.24e-06)	5.10e-06	(7.49e-06)
3574.9 GHz	83.861	598.7	1.36e-06	(2.71e-06)	1.64e-06	(3.06e-06)	2.18e-06	(3.16e-06)
3581.3 GHz	83.709	551.3	2.70e-06	(5.43e-06)	3.26e-06	(6.15e-06)	4.31e-06	(6.32e-06)

Transition	λ (μm)	E_{up} (K)	v30b1.5, M1	(v30b1.5, M2)	v30b2, M1	(v30b2, M2)	v30b2.5, M1	(v30b2.5, M2)
572.5 GHz	523.66	27.5	2.55e-05	(8.33e-05)	2.94e-05	(8.66e-05)	3.57e-05	(9.07e-05)
1214.9 GHz	246.77	85.8	6.83e-05	(2.41e-04)	8.44e-05	(2.71e-04)	1.02e-04	(2.92e-04)
1763.5 GHz	170.00	170.4	3.88e-05	(1.20e-04)	5.19e-05	(1.48e-04)	6.39e-05	(1.65e-04)
2358.6 GHz	127.11	236.7	5.85e-05	(1.64e-04)	7.53e-05	(1.96e-04)	9.35e-05	(2.16e-04)
2400.0 GHz	124.91	285.6	1.61e-05	(4.37e-05)	2.12e-05	(5.37e-05)	2.64e-05	(6.02e-05)
2405.1 GHz	124.65	237.8	4.70e-05	(1.32e-04)	6.17e-05	(1.62e-04)	7.61e-05	(1.82e-04)
2948.4 GHz	101.68	427.1	5.84e-06	(1.57e-05)	7.78e-06	(1.90e-05)	9.83e-06	(2.11e-05)
2950.8 GHz	101.60	379.4	1.23e-05	(3.29e-05)	1.65e-05	(4.05e-05)	2.06e-05	(4.53e-05)
2994.8 GHz	100.10	380.5	1.62e-05	(4.34e-05)	2.15e-05	(5.36e-05)	2.69e-05	(6.00e-05)
3540.3 GHz	84.680	550.4	4.15e-06	(1.11e-05)	5.59e-06	(1.35e-05)	7.09e-06	(1.50e-05)
3574.9 GHz	83.861	598.7	1.74e-06	(4.71e-06)	2.35e-06	(5.75e-06)	3.02e-06	(6.38e-06)
3581.3 GHz	83.709	551.3	3.47e-06	(9.39e-06)	4.67e-06	(1.14e-05)	5.95e-06	(1.27e-05)

Transition	λ (μm)	E_{up} (K)	v40b2, M1	(v40b2, M2)	v40b2.5, M1	(v40b2.5, M2)	v40b3, M1	(v40b3, M2)
572.5 GHz	523.66	27.5	9.13e-07	(1.10e-04)	2.85e-05	(1.12e-04)	3.99e-05	(1.16e-04)
1214.9 GHz	246.77	85.8	1.14e-06	(3.31e-04)	7.80e-05	(3.62e-04)	1.18e-04	(3.84e-04)
1763.5 GHz	170.00	170.4	8.74e-07	(1.73e-04)	4.70e-05	(2.08e-04)	7.70e-05	(2.29e-04)
2358.6 GHz	127.11	236.7	1.98e-06	(2.31e-04)	6.97e-05	(2.71e-04)	1.09e-04	(2.96e-04)
2400.0 GHz	124.91	285.6	5.26e-07	(6.28e-05)	1.92e-05	(7.58e-05)	3.11e-05	(8.41e-05)
2405.1 GHz	124.65	237.8	1.23e-06	(1.89e-04)	5.62e-05	(2.28e-04)	9.05e-05	(2.53e-04)
2948.4 GHz	101.68	427.1	2.62e-07	(2.25e-05)	6.98e-06	(2.69e-05)	1.14e-05	(2.97e-05)
2950.8 GHz	101.60	379.4	4.76e-07	(4.75e-05)	1.48e-05	(5.76e-05)	2.43e-05	(6.41e-05)
2994.8 GHz	100.10	380.5	5.64e-07	(6.27e-05)	1.92e-05	(7.56e-05)	3.14e-05	(8.39e-05)
3540.3 GHz	84.680	550.4	2.02e-07	(1.60e-05)	4.97e-06	(1.92e-05)	8.25e-06	(2.13e-05)
3574.9 GHz	83.861	598.7	8.78e-08	(6.80e-06)	2.09e-06	(8.16e-06)	3.48e-06	(9.03e-06)
3581.3 GHz	83.709	551.3	1.70e-07	(1.35e-05)	4.16e-06	(1.61e-05)	6.88e-06	(1.78e-05)

Table 16: Intensities of para-NH_3 lines (erg cm^{-2} s^{-1} sr^{-1}) for shocks with velocity V_s = 20 km s^{-1} (top), V_s = 30 km s^{-1} (middle),and V_s = 40 km s^{-1} (bottom) and the magnetic field strengths listed in Table 1. Results are given for models M1, which include grain-grain processing, and M2 (in parentheses), which neglect grain-grain processing. The preshock density is $n_H = 10^5$ cm^{-3}.

Transition	λ (μm)	E_{up} (K)	v20b1, M1	(v20b1, M2)	v20b1.5, M1	(v20b1.5, M2)	v20b2, M1	(v20b2, M2)
1168.5 GHz	256.57	57.2	3.28e-05	(9.81e-05)	3.89e-05	(1.10e-04)	4.37e-05	(9.74e-05)
1215.2 GHz	246.69	58.3	3.44e-05	(1.03e-04)	4.09e-05	(1.16e-04)	4.59e-05	(1.02e-04)
1763.6 GHz	169.99	143.0	2.76e-05	(6.90e-05)	3.36e-05	(8.11e-05)	4.03e-05	(7.71e-05)
1763.8 GHz	169.97	127.0	1.66e-05	(3.95e-05)	2.04e-05	(4.75e-05)	2.50e-05	(4.66e-05)
1808.9 GHz	165.73	144.0	1.70e-05	(4.05e-05)	2.09e-05	(4.86e-05)	2.56e-05	(4.77e-05)
1810.4 GHz	165.60	128.1	2.83e-05	(7.04e-05)	3.44e-05	(8.27e-05)	4.13e-05	(7.88e-05)
2357.2 GHz	127.18	257.2	6.58e-06	(1.38e-05)	7.90e-06	(1.60e-05)	1.02e-05	(1.64e-05)
2357.7 GHz	127.15	241.2	8.88e-06	(1.87e-05)	1.07e-05	(2.19e-05)	1.37e-05	(2.24e-05)
2400.6 GHz	124.88	258.2	6.70e-06	(1.40e-05)	8.03e-06	(1.63e-05)	1.03e-05	(1.66e-05)
2402.3 GHz	124.80	242.3	9.04e-06	(1.90e-05)	1.09e-05	(2.23e-05)	1.39e-05	(2.28e-05)
2948.7 GHz	101.67	399.7	1.82e-06	(3.68e-06)	2.19e-06	(4.22e-06)	2.86e-06	(4.34e-06)
2949.5 GHz	101.64	383.8	2.50e-06	(5.07e-06)	3.00e-06	(5.82e-06)	3.92e-06	(5.99e-06)
2952.6 GHz	101.53	320.1	1.12e-05	(2.33e-05)	1.34e-05	(2.67e-05)	1.72e-05	(2.72e-05)
2989.6 GHz	100.28	400.6	1.85e-06	(3.74e-06)	2.23e-06	(4.29e-06)	2.91e-06	(4.42e-06)
2991.6 GHz	100.21	384.8	2.54e-06	(5.16e-06)	3.05e-06	(5.92e-06)	3.98e-06	(6.10e-06)
2999.4 GHz	99.950	321.2	1.13e-05	(2.37e-05)	1.36e-05	(2.72e-05)	1.75e-05	(2.77e-05)

Transition	λ (μm)	E_{up} (K)	v30b1.5, M1	(v30b1.5, M2)	v30b2, M1	(v30b2, M2)	v30b2.5, M1	(v30b2.5, M2)
1168.5 GHz	256.57	57.2	4.19e-05	(1.57e-04)	5.25e-05	(1.76e-04)	6.39e-05	(1.89e-04)
1215.2 GHz	246.69	58.3	4.40e-05	(1.64e-04)	5.53e-05	(1.85e-04)	6.74e-05	(1.99e-04)
1763.6 GHz	169.99	143.0	3.64e-05	(1.16e-04)	4.73e-05	(1.39e-04)	5.83e-05	(1.53e-04)
1763.8 GHz	169.97	127.0	2.21e-05	(6.82e-05)	2.95e-05	(8.38e-05)	3.64e-05	(9.36e-05)
1808.9 GHz	165.73	144.0	2.27e-05	(6.98e-05)	3.03e-05	(8.58e-05)	3.74e-05	(9.59e-05)
1810.4 GHz	165.60	128.1	3.72e-05	(1.18e-04)	4.85e-05	(1.42e-04)	5.98e-05	(1.56e-04)
2357.2 GHz	127.18	257.2	8.59e-06	(2.34e-05)	1.13e-05	(2.85e-05)	1.41e-05	(3.18e-05)
2357.7 GHz	127.15	241.2	1.16e-05	(3.18e-05)	1.53e-05	(3.89e-05)	1.90e-05	(4.36e-05)
2400.6 GHz	124.88	258.2	8.73e-06	(2.37e-05)	1.15e-05	(2.90e-05)	1.43e-05	(3.24e-05)
2402.3 GHz	124.80	242.3	1.18e-05	(3.24e-05)	1.56e-05	(3.97e-05)	1.94e-05	(4.44e-05)
2948.7 GHz	101.67	399.7	2.36e-06	(6.31e-06)	3.13e-06	(7.69e-06)	3.95e-06	(8.56e-06)
2949.5 GHz	101.64	383.8	3.23e-06	(8.66e-06)	4.29e-06	(1.06e-05)	5.39e-06	(1.18e-05)
2952.6 GHz	101.53	320.1	1.45e-05	(3.94e-05)	1.89e-05	(4.75e-05)	2.36e-05	(5.28e-05)
2989.6 GHz	100.28	400.6	2.39e-06	(6.41e-06)	3.19e-06	(7.82e-06)	4.02e-06	(8.71e-06)
2991.6 GHz	100.21	384.8	3.29e-06	(8.81e-06)	4.36e-06	(1.07e-05)	5.49e-06	(1.20e-05)
2999.4 GHz	99.950	321.2	1.47e-05	(4.01e-05)	1.92e-05	(4.83e-05)	2.41e-05	(5.37e-05)

Transition	λ (μm)	E_{up} (K)	v40b2, M1	(v40b2, M2)	v40b2.5, M1	(v40b2.5, M2)	v40b3, M1	(v40b3, M2)
1168.5 GHz	256.57	57.2	8.00e-07	(2.16e-04)	4.80e-05	(2.36e-04)	7.39e-05	(2.49e-04)
1215.2 GHz	246.69	58.3	8.32e-07	(2.27e-04)	5.05e-05	(2.49e-04)	7.80e-05	(2.63e-04)
1763.6 GHz	169.99	143.0	8.77e-07	(1.65e-04)	4.33e-05	(1.92e-04)	6.90e-05	(1.30e-04)
1763.8 GHz	169.97	127.0	5.41e-07	(9.84e-05)	2.67e-05	(1.18e-04)	4.38e-05	(2.09e-04)
1808.9 GHz	165.73	144.0	5.54e-07	(1.01e-04)	2.74e-05	(1.21e-04)	4.49e-05	(1.34e-04)
1810.4 GHz	165.60	128.1	9.02e-07	(1.68e-04)	4.44e-05	(1.96e-04)	7.08e-05	(2.14e-04)
2357.2 GHz	127.18	257.2	3.00e-07	(3.35e-05)	1.03e-05	(4.01e-05)	1.65e-05	(4.44e-05)
2357.7 GHz	127.15	241.2	3.84e-07	(4.57e-05)	1.39e-05	(5.50e-05)	2.25e-05	(6.09e-05)
2400.6 GHz	124.88	258.2	3.06e-07	(3.41e-05)	1.04e-05	(4.08e-05)	1.68e-05	(4.51e-05)
2402.3 GHz	124.80	242.3	3.92e-07	(4.65e-05)	1.42e-05	(5.60e-05)	2.29e-05	(6.21e-05)
2948.7 GHz	101.67	399.7	1.02e-07	(9.09e-06)	2.81e-06	(1.09e-05)	4.60e-06	(1.20e-05)
2949.5 GHz	101.64	383.8	1.35e-07	(1.25e-05)	3.86e-06	(1.49e-05)	6.29e-06	(1.65e-05)
2952.6 GHz	101.53	320.1	5.51e-07	(5.60e-05)	1.73e-05	(6.64e-05)	2.76e-05	(7.32e-05)
2989.6 GHz	100.28	400.6	1.04e-07	(9.24e-06)	2.86e-06	(1.11e-05)	4.68e-06	(1.22e-05)
2991.6 GHz	100.21	384.8	1.37e-07	(1.27e-05)	3.92e-06	(1.52e-05)	6.40e-06	(1.68e-05)
2999.4 GHz	99.950	321.2	5.66e-07	(5.70e-05)	1.75e-05	(6.76e-05)	2.80e-05	(7.45e-05)

Table 17: Intensities of SiO lines (erg cm^{-2} s^{-1} sr^{-1}) for shocks with velocity V_s = 20 km s^{-1} and the magnetic field strengths listed in Table 1. Results are given for models M1, which include grain-grain processing, and M2 (in parentheses), which neglect grain-grain processing. The preshock density is n_H = 10^5 cm^{-3}.

Transition	Freq. (GHz)	λ (μm)	v20b1, M1	(v20b1, M2)	v20b1.5, M1	(v20b1.5, M2)	v20b2, M1	(v20b2, M2)
SiO (1–0)	43.424	6903.9	9.92e-11	(5.42e-18)	1.75e-18	(9.29e-18)	3.29e-18	(9.33e-18)
SiO (2–1)	86.847	3452.0	2.68e-09	(1.27e-16)	3.09e-17	(1.95e-16)	5.06e-17	(1.77e-16)
SiO (3–2)	130.27	2301.3	1.32e-08	(4.91e-16)	1.17e-16	(6.63e-16)	1.68e-16	(5.63e-16)
SiO (4–3)	173.69	1726.0	2.81e-08	(7.60e-16)	2.04e-16	(9.26e-16)	2.70e-16	(7.66e-16)
SiO (5–4)	217.10	1380.9	3.76e-08	(7.11e-16)	2.36e-16	(8.18e-16)	3.02e-16	(6.95e-16)
SiO (6–5)	260.52	1150.8	3.92e-08	(5.45e-16)	2.25e-16	(6.17e-16)	2.89e-16	(5.55e-16)
SiO (7–6)	303.93	986.40	3.64e-08	(4.04e-16)	1.99e-16	(4.60e-16)	2.59e-16	(4.39e-16)
SiO (8–7)	347.33	863.13	3.21e-08	(3.09e-16)	1.70e-16	(3.53e-16)	2.25e-16	(3.51e-16)
SiO (9–8)	390.73	767.27	2.76e-08	(2.44e-16)	1.43e-16	(2.79e-16)	1.92e-16	(2.84e-16)
SiO (10–9)	434.12	690.57	2.33e-08	(1.96e-16)	1.19e-16	(2.23e-16)	1.62e-16	(2.30e-16)
SiO (11–10)	477.50	627.83	1.93e-08	(1.57e-16)	9.79e-17	(1.77e-16)	1.33e-16	(1.84e-16)
SiO (12–11)	520.88	575.55	1.57e-08	(1.24e-16)	7.91e-17	(1.40e-16)	1.08e-16	(1.46e-16)
SiO (13–12)	564.25	531.31	1.26e-08	(9.78e-17)	6.30e-17	(1.09e-16)	8.61e-17	(1.15e-16)
SiO (14–13)	607.61	493.40	9.99e-09	(7.60e-17)	4.96e-17	(8.46e-17)	6.78e-17	(8.87e-17)
SiO (15–14)	650.96	460.54	7.77e-09	(5.81e-17)	3.83e-17	(6.42e-17)	5.25e-17	(6.74e-17)
SiO (16–15)	694.29	431.79	5.97e-09	(4.40e-17)	2.93e-17	(4.82e-17)	4.00e-17	(5.07e-17)
SiO (17–16)	737.62	406.43	4.51e-09	(3.27e-17)	2.20e-17	(3.57e-17)	3.01e-17	(3.75e-17)
SiO (18–17)	780.93	383.89	3.36e-09	(2.40e-17)	1.63e-17	(2.60e-17)	2.22e-17	(2.73e-17)
SiO (19–18)	824.24	363.72	2.46e-09	(1.73e-17)	1.18e-17	(1.86e-17)	1.62e-17	(1.96e-17)
SiO (20–19)	867.52	345.57	1.77e-09	(1.23e-17)	8.49e-18	(1.31e-17)	1.16e-17	(1.38e-17)
SiO (21–20)	910.80	329.15	1.25e-09	(8.55e-18)	5.96e-18	(9.09e-18)	8.11e-18	(9.56e-18)
SiO (22–21)	954.05	314.23	8.52e-10	(5.76e-18)	4.05e-18	(6.09e-18)	5.50e-18	(6.40e-18)
SiO (23–22)	997.30	300.61	5.61e-10	(3.74e-18)	2.65e-18	(3.93e-18)	3.59e-18	(4.13e-18)
SiO (24–23)	1040.5	288.12	3.48e-10	(2.29e-18)	1.64e-18	(2.39e-18)	2.21e-18	(2.51e-18)
SiO (25–24)	1083.7	276.63	1.92e-10	(1.25e-18)	8.98e-19	(1.29e-18)	1.21e-18	(1.36e-18)
SiO (26–25)	1126.9	266.03	8.05e-11	(5.17e-19)	3.75e-19	(5.34e-19)	5.05e-19	(5.62e-19)

Table 18: Intensities of SiO lines (erg cm^{-2} s^{-1} sr^{-1}) for shocks with velocity V_s = 30 km s^{-1} and the magnetic field strengths listed in Table 1. Results are given for models M1, which include grain-grain processing, and M2 (in parentheses), which neglect grain-grain processing. The preshock density is n_H = 10^5 cm^{-3}.

Transition	Freq. (GHz)	λ (μm)	v30b1.5, M1	(v30b1.5, M2)	v30b2, M1	(v30b2, M2)	v30b2.5, M1	(v30b2.5, M2)
SiO (1–0)	43.424	6903.9	1.05e-09	(5.30e-09)	1.55e-10	(8.09e-10)	1.12e-14	(3.96e-13)
SiO (2–1)	86.847	3452.0	2.65e-08	(8.60e-08)	3.92e-09	(1.70e-08)	2.71e-13	(8.58e-12)
SiO (3–2)	130.27	2301.3	1.27e-07	(3.17e-07)	1.76e-08	(6.20e-08)	1.09e-12	(2.92e-11)
SiO (4–3)	173.69	1726.0	2.96e-07	(6.48e-07)	3.50e-08	(9.86e-08)	1.77e-12	(3.96e-11)
SiO (5–4)	217.10	1380.9	4.59e-07	(8.91e-07)	4.36e-08	(9.03e-08)	1.75e-12	(3.26e-11)
SiO (6–5)	260.52	1150.8	5.46e-07	(8.62e-07)	4.26e-08	(6.11e-08)	1.37e-12	(2.20e-11)
SiO (7–6)	303.93	986.40	5.42e-07	(5.86e-07)	3.74e-08	(3.73e-08)	9.75e-13	(1.42e-11)
SiO (8–7)	347.33	863.13	4.88e-07	(3.30e-07)	3.17e-08	(2.32e-08)	6.83e-13	(9.47e-12)
SiO (9–8)	390.73	767.27	4.21e-07	(1.91e-07)	2.64e-08	(1.53e-08)	4.85e-13	(6.60e-12)
SiO (10–9)	434.12	690.57	3.55e-07	(1.20e-07)	2.19e-08	(1.06e-08)	3.53e-13	(4.77e-12)
SiO (11–10)	477.50	627.83	2.93e-07	(8.10e-08)	1.79e-08	(7.66e-09)	2.62e-13	(3.52e-12)
SiO (12–11)	520.88	575.55	2.39e-07	(5.72e-08)	1.45e-08	(5.62e-09)	1.96e-13	(2.61e-12)
SiO (13–12)	564.25	531.31	1.91e-07	(4.13e-08)	1.16e-08	(4.15e-09)	1.47e-13	(1.95e-12)
SiO (14–13)	607.61	493.40	1.52e-07	(3.01e-08)	9.14e-09	(3.06e-09)	1.10e-13	(1.44e-12)
SiO (15–14)	650.96	460.54	1.18e-07	(2.19e-08)	7.10e-09	(2.25e-09)	8.17e-14	(1.06e-12)
SiO (16–15)	694.29	431.79	9.10e-08	(1.59e-08)	5.45e-09	(1.64e-09)	6.03e-14	(7.75e-13)
SiO (17–16)	737.62	406.43	6.90e-08	(1.15e-08)	4.12e-09	(1.18e-09)	4.39e-14	(5.59e-13)
SiO (18–17)	780.93	383.89	5.15e-08	(8.17e-09)	3.07e-09	(8.44e-10)	3.17e-14	(3.99e-13)
SiO (19–18)	824.24	363.72	3.78e-08	(5.75e-09)	2.25e-09	(5.94e-10)	2.25e-14	(2.80e-13)
SiO (20–19)	867.52	345.57	2.73e-08	(4.00e-09)	1.62e-09	(4.12e-10)	1.57e-14	(1.94e-13)
SiO (21–20)	910.80	329.15	1.93e-08	(2.74e-09)	1.14e-09	(2.81e-10)	1.08e-14	(1.32e-13)
SiO (22–21)	954.05	314.23	1.32e-08	(1.82e-09)	7.82e-10	(1.86e-10)	7.21e-15	(8.72e-14)
SiO (23–22)	997.30	300.61	8.75e-09	(1.17e-09)	5.16e-10	(1.19e-10)	4.64e-15	(5.56e-14)
SiO (24–23)	1040.5	288.12	5.44e-09	(7.06e-10)	3.20e-10	(7.16e-11)	2.82e-15	(3.34e-14)
SiO (25–24)	1083.7	276.63	3.01e-09	(3.82e-10)	1.77e-10	(3.85e-11)	1.53e-15	(1.79e-14)
SiO (26–25)	1126.9	266.03	1.27e-09	(1.57e-10)	7.43e-11	(1.58e-11)	6.30e-16	(7.34e-15)

Table 19: Intensities of SiO lines (erg cm^{-2} s^{-1} sr^{-1}) for shocks with velocity V_s = 40 km s^{-1} and the magnetic field strengths listed in Table 1. Results are given for models M1, which include grain-grain processing, and M2 (in parentheses), which neglect grain-grain processing. The preshock density is n_H = 10^5 cm^{-3}.

Transition	Freq. (GHz)	λ (μm)	v40b2, M1	(v40b2, M2)	v40b2.5, M1	(v40b2.5, M2)	v40b3, M1	(v40b3, M2)
SiO (1–0)	43.424	6903.9	3.87e-09	(5.94e-09)	3.49e-09	(1.57e-08)	3.54e-09	(1.88e-08)
SiO (2–1)	86.847	3452.0	9.94e-08	(9.64e-08)	7.46e-08	(1.82e-07)	6.67e-08	(2.11e-07)
SiO (3–2)	130.27	2301.3	5.09e-07	(3.60e-07)	3.28e-07	(6.54e-07)	2.70e-07	(7.54e-07)
SiO (4–3)	173.69	1726.0	1.35e-06	(7.45e-07)	7.66e-07	(1.44e-06)	5.90e-07	(1.67e-06)
SiO (5–4)	217.10	1380.9	2.53e-06	(1.04e-06)	1.27e-06	(2.36e-06)	9.12e-07	(2.78e-06)
SiO (6–5)	260.52	1150.8	3.88e-06	(1.02e-06)	1.69e-06	(3.06e-06)	1.11e-06	(3.71e-06)
SiO (7–6)	303.93	986.40	5.15e-06	(7.04e-07)	1.90e-06	(3.10e-06)	1.12e-06	(3.96e-06)
SiO (8–7)	347.33	863.13	6.10e-06	(3.95e-07)	1.86e-06	(2.32e-06)	9.73e-07	(3.20e-06)
SiO (9–8)	390.73	767.27	6.61e-06	(2.30e-07)	1.64e-06	(1.27e-06)	7.83e-07	(1.93e-06)
SiO (10–9)	434.12	690.57	6.58e-06	(1.51e-07)	1.37e-06	(6.43e-07)	6.24e-07	(1.01e-06)
SiO (11–10)	477.50	627.83	6.09e-06	(1.08e-07)	1.11e-06	(3.66e-07)	4.97e-07	(5.70e-07)
SiO (12–11)	520.88	575.55	5.30e-06	(8.12e-08)	8.95e-07	(2.37e-07)	3.96e-07	(3.59e-07)
SiO (13–12)	564.25	531.31	4.41e-06	(6.21e-08)	7.11e-07	(1.65e-07)	3.14e-07	(2.44e-07)
SiO (14–13)	607.61	493.40	3.56e-06	(4.76e-08)	5.59e-07	(1.20e-07)	2.46e-07	(1.73e-07)
SiO (15–14)	650.96	460.54	2.81e-06	(3.62e-08)	4.33e-07	(8.77e-08)	1.91e-07	(1.24e-07)
SiO (16–15)	694.29	431.79	2.18e-06	(2.73e-08)	3.32e-07	(6.44e-08)	1.47e-07	(9.00e-08)
SiO (17–16)	737.62	406.43	1.66e-06	(2.03e-08)	2.51e-07	(4.70e-08)	1.11e-07	(6.49e-08)
SiO (18–17)	780.93	383.89	1.24e-06	(1.49e-08)	1.87e-07	(3.39e-08)	8.28e-08	(4.64e-08)
SiO (19–18)	824.24	363.72	9.17e-07	(1.08e-08)	1.37e-07	(2.42e-08)	6.07e-08	(3.28e-08)
SiO (20–19)	867.52	345.57	6.63e-07	(7.71e-09)	9.89e-08	(1.70e-08)	4.38e-08	(2.29e-08)
SiO (21–20)	910.80	329.15	4.69e-07	(5.39e-09)	7.00e-08	(1.18e-08)	3.10e-08	(1.57e-08)
SiO (22–21)	954.05	314.23	3.21e-07	(3.65e-09)	4.79e-08	(7.88e-09)	2.13e-08	(1.05e-08)
SiO (23–22)	997.30	300.61	2.12e-07	(2.39e-09)	3.16e-08	(5.10e-09)	1.40e-08	(6.73e-09)
SiO (24–23)	1040.5	288.12	1.32e-07	(1.47e-09)	1.97e-08	(3.11e-09)	8.73e-09	(4.08e-09)
SiO (25–24)	1083.7	276.63	7.29e-08	(8.04e-10)	1.09e-08	(1.69e-09)	4.83e-09	(2.21e-09)
SiO (26–25)	1126.9	266.03	3.05e-08	(3.36e-10)	4.58e-09	(7.01e-10)	2.03e-09	(9.11e-10)

7

SUMMARY

In the previous chapters, we have investigated the effects of grain-grain processing on molecular line emission.

Guillet et al. (2011) had demonstrated grain-grain processing to be an indispensable ingredient of shock modelling in high density environments ($n_{\rm H} \geq 10^5$ cm^{-3}), based on a multi-fluid approach to the dust dynamics and a detailed calculation of the grain charge distribution. However, this study left open a couple of issues being important for the use of the results in the actual interpretation of shock emission in dense clouds. Besides the question for the influence of variations of the magnetic field strength, this in particular concerned the question for the consequences of grain-grain processing on molecular line emission.

In order to answer these questions, we incorporated the main features of grain-grain processing into a 2-fluid shock model. This treatment of shattering and SiO-vaporisation, leading to a saving in computation time by a factor of ~100 compared to the multi-fluid model, could then be implemented into an existing shock code including a self-consistent treatment of the line transfer of the most important molecular coolants, such as CO, OH, H_2O, NH_3, and SiO.

Using this model, combining grain-grain processing with a detailed radiative transfer, we computed a grid of nine models for three different shock velocities and magnetic field strengths, respectively. We found the influence of grain-grain processing to remain significant also for higher values of the magnetic field strength than studied by Guillet et al. (2011): all shocks showed higher peak fluid temperatures and reduced shock widths than the corresponding models without grain-grain processing. Vaporization of SiO from silicate grain cores was shown to have a significant influence on the gas-phase SiO abundance only for fast shocks with a low magnetic field.

The molecular line emission was influenced by grain-grain processing in two ways: the reduced shock widths bring about a lower column density of shock-heated gas and thus tend to reduce the molecular emission from shock-heated gas. On the other hand, the higher peak temperatures can modify the chemistry and enhance the fractional abundance of molecules in highly excited states. The resulting integrated intensities for H_2, CO, OH and H_2O were presented and discussed. The emission of NH_3 was added in Sect. 6.2 as additional material.

The main focus of the study was on the emission of the SiO molecule, which belongs to the most characteristic chemical tracers of shock waves, and which is influenced by the vaporization of SiO from silicate grain cores. We found the integrated intensities of SiO rotational lines to be enhanced, mainly from highly excited levels. This effect is, however, counteracted by the reduced column density of shock-heated gas. For the same reason, the widths of the SiO rotational lines were not significantly broadened by the release of SiO due to vaporization, which happens early in the shock. It is important that this release occurs directly, while SiO has only to be formed by gas-phase reactions from Si and thus shows a chemical delay if only sputtering of grain cores is considered. We also compared these results with a scenario where SiO is contained in grain mantles and is directly released

by sputtering already early in the shock. The effect of vaporization on [C I] emission lines was found to be less than for SiO rotational lines.

Having developed a simple recipe for the implementation of shattering and SiO vaporization into a 2-fluid shock model, it will now be possible to also study the effects of these processes on the emission of J-type, non-stationary and more-dimensional shocks in the near future.

Part III

OBSERVATIONAL DATA

These features of data — the fact that data are typically the result of complex interactions among a large number of disparate causal factors which are idiosyncratic to a particular experimental situation – are closely tied to the evidential role that data are expected to play in science. Often the characteristics which data must have to be useful as evidence can only be purchased at the cost of tolerating a great deal of complexity and idiosyncrasy in the causal processes which produce that data.

James Bogen & James Woodward 1988

8

INTRODUCTION

The following chapters concern the application of shock models within the interpretation of spectral line emission from shock-heated gas. The shock models used here are based on the numerical code as described in Part II, but most of them do not account for grain-grain processing because the grid of models was computed before our study of grain-grain processing was completed. However, because the effect of shattering only becomes significant for preshock densities $\geq 10^5$ cm^{-3}, this issue is only relevant for a small part of the grid. In particular, as will be seen, it does not concern the best-fitting models of our observations because the observed regions do not reach these high densities. The models including shattering and vaporisation as presented in Chapter 5 were finally added to the grid and taken into account for the study of W44. Besides C-type shocks, the grid of models also contains J-type and non-stationary shocks.

While the previous chapters only concerned the numerical modelling of shocks, now observational data come into play. These data have to be processed in a way that they become comparable with the numerical models. At the same time, several assumptions have to be made in order to match the simplified modelling conditions with the complex conditions found in the observed regions. The astrophysical phenomena being responsible for the shocks we observed are supernova remnants whose blast waves eventually interact with surrounding molecular clouds. These interactions give rise to a variety of molecular line emission, which can be described by our shock model. W28 and W44 are two prototype cases of such interacting supernova remnants, both at similar distances of ∼2 and ∼3 kpc, respectively. The main part of our analysis is based on CO emission lines observed with the Atacama Pathfinder EXperiment (APEX) telescope and the Stratospheric Observatory for Infrared Astronomy (SOFIA). For W28, we also had access to existing Spitzer/IRS data of rotational H_2 emission. In this introductory section we introduce the instruments and observatories we used before we briefly summarize our procedure of data reduction.

8.1 INSTRUMENTS

8.1.1 *Heterodyne receivers*

In a heterodyne receiver, the frequency of the input is transformed into another, usually lower, frequency before processing. This procedure helps to avoid feedback of the amplified signals into the frontend and subsequent instabilities. Furthermore, the signal is more easily amplified at lower frequencies. The frequency shifting is done by means of a mixer that combines the astronomical signal with the radiation of a local oscillator (LO). The resulting intermediate frequency band is either given as the sum or the difference of both frequencies. Depending on whether the frequency of the local oscillator is below or above the initial frequency, the resulting conversion is upper-sideband or lower-sideband, respectively. Because for a given local oscillator frequency, two frequency bands (above

and below the LO frequency) are shifted into the intermediate frequency band, one distinguishes between the signal and the image band. Filters can be used to reject the image band. In this case, the device is called ‘single sideband’ (SSB) as contrasted with ‘double sideband’ (DSB).

The mixing is often performed by means of superconducting devices, so-called SIS junctions, consisting of a superconducting layer, a thin insulating layer and another superconducting layer. In a superconductor, the electrons are paired in "Cooper-pairs" that act like bosons and give rise to so-called Josephson currents if a dc-voltage is applied to the junction: a tunneling of Cooper-pairs across the junction will occur, causing an ac-current. This tunneling increases the noise in the mixer and needs to be suppressed. This can be done by applying a steady magnetic field that modulates the current with a spatial oscillation, which can be adjusted such that its integrated current across the junction is zero.

The energy bands of the superconducting materials show a gap between the filled states of Cooper pairs and the allowed unfilled states of single electrons (see e.g Tucker & Feldman 1985). The bands of the superconducters can be vertically shifted relative to each other by means of a bias voltage applied at the junction. When the applied dc-voltage bias is set to a value corresponding to the value of the energy gap divided by the electron charge, the filled states on one superconductor reach the level of the unfilled states in the other superconducting layer and electrons, stemming from broken Cooper pairs, can tunnel from one side to the other. Correspondingly, the *I-V* curve will show a big jump in current at this value. If the junction is irradiated by a source of photons, the tunneling can already take place at a lower bias voltage of $h\nu/e$. The resulting *I-V* curve then shows characteristic "photon steps" if the junction is pumped by an LO, where the steps’ width corresponds to a value of $h\nu/e$ and the height is given by the probability of n-photon absorption.

If the LO waveform is differentially changed by the incoming astronomical signal, this differential change translates into a differential change in the measured dc-current, which finally corresponds to the intermediate frequency. The conversion efficiency of SIS junctions is much higher than for classical junctions and under certain conditions they can even yield a net conversion gain. A much more detailed description can be found in Tucker & Feldman (1985). The resulting intermediate frequency is then passed to the backends.

8.1.2 *Fast Fourier Transform spectrometer backends*

Spectrometers are used to measure the power spectral density of the incoming signal. In radio astronomy, digital auto-correlators have been widely used, where the voltage in time is autocorrelated and then Fourier transformed to obtain the spectral power density. It is, however, very complicated to reach high instantaneous bandwidths with these spectrometers. Another widely used spectrometer type is the acousto-optical spectrometer, which is based on the diffraction of light by ultrasonic waves. The highest bandwidths and channel numbers are possible with so-called Fast Fourier Transform (FFT) spectrometers. Here, the spectral information is obtained by means of a Fourier transformation of the time-dependent voltage input, which yields the voltage in frequency. If the sampling is done obeying the Nyquist theorem, a Fast Fourier Transform algorithm can be used. This method requires high computing power and high sampling rates of analog-to-digital converters. With the latest gener-

ation of FFTS, as for example developed for the GREAT receiver onboard SOFIA, an instantaneous bandwidth of 2.5 GHz with 88.5 kHz spectral resolution has been reached (Klein et al. 2006, 2012).

8.2 OBSERVATORIES

8.2.1 *The Stratospheric Observatory for Infrared Astronomy*

SOFIA is an airborne observatory based on a Boeing 747SP, operated by NASA and the German Aerospace Center – Deutsches Zentrum für Luft- und Raumfahrt (DLR) (Young et al. 2012). Flying at altitudes of up to 13.7 km (45,000 feet), it is able to perform observations above 99.8% of the Earth's atmospheric water vapour and thereby access regimes of the electromagnetic spectrum that are not observable from the Earth's surface, particularly in the THz regime. With its 2.7 m primary mirror, SOFIA covers a nominal operational wavelength range from 0.3 up to 1600 μm. SOFIA had its first light flight in May 2010. The spectrum presented in Chapter 9 was recorded during one of the first science flights with the GREAT (German Receiver for Astronomy at Terahertz Frequencies) spectrometer in 2011. This dual channel heterodyne instrument is able to cover the wavelength range between 60 and 200 μm. The CO (11–10) spectrum at 1267 GHz is located in the detector's low frequency window L#1. The backends used together with the mixers are Fast Fourier Transform (FFT) spectrometers.

8.2.2 *The Atacama Pathfinder EXperiment*

The Atacama Pathfinder Experiment (APEX, see Güsten et al. 2006) is a prototype antenna of the ALMA (Atacama Large Millimeter Array) project, operated as a 12m single dish telescope at an altitude of 5107 m on the Llano de Chajnantor by the Max-Planck-Institut für Radioastronomie, the Onsala Space Observatory, and the European Southern Observatory. At this very dry and high site, the amount of perceptible water vapour is typically 1.2 mm or below. It therefore offers excellent atmospheric transmission in the GHz up to THz regime. The APEX telescope hosts a variety of different observing instruments, including various heterodyne receivers and bolometer arrays, which can be mounted in two Nasmyth and one Cassegrain receiver cabins.

The studies of supernova remnants presented in the following chapters are based on CO observations with APEX using different heterodyne receivers: APEX-2, FLASH345, FLASH460, and CHAMP$^+$, the last three being PI instruments. These receivers were combined with fast Fourier transformation spectrometer backends.

8.2.3 *The Spitzer Space Telescope*

The Spitzer Space telescope is the instrument responsible for infrared wavelengths within NASA's Great Observatories Program (Werner et al. 2004). It was launched in 2003. Since the liquid helium supply was exhausted in 2009, it has been continued as the Spitzer Warm Mission. Its primary mirror has a diameter of 85 cm. Three science instruments are onboard Spitzer: The Infrared Array Camera

(IRAC, Fazio et al. 2004), which is a four-channels imaging camera operating at wavelengths of 3.6, 4.5, 5.8, and 8.0 μm, the Multiband Imaging Photometer (MIPS), which is an imaging camera at 24, 70, and 160 μm and a simple spectrometer, and the Infrared Spectrograph (IRS, Houck et al. 2004), which provides high- and low-resolution spectroscopy at mid-infrared wavelengths between 5 and 40 μm. The IRS has four different modules, detecting different wavelength regimes at different resolutions. The detector arrays are 128×128 pixels in size.

8.3 DATA REDUCTION

The CO spectra, as they were observed by the APEX telescopes in position-switching/raster mode, have different spatial resolutions depending on the observed wavelength. In order to make the maps and the corresponding spectral emission comparable, we first created 3-D data cubes with a common pixel-size and spatial resolution (by setting the corresponding GILDAS[1] map parameters and using the CLASS commands `table` and `xy_map`). As a rule of thumb, the pixel size should be chosen as $\sim 1/5$ of the beam size. We used a value of $3''$ for all maps, which corresponds to $1/3$ of the original pixel-size of the coarsest map. In order to create velocity integrated maps, we used the greg task `run moments` on these cubes. For the sake of presentation the maps were resampled once more during plotting (GREG task `resample`). For the shock analysis, the individual spectra were recreated from the 3-D cube (CLASS task `lmv`) and extracted at the chosen positions with a position matching tolerance of $3''$. The spectra had to be converted from antenna temperature to main beam temperature using the main beam and forward efficiencies of the telescope and the receiver. Finally, the spectra were baseline corrected by subtracting a linear baseline (polynomial baseline of degree 1, task `base` in CLASS). The spectral line fitting was performed using independent Gaussians with undetermined parameters (task `method Gauss` and `minimize` in CLASS).

The Spitzer H_2 data were treated similarly. Because the SOFIA data consisted of only one spectrum, only the last steps described above were necessary in the processing of this data.

1 The GILDAS package is described at `http://www.iram.fr/IRAMFR/GILDAS`.

9

PROBING MAGNETOHYDRODYNAMIC SHOCKS WITH HIGH-J CO OBSERVATIONS: W28F[1]

9.1 ABSTRACT

Context: Observing supernova remnants (SNRs) and modelling the shocks they are associated with is the best way to quantify the energy SNRs re-distribute back into the Interstellar Medium (ISM).
Aims: We present comparisons of shock models with CO observations in the F knot of the W28 supernova remnant. These comparisons constitute a valuable tool to constrain both the shock characteristics and pre-shock conditions.
Methods: New CO observations from the shocked regions with the APEX and SOFIA telescopes are presented and combined. The integrated intensities are compared to the outputs of a grid of models, which were combined from an MHD shock code that calculates the dynamical and chemical structure of these regions, and a radiative transfer module based on the 'large velocity gradient' (LVG) approximation.
Results: We base our modelling method on the higher J CO transitions, which unambiguously trace the passage of a shock wave. We provide fits for the blue- and red-lobe components of the observed shocks. We find that only stationary, C-type shock models can reproduce the observed levels of CO emission. Our best models are found for a pre-shock density of 10^4 cm^{-3}, with the magnetic field strength varying between 45 and 100 μG, and a higher shock velocity for the so-called blue shock ($\sim$25 km s^{-1}) than for the red one ($\sim$20 km s^{-1}). Our models also satisfactorily account for the pure rotational H_2 emission that is observed with *Spitzer*.

9.2 INTRODUCTION

The interstellar medium (ISM) is in constant evolution, ruled by the energetic feedback from the cosmic cycle of star formation and stellar death. At the younger stages of star formation (bipolar outflows), and after the death of massive stars (SNRs), shock waves originating from the star interact with the ambient medium. They constitute an important mechanical energy input, and lead to the dispersion of molecular clouds and to the compression of cores, possibly triggering further star formation. Studying the signature of these interactions in the far-infrared and sub-mm range is paramount for understanding the physical and chemical conditions of the shocked regions and the large-scale roles of these feedback mechanisms.

Supernovae send shock waves through the ISM, where they successively carve out large hot and ionised cavities. They subsequently emit strong line radiations (optical/UV), and eventually interact with molecular clouds, driving lower-velocity shocks. Similar to their bipolar outflow equivalents,

1 This chapter has been published as Gusdorf, A., Anderl, S., et al. (2012).

these shocks heat, compress, and accelerate the ambient medium before cooling down through molecular emission (van Dishoeck et al. 1993, Yuan & Neufeld 2011, hereafter Y11).

Valuable information has been provided by ISO (Cesarsky et al., 1999; Snell et al., 2005) and *Spitzer* (Neufeld et al. 2007, hereafter N07), but neither of those instruments provided sufficient spectral resolution to allow for a detailed study of the shock mechanisms. High-J CO emission is one of the most interesting diagnostics of SNRs. CO is indeed a stable and abundant molecule, and an important contributor to the cooling of these regions, whose high-frequency emission is expected to be a 'pure' shock tracer. Observations of the latter must be carried out from above the Earth's atmosphere. As part of a multi-wavelength study of MHD shocks that also includes *Herschel* data, we present here the first velocity-resolved CO (11–10) observations towards a prominent SNR-driven shock with the GREAT spectrometer onboard SOFIA, and combine them with new lower-J ones in a shock-model analysis.

9.3 THE SUPERNOVA REMNANT W28

W28 is an old ($>10^{4.5}$ yr, Claussen et al. 1999) SNR in its radiative phase of evolution, with a non-thermal radio shell centrally filled with thermal X-ray emission. Lying in a complex region of the Galactic disk at a distance of 1.9±0.3 kpc (Velázquez et al., 2002), its structure in the 327 MHz radio continuum represents a bubble-like shape of about 40×30 pc (Frail et al., 1993). Early on, molecular line emission peaks, not associated with star formation activity, but revealing broad lines, were suggested as evidence for interaction of the remnant with surrounding molecular clouds (Wootten, 1981). Later studies spatially resolved the shocked CO gas layers from the ambient gas (Frail & Mitchell, 1998; Arikawa et al., 1999). OH maser spots line up with the post-shock gas layers (Frail et al., 1994; Claussen et al., 1997; Hoffman et al., 2005), for which the strongest masers VLBA polarisation studies yield line-of-sight magnetic field strengths of up to 2 mG (Claussen et al., 1999). Pure rotational transitions of H_2 have been detected with ISO (Reach & Rho, 2000) and were more recently observed with *Spitzer*, better resolved spatially and spectrally, by N07 and Y11.

Recently, very high energy (TeV) γ-ray emission has been detected by HESS (Aharonian et al., 2008), Fermi (Abdo et al., 2010), and AGILE (Giuliani et al., 2010), spatially slightly extended and coincident with the bright interaction zones, W28-E and -F. If interpreted as the result of hadronic cosmic ray interactions in the dense gas (π^0 decay), a cosmic ray density enhancement by an order of magnitude is required (which is supplied/accelerated by the SNR).

9.3.1 *Sub-mm CO observations of W28F*

APEX[2] (Güsten et al., 2006) observations towards W28F were conducted in 2009 and will be the subject of a forthcoming publication (Gusdorf et al., in prep.). For the present study, we used 100″×100″ maps in the ^{13}CO (3–2), CO (3–2), (4–3), (6–5), and (7–6) transitions, described in Appendix 9.5.

2 This publication is partly based on data acquired with the Atacama Pathfinder EXperiment (APEX). APEX is a collaboration between the Max-Planck-Institut für Radioastronomie, the European Southern Observatory, and the Onsala Space Observatory.

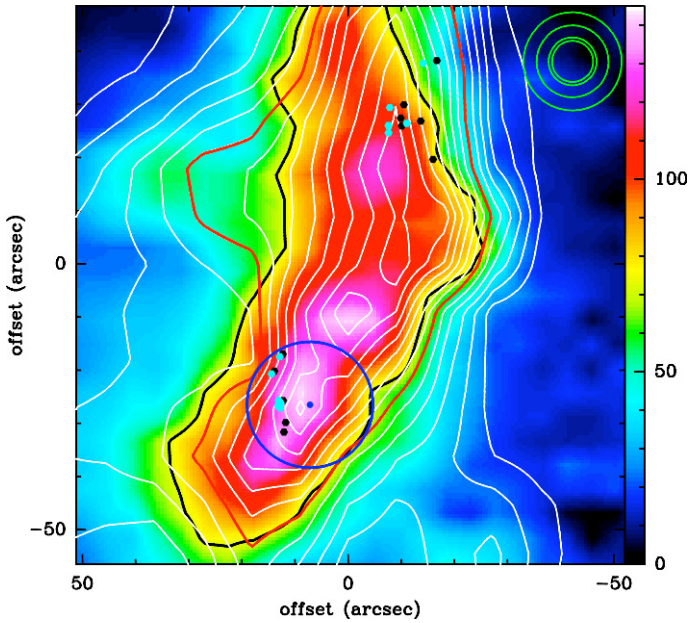

Figure 23: Overlay of the velocity-integrated CO (6–5) (colour background) with the CO (3–2) (white contours) emission observed with the APEX telescope. For both lines, the intensity was integrated between -30 and 40 km s^{-1}. The wedge unit is K km s^{-1} in antenna temperature. The CO (3–2) contours are from 30 to 160 σ, in steps of 10σ = 16 K km s^{-1}. The half-maximum contours of the CO (3–2) and (6–5) maps are indicated in red and black, respectively. The dark blue circle indicates the position and beam size of the SOFIA/GREAT observations. The APEX beam sizes of our CO (3–2), (4–3), (6–5), and (7–6) observations are also provided (upper right corner light green circles, see also Table 20). The maps are centred at (R.A.$_{[J2000]}$=$18^h01^m52^s.3$, Dec$_{[J2000]}$=$-23°19'25''$). The black and light blue hexagons mark the position of the OH masers observed by Claussen et al. (1997) and Hoffman et al. (2005).

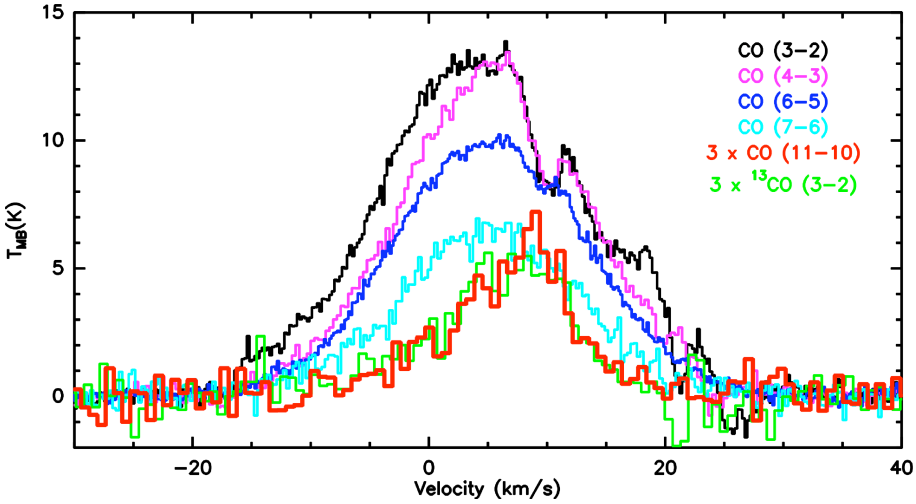

Figure 24: CO transitions observed in the position (+7″,-26″) indicated in Fig. 23: APEX (3–2), black (corresponding ^{13}CO, green); (4–3), pink; (6–5), dark blue; (7–6), light blue; and SOFIA (11–10), red. The ^{13}CO (3–2) and CO (11–10) profiles were multiplied by three for comparison purposes. Respective CO spectral resolutions are 0.212, 0.318, 0.159, 0.272, and 0.693 km s^{-1}, and 0.664 km s^{-1} for ^{13}CO (3–2).

In Fig. 23 the velocity-integrated CO (6–5) broad-line emission of W28F is shown overlaid with the CO (3–2) emission (white contours): a north-south elongated structure of about 100″ height and 30″ width traces the same warm accelerated post-shocked gas. In our high-resolution CO (6–5) data the structure is resolved, though probably still sub-structured similar to what is seen in H_2, e.g., Y11. Comparison with the distributions of excited H_2 and OH masers (whose locations also mark the leading edge of the non-thermal radio shell) suggests a textbook morphology of an SNR-molecular cloud interaction: the shock propagates E-NE into the ambient cloud that extends east for several arcmins. Hot H_2 and OH masers mark the first signposts of the shock-compressed gas. Farther downstream, the gas cooling is seen prominently in warm CO. The shock impact appears edge-on, but the fact that high - projected - streaming velocities are indeed observed (-30 km s^{-1} with respect to the ambient cloud) requires a significant inclination angle.

We have selected the most prominent position in the southern extension of W28F, marked with the blue circle in Fig. 23, for our shock analysis. This position was also covered by *Spitzer*, offering a set of complementary H_2 data. Fig. 24 shows the APEX spectra obtained towards this position, in main beam temperature units, all convolved to the 23.7″ beam of the SOFIA observations (Sect. 9.3.2). Absorption notwithstanding, the spectra show Gaussian profiles, with all line wings extending in blue (-30 km s^{-1}) and red (+15 km s^{-1}) velocities with respect to the ambient cloud (~10 km s^{-1}). The higher the line frequency, the narrower the line profile, with a typical linewidth of about 20 km s^{-1} for CO (7–6). We detect red-shifted line-of-sight absorption features in all lines up to CO (6–5), the deepest arising at the ambient cloud velocity. Off-position contamination results in minor absorption features at 20 and 25 km s^{-1} in the (3–2) and (4–3) profiles. Comparison with the ^{13}CO(3-2) profile is also shown in Fig. 24. An analysis of the line temperature ratio of ^{12}CO/^{13}CO yields an optical thickness value of 3–7 in the wings of the ^{12}CO (3–2), assuming a typical interstellar abundance ratio of 50–60 (e.g., Langer & Penzias 1993).

9.3.2 *Far-infrared CO spectroscopy with GREAT/SOFIA*

The observations towards W28F were conducted with the GREAT[3] spectrometer (Heyminck et al. 2012) during SOFIA's flight from Stuttgart to Washington on September 21 2011. Only one position could be observed, towards the southern tip of the shocked cloud at offset (+7″,-26″) (Fig. 23). The CO (11–10) line was tuned to the frequency 1267.015 GHz LSB. The receiver was connected to a digital FFT spectrometer (Klein et al. 2012) providing a bandwidth of 1.5 GHz with a spectral resolution of 0.05 km s^{-1}. The observations were performed in double beam-switching mode, with an amplitude of 80″ (or a throw of 160″) at the position angle of 135° (NE–SW), and a phase time of 0.5 sec. The nominal focus position was updated regularly against temperature drifts of the telescope structure. The pointing was established with the optical guide cameras to an accuracy of ∼5″. The beam width Θ_{mb} is 23.7″; the main beam and forward efficiencies are $\eta_{mb} = 0.54$ and $\eta_f = 0.95$. The integration time was 13 min ON source, for a final r.m.s of 0.66 K. The data were calibrated with the KOSMA/GREAT calibrator (Guan et al. 2012), removing residual telluric lines, and subsequently processed with the CLASS software[4].

The CO (11–10) spectrum, overlaid on the sub-mm lines in Fig. 24, reveals a markedly different profile: weak emission only is seen from the high-velocity gas, while the line is more prominent at low velocities. The profile basically follows the shape of the optically thin ^{13}CO(3-2).

9.4 DISCUSSION

9.4.1 *The observations*

Although most likely part of a single original shock clump, we separated the profiles into a blue lobe (-30 to 7.5-12.5 km s^{-1}) and a red lobe (7.5-12.5 to 40 km s^{-1}), and fited the data independently. The uncertainty of the upper (lower) limit of those ranges reflects our lack of knowledge of the ambient velocity component. In Fig. 25 we plot the velocity-integrated intensities of the CO lines, all convolved to the same angular resolution of 23.7″, against the rotational quantum number of their upper level in a so-called 'spectral line energy distribution' (or SLED, filled black squares with errorbars). The underlying assumption is that the filling factor is the same for all CO lines, which is validated by the similarity between their emitting regions (see for instance Fig. 23, where the half-maximum contours of CO (3–2) and (6–5) coincide at the available resolution). For Fig. 25, the assumption was made that all observed transitions present a circular emission region of radius 25″, corresponding to a filling factor of 0.53 (compatible with our maps, see Fig. 23).

The upper (lower) panel shows the diagram associated with the blue (red) shock component. The lower limit to the integrated intensity corresponds to the integration of the observed profile in the smallest velocity range, whereas upper limits were obtained by integrating Gaussian fits to the observation on the largest velocity range. The fits were adjusted to recover the shock flux lost through absorption and based on the un-absorbed parts of the profiles. Although yielding high errorbars on our

3 GREAT is a development by the MPI für Radioastronomie and the KOSMA / Universität zu Köln, in cooperation with the MPI für Sonnensystemforschung and the DLR Institut für Planetenforschung.

4 http://www.iram.fr/IRAMFR/GILDAS

measurements, specially for low $J_{\rm up}$ values, this method also provides the most conservative approach to our blue-red decomposition of the CO emission.

9.4.2 *The models*

We then compared the resulting integrated intensity diagrams to modelled ones. To build those, we used a radiative transfer module based on the 'large velocity gradient' (LVG) approximation to characterise the emission from the CO molecule over outputs generated by a state-of-the-art model that calculates the structure of one-dimension, stationary shock layers (or approximations of non-stationary layers). This method has already been used and extensively introduced in Gusdorf et al. (2008b). Since then, the LVG module has been modified to incorporate the latest collisional rate coefficients of CO with H_2 computed by Yang et al. (2010), but the shock model is the same. Based on a set of input parameters (pre-shock density, shock velocity, type, and age, and magnetic field parameter value b such as $B[\mu G] = b \times \sqrt{n_{\rm H}\ [{\rm cm}^{-3}]}$), it calculates the structure of a shock layer, providing dynamical (velocity, density, temperature), and chemical (fractional abundances of more than 125 species linked by over 1000 reactions) variables values at each point of the layer. The relevant outputs are then used by our LVG module, which calculates the level population and line emissivities of the considered molecule. In the present case, the line temperatures were computed for transitions of CO up to (40–39) at each point of the shock layer, over which they were then integrated to form our model's SLED. Because of the importance of H_2 (key gas coolant, abundant molecule), its radiative transfer was treated within the shock model. Its abundance was calculated at each point of the shock layer, based on the processes listed in Le Bourlot et al. (2002), and the populations of the 150 first levels were also calculated inside the shock code, their contribution to the cooling being included in the dynamical calculations. It is hence also possible to associate an H_2 excitation diagram to each model of the grid, see Sect. 9.6.2.

Our model grid consists of a large sample of integrated intensity diagrams, obtained for stationary C- and J-type, and non-stationary CJ-type shocks. It covers four pre-shock densities (from 10^3 to 10^6 cm^{-3}), $0.45 \leq b \leq 2$, over a range of velocities spanning from 5 km s^{-1} up to the maximum, 'critical' value above which a C-shock can no longer be maintained, which depends on the other parameters. We then independently compared the observed blue- and the red-shock component to the whole grid diagrams. We used a χ^2 routine that was set up to provide the best fits to our purest shock-tracing lines: CO (6–5), (7–6), and (11–10), to reduce any effect induced by ambient emission contamination on the lower-lying transitions.

9.4.3 *The results*

The upper (lower) panel of Fig. 25 shows our best-fitting models for the blue (red) component. We found that only stationary, C-type shock models can reproduce the levels of observed CO (6–5), (7–6) and (11-10) integrated intensities. In both cases, the pre-shock density is 10^4 cm^{-3}, for which a stationary state is typically reached for a shock age of 10^4 years, in agreement with the age of the remnant of 3.5×10^4 years quoted by Giuliani et al. (2010). The modelled shock velocities, 25 and 20 km s^{-1}, respectively, are rough upper limits to the observed ones, an expected conclusion given

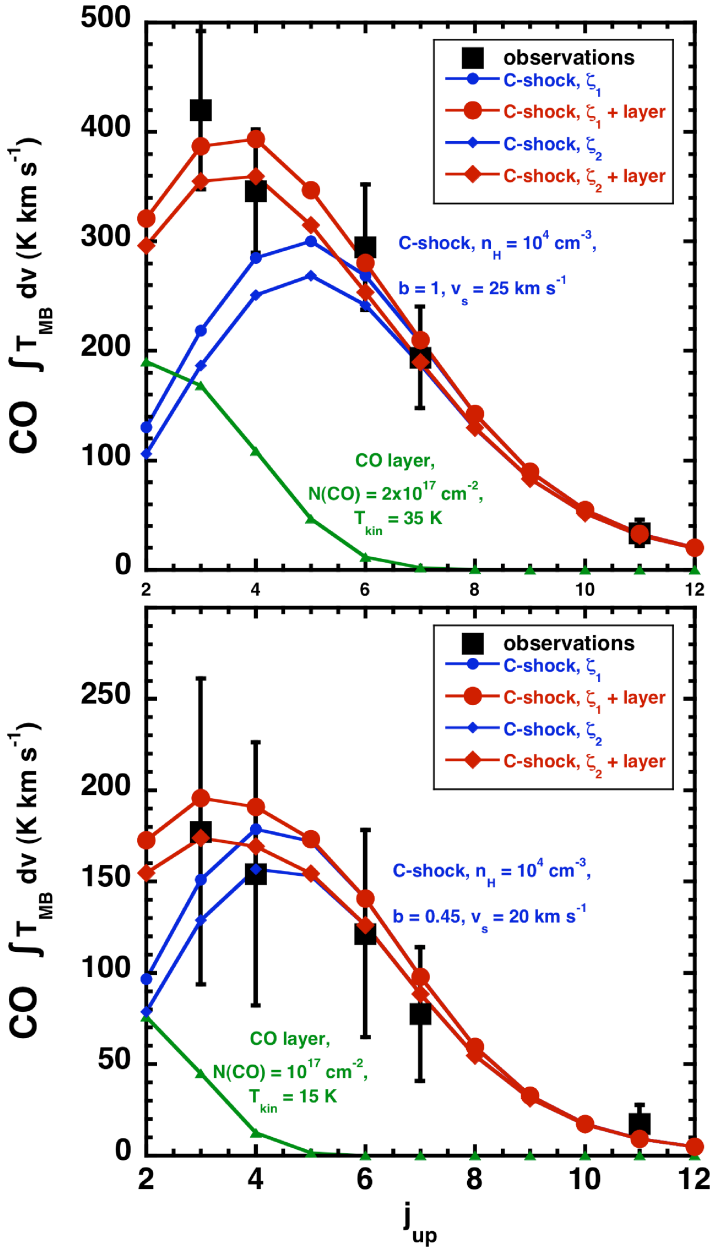

Figure 25: Best-model comparisons between CO observations and models for each observed shock: the blue- (upper panel) and the red- (lower panel) components. Observations are marked by the black squares, our individual best-shock models are in blue line and circles (ζ_1) or diamonds (ζ_2), the warm layer that we used to compensate the ambient emission affecting the (3–2) and (4–3) transitions in green line and triangles, and the sum of each of these components is represented by a red line and circles or diamonds.

the one-dimensional nature of our models. Additionally, our models provide respective constraints to the magnetic field component perpendicular to the shock layers, with parameter b of 1 and 0.45. The difference between those two values can be explained by a projection effect. In both cases, the direct post-shock density is of the order of 2-3$\times10^5$cm^{-3}, yielding expected post-shock values for this component of 0.05–0.55 mG, compatible with those inferred by Claussen et al. (1999) (2 mG for the total post-shock magnetic field), and by Hoffman et al. (2005) (0.3–1.1 mG based on the OH maser measurements in the positions indicated in Fig. 23 located within the blue beam). Finally, our models produce typical OH column densities of a few 10^{16} cm^{-2}. This complies with the list of requirements set out by Lockett et al. (1999) for exciting the observed OH 1720 MHz masers, together with the C-nature of the considered shocks, as well as the temperature and density conditions they create.

The respective CO column density found in each of the red and blue shock models is 11 and 5×10^{17}cm^{-3}. However, our shock models failed to account for the important observed levels of CO (3–2) and (4–3) emission. We found it possible to model this lower-J surplus emission by adding a thin layer of gas to our shock model results. Its corresponding emission was calculated with our LVG module used in a 'homogeneous slab' mode, and indeed generated significant emission only from the (3–2) and (4–3) lines, as can also be seen in Fig. 25. We used a linewidth of 10 km s^{-1} and a density of $n_{\rm H} = 10^4$ cm^{-3} with a fractional abundance of $X({\rm CO}) = 10^{-4}$ for the blue and red cases. We found that this 'CO layer' is warm (35 K and 15 K for the blue and red components, respectively), and adds to the pure-shock CO column density in both components, from 2×10^{17} cm^{-2} for the blue component, and 10^{17} cm^{-2} for the red one. Our final result, the sum of the C-shock and 'CO layer', is also shown in Fig. 25.

To understand the physical origin of this emitting layer, we varied the cosmic ray ionisation rate in our best-fitting models from its solar value $\zeta_1 = 5\times10^{-17}$ s^{-1} to the $\zeta_2 = 3.4\times10^{-16}$ s^{-1} indicated by Hewitt et al. (2009) in the specific case of W28. In our modelling, this modification impacts on the chemistry (higher ionisation fraction) and the physics (warmer gas) of our outputs. The resulting shock profile is more narrow (hence generating slightly less CO emission, see Fig. 25), with higher post-shock temperatures close to the aforementioned CO layer. Because one of the limitations of our shock model is the absence of significant velocity gradient in the post-shock region, the warm CO layer component might correspond to a post-shock layer of gas mildly heated by the energetic radiation that seems to exist in the region (UV or more energetic, as characterised by Hewitt et al. 2009). The rigorous inclusion of these radiative effects in our shock model is still in progress. In Sect. 9.6 we present a consistency check based on the use of the *Spitzer* H_2 observations.

ACKNOWLEDGEMENTS. We thank the SOFIA engineering and operations teams, whose support has been essential during basic science flights, and the DSI telescope engineering team. Based [in part] on observations made with the NASA/DLR Stratospheric Observatory for Infrared Astronomy. SOFIA Science Mission Operations are conducted jointly by the Universities Space Research Association, Inc., under NASA contract NAS2-97001, and the Deutsches SOFIA Institut under DLR contract 50 OK 0901. S. Anderl acknowledges support by the Deutsche Forschungsgemeinschaft within the SFB 956 "Conditions and impact of star formation", the International Max Planck Research School (IMPRS) for Radio and Infrared Astronomy at the Universities of Bonn and Cologne, and the Bonn-Cologne Graduate School of Physics and Astronomy. A. Gusdorf acknowledges support by the grant

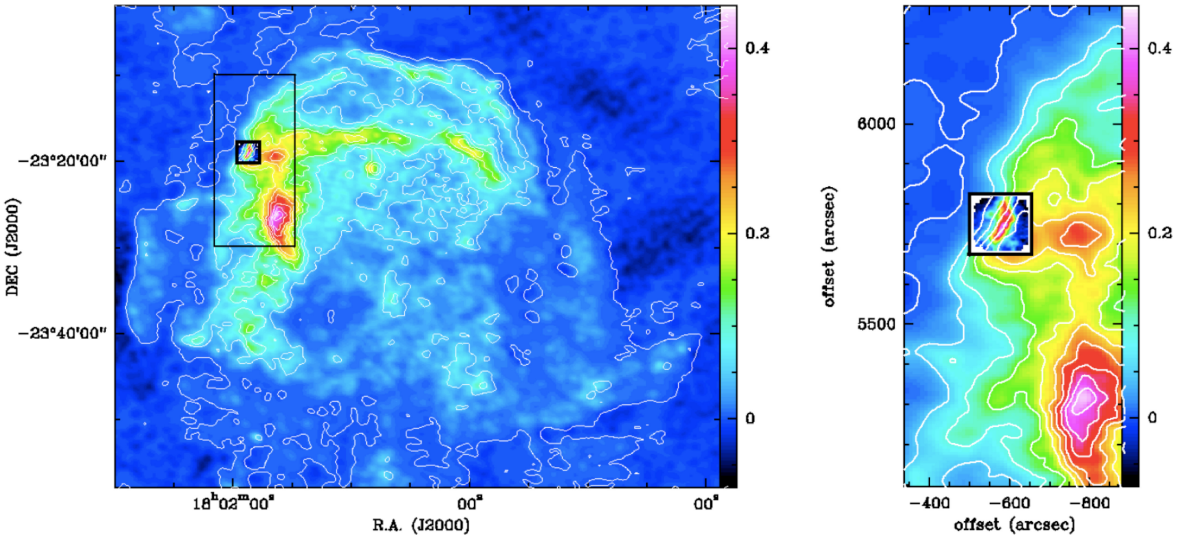

Figure 26: Location of the field covered by our CO observations on the larger-scale radio continuum image at 327 MHz taken from Claussen et al. (1997): entire SNR in the left panel, zoom in the right panel. The shown CO observations are the (6–5) map, also displayed in Fig. 23.

ANR-09-BLAN-0231-01 from the French *Agence Nationale de la Recherche* as part of the SCHISM project.

9.5 APPENDIX - THE APEX OBSERVATIONS

APEX observations towards the supernova remnant W28F were conducted in several runs in the year 2009 (in May, June, August and October). We used of a great part of the suite of heterodyne receivers available for this facility: APEX–2 Risacher et al. (2006), FLASH460 Heyminck et al. (2006), and CHAMP$^+$ Kasemann et al. (2006); Güsten et al. (2008), in combination with the MPIfR fast Fourier transform spectrometer backend (FFTS, Klein et al. 2006). The central position of all observations was set to be $\alpha_{[\mathrm{J2000}]}$=$18^h01^m51^s.78$, $\beta_{[\mathrm{J2000}]}$=$-23°18'58''50$. Focus was checked at the beginning of each observing session, after sunrise and/or sunset on Mars, or on Jupiter. Line and continuum pointing was locally checked on RAFGL1922, G10.47B1, NGC6334-I or SgrB2(N). The pointing accuracy was found to be of the order of 5″ r.m.s., regardless of the receiver that was used. Table 20 contains the main characteristics of the observed lines and corresponding observing set-ups: frequency, beam size, sampling, used receiver, observing days, forward and beam efficiency, system temperature, spectral resolution, and finally the velocity interval that was used to generate the integrated intensity maps. The observations were performed in position-switching/raster mode using the APECS software Muders et al. (2006). The data were reduced with the CLASS software[5]. For all observations, the maximum number of channels available in the backend was used (8192), except for CO (4–3), for which only 2048 channels were used, leading to the spectral resolutions indicated in Table 20. Maps were obtained for all considered transitions, covering the field introduced in Fig. 23 and put in the perspective of the whole SNR in Fig. 26.

5 see `http://www.iram.fr/IRAMFR/GILDAS`

Table 20: Observed lines and corresponding telescope parameters for the APEX observations of W28F.

line	CO (3–2)	CO (4–3)	CO (6–5)	CO (7–6)	^{13}CO (3–2)
ν (GHz)	345.796	461.041	691.473	806.652	330.588
FWHM ($''$)	18.1	13.5	9.0	7.7	18.9
sampling ($''$)	10	7	4	4	10
receiver	HET345	FLASH460	CHAMP$^+$	CHAMP$^+$	HET345
observing days	04-05/08	04/06	13-14-15/08	13-14-15/08	05-06-07/08
$F_{\rm eff}$	0.97	0.95	0.95	0.95	0.97
$B_{\rm eff}$	0.73	0.60	0.52	0.49	0.73
$T_{\rm sys}$ (K)	279–288	372–439	1330–1722	3524–5850	357–377
Δv (km s^{-1})	0.106	0.318	0.079	0.068	0.166
reference offset ($''$)	(-100,-50)	(-120,0)	(-100,-50)	(-100,-50)	(-100,-50)
v interval (km s^{-1})	-30/40	-30/40	-30/40	-10/25	-30/40

9.6 APPENDIX - THE H_2 OBSERVATIONS

9.6.1 *The dataset*

As a consistency check for our models, we used of the *Spitzer*/IRS observations of the H_2 pure rotational transitions (0–0 S(0) up to S(7)), reported and analysed in N07 and Y11. Although the original dataset also includes other ionised species, we chose to use only the H_2 data. The raw product communicated to us by David Neufeld contains rotational transitions maps, with 1.2$''$ per pixel, centred on $\alpha_{[\rm J2000]}$=18^{h}01^{m}52^s.32, $\beta_{[\rm J2000]}$=−23°19′24″92. Fig. 27 shows an overlay of our APEX CO (6–5) map with the H_2 0–0 S(5) region observed by *Spitzer*. The figure shows coinciding maxima between the two datasets in the selected position, and a slightly different emission distribution. This might be the effect of the better spatial resolution of the H_2 data, which reveal more peaks than in CO. This overlay also shows the slightly different morphology of the emission of the S(2) (half maximum contour in black) and S(5) (half maximum contour in green) transitions, at the available resolution.

9.6.2 *Excitation diagram*

We performed a consistency check on our modelling (see Sect. 9.4) using the excitation diagram derived for the selected emission region. The H_2 excitation diagram displays $\ln(N_{vj}/g_j)$ as a function of $E_{vj}/k_{\rm B}$, where N_{vj} (cm^{-2}) is the column density of the rovibrational level (v, J), $E_{vj}/k_{\rm B}$ is its excitation energy (in K), and $g_j = (2j+1)(2I+1)$ its statistical weight (with $I = 1$ and $I = 0$ in the respective cases of ortho- and para-H_2). If the gas is thermalised at a single temperature, all points in the diagram fall on a straight line. The selected position for the present study was introduced in Sect. 9.3.1, and can be seen in Figs. 23 and 27. The column density of the higher level of each considered transition was extracted by averaging the line intensities in a 11.85$''$ radius circular region, consistent with our handling of the CO data. In the process, we corrected the line intensities for extinction, adopting the visual extinction values from N07, $A_v = 3-4$, and using the interstellar extinction law of Rieke & Lebofsky (1985). The resulting excitation diagram can be seen in Fig. 28.

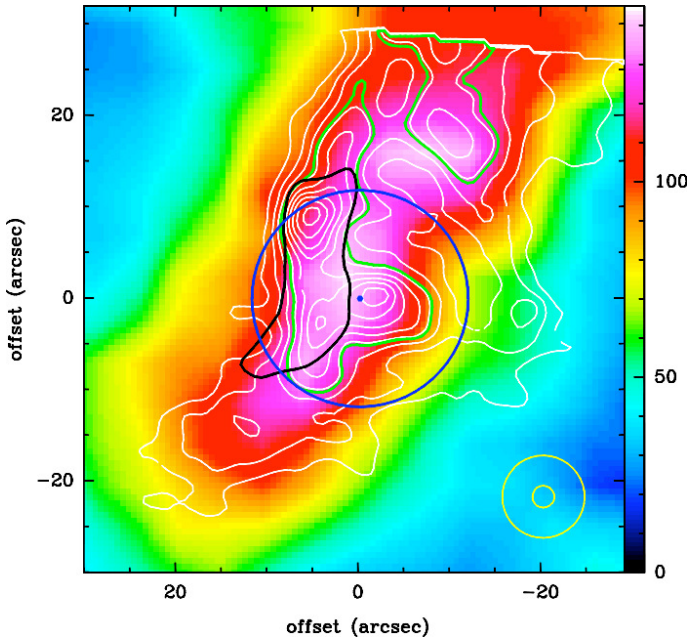

Figure 27: Overlay of the map of CO (6–5) emission observed by the APEX telescope (colour background) with the H_2 0–0 S(5) emission (white contours), observed with the *Spitzer* telescope. The wedge unit is K km s^{-1} (antenna temperature) and refers to the CO observations. The H_2 0–0 S(5) contours are from 50 to 210 σ, in steps of $20\sigma \simeq 1.6 \times 10^{-4}$ erg cm^{-2} s^{-1} sr^{-1}. The green contour defines the half-maximum contour of this transition. Like in Fig. 23, the blue circle indicates the beam size of the SOFIA/GREAT observations, on the position of the centre of the circle, marked by a blue dot. The beam and pixel sizes of the CO (6–5), and H_2 0–0 S(5) observations are also provided in yellow (big and small, respectively) circles in the lower right corner. The black contour delineates the half-maximum contour of the H_2 0–0 S(2) transition. The field is smaller than in Fig. 23, and the (0,0) position is that of the *Spitzer* observations (see Appendix 9.6).

We note that the intensity of the H_2 0–0 S(6) transition ($J = 8$) cannot be determined reliably, because the line is blended with a strong 6.2 μm PAH feature.

9.6.3 *Comparisons with our models*

Unlike our CO observations, the *Spitzer*/IRS observations are not spectrally resolved (owing to the relatively low resolving power of the short low module in the range 60–130). On the other hand, given the minimum energy of the levels excited in the H_2 transitions (for 0–0 S(0), $E_u \sim 509.9$ K), we can make the double assumption that the lines are not contaminated by ambient emission or self-absorption, and that the measured line intensities are the result from the blue- and red-shock present in the line of sight. Therefore, one must compare the observed H_2 level populations to what is generated by the sum of our best-fitting blue- and red- shock models. Fig. 28 shows the comparison between the excitation diagram derived from the sum of our two CO best-fitting models and the observed one. The H_2 excitation diagram comprising the sum of our CO best-fitting models is shown in both panels in red circles, and provides a satisfying fit to the observations. With the aim of improving the quality of this fit, we also studied the influence of the initial ortho-to-para ratio (OPR) value, upper panel, and of the cosmic ray ionisation rate value, lower panel.

In the upper panel, for a cosmic ray ionisation rate value adopted as the solar one, $\zeta_1 = 5 \times 10^{-17}$ s^{-1}, the influence of the initial OPR value is studied. In their models, N07 inferred a value of 0.93 for the 'warm' component (~322 K). On the other hand, the value associated to their 'hot' (~1040 K) component could not be estimated, owing to the large uncertainty associated to the determination of the H_2 0–0 S(6) flux. In our shock models, the OPR value is consistently calculated at each point of the shocked layer, and is mostly the result of conversion reactions between H_2 and H, H^+ or H_3^+. The heating associated to the passage of the wave increases the OPR value towards the equilibrium value of 3.0. Nevertheless, this value is reached only when it is also the initial one. The N07 situation is then probably adequately approximated in our models where the OPR initial value is less than 3. However, the influence of this parameter is minimal on the excitation diagram, where it only seems to create a slight saw-tooth pattern between the odd and even values of J.

We finally investigated the effects of the high-energy radiation field on the excitation diagram in the lower panel of Fig. 28. The limits of our modelling are reached because the only handle that we have to study this effect on our outputs is the variation of the cosmic ray ionisation rate value, which affects the corresponding chemistry (higher ionisation fraction) and physics (warmer gas). A proper treatment of the energetic radiation components listed in Hewitt et al. (2009) should indeed incorporate UV pumping or self-shielding, as would be the case in PDR regions (e.g., Habart et al. 2011), as well as chemical and H_2 excitation effects by X-ray (see Dalgarno et al. 1999) and cosmic rays (e.g., Ferland et al. 2008). Keeping these limits in mind, we found that even strong modifications of the cosmic ray ionisation rate from the solar value of $5{\times}10^{-17}$ s^{-1} to the more extreme value of 10^{-14} s^{-1} have only very limited effects on the excitation diagram. The rather convincing fits to the H_2 data seem to indicate that these excitation effects by energetic photons could well be minimal in our case, but we repeat that their proper inclusion to our models is work in progress.

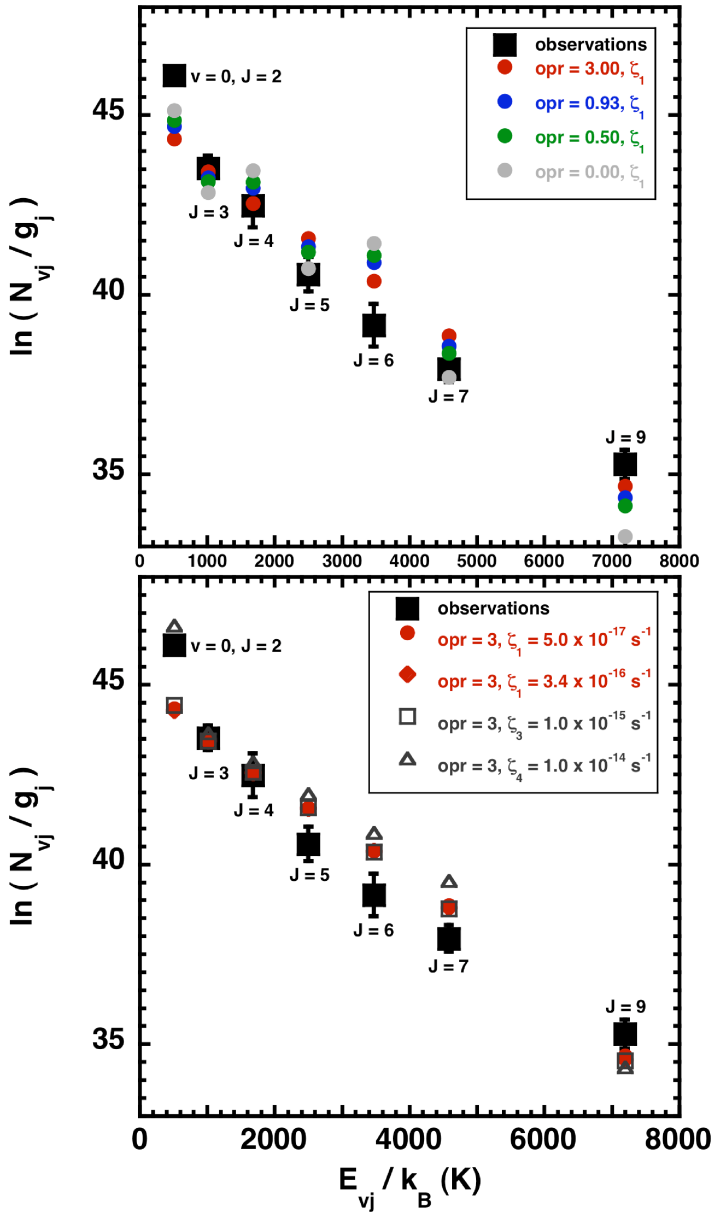

Figure 28: H_2 excitation diagram comparisons. *Upper panel:* Evolution of the modelled excitation diagram obtained for $\zeta_1 = 5 \times 10^{-17}$ s^{-1}, varying the initial value of the OPR from the unrealistic, extreme-case 0 value to its equilibrium one, 3. *Lower panel:* Influence of the cosmic ray ionisation rate variation on our modelled excitation diagram, with the initial OPR set to 3.

10

SUMMARY

Supernova remnants send shock waves through the interstellar medium that can eventually interact with molecular clouds, driving lower-velocity shocks into the cloud interior. In the previous chapter, we have presented new CO observations with the APEX and SOFIA telescopes from shocked gas in the so-called F knot region of the supernova remnant W28. The SOFIA CO (11–10) spectrum was obtained as one of the first observations with the GREAT spectrometer onboard SOFIA. The integrated intensities of CO (3–2), (4–3), (6–5), (7–6), and (11–10) were extracted at the most prominent position of the observed region and compared to a large grid of 1-dimensional, plane-parallel shock models, using a χ^2 routine. The grid consists of stationary C- and J-type and non-stationary CJ-type shocks, covering four preshock densities (from 10^3 to 10^6 cm^{-3}), a range of magnetic field strengths ($0.45 \leq b \leq 2$), and velocities spanning from 5 km s^{-1} up to the maximum, 'critical' velocity for C-type shocks, and from 10 up to 100 km s^{-1} for J-type shocks. The independent χ^2-fits of the observed blue- and red-shifted shock components were based on the purest shock-tracing lines: CO (6–5), (7–6), and (11–10).

We found that only C-type shock models can reproduce the levels of the observed CO integrated intensities. For both wings, the obtained preshock density is 10^4 cm^{-3}, the modelled shock velocities are 25 (blue lobe) and 20 km s^{-1} (red lobe), and the magnetic field component perpendicular to the shock layers is constrained with parameters b of 1 and 0.45. These values are consistent with previous estimates of the conditions in this region. However, our shock models failed to account for the emission of CO (3–2) and (4–3). In order to compensate for expected emission of non-shocked gas in these transitions, we added a thin layer of gas to our shock modelling results, calculated with our LVG module in a 'homogeneous slab' mode. The line width of this gas was set as 10 km s^{-1}, the density as 10^4 cm^{-3} and the fractional abundance of X(CO) as 10^{-4}. The CO layer found to compensate for the missing emission in the lowest transitions is warm (35 K and 15 K for the blue and the red components, respectively) with CO column densities of $\sim 10^{17}$ cm^{-2}. From our best-fitting models, we also derived predictions for the integrated intensities of H_2 pure rotational transitions (0-0 S(0) up to S(7)). These predictions were compared with Spitzer/IRS observations. This consistency check yielded a satisfying fit between predictions and observations. We also studied the influence of the initial ortho-to-para ratio and of the cosmic ray ionisation rate value. Both parameters were found to have only minimal influence on the H_2 excitation diagram.

11

INTRODUCTION

The supernova remnant W44 is similar to W28 in a few respects. Both remnants are bright radio sources and paradigmatic cases of the "mixed-morphology" class of SNRs. They are both located in close vicinity to molecular clouds at similar distances of ~3 and ~2 kpc and give rise to an SNR-cloud interaction. Studies on shocked molecular gas in SNRs have often been accomplished for these both remnants together (e.g. Reach et al. 2005; Claussen et al. 1999). So, after the restricted pilot study of probing MHD shocks with high-J CO observations in W28F where the main focus lay on the presentation of the SOFIA CO (11-10) spectrum, it appeared natural to conduct a more detailed study of molecular shock conditions in W44. This second study extends and refines the methods established in the previous chapter, particularly with respect to the extraction of integrated intensities and the error estimation procedure. The observed regions in W44 correspond to regions E and F as designated in Claussen et al. (1997) where OH maser emission confirms the presence of shock interaction. As no H_2 observations were at hand for the regions studied, the shock analysis was solely based on CO emission. The most remarkable result is that the observations are compatible with non-stationary shocks, which seems very plausible given the time of 10^4 years typically needed for a C-type shock to become stationary. This result appears to be robust with respect to modelling degeneracies.

APEX OBSERVATIONS OF SUPERNOVA REMNANTS - I. NON-STATIONARY MAGNETOHYDRODYNAMIC SHOCKS IN W44[1]

12.1 ABSTRACT

Context: When supernova blast waves interact with nearby molecular clouds, they send slower shocks into these clouds. The resulting interaction regions provide excellent environments for the use of MHD shock models to constrain the physical and chemical conditions in these regions.
Aims: The interaction of supernova remnants (SNRs) with molecular clouds gives rise to strong molecular emission in the far-IR and sub-mm wavelength regimes. The application of MHD shock models in the interpretation of this line emission can yield valuable information on the environmental impact of supernova remnants.
Methods: New mapping observations with the APEX telescope in ^{12}CO (3–2), (4–3), (6–5), (7–6) and ^{13}CO (3–2) towards two regions in the supernova remnant W44 are presented. Integrated intensities are extracted on five different positions, corresponding to local maxima of CO emission. The integrated intensities are compared to the outputs of a grid of models, which combine a magnetohydrodynamic (MHD) shock code with a radiative transfer module based on the 'large velocity gradient' approximation.
Results: The shock model fits were based only on the highest-lying transitions that unambiguously trace the shock-heated gas. We find that the observed CO line emission is compatible with non-stationary shocks and a preshock density of 10^4 cm^{-3}. The ages of the modelled shocks scatter between values of ∼1000 and ∼3000 years. The shock velocities in W44F are found to lie between 20 and 25 km s^{-1}, while in W44E fast shocks (30–35 km s^{-1}) as well as slower shocks (∼20 km s^{-1}) are compatible with the observed spectral line energy diagrams. The magnetic field strength components perpendicular to the line-of-sight in both regions have values between 100 and 200 μG. Our best-fitting models allow us to predict the water emission of these shocks, the full ladder of CO transitions, and the contribution of such SNRS to, e.g., the galactic energy balance and the momentum-injection into the surrounding interstellar medium.

12.2 INTRODUCTION

Supernova explosions strongly affect the dynamical state of the interstellar medium (ISM). These explosions represent an injection of about 10^{51} erg into the ISM, immediately creating regions of very hot and tenuous gas (e.g. Cox 2005). The shock waves originating from these explosions disperse molecular clouds, sweep up, and compress the ambient medium (McKee & Cowie 1977). The evolution of the supernova remnant (SNR) can be described by four successive phases (Woltjer 1972): a free expansion phase, where the density of the ejected matter is much larger than that of the surround-

1 This chapter will be submitted to A&A as Anderl, S., Gusdorf, A., & Güsten, R., (2013).

ing medium, a phase of adiabatic expansion, where the gas is too hot to undergo efficient radiative cooling, a radiative phase, where a dense, radiatively cooling shell of swept up gas is formed, and finally a fade-away phase, when the shock wave has slowed down so much that it has turned into a sound wave.

If the supernova blast wave encounters ambient molecular clouds, it drives slower shocks into these clouds at a velocity that relates to the shock velocity in the intercloud medium via the density contrast between cloud- and intercloud gas (McKee & Cowie 1975). These slow shocks are similar to shocks originating in bipolar outflows of very young stars (e.g. Gusdorf et al. 2011): they strongly cool through molecular emission and can be observed in the far-IR and sub-mm wavelength regime (e.g. Frail & Mitchell 1998; Neufeld et al. 2007). Clear evidence for an interaction between a SNR and molecular clouds is typically provided by the detection of broad line wings, maser emission, highly excited far-IR CO and near- and mid-infrared H_2 emission (Reach et al. 2005). However, the modelling of these shocks differs from that of their star-forming counterparts because they are not irradiated by an embedded proto-star and they do not show any envelope or infall processes. The study of these interactions between SNRs and molecular clouds can yield valuable information on the supernova explosion and its impact on the surrounding medium. At the same time, it can improve our understanding of the molecular clouds themselves. This information is needed for the understanding of various astrophysical questions, such as the energy balance of galaxies, triggered star formation, and the origin and acceleration of cosmic rays.

High-J CO line emission is a very good diagnostic in this context because of the high abundance of CO in the molecular ISM, its important role for the cooling of the medium, and the fact that its rotational transitions between higher energy levels are expected to trace shock conditions (e.g. Flower & Pineau des Forêts 2010; Meijerink et al. 2013). Here, we present new APEX CO observations towards two regions in one of the prototype of interacting SNRs, W44, which has been the subject of many observational studies. We find MHD models compatible with our observations of CO emission and explore the consequences of the corresponding shock scenarios with respect to the impact of the SNR on its environment.

This paper builds on our previous study of MHD shocks based on high-J CO observations towards the SNR W28 (Gusdorf et al. 2012) but refines and extends the methods established there. The structure of the paper is as follows. In Sect. 12.3 we give a short review of the supernova remnant W44. In Sect. 12.4, we present our observations together with more detailed information on the observed regions W44E and W44F. Section 12.5 provides information on the molecular environment of W44. In Sect. 12.6, we show the CO maps observed towards both regions, while Sect. 12.7 focuses on the observed spectra towards the positions of our shock analysis. Our modelling approach with respect to the processing of observations and the grid of models is described in Sect. 12.8. In Sect. 12.9, the results are presented and discussed in Sect. 12.10. We summarize our findings in the concluding Sect. 12.11.

12.3 THE SUPERNOVA REMNANT W44

W44 (a.k.a. G34.7–0.4, or 3C 392) is a prototype of the so-called "mixed-morphology" supernova remnant as described by Rho & Petre (1998). This class refers to SNRs with centrally concentrated

X-ray emission and a shell-like radio morphology. The size of this semi-symmetric SNR is about 30′ (Rho & Petre 1998). It is probably located in the Sagittarius arm (Castelletti et al. 2007) at the base of the Aquila supershell (Maciejewski et al. 1996) in a very obscured, complex region in the Galactic plane. Its distance has been estimated on the basis of H I 21 cm absorption measurements as ∼3 kpc (Radhakrishnan et al. 1972; Caswell et al. 1975; Green 1989) and confirmed as 2.9 ± 0.2 kpc through molecular observations using the solar constants $R_0 = 7.6$ kpc and $\Omega_0 = 27.2$ km s^{-1} kpc^{-1} (Castelletti et al. 2007). In this paper, we use the distance value of 3 kpc as, e.g., Seta et al. (2004), Paron et al. (2009), and Abdo et al. (2010). Based on this distance, the SNR's size of ∼30′ corresponds to ∼26 pc. W44 is believed to be in a radiative phase over much of its surface due to its estimated age of $2{\times}10^4$ years (see below) and the observed cooling radiation (Cox et al. 1999; Chevalier 1999).

As first reported by Wolszczan et al. (1991), this type II SNR harbours a fast-moving 267 millisecond radio pulsar, PSR B1853+01, within the W44 radio shell, about 9′ south from its geometrical centre. Its progenitor is assumed to have had little influence on the parental molecular cloud on the scale of the SNR (Reach et al. 2005). The pulsar's spin-down age amounts to $2{\times}10^4$ years, while its distance, derived from the dispersion measure, is consistent with that of the SNR (Taylor & Cordes 1993). The pulsar wind powers a small synchrotron nebula observed in radio (Frail et al. 1996) and X-ray emission (Harrus et al. 1996; Petre et al. 2002).

W44 was first detected as a radio source already in the late 50's (Westerhout 1958; Mills et al. 1958; Edge et al. 1959) and identified as a possible SNR due to its non-thermal radio spectrum (Scheuer 1963). The shell-type shape in radio-continuum maps appears northeast-southwest elongated, with a size of 25′ × 35′ at 1442.5 MHz (Giacani et al. 1997) and enhanced radio emission at the eastern portion of the SNR. A high resolution VLA radio image at 1465 MHz, observed by Jones et al. (1993), reveals several filaments across the remnant and distortions along its eastern border. A plausible explanation for this feature could be the expansion of the SNR into a cloudy interstellar medium, as already suggested by Velusamy (1988). Polarization measurements at 2.8 cm, conducted by Kundu & Velusamy (1972), show a high degree of polarization as large as 20%, possibly due to a highly regular oriented magnetic field, particularly over the main eastern and northern parts of the SNR. Based on earlier measurements between 22 and 10700 MHz and new observations at 74 and 324 MHz Castelletti et al. (2007) derived a global integrated continuum spectral index of −0.37± 0.02.

H I observations reveal a fast, expanding, shell-like structure at $v_{\rm LSR} = 125$ and 210 km s^{-1} associated with the SNR, corresponding to an expansion velocity of the H I shell of $v_{\rm exp} = 150 \pm 15$ km s^{-1} (Koo & Heiles 1995). These authors estimated the H I shell as being significantly smaller than the radio continuum shell. They interpreted this double-shell structure as originating from the supernova exploding inside a pre-existing wind bubble, whose shell constitutes the observed H I structure. Shelton et al. (1999) used a hydrocode model for W44 to show that this interpretation is not compelling if the remnant evolution is taking place in a density gradient, which leads to a spread in shell formation times for different parts of the remnant's surface. While Shelton et al. (1999) assumed the ISM to be denser on the northeastern, far side of the SNR, Seta et al. (2004) expected the strongest interaction between the SNR and the ISM to occur in the front side of the SNR, while it is the redshifted side that is visible as high-velocity expanding H I shell. This conclusion was based on observed OH absorption in their component of spatially extended moderately broad emission.

The centrally peaked X-ray morphology was first noted in observations from the Einstein Observatory Image Proportional Counter (IPC) (Watson et al. 1983; Smith et al. 1985). Assuming the X-ray emission to be thermal (Szymkowiak 1980; Jones et al. 1993), the morphology of the emission was explained by a scenario where a possible X-ray shell is unseen because it has become too cold to be detected through the intervening ISM (Smith et al. 1985; Jones et al. 1993). Observations with the ROSAT Position Sensitive Proportional Counters (PSPC) (Rho et al. 1994) confirmed the centrally peaked X-ray morphology and revealed a largely uniform temperature over the remnant. Jones et al. (1993) as well as Rho et al. (1994) interpreted this observation using an evaporation model with a two-phase interstellar medium structure of clump and interclump gas (White & Long 1991), where the material stemming from evaporating clouds increases the density of the SNR interior. More recent models stressed the important role of thermal conduction in the creation of the centrally peaked X-ray emission (Cox et al. 1999; Kawasaki et al. 2005). Thermal conduction levels out gradients of temperature in the hot interior plasma while pressure equilibrium then yields a higher density at the centre. Once the forward shock velocity has decreased such that the X-ray emission from the shell becomes too soft to pass through the ISM, the centrally brightened X-ray emission appears.

Probably due to the interaction between the SNR and a molecular cloud, the eastern limb shows a lack of X-ray emission within the radio shell, while weaker diffuse X-ray emission extends up to the northern radio boundary of W44 (Giacani et al. 1997). The existence of a non-thermal X-ray component was shown by Harrus et al. (1996) when they detected a hard X-ray source coincident with the position of the pulsar region interpreted as an X-ray synchrotron nebula.

The first detection of optical filaments in Hα and [S II] images of W44, seen in the north and southeast parts, was reported by Rho et al. (1994). These filaments are mainly confined within the X-ray emitting region and are absent in the eastern region. Along the northwest border of the remnant, there is excellent correlation between optical and radio emission at 1.4 GHz, suggesting that radiative cooling of the shocked gas immediately behind the shock front, where enhanced magnetic fields are present, is the origin of the optical radiation (Giacani et al. 1997).

The association of molecular gas with W44 was already reported by Dickel et al. (1976), who attributed the flattened shell structure of the SNR to an encounter with a dense molecular cloud. Wootten (1977) observed a broadening of line widths and an intensification of line strength in CO (1–0), which he explained by the heating and compression of the ISM by the SNR. Denoyer (1983) questioned the shock processing of the adjacent molecular cloud, referring to an absence of chemical shock characteristics and the possible explanation of broadened lines by overlapping line components along the line-of-sight. However, subsequent observations of emission from shock-tracing molecules and fine-structure line emission (Reach & Rho 1996; Seta et al. 1998; Reach & Rho 2000; Reach et al. 2005; Neufeld et al. 2007; Yuan & Neufeld 2011) as well as OH maser emission (Claussen et al. 1997; Hoffman et al. 2005) have removed doubts about the existence of an interaction with a molecular cloud.

Finally, W44 is an important site for the study of cosmic-ray production, acceleration, and propagation based on the observations of γ-rays stemming from the interaction of cosmic-rays and the interstellar medium. These interactions include high-energy electron bremsstrahlung and inverse Compton scattering of the leptonic cosmic-ray component as well as proton-proton collisions of the hadronic component creating neutral pions, whose decay generates γ-rays. A first detection in the GeV regime

Table 21: Observed lines, associated frequencies, beam sizes, sampling, and forward efficiencies.

line	CO (3–2)	CO (4–3)	CO (6–5)	CO (7–6)	^{13}CO (3–2)
ν (GHz)	345.796	461.041	691.473	806.652	330.588
FWHM ($''$)	18.05	13.54	9.02	7.74	18.88
sampling ($''$)	10	7	4	4	10
$F_{\rm eff}$	0.97	0.95	0.95	0.95	0.97

was achieved with the EGRET instrument aboard the Compton Gamma Ray Observatory, although an association with W44 was not clear (Esposito et al. 1996). The Fermi Large Area Telescope (LAT) detected a source morphology corresponding to the SNR radio-shell at energies above 200 MeV (Abdo et al. 2010). Modelling the observed emission, these authors concluded that neutral pion decays are plausibly responsible for the emission, although a bremsstrahlung scenario could not be ruled out completely. Giuliani et al. (2011) subsequently excluded leptonic emission as the main contribution based on observations at lower energies (30MeV – 50 GeV) using the AGILE instrument. They reported direct evidence for pion emission based on a steep decline of the spectral energy distribution below 1 GeV. Ackermann et al. (2013) presented observations in the sub-GeV part of the γ-ray spectrum, obtained within 4 years with the Fermi LAT, from the compact regions delineated by the radio continuum emission. Based on the observation of the characteristic pion-decay feature in their spectrum ("pion-decay bump") they could finally provide direct evidence for the acceleration of cosmic-ray protons.

12.4 OBSERVATIONS

In this Section, we introduce the observed regions, W44E and W44F, and present our observations of CO and ^{13}CO species performed with the Atacama Pathfinder EXperiment (APEX[2] telescope, Güsten et al. 2006). In Table 21, we provide observing characteristics associated to each observed line (frequencies, beam sizes, corresponding sampling, and forward efficiencies).

12.4.1 *W44E*

12.4.1.1 *Region*

As displayed in Fig. 29, W44E lies in the northeastern flattened part of the radio shell, where the SNR is interacting with the densest part of the molecular cloud (Wootten 1977). Eastern of this region, Seta et al. (2004) located an "Edge" in CO (1–0) emission, where the CO intensity drops by a factor of $\sim$2 and the emission lines are broadened and velocity-shifted with respect to the emission outside the SNR. They attribute this morphological feature to the interaction of the SNR with a clumpy molecular cloud, referring to the model of Chevalier (1999) where a radiative shell formed in the diffuse interclump gas drives slow molecular shocks into the clumps. The interaction between the

2 This publication is based on data acquired with the Atacama Pathfinder EXperiment (APEX). APEX is a collaboration between the Max-Planck-Institut für Radioastronomie, the European Southern Observatory, and the Onsala Space Observatory.

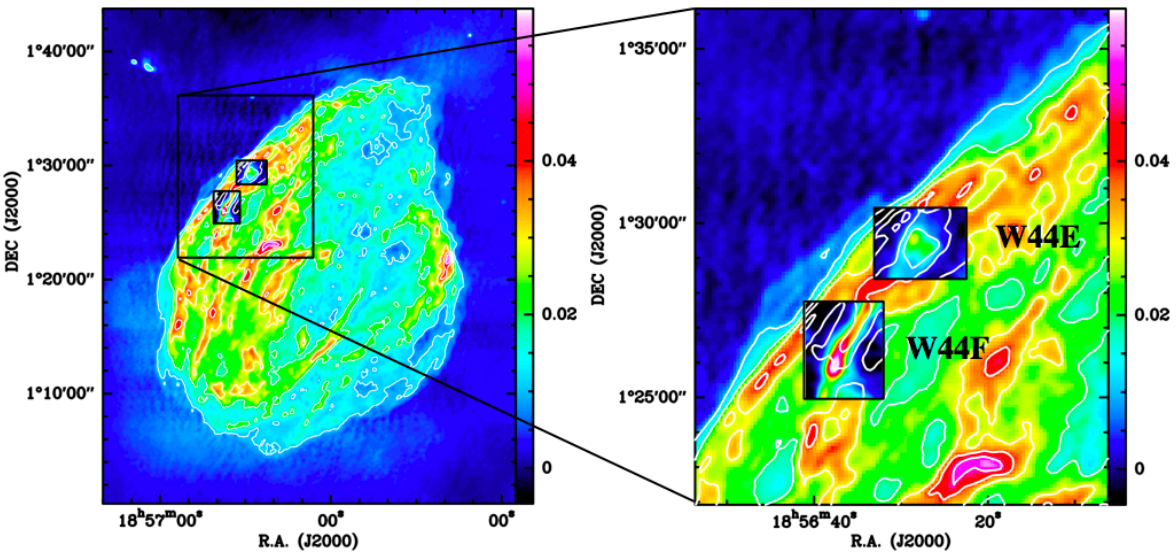

Figure 29: Location of the fields covered by our CO observations on the larger-scale radio continuum image at 1442.5 MHz, taken from Giacani et al. (1997). The wedges indicate the intensity of the continuum in Jy/beam. Left panel: entire SNR, right panel: zoom in the regions W44E and W44F. The shown CO observations are the (6–5) maps, integrated between 20 km s^{-1} and 70 km s^{-1}, for which the colourscale is in the range 0–50 K km s^{-1}, and the contours are radio continuum in steps of 10 mJy. The size of the zoombox is 10.3 × 12.4 pc.

giant molecular cloud and the SNR is believed to take place on the front side of the remnant where no OH absorption is detected. The drop in molecular column density is then attributed to dissociation of molecules and evaporation of molecular mass. Seta et al. (2004) did not detect wing emission towards W44E in CO (1–0), defined as lines with full velocity widths greater than 25 km s^{-1}. This is expected, though, given the excitation conditions found in shocks. Wing emission was detected in CO (3–2) by Frail & Mitchell (1998) and in CO (2–1) by Reach & Rho (2000) and Reach et al. (2005). Both lines show a narrow component, tracing the unshocked gas also visible in ^{13}CO (FWHM ∼ 5 km s^{-1}, centred at ∼ 45 km s^{-1}), and a broad component (FWHM ∼ 30 km s^{-1}) tracing the shocked gas. Combining these observations with infrared spectroscopy, Reach & Rho (2000) concluded to the existence of different shocks into moderate (∼10^2 cm^{-3}) and high-density (∼10^4 cm^{-3}) environments. In that picture, bright H_2 emission together with emission of CO requires higher density gas residing in clumps that survived the initial blast wave. In a similar manner, Neufeld et al. (2007) identified five different groups of emission features towards W44E, classified on the basis of their spatial distribution. The pure rotational lines of H_2 ($J > 2$), together with lines of S, constituted one of these groups, likely originating in molecular material subject to a slow, non-dissociative shock.

In addition to the broad CO line emission, the observed H_2 emission, and atomic fine structure lines, the existence of OH maser emission constitutes another strong indication of an interaction between the SNR and a molecular cloud. Claussen et al. (1997) detected ten OH maser features at 1720 MHz in W44E, two of them were shown to have multiple angular components (Hoffman et al. 2005). The masers appear along the continuum edges of the synchrotron emission. Claussen et al. (1997) interpreted this region of enhanced synchrotron emission as featuring particle acceleration in a shock, referring to Blandford & Eichler (1987). However, the enhancement could also be explained

without the claim of new particle acceleration, originating from the compression of the magnetic field and pre-existing relativistic electrons (Blandford & Cowie 1982; Frail & Mitchell 1998). The velocity of the masers have a low dispersion (< 1 km s^{-1}) around a mean value of $v_{LSR} = 44.7$ km s^{-1}, which agrees very well with the systemic velocity of W44 of $v_{LSR} = 45$ km s^{-1}. The explanation for this low dispersion was given in terms of tangential amplification (Frail et al. 1996): the maser emission is only seen where the acceleration of the gas is transverse to the line of sight. From the strong inversion of the OH (1720 MHz) line through collisions with H_2, possible excitation conditions can be inferred: kinetic temperatures should lie between 25 K $\leq T_k \leq$ 200 K, while the density is expected to be 10^3 $cm^{-3} \leq n_{H_2} \leq 10^5$ cm^{-3} (Elitzur 1976). Lockett et al. (1999) derived tighter physical conditions in the region, as they constrained a kinetic temperature of 50 K $\leq T_k \leq$ 125 K, a molecular hydrogen density of 10^5 cm^{-3}, and OH column densities of $\sim 10^{16}$ cm^{-2}. Frail & Mitchell (1998) presented a map in CO (3–2) towards W44E where they show that the masers delineate the forward edge of molecular gas, preferentially located nearer to the edge of the shock (as traced by the non-thermal emission) than the peak of CO. They reported a correlation between the integrated CO (3–2) maps and the radio continuum.

The line-of-sight magnetic field strength $B_{\|}$ in the region was determined by Claussen et al. (1997) to be within a factor 3 of 0.2 mG (with the expectation value of the total magnetic field given as $B = 2B_{\|}$) in all maser locations using Zeeman splitting between the right- and left-circularly polarized maser lines in OH (1720 MHz). They found the direction of the field throughout the remnant to be constant. Hoffman et al. (2005) constrained the strength of the magnetic field as ∼1 mG on the basis of MERLIN and VLBA circular polarization observations of OH maser lines. The position angle of the magnetic field based on linear polarization of the masers aligns with the direction of the shocked dense gas filament.

12.4.1.2 *Data*

Observations towards the supernova remnant W44E were conducted in one run, in July 2010. We made use of a great part of the suite of heterodyne receivers available for this facility: FLASH345[3], FLASH460 (Heyminck et al. 2006), and CHAMP$^+$ (Kasemann et al. 2006; Güsten et al. 2008), in combination with the MPIfR Fast Fourier Transform Spectrometer backend (FFTS, Klein et al. 2006), or with the newly commissioned MPIfR X-Fast Fourier Transform Spectrometer backends (XFFTS, Klein et al. 2012). The central position of all the observations was set to be ($\alpha_{[J2000]} = 18^h56^m28^s.4$, $\beta_{[J2000]} = 01°29'59.0''$). Focus was checked at the beginning of each observing session, after sunrise and/or sunset on Mars, Jupiter, or Saturn. Continuum and line pointing was locally checked on G34.26 and R-Aql. The pointing accuracy was found to be of the order of 5″ r.m.s, regardless of the receiver that was used. Table 22 contains the main characteristics of the telescope, and of the observing set-up for each observed transition: used receiver, corresponding observing days, beam efficiency, system temperature, spectral resolution, and reference position offset. The observations were performed in position-switching/raster mode using the APECS software (Muders et al. 2006). The data were reduced with the CLASS software (see http://www.iram.fr/IRAMFR/GILDAS). For all

3 This First Light APEX Submillimeter Heterodyne receiver was developed by Max Planck Institut für Radioastronomie, MPIfR, and commissioned in May 2010. In the 345 GHz band the dual-polarization receiver FLASH operates a 2SB SIS mixer provided by IRAM (Maier et al. 2005).

Table 22: Observed lines and corresponding telescope parameters–the case of W44E. [(a)]The observations were carried out with this off position, and were corrected a posteriori from its potential contamination, by means of an off spectrum on the (100,0) position taken with an off position at (-3600,0). [(b)] The observations were carried out with this off position, and were corrected a posteriori from its potential contamination, by means of an off spectrum on the (100,0) position taken with an off position at (0,-3600).

line	CO (3–2)	CO (4–3)	CO (6–5)	CO (7–6)	^{13}CO (3–2)
receiver	FLASH345	FLASH460	CHAMP$^+$	CHAMP$^+$	FLASH345
observing days	13/07	13/07	14/07	14/07	15/07
$B_{\rm eff}$	0.73	0.60	0.48	0.48	0.73
$T_{\rm sys}$ (K)	162–205	436–573	1008–1643	2404–6455	192-228
Δv (km s^{-1})	0.066	0.476	0.635	0.544	0.069
reference offset ($''$)	(0,-3600)	(0,-3600)	(100,0)^a	(100,0)^a	(100,0)^b

the observations, various channel numbers were used in the backends, ranging from 1652 (CO (6–5) and (7–6)) to 52429 (CO (3–2) and ^{13}CO (3–2)), via 2730 (for CO (4–3)), leading to the spectral resolutions indicated in Table 22.

12.4.2 *W44F*

12.4.2.1 *Region*

The W44F region lies southeastern of W44E and hosts a thin filament of gas ranging from the northwest to the southeast, aligned with the radio continuum contours (see Fig. 29). According to the radio continuum emission, the long axis of the filament seems to be parallel to the shock front. Claussen et al. (1997) detected three OH 1720 MHz masers in this region with an average velocity of 46.6 km s^{-1}. In the CO (3–2) map of Frail & Mitchell (1998) the masers border the northern CO emission peak, integrated over the red-shifted spectral wing between 49 km s^{-1} and 60 km s^{-1}. The spectrum in CO (3–2) that they observed towards W44F has a double-peak structure with peaks at 39 km s^{-1} and 50 km s^{-1}. This double-peak structure is also visible in the spectrum of CO (2–1) (Reach et al. 2005). Although this could possibly be interpreted as a superposition of two moderately broad components in the line of sight, the deep trough's alignment with the peak in the ^{13}CO (1–0) spectrum, that they also observed, reveals that it actually is broad-line emission being absorbed by cold foreground gas. The magnetic field strength was also measured in W44F using Zeeman splitting between the right- and left-circularly polarized maser lines in OH (1720 MHz) (Frail & Mitchell 1998; Hoffman et al. 2005). The results were the same as in W44E, as well as the orientation of the position angle of the magnetic field being aligned with the filament of shocked gas.

12.4.2.2 *Data*

Observations towards the region W44F were conducted in several runs in the year 2009 (in June and August), and also in July 2012 (for ^{13}CO (3–2)). The central position of all the observations was set to be $(\alpha_{[\rm J2000]} = 18^{\rm h}56^{\rm m}36^{\rm s}.9, \beta_{[\rm J2000]} = 01°26'34.6'')$. Focus was checked at the beginning of each observing session, after sunrise and/or sunset on Mars, Jupiter, or Saturn. Continuum and line pointing

Table 23: Observed lines and corresponding telescope parameters–the case of W44F. $^{(a)}$ The observations were carried out with this off position, and were corrected a posteriori from its potential contamination, by means of an off spectrum on the (90,0) position taken with an off position at (-3000,3000). $^{(b)}$ The observations were carried out with this off position, and were corrected a posteriori from its potential contamination, by means of an off spectrum on the (360,0) position taken with an off position at (0,-3600).

line	CO (3–2)	CO (4–3)	CO (6–5)	CO (7–6)	^{13}CO (3–2)
receiver	HET345	FLASH460	CHAMP$^+$	CHAMP$^+$	FLASH345
observing days	05/08	07/06	06/08	05/08	26/06/12
$B_{\rm eff}$	0.73	0.60	0.52	0.49	0.73
$T_{\rm sys}$ (K)	278–284	410–484	1350–2024	3860–6079	256-337
Δv (km s^{-1})	0.106	0.318	0.635	2.178	0.035
reference offset ($''$)	(90,0)^a	(90,0)	(120,0)	(120,0)	(360,0)^b

was locally checked on G34.26 and R-Aql. The pointing accuracy was found to be of the order of 5$''$ r.m.s, regardless of the receiver that was used. Table 23 contains the same parameters as Table 22, for observations of W44F. The observations were performed in position-switching/raster mode using the APECS software (Muders et al. 2006). The data were reduced with the CLASS software. For all the observations, the number of channels used ranged from 413 (CO (7–6) to 65536 (^{13}CO (3–2)), via 1652 (CO (6–5)), 2048 (CO (4–3)) and 8192 (CO (3–2)), leading to the spectral resolutions indicated in Table 23.

12.5 AVERAGED CO EMISSION TOWARDS W44E AND W44F

W44 is surrounded by several molecular clouds. In order to understand the CO emission towards W44E and W44F, we have averaged all spectra obtained in each mapped region respectively, after convolving them to a common spatial resolution of 18.2$''$, that of our CO (3–2) observations. These averaged spectra are shown in Fig. 30. The value for the systemic velocity of W44 that we found in the literature is 45 km s^{-1}. The peaks of our spectra agree with this value. In the averaged spectra of W44F, we detect strong absorption between ~40 km s^{-1} and ~50 km s^{-1} in all transitions up to CO (6–5), which is attributed to absorption by cold foreground gas.

Seta et al. (1998, 2004) have studied the vicinity of W44 in CO (1–0) and CO (2–1). In their earlier paper, presenting observations at low spatial resolution[4], they divided the CO emission towards W44 into three velocity components at $v_{\rm LSR}$ = 13 km s^{-1}, 30–65 km s^{-1}, and 70–90 km s^{-1}. The 13 km s^{-1} component corresponds to well-known foreground clouds in the solar neighbourhood, in earlier publications attributed to the dust cloud Khavtassi3 at 15 km s^{-1} (Knapp & Kerr 1974; Wootten 1977; Scoville et al. 1987). We detect this component clearly in CO (3–2) towards both regions, although towards W44F it is mostly seen in absorption. In both fields, this component is rather spatially uniform, although towards W44E the intensity of this feature increases in the southeastern direction.

4 Because Seta et al. (1998) were only able to separate structures larger than ~15 pc, their observations cannot differentiate between W44E and F.

The 70–90 km s^{-1} component was attributed to clouds behind W44 with an uncertain fraction of emission from accelerated gas from W44[5]. The integrated spectrum in CO (3–2) towards W44E shows a weak peak at 78 km s^{-1} that might corresponds to cloud 10 (CO G34.7–0.1, v=78 km s^{-1}) in the labelling of Seta et al. (1998), although the spatial distribution of the emission is difficult to disentangle from highly red-shifted shocked gas. Towards W44F, we notice a broad emission feature in the velocity regime between 70 and 90 km s^{-1} in CO (3–2), peaking at 72 km s^{-1}, together with a narrow peak at 86 km s^{-1} that is also seen in absorption in CO (4–3). Both features appear spatially uniform over the observed field.

The 30–65 km s^{-1} component is considered to be associated with W44. Towards W44E, this central component appears even broader in our data (15–70 km s^{-1}), and also towards W44F the wings seem to stretch further. Seta et al. (1998) identified six molecular clouds in this velocity range, three of which are candidates for an interaction (given their spatial coincidence with the SNR and similar estimated radial velocities) and one that is probably interacting with W44 (G34.8–0.6, v=48 km s^{-1}), showing increased line widths and an abrupt shift in radial velocity at the rim of the SNR. At 54 km s^{-1}, we detect another emission peak towards W44E, which could correspond to the absorption dip towards W44F at 54.5 km s^{-1}. The emission at this velocity is strongly spatially varying. Its intensity increases towards the south of W44E, where it becomes comparable in intensity to the main peak. The origin might be a confined clump of material moving within the molecular cloud.

12.6 CO MAPS

12.6.1 *CO maps towards W44E*

Figure 31 shows maps of integrated CO emission in CO (6–5) with contours of integrated CO (3–2), (4–3), and (7–6) (respectively 1st, 2nd, and 3rd column) emission overlayed towards W44E, for the blue wing (top row, 20–40 km s^{-1}), the red wing (bottom row, 50–70 km s^{-1}) and the ambient velocity regime (central row, 40–50 km s^{-1}). The positions of OH masers detected towards W44E are also displayed. The lower integration boundary of the blue wing of 20 km s^{-1} was chosen to avoid the contribution of the foreground cloud at ∼13 km s^{-1} in CO (3–2). Similarly, we chose the upper integration boundary of the red wing as 70 km s^{-1} because at higher velocities the contribution of red-shifted gas related to W44 and background cloud emission reported by Seta et al. (1998) is difficult to disentangle.

The emission distribution peaks in all CO maps behind the line of masers, which trace the shock front moving eastward into the ambient molecular gas (Claussen et al. 1997). However, for the wing emission in CO (7–6) this is only true for the maps convolved to the angular resolution of the CO (3–2) map (not shown here), while at its original resolution the noise in the map prevents a clear statement. The eastern peak exhibits strong wings towards higher and lower velocities relative to the systemic velocity of W44. There is another emission peak towards the interior of W44 close to the second masering region, distinct from the delineated masers to the east. This peak is mostly seen in

5 Wootten (1977) notes that there are no molecular absorption features in this velocity regime. Therefore, he concludes that the emitting gas is situated beyond the remnant.

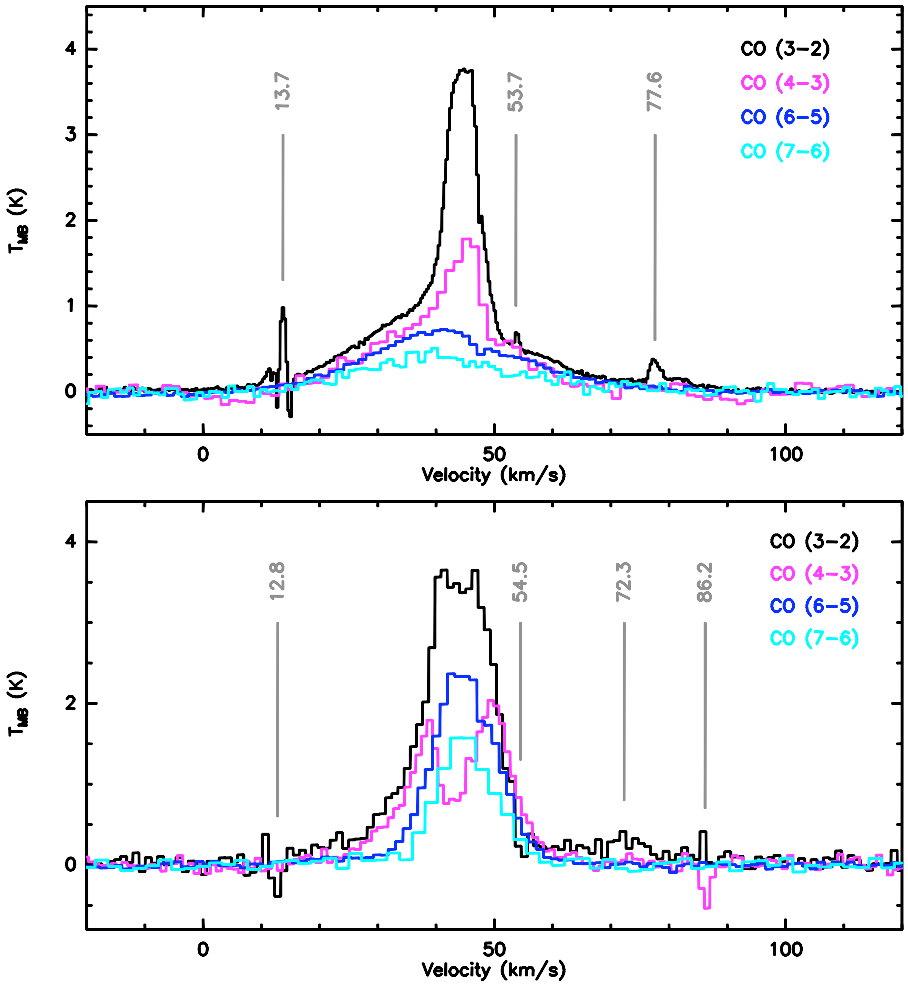

Figure 30: CO spectra (in $T_{\rm MB}$) averaged over the W44E (top) and W44F (bottom) regions. The spectra correspond to the transitions of CO (3–2) (black), CO (4–3) (pink), CO (6–5) (blue), and CO (7–6) (light blue). Respective CO spectral resolutions are 0.33, 1.43, 1.27, and 1.09 km s^{-1}, respectively, in W44E and 1.06, 0.95, 1.27, and 2.18 km s^{-1} in W44F.

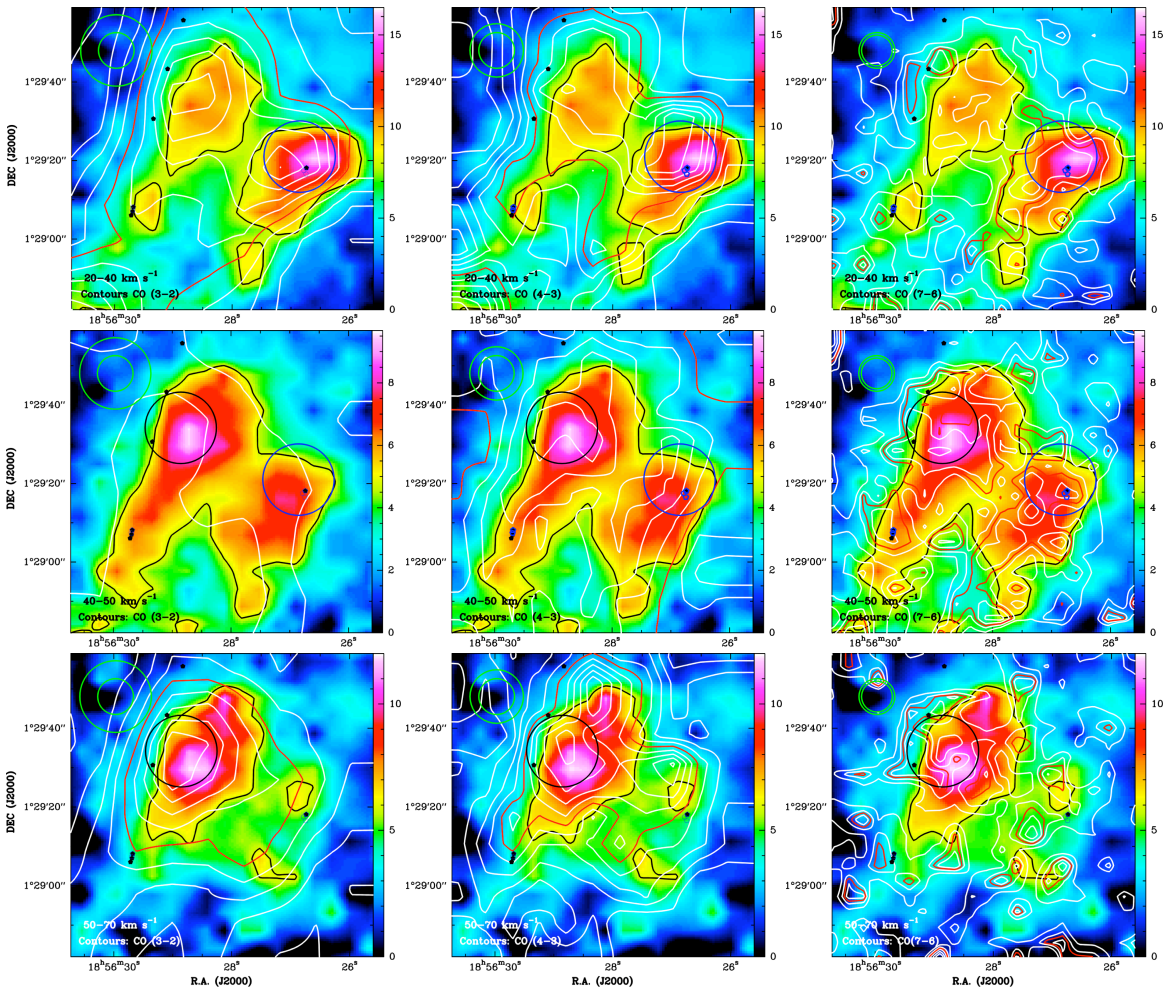

Figure 31: Overlays of the velocity-integrated maps of CO (3–2) (left column), CO (4–3) (middle column), and CO (7–6) (right column) as white contours on the CO (6–5) emission (colour background) observed towards W44E with the APEX telescope. The maps are in their original resolution (7.7″ for CO (7–6), 9.0″ for CO (6–5), 13.5″ for CO (4–3), and 18.2″ for CO (3–2)) . The intensity was integrated between 20–40 km s^{-1} (blue wing, top row), 40–50 km s^{-1} (ambient emission, middle row), and 50–70 km s^{-1} (red wing, bottom row). The wedge unit is K km s^{-1} in antenna temperature. The contours are in steps of 20% of the map peak value for CO (7–6) and in steps of 10% for CO (3–2) and CO (4–3). The half-maximum contours of the colour and contour maps are indicated in black and red, respectively. The blue and black circles indicate the position of our shock modelling analysis. The APEX beam sizes of the observations displayed are given in the upper left corner of each map. The maps are centred at ($\alpha_{[\mathrm{J2000}]}$ = 18$^{\mathrm{h}}$56$^{\mathrm{m}}$28$^{\mathrm{s}}$.4, $\beta_{[\mathrm{J2000}]}$ = 01°29′59.0″). The black and blue hexagons mark the positions of the OH masers observed by Claussen et al. (1997) and Hoffman et al. (2005). At the assumed distance of 3 kpc, the 18.2″ beam of CO (3–2) corresponds to a spatial resolution of 0.26 pc.

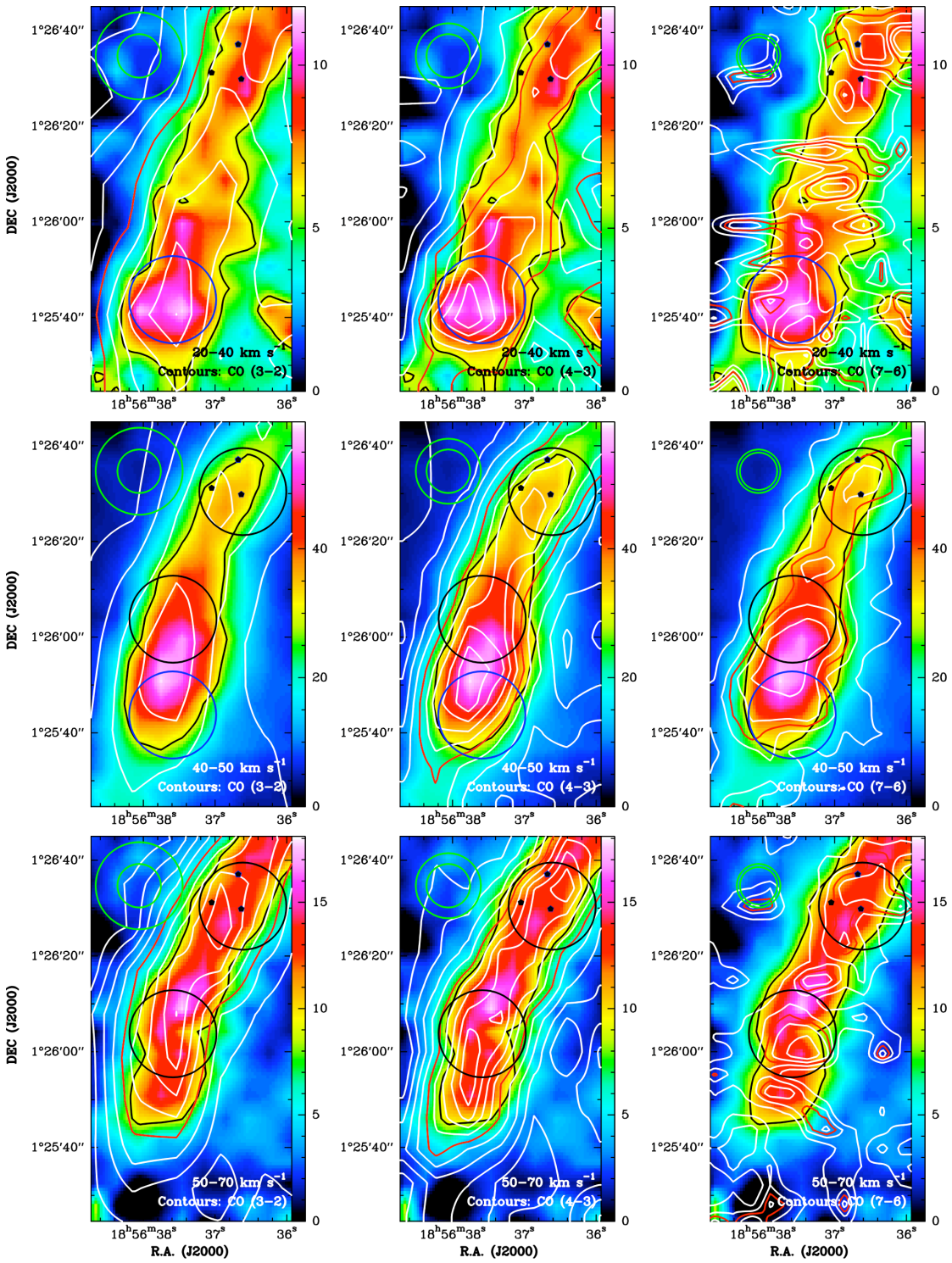

Figure 32: Same as Fig. 31, but observed towards W44F. The maps are centred at $(\alpha_{[\mathrm{J2000}]} = 18^{\mathrm{h}}56^{\mathrm{m}}36^{\mathrm{s}}.9, \beta_{[\mathrm{J2000}]} = 01°26'34.6'')$. The black and blue hexagons mark the positions of the OH masers observed by Claussen et al. (1997) and Hoffman et al. (2005).

Table 24: The positions of our analysis.

Position	$\alpha_{[J2000]}$	$\beta_{[J2000]}$
W44E Red	$18^h56^m28^s.90$	$01°29'34.2''$
W44E Blue	$18^h56^m26^s.90$	$01°29'21.0''$
W44F RedN	$18^h56^m36^s.61$	$01°26'30.5''$
W44F RedS	$18^h56^m37^s.58$	$01°26'03.8''$
W44F Blue	$18^h56^m37^s.59$	$01°25'43.8''$

the blue-shifted velocity regime. Here, the spatial displacement between maser and CO emission is less clear than for the other peak.

For our shock analysis, we aimed at choosing positions of clearly shocked gas, defined as positions of maximum CO emission in a given velocity range for a maximum number of observed transitions. Therefore, we first determined the local maxima of CO emission in all of our transition maps in the various velocity regimes and then chose the positions of our analysis based on these maxima. In the centre panel of Fig. 33, we show the two positions resulting from this procedure: the one close to the line of masers tracing the outer shock front (black circle, denoted as "W44E Red", as it is the dominant maximum in the red wing maps) and the one towards the interior (blue circle, denoted as "W44E Blue", as it mostly appears in the blue wings of the spectra). The coordinates of W44E Red and Blue are listed in Table 24.

12.6.2 *CO maps towards W44F*

The corresponding maps of integrated CO emission for the three velocity regimes towards W44F, together with observed maser positions, are shown in Figure 32. The maps in the ambient velocity regime (central row) in CO (3–2) and CO (4–3) have to be treated with some caution as they suffer from substantial absorption in the line centres, as can be seen in Fig. 30 and Fig. 34. In all velocity regimes, a thin filament of gas from the northwest to the southeast of the maps can be traced. However, as for W44E, for the wing emission in CO (7–6) this is only true for the maps convolved to the angular resolution of the CO (3–2) map (not shown here) due to bad signal-to-noise in the original map. The extent of the filament stretches further to the south for the blue wing emission than for the red wing. Again, we defined the positions of clear shock interaction as showing maximum CO emission in a given velocity range for a maximum number of observed transitions. Accordingly, based on the local maxima of CO emission in all our transition maps, we selected three positions in W44F for our modelling analysis. These positions are displayed in the central panel of Fig. 34. The first position in the north covers the maser locations observed by Claussen et al. (1997) and Hoffman et al. (2005). It is particularly prominent in the redshifted velocity regime (northern black circle in Fig. 34, denoted as "W44F RedN"). There is a further maximum in the red wing regime (southern black circle in Fig. 34, denoted as "W44F RedS"), while the emission integrated over the blue wing peaks still further to the south (blue circle in Fig. 34, denoted as "W44F Blue"). The corresponding coordinates are listed in Table 24.

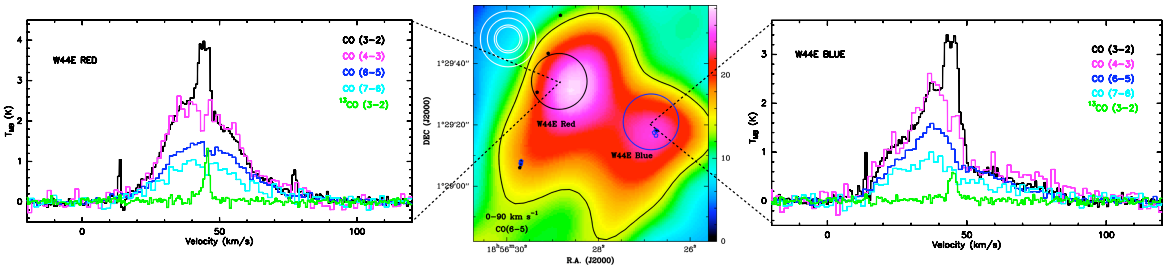

Figure 33: Central Panel: Positions of our analysis in W44E (W44E Red: black circle, W44E Blue: blue circle) on the velocity-integrated CO (6–5) emission ($T_{\rm A}^{*}$ integrated between 0 and 90 km s^{-1}) convolved to the CO (3–2) angular resolution of 18.2″ (colour background) with a half-maximum contour in black. The wedge unit is K km s^{-1}. The blue and black circles indicate the APEX beam size of our observations in CO (3–2). The APEX beam sizes of our CO (3–2), CO (4–3), CO (6–5), and CO (7–6) observations are also provided (upper left corner, see also Table 21). The black and light blue hexagons mark the position of the OH masers observed by Claussen et al. (1997) and Hoffman et al. (2005). Left Panel: Spectra observed in the position W44E Red (in $T_{\rm MB}$), CO (3–2), black; CO (4–3), pink; CO (6–5), dark blue; CO (7–6), light blue; ^{13}CO (3–2), green. Respective CO spectral resolutions are 0.66, 1.43, 1.27, and 1.63 km s^{-1}, and 0.69 km s^{-1} for ^{13}CO (3–2). Right panel: Spectra observed in the position W44E Blue, same colours as in the left panel.

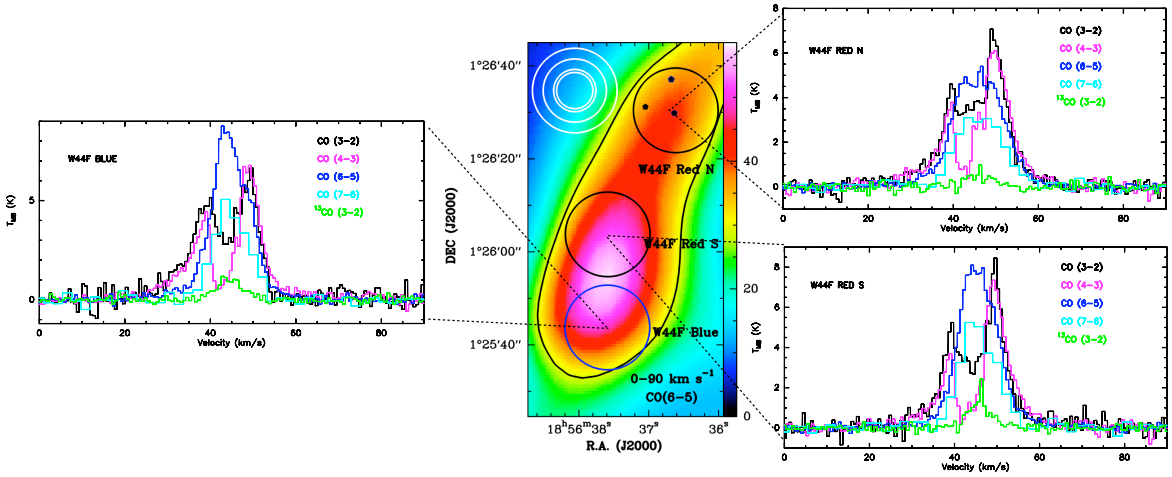

Figure 34: Same as Fig. 33 but towards W44F. The positions in the central panel are W44F RedN, W44F Red S, and W44F Blue (north to south). Left panel: Spectra observed in the position W44F Blue. Right panel: Spectra observed in the position W44F RedN (top) and W44F RedS (bottom). CO spectral resolutions are 0.64 for CO (3–2), 0.64 for CO (4–3), 0.64 for CO (6–5), and 2.18 km s^{-1} for CO (7–6), and 0.70 km s^{-1} for ^{13}CO (3–2).

12.7 INDIVIDUAL SPECTRA OF ^{12}CO AND ^{13}CO

12.7.1 *Analysis positions in W44E*

The individual spectra towards our positions of analysis in W44E as shown in Fig. 33 exhibit a complex structure. In CO (3–2) two components are seen, as already observed by Frail & Mitchell (1998), Reach & Rho (2000), and Reach et al. (2005) in CO (3–2) and CO (2–1): There is a narrow component tracing the cold ambient gas and a broad component due to emission from shocked gas.

Towards W44E Red, the emission of the cold quiescent gas in ^{13}CO (3–2) is confined between 40 and 50 km s^{-1}, showing two components: one centred at 44.5 km s^{-1} with a FWHM of 5.2 km s^{-1} and another very narrow component (FWHM = 1 km s^{-1}) at 45.6 km s^{-1}. The FWHM of the former component is identical to the FWHM determined by Reach et al. (2005) for the central peak in CO (2–1), and its central velocity is close to the average OH (1720 MHz) maser velocity of 44.7 km s^{-1}. The emission in ^{13}CO aligns with the central, narrow peak in our spectrum of ^{12}CO (3–2), although probable self-absorption renders the determination of the FWHM of the peak of the latter difficult. The lines in CO (4–3), (6–5), and (7–6) show self-absorption features in the range between 43 and 46 km s^{-1}. These shock-broadened lines are asymmetric but similar in shape among all transitions. The red-shifted wings of the lines extend to high velocities at weak levels of emission, reaching well beyond the velocity regime of 30–65 km s^{-1} considered to be associated with W44 by Seta et al. (1998).

Towards W44E Blue, the cold gas traced by ^{13}CO (3–2) exhibits only one component centred at 44.8 km s^{-1} with an FWHM of 3.2 km s^{-1}. This cold ambient component is also visible as a narrow peak in the spectrum of ^{12}CO (3–2) at 44.6 km s^{-1}. The shape of the shock-broadened line component is again similar in all transitions. Other than in W44E Red, the main peak of the shock emission is slightly offset from the ambient emission at ∼38 km s^{-1}. Furthermore, two shoulders can be identified: one in the blue- and one in the red-shifted velocity regime, the latter again stretching out to very high velocities of 80–90 km s^{-1}.

Fig. 35 shows the spectra of ^{12}CO (3–2) and ^{13}CO (3–2) towards W44E Red and Blue (two top panels, left ordinate), resampled to a common spectral resolution of 1 km s^{-1}. The line temperature ratio of ^{12}CO (3–2)/^{13}CO (3–2) (right ordinate) is displayed in the lower velocity shift's regime, where ^{13}CO is detected at more than 2σ (orange dots) and 3σ (red dots). Because these signal-to-noise values are only reached for ^{13}CO towards the centres of the ^{12}CO lines, the optical thickness values can accordingly only be inferred at the inner parts of the ^{12}CO line wings. The line ratios yield optical thickness values of 3–7 there, assuming a typical interstellar abundance ratio of 50–60 (e.g., Langer & Penzias 1993). The line temperature ratio towards W44E at ∼13 kms^{-1}, corresponding to foreground emission, yields optical thickness values of 3–14 in this component. We note that this analysis relies on the assumption of a common excitation temperature for both isotopologues.

12.7.2 *Analysis positions in W44F*

As already observed by Frail & Mitchell (1998) and Reach et al. (2005), the broad-line emission towards W44F seems to be absorbed by foreground gas in the lower transitions of CO. This effect

is also present in our data, although additional absorption is caused by emission in our reference position. Compared to W44E, the shock emission appears narrower with an FWHM less than 45 km s^{-1} and with the lines being more symmetric.

Towards W44F RedN, the quiescent gas as visible in ^{13}CO (3–2) peaks at 46 km s^{-1} with an FWHM of 7.8 km s^{-1} (see Fig. 35), which agrees with the average OH (1720 MHz) maser velocity of 46.6 km s^{-1}. Absorption is seen in all transitions to various extents in the lines of ^{12}CO, the lowest transitions being affected in the full range between 39.5 and 50 km s^{-1}. This is similar for W44F RedS, while there the emission of ^{13}CO (3–2) shows a double-peaked structure with a broader component at 45.7 km s^{-1} (FWHM 6.7 km s^{-1}) and a narrow component at 46.4 km s^{-1} (FWHM 0.7 km s^{-1}). In W44F Blue, the narrow ambient component disappears again, the remaining component being centred at 44.4 km s^{-1} with an FWHM of 7.2 km s^{-1}. W44F Blue shows the most asymmetric profiles with a shoulder in the red-shifted wing (as visible in CO (6–5)) and pronounced emission in the blue wing.

The line temperature ratio of ^{12}CO (3–2)/^{13}CO (3–2) towards W44F in the lower velocity shift's regime, where ^{13}CO is detected at more than 2σ (orange dots) and 3σ (red dots), is displayed in Figure 35 (three bottom panels, right ordinate). As in W44E, the ratios yield optical thickness values of 3–7 in the wings.

12.8 MODELLING

12.8.1 *The observations*

As described in Sect. 12.7, all spectra we have extracted towards our five positions of maximum CO emission in W44E and W44F show broad line wing emission around a central velocity consistent with the cold ambient gas. Most likely, these profiles arise from a superposition of different shock components propagating into the dense gas of molecular clumps, which are nearly impossible to disentangle. In order to still get significant constraints on the dominant shock features and environmental conditions, we separated the profiles into a blue and a red lobe and applied our shock analysis to each of these velocity domains independently.

All line profiles, convolved to a common angular resolution of 18.2″, were fitted using a combination of up to four independent Gaussians with fully adjustable parameters. In W44E, these free fits yielded similar fit components for all transitions: two Gaussians in the Red Position and three in the Blue with one additional ambient component in CO (3–2). In W44F, the fitting procedure was hindered by the deep absorption of the line centres. Therefore, the fits for the CO (3–2) and CO (4–3) spectra could only be based on information from the wings, starting with initial values for the fitting procedure as obtained from the higher transitions. However, large uncertainties result from the lack of information for the fits of these lines. To handle this problem, we decided not to use the information of the line centres based on these fits, but rather to utilize the similar shape of emission lines among all transitions as observed in W44E. In particular, the ratio between the velocity-integrated intensities of the full lobe and the velocity-integrated intensities of only the wings turned out to be constant among all transitions within ±5% in W44E. Assuming a similar behaviour in W44F, we used this ra-

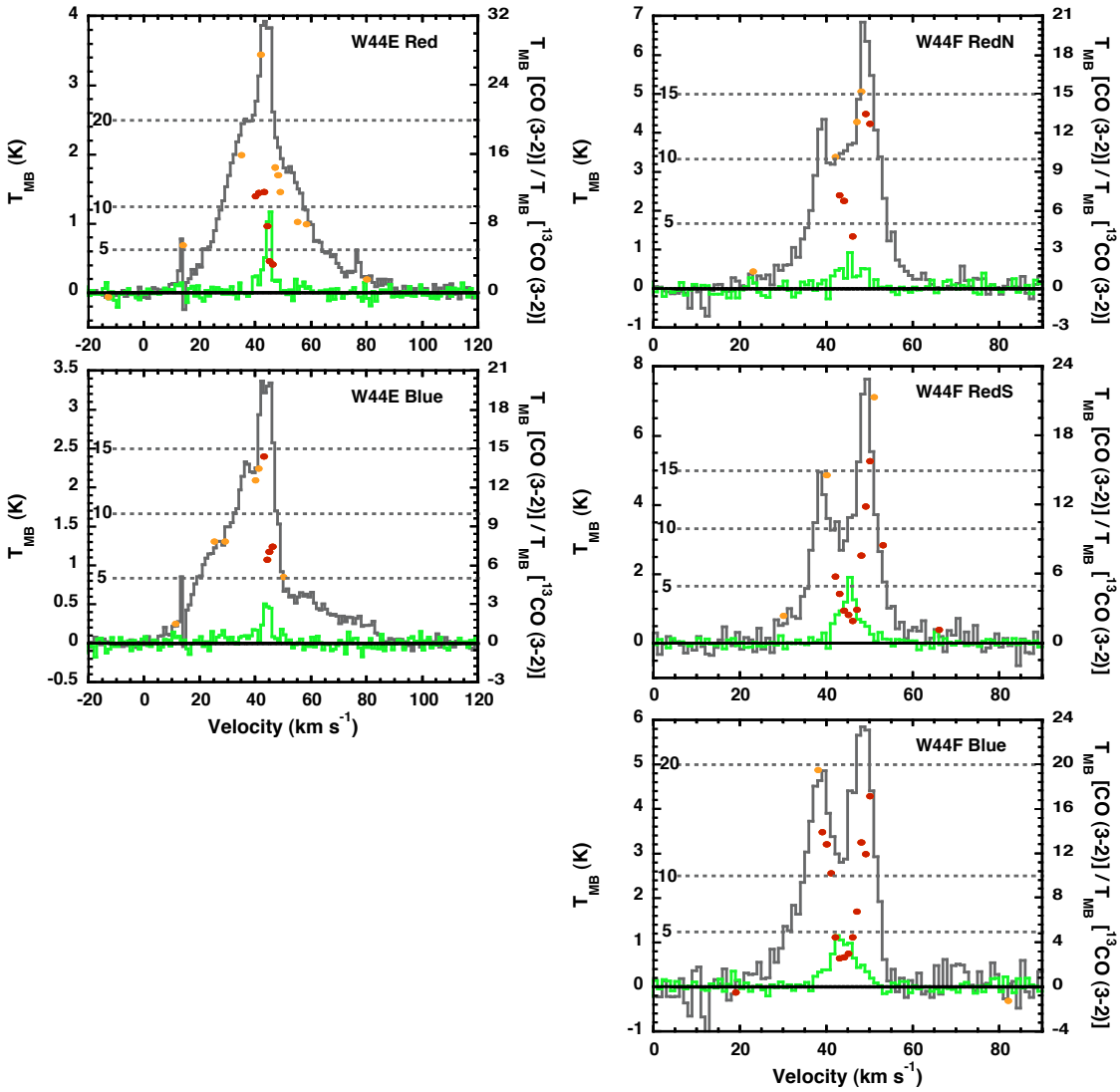

Figure 35: Spectra (in $T_{\rm MB}$) of ^{12}CO (3–2) (grey, left ordinate) and ^{13}CO (3–2) (green, left ordinate) together with the line temperature ratio of ^{12}CO (3–2)/^{13}CO (3–2) (dots, right ordinate). The ratio is shown for ^{13}CO (3–2) line temperatures higher than 2σ (orange dots) and 3σ (red dots). Grey dotted lines indicate values of the temperature ratio as displayed on the left-hand side of these lines. The positions displayed are W44E Red and Blue (left column, top and bottom), and W44F RedN, RedS, and Blue (right column, top to bottom). The corresponding values of the optical thickness in the line wings are in the range of 3–7.

tio derived from the CO (6–5) and CO (7–6) spectra to obtain estimations for the full-lobe integrated intensities in CO (3–2) and CO (4–3) based on their wing emission.

The integration intervals were determined according to our knowledge of the ambient cloud component, based on the fits of ^{13}CO (3–2) emission. To access the uncertainty of the lobe-separation with respect to the ambient velocity component, we varied the upper limit of the blue and the lower integration limit of the red lobe within the FWHM of the ^{13}CO (3–2) fit. The integration intervals for our five positions are listed in Tables 25 and 27. The errors for the integrated intensities in the CO (3–2) and CO (4–3) transitions in W44F, which were estimated based on the integrated intensities in the wings, were determined by varying the assumed lobe-wing integrated intensity ratio by ± 10 %. For the final plot of the velocity-integrated intensities of all CO lines against the rotational quantum number of their upper level (so-called 'spectral line energy distribution') we also accounted for the filling factor of the lines, which is assumed to be the same for all transitions in each position, once the maps have all been convolved to the same resolution. We based these estimations on the half-maximum contours in the maps of CO (6–5), which provides high angular resolution, has a good signal-to-noise ratio, and which is barely affected by self-absorption. We note however that a reliable estimate of these factors would require high-resolution interferometric observations of the analyzed regions, which have not been performed so far. In ambiguous cases we examined various values of the filling factor within our analysis. The final values we obtained are listed in Tables 25 and 27. To account for possible errors in the filling factor, we varied its value by ±0.1.

The errors in the integrated line intensities due to uncertainties in the integration intervals and due to assumed filling factors were combined with the errors resulting from the inherent r.m.s noise fluctuations of the profiles and the uncertainties in subtracting baselines as described by Elfhag et al. (1996). This total error of the integrated line intensities is given by

$$\Delta I = \sqrt{\Delta I^2_{\rm line} + \Delta I^2_{\rm base} + \Delta I^2_{\rm integration} + \Delta I^2_{\rm FF}} \quad (87)$$

$$= \sqrt{\frac{\sigma}{\sqrt{N}} \cdot B \sqrt{\frac{\Delta v}{B - \Delta v}} + \Delta I^2_{\rm integration} + \Delta I^2_{\rm FF}}\,, \quad (88)$$

where Δv (km s^{-1}) is the total velocity width of the spectral line, N is the total number of spectrometer channels covering a total velocity range of B km s^{-1}, and σ is the r.m.s noise per channel.

As can be seen in Fig. 36 and 37, the large errors in the integrated intensities for the (4–3) and (3–2) transitions in W44F mirror the uncertainties in the flux reconstruction, necessary in order to account for the absorption in the line centre. The errors of the spectral line energy distributions are larger in W44F than in W44E because in W44E the ratio between flux in the line wings and flux in the line centre is higher, such that the uncertainty due to the unknown value of the ambient velocity is of less consequence.

12.8.2 *The models*

For the interpretation of the observed spectral energy distributions ('SLEDs') we used a combined model consisting of a one-dimensional, plane-parallel shock model and a radiative transfer module (Gusdorf et al. 2008b, 2012). The former model solves the magneto-hydrodynamic equations in parallel with a large chemical network (including more than 100 species linked by over 1000 reactions)

for stationary C- and J-type shocks (Flower & Pineau des Forêts 2003; Flower et al. 2003) or approximated non-stationary CJ-type shocks. The theoretical elements for the computing of approximated, non-stationary shock models have been introduced in Chieze et al. (1998); Lesaffre et al. (2004a) and Lesaffre et al. (2004b). They have been proven useful mostly in the interpretation of H_2 pure rotational lines observed in shocks associated with bipolar outflows that accompany star formation, (e.g. Giannini et al. 2004; Gusdorf et al. 2008b, 2011) and associated to supernova remnants (e.g. Cesarsky et al. 1999).

The radiative transfer of H_2 as the main gas coolant is self-consistently calculated for the first 150 ro-vibrational levels within all shock models. Input parameters are the preshock density $n_{\rm H}$, the shock velocity $v_{\rm s}$, and the magnetic field parameter value b given as $B[\mu{\rm G}] = b \times \sqrt{n_{\rm H}[{\rm cm}^{-3}]}$, as well as the shock age for non-stationary shocks. The dynamical variables and chemical fractional abundances calculated with this model for each point through the shock wave are then passed on to a radiative transfer module, which calculates the emission from the CO molecule based on the 'large velocity gradient' (LVG) approximation. The integrated line temperatures of the first 40 rotational transitions of CO can then be compared to the observed SLED, as described in Gusdorf et al. (2012).

Our grid of models consists of more than 1000 integrated intensity diagrams obtained for C- and CJ-type shock models[6]. These models have velocities from 10 km s^{-1} up to the maximum velocity above which a C-type shock can no longer exist. The magnetic field parameter value b lies between 0.3 and 2, and four preshock densities (from 10^3 to 10^6 cm^{-3}) are covered. We note, however, that the coverage of our grid is not completely uniform over the range parameters. The observed SLEDs were compared with this grid using a χ^2 routine to select the best fits. In the fits, we only used the most unambiguous shock-tracing lines CO (7–6) and CO (6–5), which are not expected to be optically thick in the line wings and which are not affected by self-absorption. In W44E, a further reason for that choice is the existence of background emission unrelated to W44 in the low-lying CO transitions, which is expected in the velocity range 70-90 km s^{-1} (see Sect. 12.5). Because the redshifted line wings stretch much further in W44E than in W44F, it is impossible to discern this background emission from shocked gas related to W44E. In W44F, this problem does not exist due to the narrower line widths, but here the integrated intensities in CO (3–2) and CO (4–3) are only rough estimates based on the line wings and can therefore only serve as additional constraint for the fits based on the higher transitions.

12.9 RESULTS

12.9.1 *Shock emission*

12.9.1.1 *W44E*

Our χ^2 comparison of the observed integrated intensities in CO (7–6) and CO (6–5) towards W44E with our grid of models showed the observations to be compatible with non-stationary CJ-shocks[7]. Such shocks have not yet reached a state of dynamical equilibrium and show a structure intermediate

6 The grid also contains high-density models subject to grain-grain processing as calculated by Anderl et al. (2013).

7 For the blue lobe in W44E Blue, the integrated line intensities in CO (7–6) and CO (6–5) are also consistent with a stationary C-type shock propagating into a preshock medium at a density of 10^3 cm^{-3}. However, for consistency reasons and because

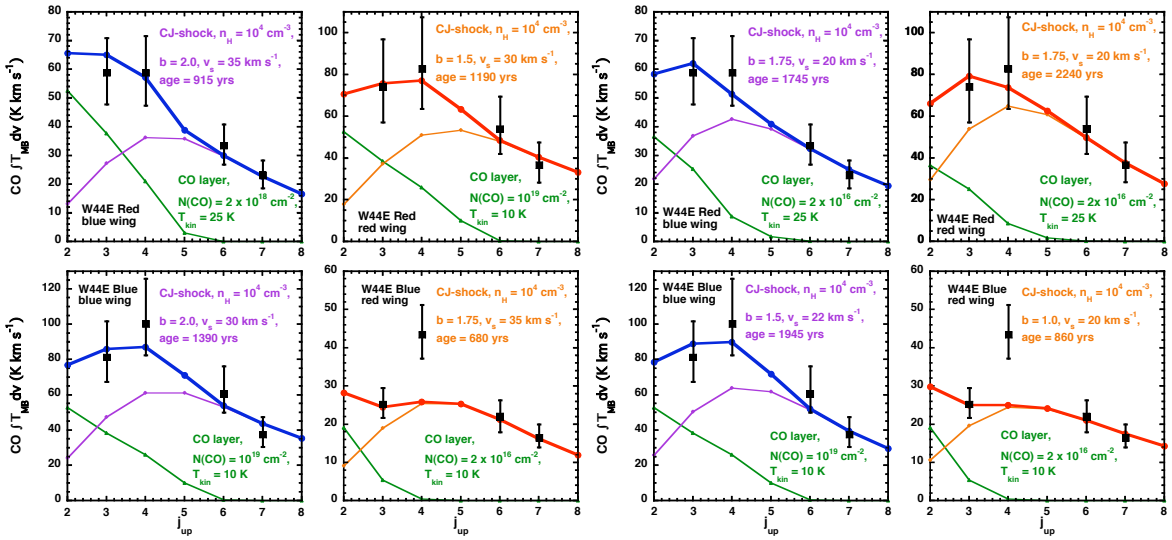

Figure 36: Best-model comparisons between CO observations and models for all positions in W44E (W44E Red: top row, W44E Blue: bottom row) for both, the blue and red shock components, respectively. The four panels on the left show the high velocity fits while the four panels on the right show the low velocity fits in each position. Observations are marked by black squares, the best-shock models are displayed in violet line (blue lobe) and orange line (red lobe) and diamonds, the CO layer, that we used to compensate the ambient emission affecting the CO (3–2) and CO (4–3) transitions, is shown in green line and triangles, and the sum of ambient and shock component in blue line (blue lobe) and red line (red lobe) with circles.

between a J- and a C-type shock, as the neutral fluid still contains a discontinuity in the flow variables. Given the presumably young age of the shocks in the molecular clumps close to the edge of the remnant (being much younger than the assumed SNR's age of 20,000 years), this result seems reasonable. The preshock density is found to be 10^4 cm^{-3}, consistent with previous estimates for the dense clump component (Reach & Rho 2000; Reach et al. 2005). The total, blue- to redshifted, velocity extent of the CO lines towards W44E, which is ~60 km s^{-1}, imposes a constraint on possible shock velocities: the gas must be accelerated to velocities $\geq$ 30 km s^{-1}. Obeying this constraint, we obtain shock velocities of 35 and 30 km s^{-1} for the blue and the red lobe in W44E Red, respectively, while in W44E Blue we get 30 and 35 km s^{-1} for the blue and the red lobe. The magnetic field component perpendicular to the shock layers in our models is constrained to $B = 200$ μG for the blue lobes and 150 or 175 μG for the red lobes in the Red and Blue positions. The difference could either be attributed to uncertainties in the analysis, be interpreted as a projection effect, or as a slight inhomogeneity of the medium. The age of the shocks scatters around 1000 years, where the shocks of the dominant lobes for each position (red in W44E Red and blue in W44E Blue) appear older than the shocks in the reverse directions. In general, the whole double-peak structure in W44E bears some bipolar characteristics, where antiparallel shocks exhibit similar parameters, pointing towards a general uniformity of the medium over the observed scales along the line of sight.

We note that the best fits to the observed SLEDs, except for the red lobe in W44E Blue, were achieved with slow CJ-shocks at ~20 km s^{-1}, which are much less consistent with the broad line

the modelled integrated intensities in CO (3–2) and CO (4–3) would strongly overtop the observed ones we discarded this fitting solution.

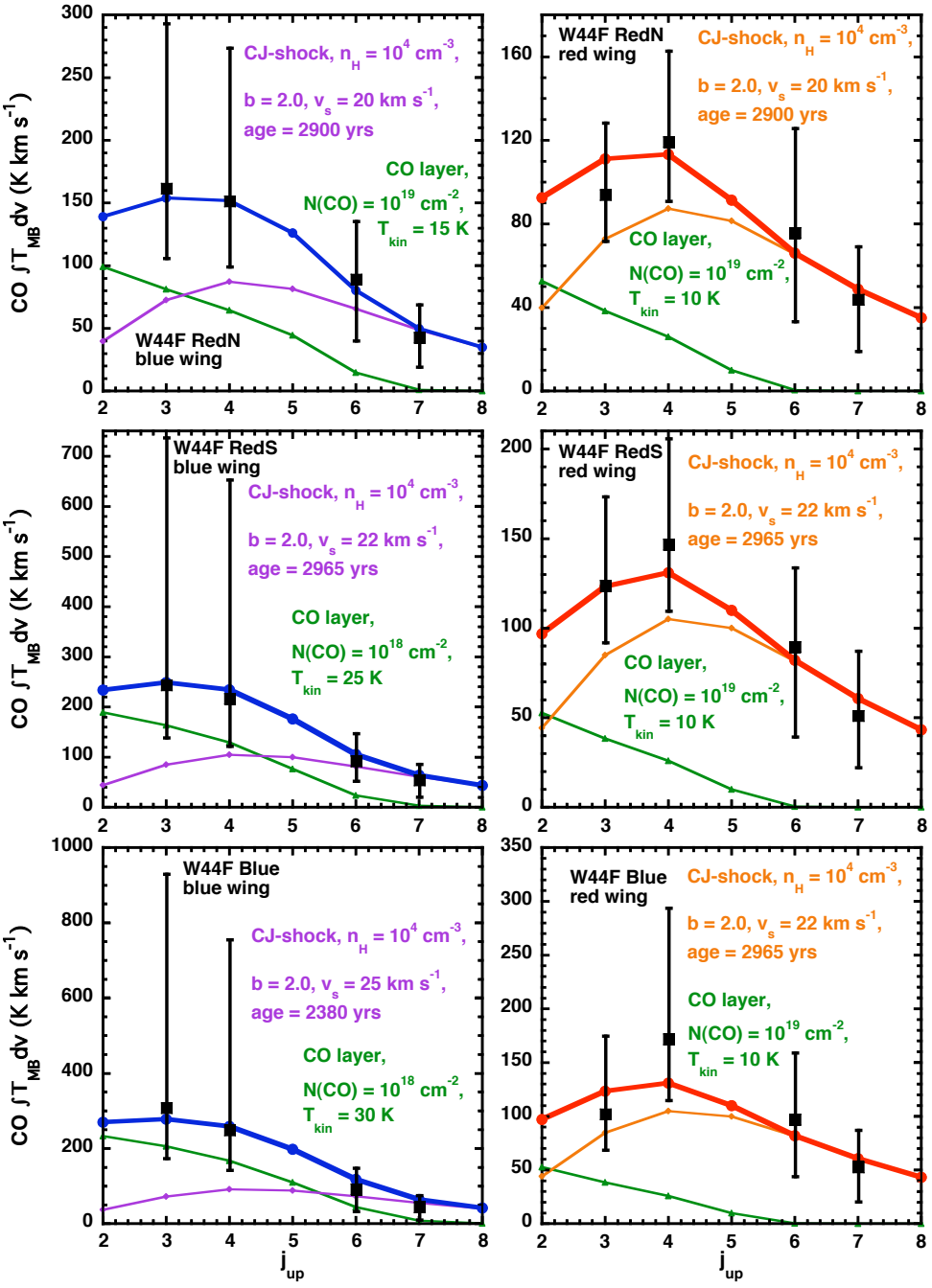

Figure 37: Best-model comparisons between CO observations and models for all positions in W44F (W44F RedN: top row, W44F RedS: central row, W44F Blue: bottom row) for both, the blue (left) and red (right) shock components, respectively. The colour code is the same as in Fig. 36.

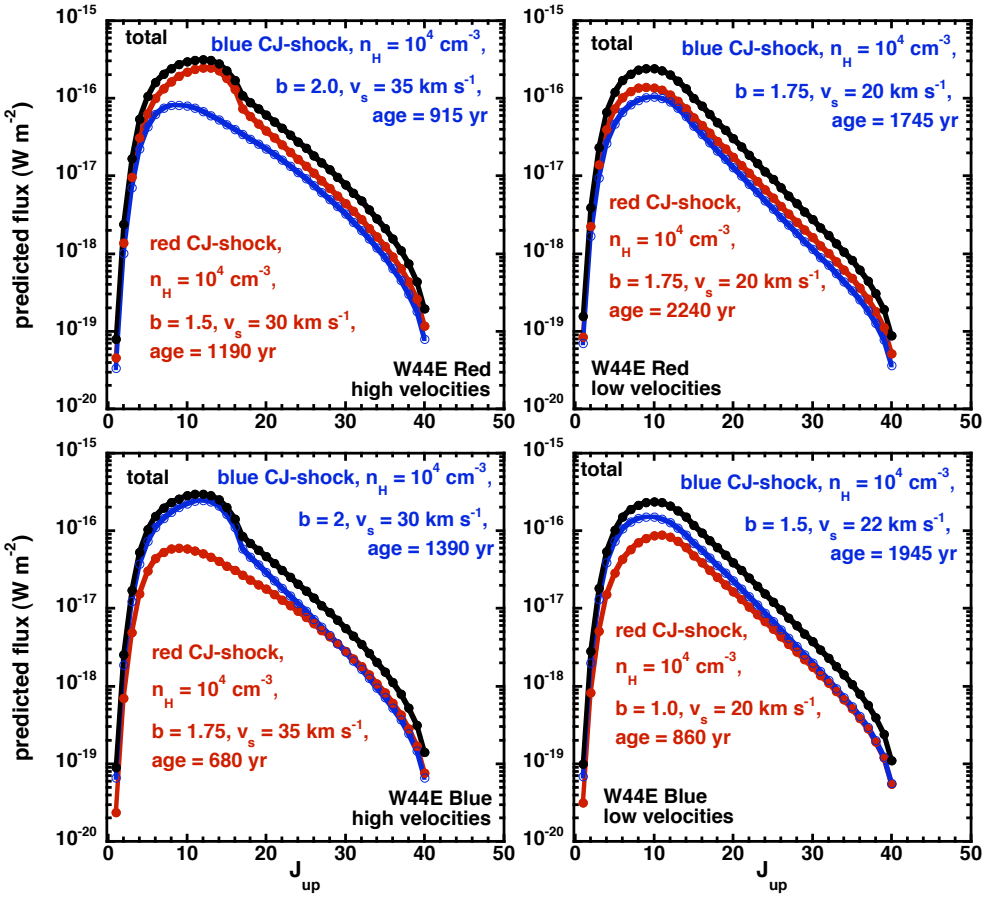

Figure 38: Integrated CO fluxes (W m^{-2}) against the rotational quantum numbers of the upper level in W44E. The highest level of $J_{\rm up} = 40$ corresponds to a maximum energy of 1806 K. Displayed are the integrated fluxes for W44E Red as predicted by the high-velocity models (left panel) and low-velocity models (right panel) for W44E Red (top row) and W44E Blue (bottom row).

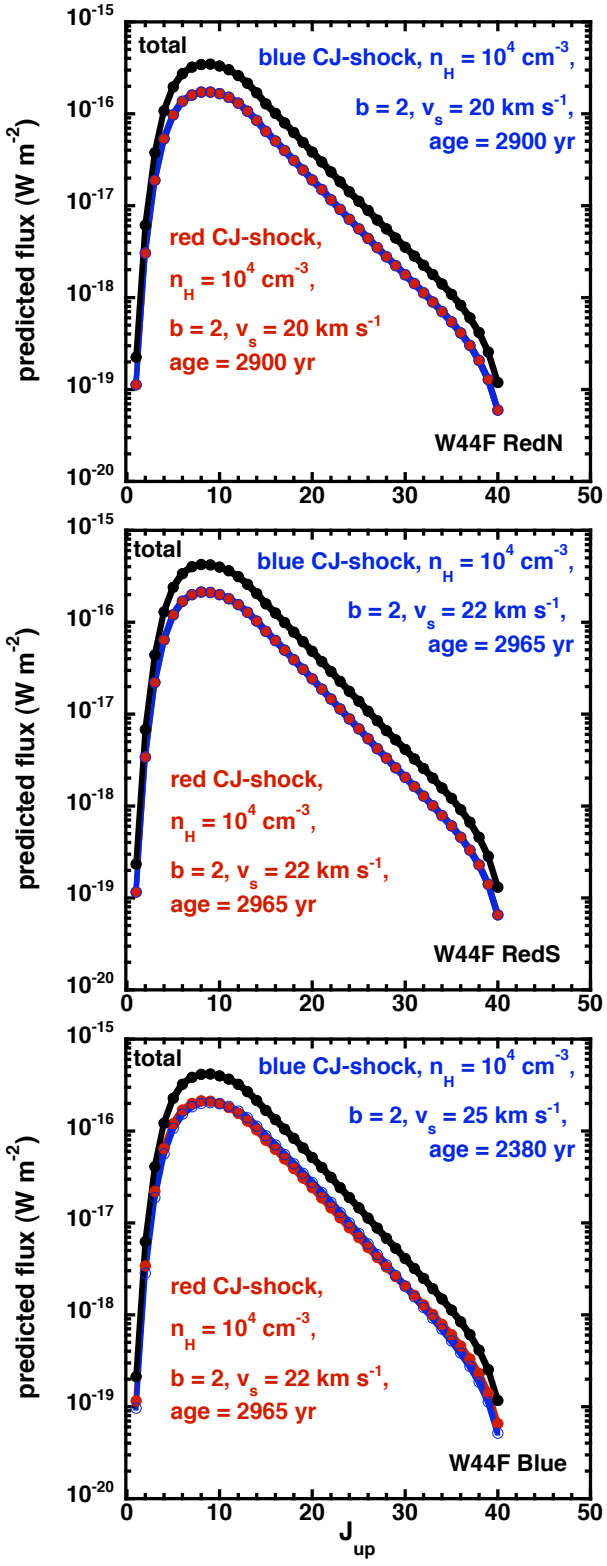

Figure 39: Integrated CO fluxes (W m^{-2}) against the rotational quantum numbers of the upper level in W44F. The highest level of $J_{up} = 40$ corresponds to a maximum energy of 1806 K. Displayed are the integrated fluxes for the positions RedN (top), RedS (middle), and Blue (bottom).

widths. We however also list them (together with the best fit in the 20 km s^{-1} velocity range towards W44E Blue, red lobe) in Table 25, as one could argue that they might constitute the dominant shock component as compared to possible faster but weaker components. They agree with the faster solutions in terms of the preshock density and the magnetic field strength value, but show higher ages of almost 2000 years.

The post-shock density of all models fitting the observations in W44E is of the order of 9×10^4 – 1.5×10^5 cm^{-3}, yielding expected post-shock values of the magnetic field for this component of 390–720 μG, compatible with the magnetic field strength estimated from maser circular polarization observations (see Sect. 12.4.1.1). The models produce OH column densities of a few 10^{14} cm^{-2}. These column densities are not high enough to allow for the observed amplification of OH 1720 MHz masers (Lockett et al. 1999). This is not necessarily critical, though, as the amplification of masers requires the column of masering gas to move at the same velocity – a situation obviously not met in the gas emitting in the CO line wings, which is described by our shock models. The CO column density in the models is of the order of 4×10^{16} – 2×10^{17} cm^{-2}.

12.9.1.2 *W44F*

The line widths in W44F are narrower than in W44E. Accordingly, we find that the observations are compatible with CJ-type shocks with velocities between 20 and 25 km s^{-1} as best fits to our observations (Table 27). The magnetic field component perpendicular to the shock layers in our models is given by $b = 2$ corresponding to 200 μG and the preshock density given as 10^4 cm^{-3}, consistent with W44E. The age of the shocks in W44F is ~2900 years. This result is somewhat puzzling given the much younger age obtained for W44E. The difference is less strong if we consider the slow shock solutions in W44E. However, the different line-widths in W44E and F already hint at a different nature of the shocks in both regions, probably linked to inhomogeneities in the interstellar medium. The post-shock density of the models consistent with the CO emission in W44F is of the order of 7×10^4 – 9×10^4 cm^{-3}, similar to W44E, with corresponding magnetic field values of ~600 μG. The OH column densities are of the order of 7×10^{14} – 1×10^{15} cm^{-2}, while for CO the column densities are ~ 3×10^{17} cm^{-2}.

12.9.2 *Degeneracies of the shock models*

To get an idea of the robustness and degeneracy of the results presented in the previous section, we have examined the best-fitting models, having χ^2 values of at most twice the smallest value, for each position in both velocity lobes. Except for the two C-type models in W44E Blue already mentioned above and some C-type cases in W44F with relatively high values of χ^2, all models are CJ-type. Furthermore, all these CJ-models agree in a preshock value of 10^4 cm^{-3}.

In W44E, the mean values of the preshock magnetic field strengths of the best-fitting models lie within the range of ~150–175 μG with standard deviations of about 40 μG[8]. The mean velocity values in W44E are located between 22 (W44E Red, red lobe) and 35 km s^{-1} (W44E Blue, red lobe) with a maximum standard deviation of 9 km s^{-1} (W44E Red, blue lobe). The largest scatter among positions

8 A somewhat special case is W44E Blue, red lobe, where the best fitting, high-velocity model and the second best model have χ^2 values that differ by a factor of 2.3, such that there is no considerable fitting degeneracy.

and velocity lobes in W44E is found with respect to the ages of the shocks, where the mean values are 1700 and 680 years in W44E Blue, blue and red lobe respectively, and 1350 and 2000 years in W44E Red, blue and red lobe respectively, with standard deviations of ∼400 years. However, as will be discussed later, the fitting of the red lobe emission in W44E is subject to increased uncertainties.

In W44F, the best-fitting models lie closer together in terms of their values of χ^2 than in W44E. The range of mean values of the preshock magnetic field strengths of the best-fitting models in W44F is the same as in W44E with standard deviations of 30–50 μG. The mean velocity values lie between 24 and 27 km s^{-1} with standard deviations of ∼5 km s^{-1}. The mean ages of the best-fitting models lie in the range of 2050–2750 years, with standard deviations of the order of 700 years.

12.9.3 *Unshocked CO layers*

As already found for W28F (Gusdorf et al. 2012), all fitting shock models underestimate the emission in CO (3–2) and CO (4–3). This is expected as we only model the shocked gas component, while emission in the lowest transitions originating from non-shocked gas also contributes to the integrated intensities, probably contaminating the lower velocity shift's regime of the spectral wings considered here. We therefore added a layer of CO to the shock models, calculated with the LVG module in 'homogeneous slab' mode. This was done by calculating a small grid with varying temperature and CO column density[9] at a local density of $n_{\rm H} = 10^4$ cm^{-3}, with a fractional abundance of X(CO) = 10^{-4}, and an assumed line width of 10 km s^{-1}. This grid of 42 models was then compared to the residuals of the shock-modelled integrated intensities in CO (3–2) and CO (4–3) using a χ^2 routine. The results are listed in Tables 26 and 28. In W44E, the layers complementing the fast shock fits are always at a low temperature of 10 K. The CO column densities are close to 10^{19} cm^{-2} except for W44E Blue, red wing. The slow shock residual fits in W44E Red are warmer at 25 K and are found for column densities of $2{\times}10^{16}$ cm^{-2} except for W44E Blue, blue wing. The best-model comparisons of the CO observations and the shock and layer components are displayed in Fig. 36. The sum of both components gives an encouraging fit to the data except for the integrated intensity of CO (4–3) in the red lobe of the W44E Blue position, which was impossible for us to fit within reasonable parameter ranges of the CO layer. As we have noted before, the corresponding spectrum extends extremely far in the red-shifted range of the spectrum, showing only weak emission and is therefore prone to possible uncertainties in the baseline subtraction. Given the expected contamination by background emission, a poor baseline quality in CO (4–3), and the fact that our grid of shock models is not well suited for these high shock velocities it might not be too surprising that our fit was not successful in this case.

The CO layers complementing the shock models in W44F show a stronger variation in temperatures than in W44E. While the fits for the red lobes result in cool layers of 10 K, the fitted layers in the blue wings are warmer with temperature values between 15 and 30 K. The higher temperatures could be explained by the heating of energetic radiation such as X-rays and γ-rays present in this region. The inferred CO column densities are always relatively high with values of 10^{18} or 10^{19} cm^{-2}. The quality of the fits, displayed in Fig. 37, is satisfying in all integrated intensity diagrams.

9 The temperature was varied between 10 K and 40 K, while the CO column density was varied between $2{\times}10^{16}$ and $1{\times}10^{19}$ cm^{-2}.

12.10 DISCUSSION

SNRs consitute an important source of energy and momentum input for the interstellar medium. Tables 29 and 30 show the mass, momentum, and energy injection calculated per beam for our best-fitting shock models. The shocked mass per beam amounts to ∼1 and ∼2 $M_{\rm Sun}$ for the models in W44E and F, respectively. The total energy input in one beam, given as the sum of the blue- and the red-lobe shock contributions, amounts to $\sim 1\times10^{46}$ erg in W44E and $\sim 1.5\times10^{46}$ erg in W44F. This contribution is quite considerable compared with the total energy of 10^{51} erg ejected by the supernova. It would mean that the interaction of the SNR with molecular clouds constitutes regions of very high energy dissipation. The values of the momentum input as sum of the red- and blue-shifted velocity lobes in one beam lies between $\sim 4\times10^{6}$ and $\sim 7\times10^{6}$ $M_{\rm Sun}$ cm s^{-1}, while in W44F it is $\sim 1\times10^{7}$ $M_{\rm Sun}$ cm s^{-1}. The results for all positions in both velocity intervals are listed in Tables 29 and 30.

Figures 38 and 39 show the integrated CO fluxes (in W m^{-2}) within our 18.2″ beam for all rotational transitions up to an upper rotational quantum number of 40 for all best-fitting shock models. Displayed are the shock models that fit the red- and blue-wing emission (red and blue dots, respectively) together with the total line integrated fluxes as sum of both wings (black dots). The asymmetry of the line profiles in W44E is mirrored in the plots, as well as the extensive symmetry of the lines in W44F. As can be seen from Figure 38, observations of higher-lying CO transitions will provide an opportunity to further remove modelling degeneracies, in particular the degeneracy between slow and fast models in W44E, because the location of the peak in the CO-ladder differs for different models. Such observations will be possible with the SOFIA telescope. We furthermore computed the radiative transfer of the water molecule for our best-fitting shock models, based on an LVG radiative transfer module with our best-fitting shock models as input. The resulting integrated intensities (in K km s^{-1}) as well as the line peak intensities (in K) of the lines observable with the PACS instrument on the Herschel Space Observatory for ortho- and para-H_2O are listed in Tables 32 – 37 in the Appendix. A detailed evaluation of this information with respect to Herschel observations, however, lies beyond the scope of the present study.

Finally, we must note that the extraction of the integrated intensities relies on some assumptions with respect to the shock geometry in the analyzed region. Following the method introduced in the study of Gusdorf et al. (2012), we split the whole spectral line into blue- and red-shifted parts without completely omitting the central line emission. Therefore, we have to add some flux corresponding to an additional CO layer with the preshock density of 10^{4} cm^{-3} to account for the ambient emission in the spectral line energy distributions. The real situation, however, is most certainly much more complex. The existence of maser spots hints at the fact that a dominant shock direction is perpendicular to the line-of-sight, with the corresponding post-shock emission thus also being found in the line centres. The broad line wings might then stem from the projected wings of a bow-shock, with the ambient medium being compressed and pushed aside.

Our analysis can only be applied to shock components propagating parallel to the line-of-sight and therefore gives averaged information on the shock conditions only in the gas being pushed towards or away from us. The derived properties, as long as they are non-directional such as the total magnetic field strength or the density, should still be valid, though. However, it is important to keep in mind that the geometrical assumptions we applied are severe and a more accurate modelling in terms of

geometry would need to account for the influence of the shock component perpendicular to the line-of-sight as well. At the same time, we note that the high level of microphysical detailedness included in our shock model cannot be maintained within fully two- or three-dimensional models. An alternative would be the use of pseudo-multidimensional models, synthesized from one-dimensional shocks, as presented by e.g. Kristensen et al. (2008) and Gustafsson et al. (2010), but in any case, a multi-dimensional modelling approach would add a set of additional, barely constraint parameters, such as the orientation of the magnetic field with respect to the shock structure, and therefore significantly increase the degeneracy of the modelling.

Table 25: Modelling results for W44E: shock emission.

Position	integration interval	filling factor	shock type	b	velocity [km s^{-1}]	$n_{\rm H}$ [cm^{-3}]	time [yr]	age [yr]
W44E Red	(-20 to 41.9-47.1 km s^{-1})	0.75	CJ	2	35	10^4	555	915
	low velocity fit:		*CJ*	*1.75*	*20*	*10^4*	*1350*	*1745*
	(41.9-47.1 to 120 km s^{-1})	0.5	CJ	1.5	30	10^4	500	1190
	low velocity fit:		*CJ*	*1.75*	*20*	*10^4*	*1500*	*2240*
W44E Blue	(-20 to 43.2-46.4 km s^{-1})	0.5	CJ	2	30	10^4	830	1390
	low velocity fit:		*CJ*	*1.5*	*22*	*10^4*	*1000*	*1945*
	(43.2-46.4 to 120 km s^{-1})	0.75	CJ	1.75	35	10^4	400	680
	low velocity fit:		*CJ*	*1.0*	*20*	*10^4*	*450*	*860*

Table 26: Modelling results for W44E: CO layers.

Position	integration interval	$n_{\rm H}$ [cm^{-3}]	Δv [km s^{-1}]	$T_{\rm kin}$ (K)	N(CO) [cm^{-2}]
W44E Red	(-20 to 41.9-47.1 km s^{-1})	10^4	10	10	$2{\cdot}10^{18}$
	low velocity fit:	10^4	*10*	*25*	*$2{\cdot}\,10^{16}$*
	(41.9-47.1 to 120 km s^{-1})	10^4	10	10	$1{\cdot}10^{19}$
	low velocity fit:	10^4	*10*	*25*	*$2{\cdot}\,10^{16}$*
W44E Blue	(-20 to 43.2-46.4 km s^{-1})	10^4	10	10	$1{\cdot}10^{19}$
	low velocity fit:	10^4	*10*	*10*	*$1{\cdot}\,10^{19}$*
	(43.2-46.4 to 120 km s^{-1})	10^4	10	10	$2{\cdot}10^{16}$
	low velocity fit:	10^4	*10*	*10*	*$2{\cdot}\,10^{16}$*

Table 27: Modelling results for W44F: shock emission.

Position	integration interval	filling factor	shock type	b	velocity [km s^{-1}]	$n_{\rm H}$ [cm^{-3}]	age [yr]	
W44F RedN	(0 to 42.3-50.1 km s^{-1})	0.5	CJ	2	20	10^4	2000	2900
	(42.3-50.1 to 90 km s^{-1})	0.5	CJ	2	20	10^4	2000	2900
W44F RedS	(0 to 42.3-49.1 km s^{-1})	0.5	CJ	2	22	10^4	1800	2965
	(42.3-49.1 to 90 km s^{-1})	0.5	CJ	2	22	10^4	1800	2965
W44F Blue	(0 to 40.8-48.0 km s^{-1})	0.5	CJ	2	25	10^4	1350	2380
	(40.8-48.0 to 90 km s^{-1})	0.5	CJ	2	22	10^4	1800	2965

Table 28: Modelling results for W44F: CO layers.

Position	integration interval	$n_{\rm H}$ [cm^{-3}]	Δv [km s^{-1}]	$T_{\rm kin}$ (K)	N(CO) [cm^{-2}]
W44F RedN	(0 to 42.3-50.1 km s^{-1})	10^4	10	15	$1{\cdot}10^{19}$
	(42.3-50.1 to 90 km s^{-1})	10^4	10	10	$1{\cdot}10^{19}$
W44F RedS	(0 to 42.3-49.1 km s^{-1})	10^4	10	25	$1{\cdot}10^{18}$
	(42.3-49.1 to 90 km s^{-1})	10^4	10	10	$1{\cdot}10^{19}$
W44F Blue	(0 to 40.8-48.0 km s^{-1})	10^4	10	30	$1{\cdot}10^{18}$
	(40.8-48.0 to 90 km s^{-1})	10^4	10	10	$1{\cdot}10^{19}$

Table 29: Mass, momentum and energy injection per beam for W44E.

Position	integration interval	filling factor	mass [$M_{\rm Sun}$]	momentum [$M_{\rm Sun}$ cm s^{-1}]	energy [erg]
W44E Red	(-20 to 41.9-47.1 km s^{-1})	0.75	1.04	$3.78{\cdot}10^6$	$7.59{\cdot}10^{45}$
	low velocity fit:	*0.75*	*1.21*	$2.55 \cdot 10^6$	$3.54 \cdot 10^{45}$
	(41.9-47.1 to 120 km s^{-1})	0.5	1.01	$3.26{\cdot}10^6$	$4.59{\cdot}10^{45}$
	low velocity fit:	*0.5*	*1.54*	$3.30 \cdot 10^6$	$4.34 \cdot 10^{45}$
W44E Blue	(-20 to 43.2-46.4 km s^{-1})	0.5	1.41	$4.42{\cdot}10^6$	$7.64{\cdot}10^{45}$
	low velocity fit:	*0.5*	*1.25*	$2.99 \cdot 10^6$	$3.73 \cdot 10^{45}$
	(43.2-46.4 to 120 km s^{-1})	0.75	0.76	$2.73{\cdot}10^6$	$5.25{\cdot}10^{45}$
	low velocity fit:	*0.75*	*0.57*	$1.21 \cdot 10^6$	$1.18 \cdot 10^{45}$

Table 30: Mass, momentum and energy injection per beam for W44F.

Position	integration interval	filling factor	mass [$M_{\rm Sun}$]	momentum [$M_{\rm Sun}$ cm s^{-1}]	energy [erg]
W44F RedN	(0 to 42.3-50.1 km s^{-1})	0.5	1.96	$4.27{\cdot}10^6$	$6.01{\cdot}10^{45}$
	(42.3-50.1 to 90 km s^{-1})	0.5	1.96	$4.27{\cdot}10^6$	$6.01{\cdot}10^{45}$
W44F RedS	(0 to 42.3-49.1 km s^{-1})	0.5	2.23	$5.28{\cdot}10^6$	$7.54{\cdot}10^{45}$
	(42.3-49.1 to 90 km s^{-1})	0.5	2.23	$5.28{\cdot}10^6$	$7.54{\cdot}10^{45}$
W44F Blue	(0 to 40.8-48.0 km s^{-1})	0.5	1.89	$5.08{\cdot}10^6$	$7.83{\cdot}10^{45}$
	(40.8-48.0 to 90 km s^{-1})	0.5	2.23	$5.28{\cdot}10^6$	$7.54{\cdot}10^{45}$

12.11 CONCLUSIONS

The main conclusions of our study are as follows:

1. We have presented new mapping observations with the APEX telescope in ^{12}CO (3–2), (4–3), (6–5), (7–6) and ^{13}CO (3–2) towards regions E and F in W44. The spectra, averaged over the respective regions, exhibit emission features at 13 km s^{-1}, corresponding to foreground emission, and emission between 70 and 90 km s^{-1}, which is at least partly due to background emission (Seta et al. 1998). The averaged lines show broad wing emission, between ∼15 and ∼90 km s^{-1} in W44E and between ∼25 and ∼60 km s^{-1} in W44F. Accordingly, the red-shifted emission in W44E is hard to disentangle from background emission.

2. The velocity integrated maps in the blue (20–40 km s^{-1}) and red (50–70 km s^{-1}) velocity regimes in W44E show one red- and one blue-shifted local maximum for all observed transitions, where the red-shifted local maximum ("W44E Red") is located just behind the forward edge of molecular gas as delineated by OH masers. The blue-shifted local maximum ("W44E Blue") is located further towards the interior of W44, where also maser emission is observed. In W44F, the thin filament of molecular gas ranging from the northwest to the southeast shows two local maxima in the red-shifted ("W44F RedN" and "W44F RedS") and one in the blue-shifted velocity regime ("W44F Blue"), the latter in the very south of the filament, where the red-shifted emission is already very weak.

3. The individual spectra in W44E Red and Blue exhibit two components: one narrow peak of ambient emission at ∼45 km s^{-1}, coincident with the emission in ^{13}CO (3–2), and a broad component of shock emission. The shock-broadened lines are asymmetric but bear similar shapes in all ^{12}CO transitions. Towards W44F, the lower transitions are subject to strong absorption in their line centres. The lines are narrower and, except for W44F Blue, also more symmetric than in W44E.

4. The integrated intensities of CO (7–6) and (6–5) of the blue- and red lobe components in all position were compared with a large grid of shock models combined with radiative transfer modules. This comparison revealed non-stationary shock models to be compatible with the observations. These relatively young shocks have ages of no more than 3000 years, consistent with the remnant's age of 20,000 years. The pre-shock density for all models was found to be 10^4 cm^{-3}. The best-fitting models in W44E have velocities of ∼20 km s^{-1}, which seems low given the broad line widths. We therefore also presented the best-fitting models with velocities ≥30 km s^{-1}. The magnetic field strengths of all best-fitting models in W44E are 100–200 μG, while in W44F we found values of 200 μG in all positions.

5. To account for the integrated emission in CO (3–2) and (4–3), CO layers corresponding to non-shocked gas had to be added to the shock models.

6. Based on the best-fitting shock models, we could estimate the shocked gas mass in one beam as well as the momentum- and energy injection per beam. In both regions, the shocked gas masses lie between ∼1 and 2 Solar masses, the momentum injection amounts to 1–5×10^6 $M_{\rm Sun}$ cm s^{-1},

and the energy injection to 1–8×10^{45} erg in one beam. The interaction between the SNR and the molecular cloud therefore dissipates a significant fraction of the total initial energy of the supernova explosion.

7. Our analysis can only be applied to shock components moving parallel to the line-of-sight, as revealed by the broad spectral line wings. Our results will therefore correspond to mean properties of the shocked gas moving towards and away from us. The existence of maser spots, however, hints at the fact that a dominant shock component propagates perpendicular to the line-of-sight. The shock geometry therefore is much certainly more complex than assumed in our analysis.

ACKNOWLEDGEMENTS We thank Dale A. Frail for kindly providing us with the radio continuum map at 1442.5 MHz. S. Anderl acknowledges support by the DFG SFB 956, the International Max Planck Research School (IMPRS) for Astronomy and Astrophysics, and the Bonn-Cologne Graduate School of Physics and Astronomy. A. Gusdorf acknowledges support by the grant ANR-09-BLAN-0231-01 from the French *Agence Nationale de la Recherche* as part of the SCHISM project.

12.12 APPENDIX: H_2O EMISSION

Table 31: Integrated intensities of para-H_2O lines (given in K km s^{-1}) observable with the PACS instrument on the Herschel Space Observatory for our best fitting shock models in W44E, as listed in Table 25. All models are CJ-type shocks at a preshock density of $n_H = 10^4$ cm^{-3}. In the table, they are labelled as (b; velocity (km s^{-1}); age (yr)).

Freq (GHz)	(2;35;915)	(1.75;20;1745)	(1.5,30,1190)	(1.75;20;2240)	(2;30;1390)	(1.5;22;1945)	(1.75;35;680)	(1;20;860)
5322.5	5.47e-04	1.45e-03	1.33e-02	2.06e-03	1.18e-02	3.81e-03	3.44e-04	3.42e-03
5280.7	2.37e-03	4.80e-04	5.03e-03	8.90e-04	4.02e-03	1.79e-03	1.82e-03	1.06e-03
5201.4	2.44e-02	8.63e-03	8.33e-02	1.61e-02	7.32e-02	2.89e-02	1.77e-02	1.48e-02
5194.9	3.06e-04	6.03e-05	7.87e-04	1.10e-04	6.31e-04	2.28e-04	2.38e-04	1.42e-04
4997.6	3.35e-04	1.08e-04	1.83e-03	1.87e-04	1.56e-03	3.92e-04	2.55e-04	2.77e-04
4850.3	1.11e-05	4.76e-05	5.26e-03	7.42e-05	4.82e-03	2.12e-04	6.99e-06	1.75e-04
4724.3	8.84e-03	1.89e-03	1.81e-02	3.53e-03	1.47e-02	7.03e-03	6.71e-03	3.89e-03
4468.6	5.19e-03	5.19e-03	8.52e-02	7.84e-03	7.98e-02	1.44e-02	3.57e-03	1.10e-02
4218.4	3.94e-03	2.12e-03	3.62e-02	3.46e-03	3.20e-02	6.96e-03	2.89e-03	5.11e-03
4190.6	2.04e-02	5.34e-03	4.91e-02	1.01e-02	4.17e-02	1.96e-02	1.52e-02	1.04e-02
3798.3	8.64e-04	4.71e-04	1.03e-02	7.60e-04	9.10e-03	1.57e-03	6.43e-04	1.23e-03
3691.3	1.11e-04	3.61e-05	6.08e-04	6.22e-05	5.18e-04	1.30e-04	8.48e-05	9.21e-05
3599.6	3.74e-02	1.30e-02	1.41e-01	2.31e-02	1.24e-01	4.44e-02	2.76e-02	2.66e-02
3331.5	9.15e-03	3.11e-02	6.42e-01	4.26e-02	6.14e-01	8.73e-02	6.16e-03	8.19e-02
3182.2	5.02e-05	5.19e-05	8.14e-04	8.33e-05	7.48e-04	1.71e-04	3.23e-05	1.31e-04
3135.0	6.82e-02	3.63e-02	4.86e-01	6.01e-02	4.44e-01	1.13e-01	4.95e-02	7.55e-02
2968.7	7.16e-02	1.77e-01	1.47e+00	2.33e-01	1.47e+00	3.74e-01	5.56e-02	3.36e-01
2884.3	4.50e-04	2.45e-04	5.44e-03	3.96e-04	4.78e-03	8.20e-04	3.35e-04	6.39e-04
2685.6	1.75e-03	9.45e-04	4.86e-02	1.55e-03	4.48e-02	3.15e-03	1.29e-03	2.32e-03
2631.0	7.45e-03	1.92e-03	1.95e-02	3.72e-03	1.71e-02	7.07e-03	5.51e-03	3.46e-03
2391.6	2.93e-01	2.21e-01	2.14e+00	3.52e-01	2.04e+00	6.32e-01	2.09e-01	4.38e-01
2365.9	1.19e-03	1.24e-02	1.82e-01	1.61e-02	1.85e-01	2.97e-02	8.18e-04	2.77e-02
2164.1	6.98e-01	7.50e-01	4.05e+00	1.10e+00	3.82e+00	1.79e+00	4.94e-01	1.32e+00
2074.4	1.38e-02	3.22e-02	9.98e-01	4.54e-02	9.35e-01	9.89e-02	1.00e-02	9.11e-02
2040.5	2.10e-04	9.12e-04	1.21e-01	1.43e-03	1.19e-01	4.30e-03	1.32e-04	3.46e-03
1919.4	4.12e-03	1.26e-01	1.19e+00	1.55e-01	1.18e+00	2.57e-01	2.77e-03	2.54e-01
1794.8	8.47e-04	3.50e-04	4.58e-03	6.17e-04	4.10e-03	1.20e-03	6.11e-04	7.36e-04
1602.2	2.60e-02	4.80e-02	7.37e-01	6.54e-02	7.03e-01	1.22e-01	1.88e-02	1.10e-01

Table 32: Same as Table 31, but for ortho-H_2O.

Freq (GHz)	(2;35;915)	(1.75;20;1745)	(1.5,30,1190)	(1.75;20;2240)	(2;30;1390)	(1.5;22;1945)	(1.75;35;680)	(1;20;860)
5500.1	4.21e-04	1.28e-04	4.19e-03	2.39e-04	3.68e-03	4.84e-04	3.09e-04	2.67e-04
5437.8	1.69e-03	3.28e-04	3.74e-03	6.15e-04	3.00e-03	1.25e-03	1.28e-03	7.13e-04
5276.5	1.05e-02	2.01e-03	2.01e-02	3.78e-03	1.59e-02	7.56e-03	8.08e-03	4.24e-03
5107.3	2.65e-02	9.93e-03	1.18e-01	1.78e-02	1.05e-01	3.28e-02	1.92e-02	1.84e-02
4764.0	8.14e-05	1.48e-05	1.73e-04	2.79e-05	1.36e-04	5.70e-05	6.23e-05	3.29e-05
4734.3	2.44e-02	5.66e-03	5.42e-02	1.07e-02	4.50e-02	2.11e-02	1.82e-02	1.15e-02
4600.4	7.48e-03	2.28e-03	3.88e-02	4.07e-03	3.36e-02	8.29e-03	5.60e-03	5.28e-03
4535.9	3.79e-03	8.86e-04	1.39e-02	1.63e-03	1.17e-02	3.35e-03	2.86e-03	2.01e-03
4512.4	1.34e-02	1.15e-02	3.25e-01	1.91e-02	3.20e-01	3.87e-02	9.16e-03	2.67e-02
4456.6	9.49e-05	2.61e-03	2.09e-01	3.63e-03	2.06e-01	9.27e-03	6.45e-05	8.90e-03
4240.2	4.80e-04	9.32e-05	1.06e-03	1.75e-04	8.52e-04	3.55e-04	3.65e-04	2.03e-04
4166.9	4.92e-02	1.37e-02	1.48e-01	2.53e-02	1.28e-01	4.97e-02	3.66e-02	2.83e-02
4000.2	2.58e-03	5.44e-04	5.56e-03	1.01e-03	4.51e-03	2.02e-03	1.96e-03	1.14e-03
3977.1	1.07e-01	9.51e-02	1.41e+00	1.48e-01	1.36e+00	2.81e-01	7.96e-02	2.21e-01
3971.0	3.50e-04	4.90e-05	5.36e-04	9.08e-05	3.86e-04	1.84e-04	2.80e-04	1.09e-04
3807.3	7.36e-02	4.19e-02	7.05e-01	7.03e-02	6.44e-01	1.40e-01	5.29e-02	9.67e-02
3654.6	1.08e-01	4.01e-02	5.07e-01	7.08e-02	4.52e-01	1.37e-01	7.90e-02	8.31e-02
3536.7	1.42e-03	3.31e-04	5.22e-03	6.11e-04	4.39e-03	1.25e-03	1.07e-03	7.52e-04
3167.6	2.92e-03	8.93e-04	2.82e-02	1.59e-03	2.48e-02	3.24e-03	2.19e-03	2.07e-03
3165.5	1.95e-04	1.51e-04	4.09e-02	2.52e-04	4.00e-02	6.53e-04	1.37e-04	4.59e-04
3013.2	3.35e-01	1.72e-01	1.99e+00	2.94e-01	1.85e+00	5.49e-01	2.41e-01	3.47e-01
2970.8	2.64e-02	1.61e-02	5.66e-01	2.60e-02	5.21e-01	5.49e-02	1.93e-02	4.17e-02
2774.0	1.78e-01	6.38e-01	3.34e+00	8.16e-01	3.29e+00	1.25e+00	1.23e-01	1.11e+00
2664.6	1.32e-03	2.33e-04	2.27e-03	4.37e-04	1.75e-03	8.76e-04	1.02e-03	4.89e-04
2640.5	7.57e-01	5.61e-01	3.83e+00	8.85e-01	3.59e+00	1.55e+00	5.45e-01	1.07e+00
2462.9	1.02e-02	1.17e-02	3.16e-01	1.82e-02	3.14e-01	4.11e-02	7.40e-03	3.29e-02
2344.3	3.96e-03	8.35e-04	8.53e-03	1.55e-03	6.92e-03	3.11e-03	3.01e-03	1.76e-03
2264.1	3.49e-02	6.64e-02	1.01e+00	9.31e-02	9.58e-01	1.81e-01	2.51e-02	1.59e-01
2221.7	2.29e-02	1.39e-02	3.91e-01	2.26e-02	3.58e-01	4.81e-02	1.67e-02	3.64e-02
2196.4	3.04e-03	5.41e-02	6.07e-01	6.71e-02	6.05e-01	1.12e-01	2.07e-03	1.12e-01
1918.5	4.50e-03	2.06e-03	3.18e-01	3.62e-03	3.02e-01	8.38e-03	3.33e-03	5.76e-03
1867.8	7.80e-03	2.38e-03	1.55e-01	4.44e-03	1.47e-01	9.01e-03	5.74e-03	4.97e-03
1716.8	3.28e+00	2.73e+00	1.09e+01	4.27e+00	1.05e+01	6.88e+00	2.31e+00	4.23e+00
1669.9	6.75e+00	4.77e+00	1.85e+01	8.04e+00	1.78e+01	1.28e+01	4.74e+00	6.83e+00
1661.0	5.46e-01	8.77e-01	3.75e+00	1.26e+00	3.72e+00	1.95e+00	3.68e-01	1.39e+00

Table 33: Peak intensities of para-H_2O lines (given in K) observable with the PACS instrument on the Herschel Space Observatory for our best fitting shock models in W44E, as listed in Table 25. All models are CJ-type shocks at a preshock density of $n_H = 10^4$ cm^{-3}. In the table, they are labelled as (b; velocity (km s^{-1}); age (yr)).

Freq (GHz)	(2;35;915)	(1.75;20;1745)	(1.5,30,1190)	(1.75;20;2240)	(2;30;1390)	(1.5;22;1945)	(1.75;35;680)	(1;20;860)
5322.5	1.42e-04	2.02e-02	1.56e-01	2.41e-02	1.34e-01	4.29e-02	1.14e-04	4.37e-02
5280.7	5.10e-04	2.33e-03	2.77e-02	3.05e-03	2.40e-02	5.89e-03	5.01e-04	5.71e-03
5201.4	5.35e-03	4.63e-02	1.10e+00	5.19e-02	9.68e-01	7.66e-02	4.89e-03	8.17e-02
5194.9	6.48e-05	2.86e-04	6.17e-03	3.80e-04	5.30e-03	8.31e-04	6.50e-05	8.27e-04
4997.6	7.28e-05	8.47e-04	2.15e-02	1.10e-03	1.85e-02	2.43e-03	7.11e-05	2.45e-03
4850.3	2.89e-06	1.06e-03	1.33e-01	1.66e-03	1.17e-01	5.39e-03	2.32e-06	4.22e-03
4724.3	1.90e-03	8.26e-03	9.05e-02	1.04e-02	7.99e-02	1.88e-02	1.84e-03	1.86e-02
4468.6	1.21e-03	5.39e-02	1.75e+00	5.87e-02	1.62e+00	1.04e-01	1.04e-03	1.05e-01
4218.4	8.70e-04	2.01e-02	5.21e-01	2.48e-02	4.54e-01	5.06e-02	8.13e-04	4.98e-02
4190.6	4.44e-03	2.43e-02	2.97e-01	2.96e-02	2.62e-01	5.30e-02	4.18e-03	5.28e-02
3798.3	1.92e-04	4.66e-03	1.52e-01	6.01e-03	1.32e-01	1.27e-02	1.82e-04	1.27e-02
3691.3	2.42e-05	2.82e-04	7.16e-03	3.66e-04	6.16e-03	8.09e-04	2.37e-05	8.16e-04
3599.6	8.16e-03	7.94e-02	1.32e+00	9.74e-02	1.19e+00	1.81e-01	7.64e-03	1.81e-01
3331.5	2.28e-03	6.82e-01	1.34e+01	8.31e-01	1.26e+01	1.62e+00	1.92e-03	1.61e+00
3182.2	1.29e-05	5.74e-04	1.06e-02	7.21e-04	9.50e-03	1.46e-03	1.07e-05	1.47e-03
3135.0	1.51e-02	3.27e-01	7.17e+00	3.90e-01	6.52e+00	6.98e-01	1.38e-02	6.88e-01
2968.7	1.87e-02	3.82e+00	3.08e+01	4.51e+00	3.01e+01	7.46e+00	1.89e-02	6.80e+00
2884.3	9.98e-05	2.43e-03	8.04e-02	3.13e-03	6.98e-02	6.60e-03	9.50e-05	6.61e-03
2685.6	3.87e-04	9.02e-03	1.15e+00	1.12e-02	1.04e+00	2.33e-02	3.62e-04	2.26e-02
2631.0	1.61e-03	7.72e-03	2.22e-01	9.11e-03	2.07e-01	1.44e-02	1.52e-03	1.43e-02
2391.6	6.48e-02	2.58e+00	3.13e+01	3.01e+00	2.99e+01	5.17e+00	5.83e-02	5.03e+00
2365.9	2.77e-04	3.29e-01	4.20e+00	3.91e-01	4.08e+00	6.49e-01	2.39e-04	5.98e-01
2164.1	1.55e-01	9.89e+00	4.38e+01	1.08e+01	4.14e+01	1.52e+01	1.37e-01	1.57e+01
2074.4	3.07e-03	7.13e-01	2.06e+01	9.08e-01	1.89e+01	1.93e+00	2.82e-03	1.86e+00
2040.5	5.45e-05	2.07e-02	2.81e+00	3.29e-02	2.70e+00	1.14e-01	4.38e-05	8.63e-02
1919.4	1.06e-03	2.65e+00	2.39e+01	3.08e+00	2.32e+01	4.94e+00	8.82e-04	4.64e+00
1794.8	1.90e-04	2.55e-03	5.90e-02	3.12e-03	5.29e-02	5.85e-03	1.74e-04	5.88e-03
1602.2	5.78e-03	8.41e-01	1.52e+01	9.68e-01	1.42e+01	1.72e+00	5.31e-03	1.63e+00

Table 34: Same as Table 33 but for ortho-H_2O.

Freq (GHz)	(2;35;915)	(1.75;20;1745)	(1.5,30,1190)	(1.75;20;2240)	(2;30;1390)	(1.5;22;1945)	(1.75;35;680)	(1;20;860)
5500.1	9.20e-05	6.54e-04	7.43e-02	7.91e-04	6.51e-02	1.83e-03	8.60e-05	1.46e-03
5437.8	3.64e-04	1.46e-03	2.28e-02	1.91e-03	1.94e-02	3.59e-03	3.55e-04	3.47e-03
5276.5	2.24e-03	8.35e-03	8.97e-02	1.09e-02	7.77e-02	1.98e-02	2.21e-03	1.91e-02
5107.3	5.83e-03	6.46e-02	1.76e+00	7.49e-02	1.59e+00	1.18e-01	5.34e-03	1.24e-01
4764.0	1.75e-05	6.50e-05	1.02e-03	8.65e-05	8.66e-04	1.63e-04	1.72e-05	1.56e-04
4734.3	5.27e-03	2.57e-02	3.04e-01	3.21e-02	2.66e-01	5.84e-02	5.03e-03	5.79e-02
4600.4	1.63e-03	1.38e-02	4.45e-01	1.76e-02	3.93e-01	3.77e-02	1.55e-03	3.79e-02
4535.9	8.20e-04	4.35e-03	1.42e-01	5.57e-03	1.24e-01	1.18e-02	7.93e-04	1.19e-02
4512.4	3.15e-03	1.42e-01	8.47e+00	1.86e-01	8.08e+00	4.31e-01	2.71e-03	3.98e-01
4456.6	2.24e-05	7.39e-02	6.29e+00	9.89e-02	5.97e+00	2.55e-01	1.91e-05	2.31e-01
4240.2	1.03e-04	4.15e-04	6.48e-03	5.44e-04	5.52e-03	1.02e-03	1.01e-04	9.85e-04
4166.9	1.07e-02	7.10e-02	1.15e+00	8.74e-02	1.02e+00	1.67e-01	1.01e-02	1.68e-01
4000.2	5.54e-04	2.41e-03	2.83e-02	3.10e-03	2.49e-02	5.77e-03	5.39e-04	5.64e-03
3977.1	2.16e-02	1.86e+00	2.60e+01	2.34e+00	2.49e+01	4.52e+00	2.08e-02	4.19e+00
3971.0	7.30e-05	1.79e-04	1.22e-03	2.53e-04	1.04e-03	4.22e-04	7.54e-05	3.77e-04
3807.3	1.63e-02	4.44e-01	1.08e+01	5.54e-01	9.81e+00	1.17e+00	1.49e-02	1.16e+00
3654.6	2.36e-02	2.61e-01	5.96e+00	3.17e-01	5.41e+00	5.96e-01	2.20e-02	5.93e-01
3536.7	3.07e-04	1.63e-03	5.33e-02	2.08e-03	4.64e-02	4.40e-03	2.96e-04	4.44e-03
3167.6	6.37e-04	5.38e-03	5.79e-01	6.89e-03	5.08e-01	1.48e-02	6.08e-04	1.48e-02
3165.5	4.48e-05	1.72e-03	1.15e+00	2.44e-03	1.08e+00	1.13e-02	3.97e-05	7.38e-03
3013.2	7.37e-02	1.45e+00	2.66e+01	1.74e+00	2.50e+01	3.21e+00	6.70e-02	3.12e+00
2970.8	5.84e-03	1.97e-01	1.18e+01	2.52e-01	1.08e+01	5.76e-01	5.42e-03	5.53e-01
2774.0	7.37e-02	1.10e+01	5.11e+01	1.22e+01	4.95e+01	1.74e+01	6.40e-02	1.70e+01
2664.6	2.81e-04	8.88e-04	7.19e-03	1.17e-03	6.33e-03	2.03e-03	2.78e-04	1.92e-03
2640.5	1.67e-01	6.22e+00	4.03e+01	6.99e+00	3.87e+01	1.07e+01	1.51e-01	1.11e+01
2462.9	2.25e-03	2.67e-01	6.39e+00	3.49e-01	6.19e+00	7.16e-01	2.06e-03	6.40e-01
2344.3	8.51e-04	3.70e-03	4.35e-02	4.75e-03	3.82e-02	8.87e-03	8.28e-04	8.66e-03
2264.1	7.75e-03	1.33e+00	1.76e+01	1.62e+00	1.62e+01	3.04e+00	7.04e-03	2.88e+00
2221.7	5.06e-03	1.70e-01	7.92e+00	2.18e-01	7.08e+00	5.15e-01	4.69e-03	4.79e-01
2196.4	7.16e-04	1.02e+00	1.43e+01	1.14e+00	1.39e+01	1.77e+00	6.12e-04	1.74e+00
1918.5	9.81e-04	2.67e-02	9.50e+00	3.80e-02	8.80e+00	1.03e-01	9.19e-04	8.90e-02
1867.8	1.71e-03	1.21e-02	3.65e+00	1.47e-02	3.42e+00	3.52e-02	1.60e-03	2.72e-02
1716.8	7.41e-01	2.87e+01	8.13e+01	3.07e+01	7.94e+01	3.86e+01	6.50e-01	3.85e+01
1669.9	2.92e+00	4.39e+01	1.21e+02	4.68e+01	1.18e+02	5.79e+01	2.59e+00	5.70e+01
1661.0	2.93e-01	1.29e+01	4.80e+01	1.41e+01	4.67e+01	1.90e+01	2.57e-01	1.86e+01

Table 35: Integrated intensities of para-H_2O lines (given in K km s^{-1}) observable with the PACS instrument on the Herschel Space Observatory for our best fitting shock models in W44F, as listed in Table 27. All models are CJ-type shocks at a preshock density of $n_H = 10^4$ cm^{-3}. In the table, they are labelled as (b; velocity (km s^{-1}); age (yr)).

Freq (GHz)	E_{up} (K)	(2;20;2900)	(2;22;2965)	(2;25;2380)
5322.5	552.30	1.46e-03	3.69e-03	4.47e-03
5280.7	1324.0	7.48e-04	1.74e-03	2.40e-03
5201.4	454.30	1.57e-02	3.33e-02	3.98e-02
5194.9	1270.3	9.06e-05	2.12e-04	3.02e-04
4997.6	1021.0	1.42e-04	3.68e-04	5.10e-04
4850.3	552.30	4.19e-05	1.74e-04	3.33e-04
4724.3	1070.0	3.10e-03	6.99e-03	9.57e-03
4468.6	410.40	6.53e-03	1.53e-02	1.88e-02
4218.4	598.80	2.71e-03	6.68e-03	9.09e-03
4190.6	843.80	9.15e-03	2.04e-02	2.69e-02
3798.3	781.10	5.53e-04	1.45e-03	2.01e-03
3691.3	1021.0	4.72e-05	1.22e-04	1.70e-04
3599.6	642.70	2.02e-02	4.61e-02	6.00e-02
3331.5	296.80	2.92e-02	7.80e-02	1.12e-01
3182.2	877.80	5.92e-05	1.70e-04	2.20e-04
3135.0	469.90	5.13e-02	1.18e-01	1.51e-01
2968.7	195.90	1.84e-01	3.46e-01	4.46e-01
2884.3	781.10	2.88e-04	7.57e-04	1.05e-03
2685.6	598.80	1.21e-03	3.00e-03	4.23e-03
2631.0	725.10	3.53e-03	7.67e-03	9.88e-03
2391.6	319.50	3.07e-01	6.73e-01	8.32e-01
2365.9	410.40	1.08e-02	2.62e-02	3.77e-02
2164.1	204.70	9.75e-01	1.95e+00	2.23e+00
2074.4	396.40	2.99e-02	8.22e-02	1.31e-01
2040.5	552.30	7.97e-04	3.48e-03	7.28e-03
1919.4	296.80	1.10e-01	2.27e-01	3.01e-01
1794.8	867.30	5.26e-04	1.26e-03	1.62e-03
1602.2	396.40	4.78e-02	1.09e-01	1.52e-01

Table 36: Integrated intensities of ortho-H_2O lines (given in K km s^{-1}) observable with the PACS instrument on the Herschel Space Observatory for our best fitting shock models in W44F, as listed in Table 27. All models are CJ-type shocks at a preshock density of $n_H = 10^4$ cm^{-3}. In the table, they are labelled as (b; velocity (km s^{-1}); age (yr)).

Freq (GHz)	E_{up} (K)	(2;20;2900)	(2;22;2965)	(2;25;2380)
5500.1	732.10	2.15e-04	5.02e-04	7.09e-04
5437.8	1274.2	5.26e-04	1.21e-03	1.69e-03
5276.5	1323.9	3.27e-03	7.35e-03	1.02e-02
5107.3	550.40	1.65e-02	3.58e-02	4.46e-02
4764.0	1552.6	2.35e-05	5.43e-05	7.69e-05
4734.3	1070.7	9.47e-03	2.14e-02	2.89e-02
4600.4	795.50	3.38e-03	8.12e-03	1.12e-02
4535.9	1013.2	1.38e-03	3.25e-03	4.53e-03
4512.4	410.70	1.61e-02	4.25e-02	5.50e-02
4456.6	410.70	2.04e-03	7.04e-03	1.35e-02
4240.2	1274.2	1.50e-04	3.45e-04	4.82e-04
4166.9	843.50	2.23e-02	5.11e-02	6.79e-02
4000.2	1125.7	8.76e-04	1.99e-03	2.74e-03
3977.1	305.30	1.20e-01	2.57e-01	3.61e-01
3971.0	1805.9	7.62e-05	1.67e-04	2.42e-04
3807.3	432.20	5.95e-02	1.42e-01	1.90e-01
3654.6	643.50	6.20e-02	1.42e-01	1.85e-01
3536.7	1013.2	5.16e-04	1.22e-03	1.69e-03
3167.6	795.50	1.32e-03	3.17e-03	4.38e-03
3165.5	702.30	1.87e-04	5.78e-04	1.21e-03
3013.2	468.10	2.62e-01	5.89e-01	7.42e-01
2970.8	574.70	2.01e-02	5.13e-02	7.50e-02
2774.0	194.10	6.59e-01	1.29e+00	1.48e+00
2664.6	1339.9	3.79e-04	8.38e-04	1.18e-03
2640.5	323.50	7.82e-01	1.67e+00	2.00e+00
2462.9	550.40	1.24e-02	3.63e-02	5.69e-02
2344.3	1125.7	1.34e-03	3.05e-03	4.21e-03
2264.1	432.20	6.65e-02	1.62e-01	2.31e-01
2221.7	574.70	1.74e-02	4.50e-02	6.55e-02
2196.4	410.70	4.78e-02	9.83e-02	1.29e-01
1918.5	642.40	2.81e-03	7.73e-03	1.24e-02
1867.8	732.10	3.99e-03	9.33e-03	1.33e-02
1716.8	196.80	4.08e+00	8.37e+00	9.09e+00
1669.9	114.40	8.24e+00	1.64e+01	1.73e+01
1661.0	194.10	1.15e+00	2.28e+00	2.45e+00

Table 37: Peak intensity of para-H_2O lines (given in K) observable with the PACS instrument on the Herschel Space Observatory for our best fitting shock models in W44F, as listed in Table 27. All models are CJ-type shocks at a preshock density of $n_H = 10^4$ cm^{-3}. In the table, they are labelled as (b; velocity (km s^{-1}); age (yr)).

Freq (GHz)	E_{up} (K)	(2;20;2900)	(2;22;2965)	(2;25;2380)
5322.5	552.30	1.75e-02	3.43e-02	5.11e-02
5280.7	1324.0	2.05e-03	4.64e-03	7.04e-03
5201.4	454.30	4.13e-02	6.39e-02	8.06e-02
5194.9	1270.3	2.41e-04	6.21e-04	1.05e-03
4997.6	1021.0	7.00e-04	1.80e-03	3.12e-03
4850.3	552.30	7.77e-04	4.11e-03	9.29e-03
4724.3	1070.0	7.33e-03	1.51e-02	2.25e-02
4468.6	410.40	4.79e-02	7.65e-02	1.44e-01
4218.4	598.80	1.70e-02	3.91e-02	6.70e-02
4190.6	843.80	2.14e-02	4.22e-02	6.31e-02
3798.3	781.10	3.97e-03	9.55e-03	1.65e-02
3691.3	1021.0	2.33e-04	5.98e-04	1.04e-03
3599.6	642.70	6.95e-02	1.43e-01	2.26e-01
3331.5	296.80	5.52e-01	1.28e+00	2.19e+00
3182.2	877.80	4.83e-04	1.11e-03	1.82e-03
3135.0	469.90	2.82e-01	5.68e-01	9.08e-01
2968.7	195.90	3.32e+00	6.55e+00	9.70e+00
2884.3	781.10	2.07e-03	4.98e-03	8.60e-03
2685.6	598.80	7.62e-03	1.79e-02	3.38e-02
2631.0	725.10	6.96e-03	1.21e-02	1.66e-02
2391.6	319.50	2.21e+00	4.27e+00	6.69e+00
2365.9	410.40	2.83e-01	5.70e-01	8.69e-01
2164.1	204.70	8.81e+00	1.30e+01	1.69e+01
2074.4	396.40	5.72e-01	1.49e+00	2.67e+00
2040.5	552.30	1.50e-02	8.57e-02	2.14e-01
1919.4	296.80	2.33e+00	4.32e+00	6.36e+00
1794.8	867.30	2.18e-03	4.59e-03	7.13e-03
1602.2	396.40	7.30e-01	1.40e+00	2.37e+00

Table 38: Peak intensity of ortho-H_2O lines (given in K) observable with the PACS instrument on the Herschel Space Observatory for our best fitting shock models in W44F, as listed in Table 27. All models are CJ-type shocks at a preshock density of $n_H = 10^4$ cm^{-3}. In the table, they are labelled as (b; velocity (km s^{-1}); age (yr)).

Freq (GHz)	E_{up} (K)	(2;20;2900)	(2;22;2965)	(2;25;2380)
5500.1	732.10	5.70e-04	1.26e-03	4.41e-03
5437.8	1274.2	1.31e-03	2.84e-03	4.29e-03
5276.5	1323.9	7.56e-03	1.60e-02	2.32e-02
5107.3	550.40	5.75e-02	9.69e-02	1.28e-01
4764.0	1552.6	5.94e-05	1.31e-04	1.93e-04
4734.3	1070.7	2.26e-02	4.67e-02	7.01e-02
4600.4	795.50	1.16e-02	2.81e-02	5.01e-02
4535.9	1013.2	3.71e-03	8.75e-03	1.51e-02
4512.4	410.70	1.12e-01	3.37e-01	6.74e-01
4456.6	410.70	5.62e-02	1.93e-01	4.12e-01
4240.2	1274.2	3.72e-04	8.08e-04	1.22e-03
4166.9	843.50	6.10e-02	1.30e-01	2.05e-01
4000.2	1125.7	2.14e-03	4.59e-03	6.89e-03
3977.1	305.30	1.53e+00	3.73e+00	6.10e+00
3971.0	1805.9	1.85e-04	3.82e-04	4.72e-04
3807.3	432.20	3.61e-01	8.89e-01	1.61e+00
3654.6	643.50	2.25e-01	4.72e-01	7.61e-01
3536.7	1013.2	1.39e-03	3.27e-03	5.66e-03
3167.6	795.50	4.54e-03	1.10e-02	1.97e-02
3165.5	702.30	1.35e-03	7.61e-03	3.33e-02
3013.2	468.10	1.24e+00	2.57e+00	4.28e+00
2970.8	574.70	1.59e-01	4.29e-01	8.48e-01
2774.0	194.10	9.86e+00	1.55e+01	2.04e+01
2664.6	1339.9	8.40e-04	1.71e-03	2.32e-03
2640.5	323.50	5.45e+00	8.90e+00	1.26e+01
2462.9	550.40	2.16e-01	5.94e-01	9.86e-01
2344.3	1125.7	3.29e-03	7.04e-03	1.06e-02
2264.1	432.20	1.10e+00	2.50e+00	4.09e+00
2221.7	574.70	1.37e-01	3.88e-01	7.81e-01
2196.4	410.70	8.99e-01	1.52e+00	2.29e+00
1918.5	642.40	2.07e-02	7.84e-02	1.73e-01
1867.8	732.10	1.06e-02	2.39e-02	8.83e-02
1716.8	196.80	2.66e+01	3.57e+01	4.28e+01
1669.9	114.40	4.13e+01	5.41e+01	6.43e+01
1661.0	194.10	1.17e+01	1.72e+01	2.18e+01

13

ADDITIONAL MATERIAL

In this chapter we present some material supplementary to the previous chapter, which was part of our shock analysis in W44 but not presented in the paper. In Sect. 13.1 we show details of the adopted spectral line fitting procedure, while in Sect. 13.2 we present maps of the observed regions in W44 that we used to estimate the filling factors of our observations.

13.1 SPECTRAL LINE FITTING

In order to extract the integrated intensities of the observed CO lines as used in the spectral line energy distribution plots, we had to fit the line profiles. These fits were necessary to avoid unrelated emission and absorption features that would have distorted the desired information. We only used unconstrained Gaussian profiles[1], and started the fitting with the CO (6–5) spectra, which have good spectral resolution and low signal-to-noise. Furthermore, this line is merely affected by absorption or ambient emission. The parameters of the best-fitting Gaussians derived from the CO (6–5) fits were then used as initial values for the fits of the other lines. The resulting Gaussians do not bear any physical meaning, because shock emission exhibits asymmetric, non-Gaussian line profiles. We note, however, that a similarity in shape of the line profiles is expected if all lines stem from the same shocked material. Such a similarity is indeed found in the fits. The results can be seen in Fig. 40–44. These figures also show the minimum integration intervals of the blue and red lobes, respectively, as derived from the fits of the spectra of ^{13}CO (3–2) and as listed in Tables 25 and 27. For the CO (3–2) and (4–3) lines in W44F, we only used the line fits of the wings not affected by absorption. For these spectra, the velocity regime used to extract the integrated intensities of the wing is indicated as coloured background.

13.2 BEAM FILLING FACTORS

In the interpretation of astronomical observations, the relation between the size of the source and the telescope beam size needs to be taken into account. The observed line temperature will not correspond to the true radiation temperature of the source, unless the source is significantly larger than the telescope beam. Otherwise, a so-called filling factor is introduced that mediates between the actual and the observed temperatures. If the source and the telescope beams are Gaussian shaped, this filling factor f_{source} is defined as

$$f_{\text{source}} = \frac{\Omega_{\text{source}}}{\Omega_{\text{source}} + \Omega_{\text{beam}}}\,, \tag{89}$$

1 We used the CLASS software from the GILDAS package, described at `http://iram.fr/IRAMFR/GILDAS/doc/html/class-html/`.

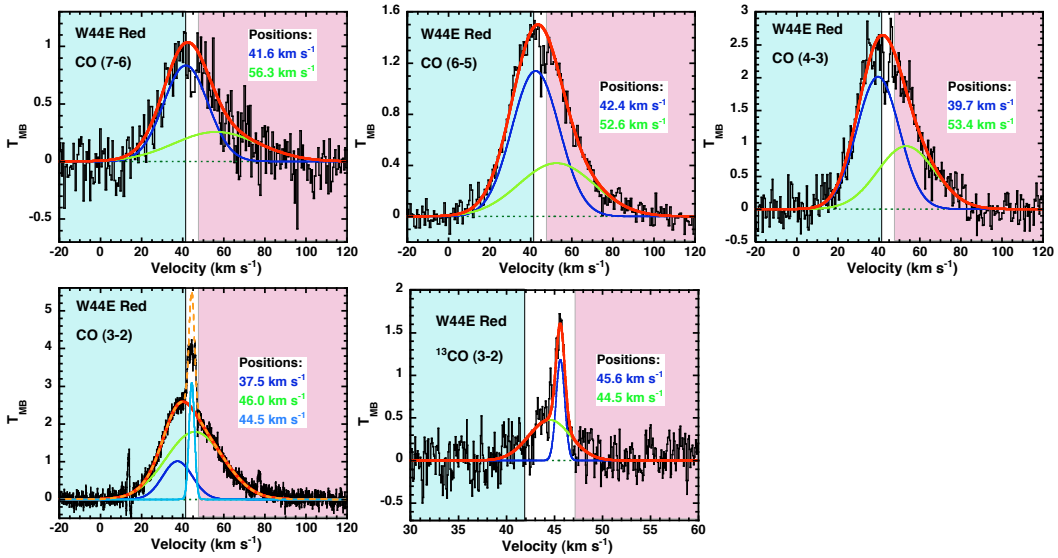

Figure 40: Fitted spectra of CO (7–6), (6–5), (4–3) (top row, left to right) and CO (3–2) and ^{13}CO (3–2) (bottom row, left and right) at their original spectral resolutions (see Table 22) in the W44E Red position. The peak locations of the Gaussians used in the fit are indicated in the plots. The red lines show the sum of all fitting components as used in the analysis. For CO (3–2), the prominent ambient peak has been subtracted. For this spectrum, the sum of all components including the ambient is shown as dashed orange line. The background colours indicate the minimum blue and red integration intervals (see also Table 25).

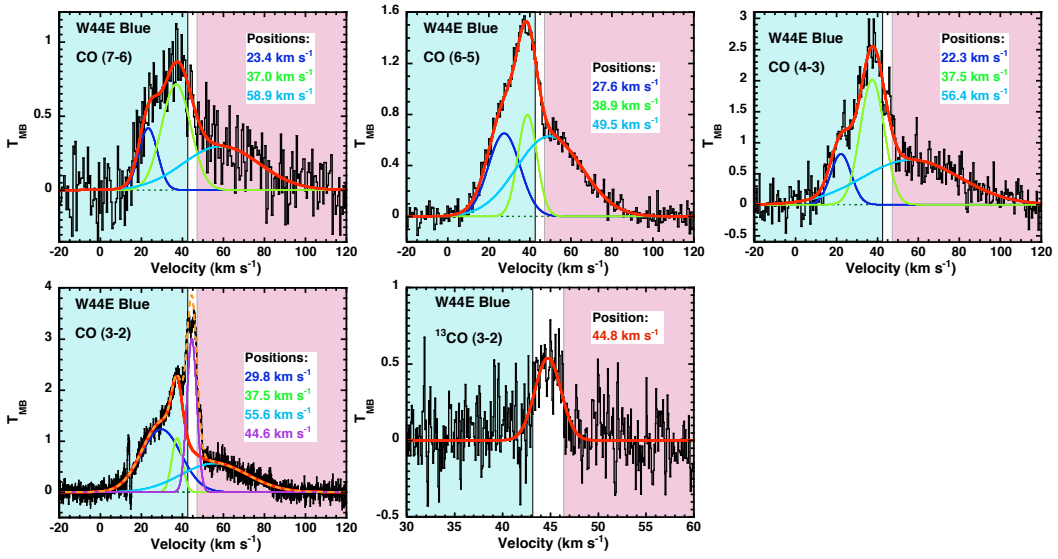

Figure 41: Same as Fig. 40, but for W44E Blue.

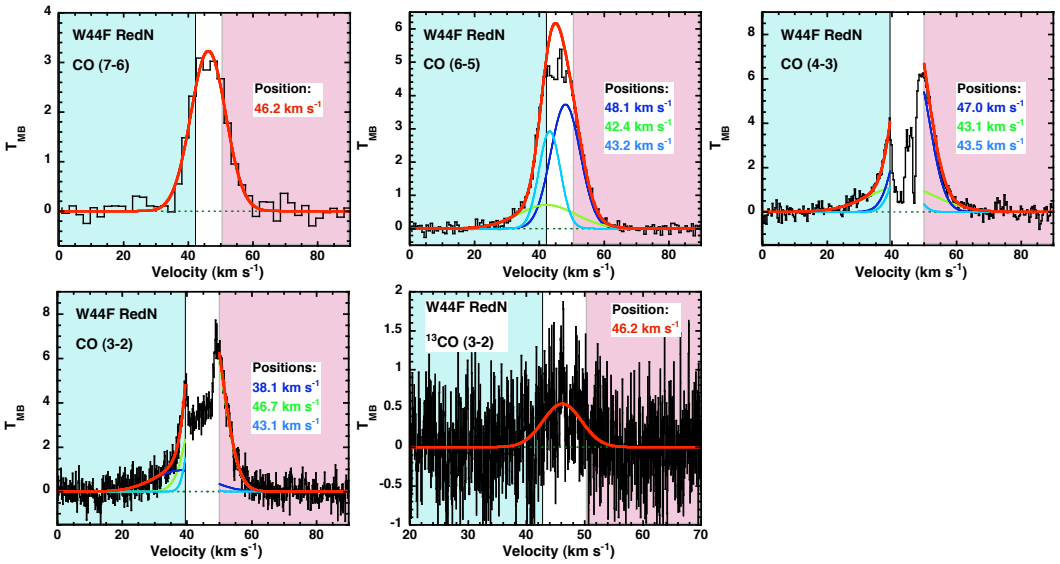

Figure 42: Fitted spectra of CO (7–6), (6–5), (4–3) (top row, left to right) and CO (3–2) and ^{13}CO (3–2) (bottom row, left and right) at their original spectral resolutions (see Table 23) in the W44F RedN position. The peak locations of the Gaussians used in the fit are indicated in the plots. The red lines show the sum of all fitting components as used in the analysis. The background colours indicate the minimum blue and red integration intervals (see also Table 27). For CO (3–2) and (4–3), only the fits of the wing emission were used in order to reconstruct the intensity in the line centre. The background colours for these spectra indicate the velocity range of the wings as used for this reconstruction.

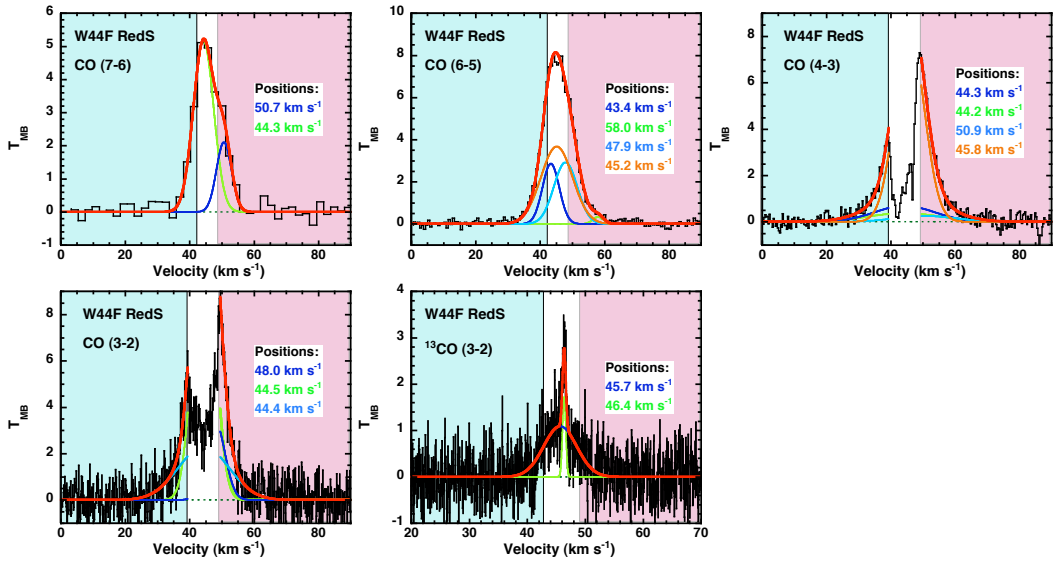

Figure 43: Same as Fig. 42, but for W44F RedS.

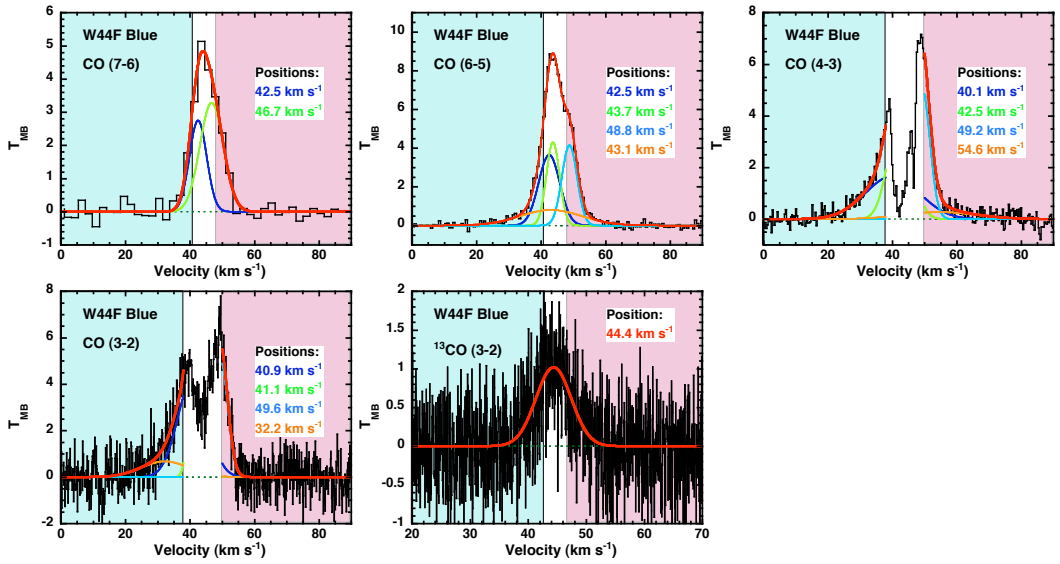

Figure 44: Same as Fig. 42, but for W44F Blue.

where $\Omega_{\rm source}$ and $\Omega_{\rm beam}$ are the solid angles covered by the source and the beam, respectively. If both solid angles are the same, the filling factor becomes 0.5. For an exact estimation of the filling factor, it is necessary to know the structure of the emitting source at sufficiently high spatial resolution. This information, however, is often not accessible. In the case of the shocked regions in W44E and W44F, the spatial resolution of the CO (6–5) maps of 9.1″ corresponds to 0.13 pc, which is of the order of the diameter of dense cores. Substructure on smaller scales is highly expected, but as the CO (7–6) maps suffer from high signal-to-noise and no observations with higher spatial resolutions have been performed yet, we used the CO (6–5) maps as basis for our estimates of the filling factors for our analysis. We therefore plotted the half-maximum contours of the local maxima corresponding to our positions of analysis to compare the emission regions with the beam size of the analyzed spectra convolved to a common spatial resolution of 18.2″. These plots can be seen in Fig. 45 and 46.

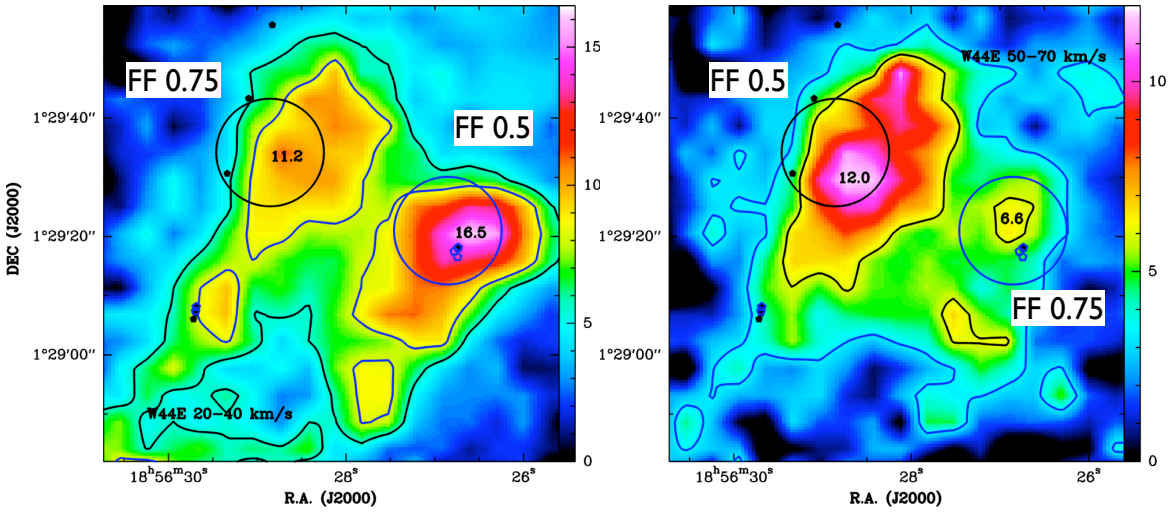

Figure 45: Velocity integrated CO (6–5) emission at its original resolution of 9.1″, integrated between 20–40 km s^{-1} (blue wing, left) and 50–70 km s^{-1} (red wing, right). The wedge unit is K km s^{-1} in antenna temperature. The peak intensity values of the local maximum emission corresponding to the positions W44E Red (black circle) and W44E Blue (blue circle) and the assumed values of the filling factors are given in the figures together with the half-maximum contours of the local maxima (W44E Red: black line, W44 Blue: blue line).

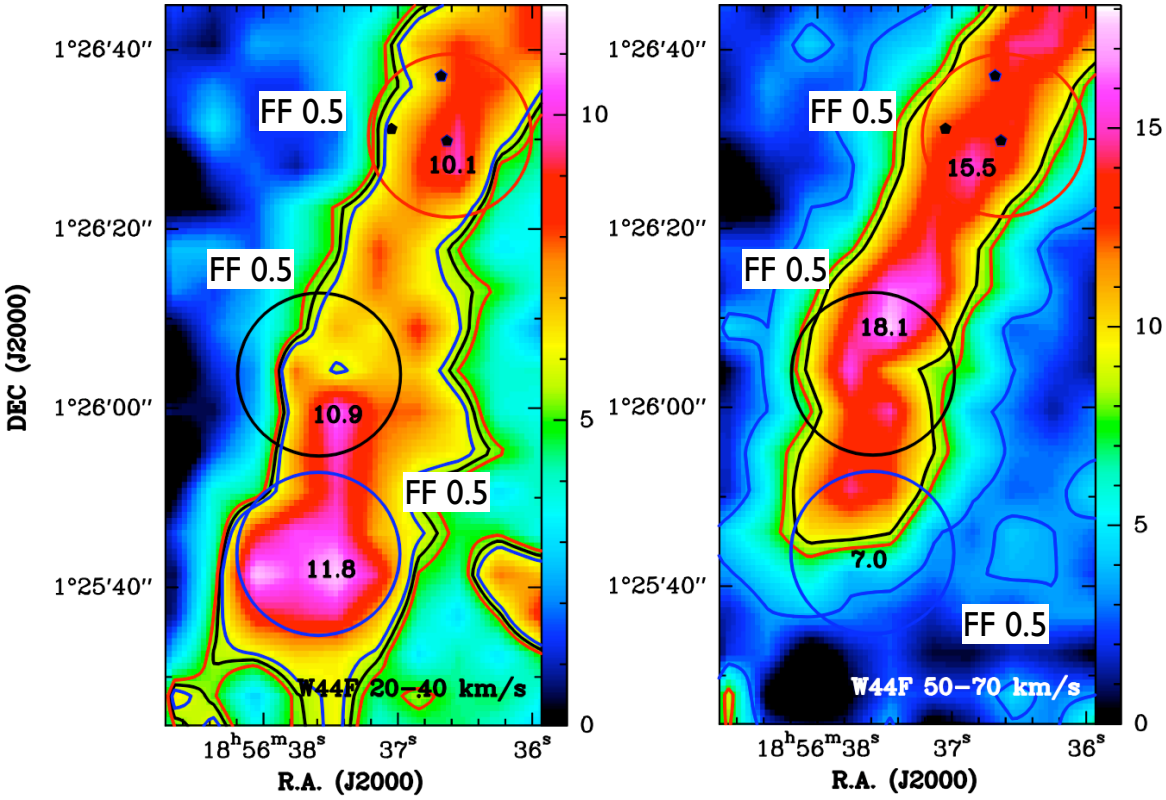

Figure 46: Velocity integrated CO (6–5) emission at its original resolution of 9.1″, integrated between 20–40 km s^{-1} (blue wing, left) and 50–70 km s^{-1} (red wing, right). The wedge unit is K km s^{-1} in antenna temperature. The peak intensity values of the local maximum emission corresponding to the positions W44F RedN (red circle), W44F RedS (black circle), and W44F Blue (blue circle) and the assumed values of the filling factors are given in the figures together with the half-maximum contours of the local maxima (W44F RedN: red line, W44F RedS: black line, W44F Blue: blue line). As the blue position does not show a local maximum in the red wing map a central value of 7 K km s^{-1} was assumed for the plot of the half-maximum contour.

14

SUMMARY

Like W28, W44 is a radio-bright, so-called mixed-morphology type supernova remnant that is interacting with a nearby molecular cloud. This interaction is evident from maser emission, highly excited far-infrared CO and near- and mid-infrared H_2 emission, and observed broad line wings. We have presented new mapping observations with the APEX telescope in ^{12}CO (3–2), (4–3), (6–5), (7–6) and ^{13}CO (3–2) towards regions E and F in W44, where also OH maser emission is observed. Within these regions, we have identified five positions of clear shock interaction, based on the local maxima of CO emission in all transition maps. Towards these positions, we extracted the integrated intensities of the observed spectra for the blue and red velocity wing separately. The integrated intensities of CO (7–6) and (6–5), which unambiguously trace the shocked gas, were compared to a large grid of models, which combine an MHD shock code (as described in Part II) with a radiative transfer module based on the 'large velocity gradient' approximation. We found that only non-stationary shock models are compatible with the observations. The relatively young age of these shocks of no more than 3000 years is consistent with the remnant's age of 20,000 years. The preshock density of all models amounts to 10^4 cm^{-3}. The best-fitting models in W44E have velocities of ~20 km s^{-1}, which seems low given the broad line widths. We therefore also presented the best-fitting models with velocities ≥30 km s^{-1}. The magnetic field strengths of all best-fitting models in W44E are 100–200 μG, while in W44F we found values of 200 μG in all positions. As already the case in W28, our best-fitting shock models underestimate the emission in CO (3–2) and CO (4–3) such that we had to add an unshocked component, calculated as a CO layer with the LVG module in 'homogeneous slab' mode. This behaviour is expected, since our shock models do not account for the unshocked gas component that contributes to emission in the lowest transitions. Based on our best-fitting shock models, we could give predictions for the expected emission of para- and ortho-H_2O and for the full ladder of CO up to an upper rotational quantum number of 40. Corresponding observations will help to reduce degeneracies of our modelling results. Furthermore, we estimated the shocked gas mass in one beam as well as the momentum- and energy injection per beam. We found that the interaction between the SNR and the molecular cloud dissipates a significant fraction of the total initial energy of the supernova explosion.

Part IV

PHILOSOPHY

Empirical sciences pursued purely for their own sake and without philosophic tendency are like a face without eyes.

Arthur Schopenhauer 1819

Philosophy of science is about as useful to scientists as ornithology is to birds.

attributed to Richard Feynman (1918 –1988)

15

PHILOSOPHICAL REFLECTIONS ON ASTROPHYSICS

Philosophy of science has become a discipline that operates in very close proximity to actual research practice. Therefore, it seems promising to use philosophical concepts in the reflection of the research I have done in recent years. On the one hand, I thereby hope to yield another example of application to the philosophical discussion, on the other hand, the aspirations and the scope of my work might become clearer. In Sect. 15.1, I will first introduce some elements of astrophysical research practice in order to supply a background for the philosophical reflection on astrophysics in general and on my own work in particular that are then described in Sect. 15.2.

15.1 ASTROPHYSICS

15.1.1 *How astronomers see themselves*

Astronomers usually put emphasis on certain specifics when presenting their scientific field to novices or the public in their introductory lectures, textbooks, public talks, or articles. For instance, they stress the early historical roots of astronomy from the Babylonians and ancient Greeks through to Kepler and Newton. Methodologically, astronomy is often seen as having been a paradigmatic case for the development of natural sciences. The astronomer Ludwik Oster, for example, characterized astronomical observation as a starting point of human efforts to understand nature beyond every-day needs:

> "Scientific methods as we understand them today were first applied in astronomy, and the results and theories of the astronomers appeal more than any others to the speculative mind. Thus, in a very real sense, the history of science begins with astronomy." (Oster 1973, p. 1).

This might be closely connected to the frequently found reference to the human eye as the first observation tool. The common way of speaking "a telescope sees X-rays, radio emission, etc." also seems to have its origin in this historical view (e.g. "No longer limited to detecting visible light, telescopes are now capable of "seeing" gamma rays, X-rays, ultraviolet light, infrared radiation, and radio signals.", Carroll & Ostlie 2006, p. 20). In early history, observations of the sky are typically described as being purely descriptive but an evolutionary cut took place as soon as *explanations* for what is being observed were sought. This transition, constituted by the application of physical methods to cosmic phenomena, is often denoted as the transition from classical astronomy to today's astrophysics. The reported success of the astrophysical method provides the particular attraction of this subject. As Albert Einstein put it: "The most incomprehensible thing about the universe is that it is comprehensible" (Einstein 1954, p. 292).

The successful application of physical theories and models stemming from laboratory experiments within astrophysics may seem surprising for several reasons. Firstly, astrophysics deals with phenom-

ena being more extreme than anything that can artificially be generated in the laboratory. Connected to this fact is the second, big "drawback" (Kutner 1954, p.1) of astrophysics: it cannot perform traditional experiments. It is impossible to change the environments of astrophysical objects or to manipulate the objects themselves. There is no way to actively direct test conditions: the distance between the astrophysicist and the object of research is too large. Accordingly, the universe itself becomes a "cosmic laboratory" that provides a variety of objects in various conditions. The missing possibility of direct intervention, marking the difference between observational and experimental sciences, puts the astronomer in a situation in which he or she is only able to study the information sent out by the astronomical objects spontaneously. Therefore, the astronomical method is often being characterized as a clever collection of clues and their interpretation:

> "We must passively study the radiation that they [the astronomical objects] give off. For this reason, we refer to astronomy as an *observational* science rather than an *experimental* one. It is because of this difference that we must be clever in using the information we do receive." (Kutner 1954, p. 1)

In his monograph "Cosmic Discovery – The Search, Scope and Heritage of Astronomy" (1981), the astrophysicist Martin Harwit reflects astrophysical research beyond the level of introductionary remarks. His theses mirror the conceptual distinction between passive observation and subsequent interpretation. Harwit emphasizes the fact that due to its observational character astrophysics seems easier to analyse than other natural sciences:

> "Observation is the most passive means for gathering data. The observer receives and analyzes information transmitted naturally by the system he is studying. The experimenter, in contrast, stimulates the system under controlled conditions to evoke responses in some observable way. [...] Observation is the simplest form of experimentation. Because of this simplicity the scope of a purely observational discipline, such as the study of the universe beyond the solar system, should be simpler to analyse than the potential wealth and complexity of an experimental science." (Harwit 1981, p. 5)

According to Harwit, only a limited number of possible information carriers[1] which can be combined with a set of elemental observational parameters[2] are available to astronomical research within the scope of technical feasibility. Thus, the phase space of possible astronomical observations is constrained in its volume. In this perspective, the corresponding historical task of astronomers is the successive coverage of this accessible phase space with real observations. This yields a natural growth in cosmic discoveries. The more the phase space of possible observations is exploited, the closer will the final aim of discovering all the cosmic phenomena become. Harwit sees an analogy between the evolution of astrophysics and the evolution of geography: In the 15th and 16th centuries geographical discoveries were made most frequently and after that basically no unknown phenomena remained on

1 These are: electromagnetic radiation, cosmic-ray particles, solid bodies, neutrinos and anti-neutrinos, and gravitational waves (Harwit 1981, p. 26).

2 These are: the type of carrier to which the observing instrument responds, the wavelength or energy of the carrier, angular resolution, spectral resolution, time resolution, polarisation if present, time, date, and the direction of the observation (Harwit 1981, p. 29).

the surface of the Earth. Harwit expects a similar development in the field of astronomical research in about 200 years.

In summary, favoured by its observational nature, astrophysics might be prone to a cumulative concept of scientific evolution: The alleged passivity of observation might suggest that we should see the fundamental historical advance of astronomy as a successive collection of new data/information. The view of the night sky seems to be the same for today's astrophysicists as it was for their ancestors several thousand years ago and this supports the idea of historical continuity. In this view, only the interpretation ("explanation") of observational data may be subject to historical change. However, because astrophysics seems to be less theory-driven than other physical disciplines, the continuous aspect of observational science evolution seems to dominate how astrophysicists see themselves. This is supported by the analogy of seeing – the modern telescope being the derivative of a Kepler telescope. While the method of how to manipulate objects of research experimentally seems to offer more historical variability due to its complexity, "mere" observations might seem epistemically unsuspicious. Against this background, it might be interesting to compare astrophysical research practice more closely with some of these common conceptions.

15.1.2 *Astronomical science practice*

The impossibility of creative, experimental interaction couples astrophysical progress closely with the development of new technological feasibility. New discoveries seem stronger correlated with the introduction of new observational techniques than with theoretical breakthroughs. Within the last decades, due to ever increasing technical requirements astrophysics has increasingly become an endeavour of international consortia, relying on the national and international coordination of science goals and science funding.

From a researcher's perspective, the genesis of astrophysical knowledge takes places within a network of interconnected processes (see Fig. 47). In a first approximation, the following processes can be distinguished:

15.1.2.1 *Application for observation time*

The need to apply for observation time has only arisen relatively recently. In the 19th century basically every university had its own observatory. Jaschek (1989) reports an exponential growth of small observatories during this time, primarily due to the founding of new universities. Motivated by the need for more complex and larger telescopes, American astrophysicists were the first to install large observatories on mountains at the end of the 19th century, financed by large private funds. Such observatories were the Lick Observatory on Mt Hamilton or the Mt Wilson Observatory on Mt Wilson. These observatories were the first to introduce a separation of the observing site from the site where observations were analysed. Subsequently, the time of national facilities began in the early 20th century. France started its Haute Provence Observatory, while the US National Science Foundation established a system of national observatories, such as the National Optical Astronomy Observatory at Kitt Peak (Jaschek 1989). Finally, multinational observatories were established, as for example the European Southern Observatory, which was set up in 1962.

Today astronomical observing instruments are usually planned, financed and operated by large international consortia. The "open skies" policy however makes it possible for scientists worldwide to apply for observation time for their individual research projects. To do so, the applicants have to elucidate the scientific question they want to explore on the basis of new data. Furthermore they have to demonstrate that they know the recent state of the art concerning that question and that they have the competence and capability to perform the necessary data analysis. The decision on the distribution of observation time is then made in a peer review process by a panel of scientists.

There are several factors that are relevant when applying for astronomical data. First of all, an astronomical observing proposal needs to be considerate of its technical feasibility. What is being proposed is furthermore influenced by the already existing knowledge about the phenomenon in question and has to correspond with this knowledge up to a certain degree[3]. Modelling is another factor that plays a role in the application process. On the one hand, models of phenomena justify what is expected to be observed, or to what extent the proposed observations are crucial for the understanding of the phenomena under study. On the other hand, a simulation of observational "dummy" data including systematic and random errors can be used to show the feasibility of the analysis method.

Obviously, the step of applying for observation time is central within the scientific practice because it is this step that decides on the empirical basis of astrophysics. The decision on observational project funding and the distribution of observation time might be subject to social and political factors. Altogether, it seems an interesting question whether the process of applying for observation time encourages conservative scientific approaches in line with existing paradigms, and in how far the possibility of non-directed, fortuitous observation is still warranted.

15.1.2.2 *Data generation*

After an observing proposal is granted time, there are several possible ways as to how to perform the observation (Longair et al. 1986; Jaschek 1989; Zijlstra et al. 1995): 1) Remote operation: the instrument is operated under remote control as the case for space telescopes. 2) Observing at the site: the astronomer carries out the observations him- or herself and is assisted by the local staff 3) Remote observing: the local staff is operating the telescope while the astronomer is not present. The astronomer is however informed in real time and can intervene. 4) Service observing: the astronomer provides the necessary technical details needed to perform the observation to the telescope staff and is sent the data after it has been recorded.

The historical development seems to indicate that service observations are also starting to prevail where ground-based observations are concerned. However, even if the astronomer travels to the site him- or herself, the technical complexity of the observing instruments usually requires a specialized technician, who knows the scope of the instrument and how to achieve optimal performance, to be present. Physical theories relevant for the operation and usage of observational instruments are for instance solid state physics, low temperature physics and electrodynamics (see e.g. Subsect. 8.1.1).

The above mentioned elemental parameters characterising an astronomical observation (like wavelength, spatial and spectral resolution or exposure time) get fixed within the observing proposal. However, the concrete performance of an observation still gives some extra scope (tuning, calibration,

3 In a public talk at the University of Bonn in 2010 Jocelyn Bell Burnell criticized this fact in that it does not allow for really innovative projects.

reaction to weather conditions), which requires experience of the observer and determines the data quality as some kind of implicit knowledge. It is interesting that in the case of service mode observations a change of subject takes place with the correspondent possibility of information loss between the recording of raw data, and data reduction or data analysis. In order to distinguish valid results from mere artefacts, it is necessary that the observing instruments are understood on a relatively high level and it is to be ensured that no relevant information concerning the process of data generation is lost.

15.1.2.3 *Data reduction*

As soon as the users receive the raw data, they generate so-called data models (see Sect. 8.3) from the raw data. In other words, the raw data is transformed into a form that is suitable for scientific interpretation. Firstly, data of bad quality is removed ("Flagging") and the data is calibrated. Depending on the specific instrumentation (single dish telescope, interferometer, spectral receiver, continuum receiver), the manipulation of the raw data can exhibit a very complex, iterative structure and include the usage of source models or models of telescope- and atmospheric emission. The data reduction is usually performed using software packages that are publicly available for the scientific community. The documentations of these software packages show very different degrees of elaboratedness. In textbooks the task of data reduction with its relevant mathematical and technical preconditions is referred to, if at all, only in passing. The step of data reduction therefore seems strongly influenced by the individual transfer of practical experience ("tacit knowledge", Polanyi 1958), particularly with respect to ingoing parameters and methods. It might be interesting to study, how data reduction is shaped by tradition, education and familiarisation, and how a particular style of data reduction common in a particlular research group is transferred, varied, developed and tested.

15.1.2.4 *Data interpretation*

The central step in the genesis of a scientific fact is the data interpretation, the inference from observational data to the assumed astrophysical phenomenon. Within astrophysics, this is strongly linked with the application of models and statistical methods. At the same time, a proper visualisation of the data is already leading the way to the final interpretation. Which inference is being accepted and how errors in the interpretation are ruled out might be governed by the current scientific paradigm. Elements of this paradigm and differences between the paradigms of different research groups may become apparent in cases where contradicting interpretations are disputed, or if difficulties arise within a chain of reasoning.

15.1.2.5 *Modelling*

During data interpretation, but also in the course of data reduction and the planning of observations, numerical modelling becomes important. The vast distances between astrophysical phenomena and the observing scientists prevents manipulation as well as carrying through experiments. Therefore, a prominent role of astrophysical models is to enable explanatory access to the modelled phenomena (Bailer-Jones 2000). Within simulations, input-data, ingoing theory-elements, and boundary conditions can be varied and the corresponding consequences for observable quantities can be studied.

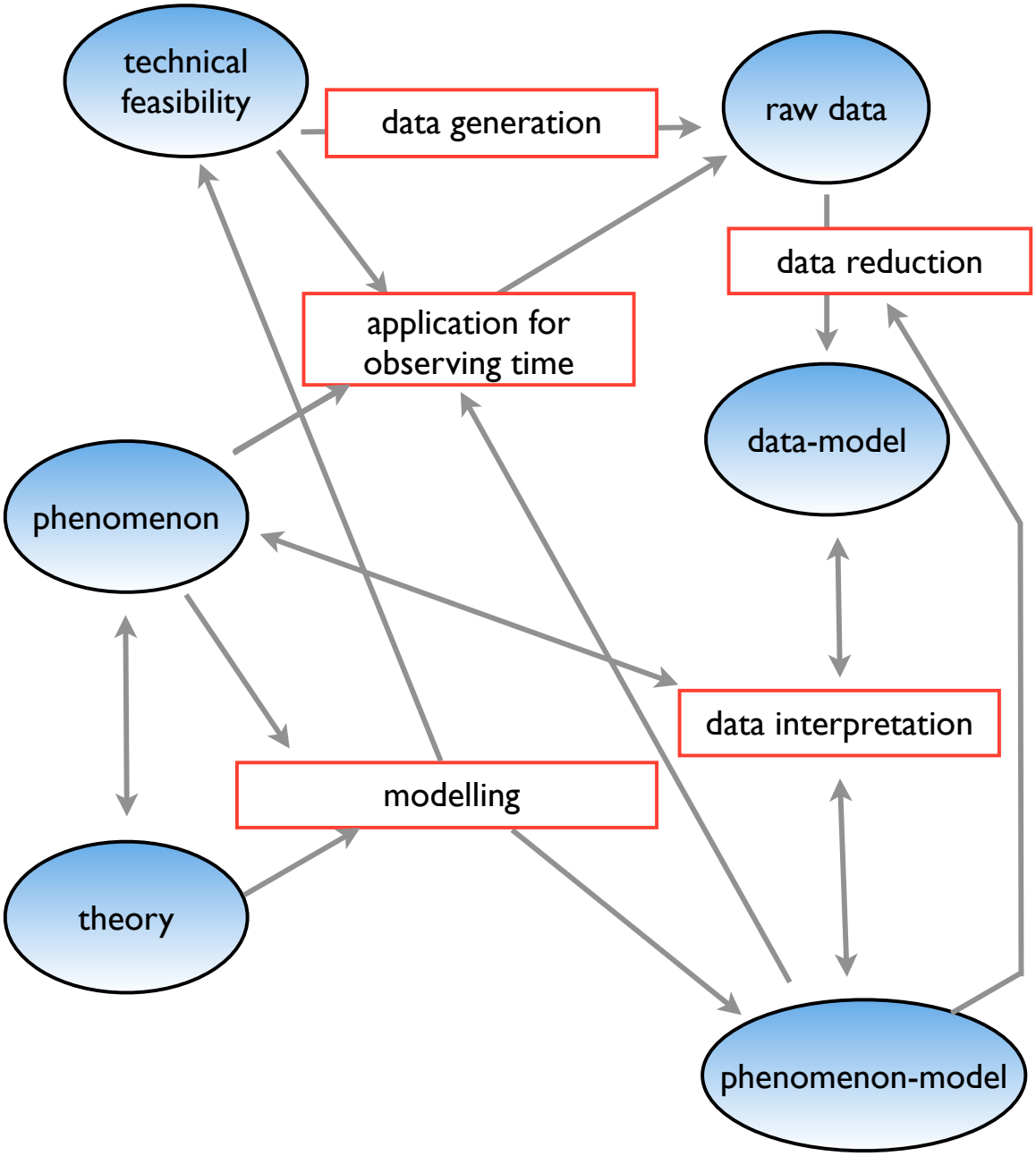

Figure 47: Schematic of astrophysical research practice. The red squares show the key research processes described in Sect. 15.1.2. Blue circles indicate key elements of astrophysical research, while arrows illustrate direct influences between these elements and processes.

Furthermore, models become increasingly important in the execution of observations as the performance of instruments is being tested with the help of simulations and as data generation explicitely relies on the use of models. Therefore, it is not possible to locate modelling solely on the side of scientific interpretation. We also face a hybrid situation on the side of empirical observation today, in the sense that empirical data builds upon and depends on modelling.

My thesis, at least implicitly, covers all of the aforementioned research processes. Chapter 5 deals with the development of a numerical model for an astrophysical phenomenon, Chapters 9 and 12 present information on data generation, and results of data reduction and interpretation. Furthermore, and in parallel with the work presented in these chapters, complementing observations were proposed at several observing facilities.

15.2 PHILOSOPHY OF SCIENCE

Traditional philosophy of science, as associated with the Vienna Circle around 1930, was mainly oriented towards (theoretical) physics as leading science. Its main concern was a logical analysis of scientific languages, its picture of science was that of a cumulative accumulation of knowledge approaching truth. Science was seen as being amenable to supratemporal analysis. Its universal criteria and concepts were thought to be extractable by philosophy largely independent of the empirical sciences. Typical questions within this tradition, for instance, were the criterion of meaningfulness of empirical sentences, the problem of inference to general natural laws or the structure of scientific explanations (Hoyningen-Huene 1995). A historical perspective on science that is subject to social and historically contingent factors was only established when Thomas S. Kuhn published his monograph "The Structure of Scientific Revolutions" (Kuhn 1962). The analysis of massive inconsistencies within the history of science and the claim that valid knowledge is understood and evaluated only against the background of the leading paradigm created a twofold crisis for the philosophy of science (Hacking 1983). At stake was the assumption of a time-transcending rationality that leads science and is able to ensure scientific progress. Furthermore, a realistic interpretation of scientific theories and of its postulated entities seemed to be endangered. The result was a reorientation of philosophy of science in the 1960s. Its focus shifted towards scientific practice and its plurality, as well as to questions that are characteristic of individual scientific disciplines. At the same time, the so far strongly theory-dominated discussion was expanded by an appreciation of experimental practice. Ian Hacking paved the way for a philosophy of experiment. Claiming that "experiments have a life of their own" (Hacking 1983), he considered experimental work as being tantamount to theory construction. A philosophy of the experiment would then deal with, e.g., the reliability of data and the different roles of experiments within scientific practice. On the other hand, Nancy Cartwright highlighted the distinction between fundamental and phenomenological laws in her monograph "How the laws of physics lie" (Cartwright 1983). While the former are supposed to yield theoretical explanations, the latter describe the actual phenomena: "Phenomenological laws describe what happens." (Cartwright 1983, p. 2). Accordingly, Cartwright specifies the structure of scientific explanations: fundamental laws are not directly applied to reality. Rather, a model is derived from the theory, yielding a phenomenological model applicable to reality. The philosophical reflection of models and, since the late

1970s also of numerical simulations, is another branch of philosophy of science that has strongly been acknowledged in recent years.

There are only relatively few publications within the philosophy of science dealing with the scientific practices of astrophysics. In spite of the alleged specifics of astrophysics, often mentioned by astrophysicists and summarized in Sect. 15.1.1, a "philosophy of astrophysics" does not exist. However, three main discussions based on astrophysics can be identified: the question of realism within astrophysics, the discussion of scientific observations, and the study of modelling and simulation in astrophysics. Another interesting issue which has attracted growing attention in recent years and which is also highly relevant for astrophysics is the question of how to handle data. In the following Sections, we will go through these topics and, after a brief summary of the literature, apply it to the topics of this thesis.

15.2.1 *Astronomy and antirealism*

15.2.1.1 *Hacking's claim of astronomical antirealism*

In his book "Representing and Intervening" (Hacking 1983) Ian Hacking tried to link scientific realism to the manipulability of the object of research. Accordingly, he cannot attribute the claim of realism to astrophysics because a direct interaction with cosmic phenomena[4] is impossible. In his paper "Extragalactic Reality: The Case of Gravitational Lensing" (Hacking 1989) he thus argues for an antirealism with respect to cosmic phenomena. His argument is exemplarily based on the difficulties concerning the observation of theoretically predicted gravitational lenses. If, as he claims, there could be numerous non-detectable micro lenses, astronomical observations would be inherently untrustworthy, because a distorting influence of microlenses on the observed photon fluxed could never be precluded. In this context, he revisits Barnothy's hypothesis from 1965, saying that quasars are no separate class of cosmic objects but rather Seyfert galaxies that are subject to gravitational lensing. While an interaction with the object of research enables systematic tests of possible sources of error in experimental disciplines, this option is prohibited in astrophysics. Instead, astrophysics depends on the use of models brought in line with the observed phenomenon – a fact on which Hacking builds his second argument against astrophysical realism. The confinedness of the modelling approach together with the fact that cosmic phenomena are described by a multitude of contradicting models shows, according to Hacking, that astrophysics make a claim to realism understood as a convergence of scientific descriptions towards the truth. On the basis of these considerations, he then claims a methodological otherness of astronomy and astrophysics compared with other, realistic scientific disciplines in a third argument: The transition towards a natural science, according to Hacking, is marked by the transition towards an experimental method. Astronomy has not made that transition. Although astronomical technology has changed drastically since the historical beginnings of this discipline, Hacking sees the method having remained the same: "Observe the heavenly bodies. Construct models of the (macro)cosmos. Try to bring observations and models into line" (Hacking 1989, S. 577).

4 Here and in the following we restrict ourselves to cosmic phenomena outside of the solar system.

15.2.1.2 *Replies and References to Hacking*

Dudley Shapere argued against such an exclusion of astronomy and astrophysics from the canon of natural sciences in his paper "Astronomy and Antirealism" (1993). Based on astrophysical arguments, he tries to prove Hacking's description of the problems related to gravitational lenses either incomplete or incorrect. The result then for Shapere is not antirealism, but rather the claim that astronomy indeed studies the composition, the structure and the evolution of the universe. He accuses Hacking of consequently underestimating the gained understanding of the astronomers. Furthermore, he criticizes Hacking for his non-representative choice of gravitational lensing as a very young scientific field of research at that time. Apart from that, and according to Shapere, the part of Hacking's argument that is based on the use of models, reaches well beyond astrophysics. In addition, astrophysical models are permanently refined and improved, and observations are used to get rid of ambiguities between different models. Instead of antirealism, this point should rather yield agnosticism: even when our possible knowledge is limited, we have good reasons to speak about the existence of astronomical objects. From a philosophical perspective, Shapere shows that the requirements for a realistic science developed in Hacking's third argument are also applicable to astrophysics due to a lack of conceptual clarity: Hacking demands real entities to be used as instruments by means of which experiments can be done. Shapere shows that the "use" of cosmic phenomena in the investigation of others is well possible, even when they cannot be manipulated. Gravitational lenses, for instance, can be used for the detection of dark matter and for distance determination. For Shapere the scientific method is not so much based on experimental interaction, but rather on the practice to extrapolate from knowledge already obtained to something new. In this perspective, astronomy is perfectly in line with the other natural sciences.

Michelle Sandell (2010) criticizes Hacking's experimental requirements for realism as being too restrictive. Firstly, they would exclude too many sciences, secondly, only phenomena created in a laboratory would accordingly be real, and thirdly, it remains unclear to what extent these phenomena can be seen as being representative of the undisturbed nature. Furthermore, she argues that astronomers do in fact carry through experiments, also within Hacking's meaning of manipulating the causal power of phenomena. Astronomical objects also possess causal impacts, which can be used by astronomers to generate stable phenomena, e.g. measurement results of a receiver.

The question for realism within astronomy was taken up again from a sociologist's perspective by Götz Hoeppe in 2012. In an ethnographic field study he finds that the idea of the reality of cosmic phenomena manifests itself for the astronomers when they witness the recording of astronomical observations at a telescope, e.g. when the picture of the observed phenomena appears on the monitor of the observing computer in real time.

15.2.1.3 *Are shocks real?*

First of all, it is to be noted that the question of the reality of shocks is one that does not arise within science[5]. On a basic level, the reality of shocks, understood as supersonic motions of matter traced

5 Therefore, one could question the justification of this discussion, e.g. following Margaret Morrison: "I think the more interesting question is epistemological issues that arise within science, and there are many of them. We don't need to look to philosophy to create problems." (Interview at the meeting of the German Society for Philosophy of Science, Hanover 2013).

by the Doppler-shifting of spectral lines, is tacitly presupposed. On a more model-specific level, the reality of particular shocks (such as plane-parallel J-type or C-type as described in Subsect. 1.1.1 and 1.2.4) is mostly not assumed anyway, because the assumptions and simplifications entering the mathematical descriptions and numerical models are too severe for a literal trust in their results. We will return to the latter point in Subsect. 15.2.3.

One might, however, be reminded of Hacking when Lequeux (2005) says: "It is not really possible to directly observe shocks. However, the radiation of the medium heated by a shock is observable and can serve as a diagnostic for the existence and properties of a shock." (p. 257). The (J-type) shockfront itself as a region where bulk kinetic energy is transformed into thermal energy is (yet) too thin to be resolved by our telescopes. In this respect, shocks seem to resemble gravitational lenses in that it is only their effects being observable for us. So, would Hacking's arguments work in the case of interstellar shocks?

To start with, the case for shocks is much clearer than the case of gravitational lenses at the time of Hacking's article. While the objects responsible for the lensing effect, in particular, the "quasi-stellar-objects", still gave rise to many uncertainties and speculations, the objects and processes related to shocks in the interstellar medium are very well known today. Of course, there always remains a theoretical possibility that all our astronomical observations could be systematically distorted by some enigmatic, unknown phenomenon. But this phenomenon would need to influence all our observations in a way that is remarkably consistent with the models and theories we use today. In particular, it should render general statements about cosmic phenomena as presented in Part I of this thesis very difficult, because the properties of the "distorted" cases would be determined by an additional causal factor not included in theories and models, while these would probably work well for "undistorted" cases. Therefore, the existence of such a distorting influence seems very unlikely, at least for galactic phenomena where a wealth of different, high-resolution observational information is accessible[6].

The (weak) claim that shocks exist in the interstellar medium does not more than mantaining that there is matter moving at velocities exceeding the local speed of sound. If we believe the Doppler shift of spectral lines to be a well-established physical phenomenon (explorable in the laboratory), the broadening of spectral lines would already proof the reality of shocks, given that the physics outside of our solar system is not fundamentally different from that on earth. Furthermore, the general properties of J-type shocks can also be explored in earthly laboratories. To say that shocks in the interstellar medium are not real, would thus correspond to saying electrons outside of the laboratory are not real. We therefore agree with Michelle Sandell when she asserts that an ontological distinction between entities found in laboratories and entities found in the "untouched" nature does not make sense. It is important to note that the application of the concept of J-type shocks was not successful in some cases of observed shocks where the predicted dissociation of molecular hydrogen contradicted the observed strong radiation of rotational lines of molecular hydrogen (e.g. Draine et al. 1983). This anomaly was finally resolved by the introduction of C-type shocks, which had not been known from laboratory studies before. This development might serve as an example for the fact mentioned by Shapere that

6 The absence of an unknown factor systematically distorting astronomical observations does not logically follow from the overall consistency of observations with models based on physics we know from experiments. The type of inference would be an "abduction" or "Inference to the best explanation", as for instance described by Charles Sanders Peirce. We note that this kind of inference has been well debated on its own (for an overview see e.g. Douven 2011).

there is a close interplay between modelling and observations, where shortcomings of the models are identified (in this case the false assumption of a single-fluid description) and subsequently eliminated.

Finally, shocks are a very good example for an astronomical phenomenon being frequently used as a tool in the understanding of other phenomena. That is the case because shocks give rise to a very strong emission of electromagnetic radiation, they make processes visible that might otherwise be hidden from the astronomer's eyes. A case in point is the understanding of the early stages of star formation hidden in dense, dusty clouds. Here, shocks caused by bipolar jets and outflows can yield valuable information on the processes taking place that would not be available otherwise.

As already mentioned before and as further elaborated in Subsect. 15.2.3, the awareness of modelling limitations in view of the vast complexity of astrophysical phenomena lead to a rather modest use of ontological statements in astrophysics with respect to detailed modelling results. Astronomical observations however offer a lot of different routes to examine cosmic phenomena available in many different environments and evolutionary stages in our Galaxy and beyond. The possibility of manipulation does not seem to add a substantially new quality to these possible routes of examination. Furthermore, the impossibility of an experimental manipulation is also found for some phenomena that are subject to scientific inquiry on earth (for instance the global climate, weather phenomena, etc.) the reality of which nobody would doubt.

So, what major differences between experiments and observations could there be? One might say that a) there are less unknown / uncontrollable, casually relevant factors in experiments and b) parameters can be individually varied and their influence be studied. Stating an ontological difference between entities subject to experimentation and entities that are observed would then, according to a), result in a coupling of ontology to a possibility of reduced complexity and therefore creating a general problem for the reality of complex, not directly observable phenomena where not all causally relevant factors can be controlled (like the climate or weather phenomena). An astronomer's response to b) would be that although we cannot vary individual parameters, we can still choose appropriate cases from the vast variety of different phenomena being observable in the universe (the "cosmic laboratory"). This method, strongly relying on statistics and an appropriate choice of samples, might be epistemologically more uncertain than the "simple" experimental manipulation of parameters. However, a coupling of realism to the degree of epistemological certainty again would not exclusively concern astrophysics.

Therefore, we conclude that there is no fundamental difference between astrophysics and other scientific disciplines in terms of scientific realism, neither based on the example of shocks, nor based on general considerations.

15.2.2 *Astronomy and scientific observation*

The concept of observation became philosophically famous through discussions of logical empiricists and positivists in the early 20th century (e.g. Bogen 2013). At the same time, the strict distinction between experiment and observation was abandoned by attributing a central role to observational descriptions also in experimental contexts. Thereby, the concept of observation became closely related to subjective, direct sense perception. Dudley Shapere, however, dissociated himself from this usage of the concept of observation (Shapere 1982). He analyses to what extent one can say, as is

found in astrophysical literature, that by means of neutrino detections one can directly observe the centre of the sun. He subsequently defines a direct observation as a receipt of information with an appropriate receptor, where the information was directly transmitted, without interference, between the observed entity and the receptor. According to Shapere, the understanding of the three elements of an observation (release of information by the source, transmission of information, and the receptor of information) is based on currently valid physical knowledge. Astrophysics provides a particularly simple case for Shapere's analysis, because the theory of the source, the theory of transmission, and the theory of the detector are mostly separated.

Shapere stresses that the "theory-ladenness" of observation does not necessarily yield an epistemological relativism, because the relevant background knowledge is reliable and its uncertainty assessable or independently testable.

His general definition of the term "observation" now enables Shapere to see the human eye as only one special type of a receptor, sensitive to electromagnetic radiation in a very limited wavelength regime. The growth of our physical knowledge then leads to a reasonable extension and generalisation of the concept of observation beyond the limits of sense perception. With this argument Shapere separates the perceptual aspect of the concept of observation from the epistemic aspect and, to a certain degree, makes it independent of a human context: also events registered by a computer can count as observation and scientific evidence. Shapere also adapts the dependence of scientific observations on background knowledge to the case of sense perception. Here previous knowledge is also presupposed and only critically tested in case doubts are raised. Just like pure sense-data do not exist, there are no pre-theoretical scientific observations. According to Shapere, the astrophysical mode of speaking about a direct observation of the center of the sun is therefore fully justified.

15.2.2.1 *Replies and References to Shapere*

Jutta Schickore (1999) criticizes Shapere's generalisation of the concept of observation. According to her, human perception is not satisfactorily covered by such an approach. Using the example of a quasar being subject to gravitational lensing, she demonstrates to what extend astronomical research practice is determined by a qualitative assessment of the visual appearance of generated data. These assessments go well beyond a mere reading of data values. Thereby, Schickore argues for a differentiation of the concept of observation, rather than a generalisation, because within astrophysical research very diverse empirical procedures of observation can be found. As one example she suggests an analysis of the meaning of pictoral (re-)presentations of the phenomena under study, as has already been done for the life sciences (e.g. Lynch & Woolgar 1990).

The role of visual representations has been discussed within sociology by a couple of studies. Lynch & Edgerton (1988), for instance, studied the influence of aesthetic judgments on the production of astronomical images. Hentschel & Wittmann (2000) published a collection of essays, also covering a historical perspective, on the role of visual representations within astronomy. Adelmann et al. (2009) published articles on the visualisation of astrophysical simulations.

15.2.2.2 *Shock observations*

In this thesis I have stated several times that we have observed shocks generated by the interaction of supernova remnants (SNRs) with molecular clouds. We have done that by detecting spectrally

resolved emission of carbon monoxide. Now, as in Shapere's example of the observation of the sun's centre by means of neutrino detections, one might wonder whether this assertion is indeed justified. The claim of shock observation also included a complex chain of reasoning. Generally speaking, we believe that pressure disturbances are sent into a molecular cloud by the SNR, which are supersonicly relative to the sound speed within the cloud, that these pressure disturbances subsequently heat the cloud gas and that this heating (and not something else like a strong radiation field) leads to emission in the high transitions of CO, which we can then observe without severe distortion between the source and our telescope. Shall we be more modest and rather say that we have observed photons of a certain wavelength stemming from a certain direction in the sky and then applied a theoretical interpretation on that finding?

Concerning shocks, we can also speak about a theory of the source (as presented in Chapter 1), a theory of the transmission (line radiative transfer), and the theory of the receptor (as e.g. outlined in Section 8.1). As in Shapere's example, we have seen that the theory of the source relies on modelling and incorporates many assumptions and uncertainties. These uncertainties, however, are critically assessed by a careful study of the model and of the robustness of the predictions. The general statements which, as summarized above, connect the observation of highly excited CO lines with shock interaction in these regions, seems very reliable at present and are shared by different shock models. With respect to the theory of transmission, we have to be concerned with the general knowledge about possible kinds of photon interactions and the particular knowledge about the conditions being present in the specific case of our observations. Regarding the latter, one could in principle question that all observed photons have their origin in the same galactic region (as was done for lower transitions in early publications, see Denoyer 1983). But because highly excited transitions, such as CO (7–6) and (6–5), only originate from hot gas (much hotter than usual in molecular clouds), it seems very unlikely that several molecular clouds would show such conditions, even if there were several clouds along the line-of-sight. Furthermore, independent confirmation of shock interaction argues for Doppler broadening of the lines rather than a line broadening due to superposition of different emission components along the line of sight. Together with the fact that we do not expect these photons to interact otherwise on their way, it seems reasonable to assume that the information has been transmitted directly between our telescope and the SNR. Finally, the theory of the receptor requires knowledge of the telescope and its optics as well as the particular receiver being used. As we have outlined, in our case the use of SIS junctions allows highly sensitive front ends with a very good noise performance, while Fourier Transform Spectrometer back ends offer high spectral resolution together with a large bandwidth. These technologies have been thoroughly tested and are believed to be highly reliable, although they rest on very complex theoretical foundations. So in summary, as in Shapere's example, prior information plays a major role in the observation of shocks.

Based on his astrophysical example, Shapere opts for a generalisation of the term "observation", where the human eye is only one receptor among others. This generalisation relies on a separation of the perceptual from the epistemic aspects of observations. The separation requires that the seeming dependence of non-perceptual observation on prior information does not make these observations epistemically more uncertain than perceptual observations. In fact, the generalisation of the term "observation" in astrophysics, as Shapere argues, is based on good reasoning, and therefore these non-perceptual observations indeed play the same epistemic role in knowledge acquisition as seeing

the stars with the naked eye. Alleged "theory-ladenness" of observation is therefore shown not to be a problem for the attainment of knowledge: science builds on what is already known in a way that the background information does not include that part of knowledge being tested. In line with this, this thesis can be understood as a presentation of a large part of the elements of background knowledge necessary in the derivation of the scientific results that were published. It comprises general, theoretical knowledge together with specific knowledge with respect to the observed sources and the actual observations and an understanding of uncertainties and possible errors. One may therefore say that this thesis provides the ground to say: we have observed shocks (in the epistemical sense of the term "observing").

The importance of the distinction between the perceptual and the epistemic aspects of astronomical observations frequently becomes obvious in public dialogue. Astronomy, probably due to its history of optical observations, is still very much confronted with the public conflation of perception and epistemic certainty. This becomes visible when the media gets excited about the fact that many astronomical images do not show cosmic objects "as they really look like" because they include colour representations of non-visible wavelength regimes. The expressed worry is that an arbitrary element is introduced by the astronomers as to "fool" the public. "Epistemical" images are misconceived as "perceptual" images. Shapere's work might offer a good framework to clarify this discussion.

On the other hand, Shapere's claim that there is no difference between the eye as a receptor and "non-human" receptors might go a bit too far. Jutta Schickore has made a valid point: Shapere widely neglects the whole part of data selection, -analysis, and -interpretation, which constitutes a central part of what we call astronomical observations. These procedures indeed require a qualitative assessment of the recorded data. This does not make these steps inherently subjective but Shapere's approach remains incomplete if these (human) activities are neglected. We will come back to this point in Subsect. 15.2.4.

15.2.3 *Models and simulations*

Scientific modelling constitutes a central part of science: "Partial models, imperfect as they may be, are the only means developed in science for understanding the universe." (Rosenblueth & Wiener 1945, p. 321). Hacking (1989) considered this as being particularly true for astrophysics: "I suspect that there is no branch of natural science in which modeling is more endemic than astrophysics, nor one in which at every level modeling is more central." (p. 573f). No matter if one is willing to acknowledge such a special role for astrophysics, its scientific practice seems determined by modelling on many different levels. An understanding of the epistemology of models and simulations therefore seems important for a philosophical understanding of astrophysical research.

Within a context of theory construction, two influential approaches in the understanding of models can be distinguished. Within logical positivism, a syntactic view on models was advocated. In this view, a theory is a set of sentences, consisting of a logical theoretical skeleton without empirical meaning, and semantic rules, providing some elements of the calculus with an empirical interpretation. Theoretical terms, referring to unobservable entities, acquire their meaning not on the basis of semantic rules, but in virtue of their position within the calculus. A model, in this regard, is then an interpretation of the theoretical structure, which also interprets theoretical terms by means of seman-

tic rules (e.g. Carnap 1939; Braithwaite 1953). A theory and a model therefore have the same formal structure, but differ in their epistemic status. This position, although being very influential, has been frequently criticized (e.g. Spector 1965; Achinstein 1968).

An opposite point of view has been taken by the semantic view of theories, which understands a theory as a family of models. Models are here seen as logical structures, consisting of a set of individuals, operations, and relations among the individuals. These structures bear a certain relation (e.g. isomorphism or similarity) to structures in the world, thus gaining their representational power. Along with this position comes the assumption that the modelling concept in the empirical sciences can be ascribed to the mathematical modelling concept (Suppes 1960, a recent revision of the semantic view is found in da Costa & French 2003). The semantic view of theories has become a widely accepted account on theories and models, in particularly promoted by structuralist approaches in the philosophy of science. However, it is still a controversial matter to what extend such a mathematisation of the modelling concept is actually able to capture the modelling activity within the empirical sciences and whether the semantic view is contended with difficulties (e.g. Downes 1992; Portides 2005; Frigg 2006).

While these approaches were aiming for a unified modelling concept, the existing multiplicity of different models and their various roles within science were also analysed. For instance, one can distinguish models that are experimentally investigated instead of the studied phenomenon (Rosenblueth & Wiener 1945: "material model", Groenewold 1960: "representative model"), models which allow for an application of a complicated theory to actual observations or which mathematically summarize observations (Achinstein 1968: "impoverished theory", Redhead 1980: "heuristic role of models", McMullin 1968: "phenomenological model", Morton 1993, Morrison & Morgan 1999: "models as mediators") and models that deliberately neglect essential aspects of the studied phenomenon for learning purposes (Groenewold 1960: "study model", Hartmann 1995: "toy model"). The epistemology of the latter class of models has been discussed at length amongst economists. That is so because the question arises to what extent a model can give valid results if it is based on false assumptions (Gibbard & Varian 1978: "caricature models", Musgrave 1981).

The diversity of models and their roles seems to hint at the diversity of scientific practices and thereby at the actual use of models within knowledge acquisition. This extends the initially binary relation between phenomenon and model to a three-figure relation, where the scientist becomes involved as an interpreting, interacting user of models within a certain research practice. Within this approach the question of how learning is possible with models does not refer to the abstract question of how models represent anymore. It rather addresses the problem of how models are epistemically used (Hartmann 1995, 1999; Keller 2000; Bailer-Jones 2002; Knuuttila & Merz 2009). Models thereby acquire "a life of their own". This is related to the fact that knowledge is already attained in the course of their construction and manipulation (Redhead 1980; Morrison & Morgan 1999).

The modelling discussion experienced an expansion when the use of computers and associated numerical modelling and simulation became an inherent part of science (for a recent overview see Winsberg 2013). For the first time, this development granted epistemical access to complex systems with many degrees of freedom, often described by systems of differential equations. While the analytic solution of these was often impossible before, it became solvable by computers in a discretized form. Thus, dynamic computer simulations have obtained some similarity to the experimental method

(Rohrlich 1990: "theoretical model experiments"; Morrison 2009), a feature making simulations a particularly central tool for disciplines without or with only a restricted possibility of classical experiments. Simulations seem to require their own epistemology (Rohrlich 1990; Winsberg 1999, 2001, 2003; Humphreys 2004). Winsberg (1999) analysed the process of simulation to include several characteristic steps[7] and transferred rational testing strategies to simulation results, as originally elaborated by Franklin (1986) for an experimental context (see Subsect. 15.2.4). Winsberg's conclusion is that the epistemology of simulation is an empirical epistemology, not merely a mathematico-logical one. As such it depends on several factors, e.g. on what we know about our computers, our graphical techniques and our confidence in ad-hoc models derived from laboratory and observational experience.

The possibility of the usage of powerful computers in the investigation of the temporal evolution of complex dynamical systems thereby also brings about epistemological problems. On the one hand, ingoing approximations and idealisations easily disappear from view in extensive numerical source codes. On the other hand, it is possible to achieve empirical adequacy by introducing additional parameters and ad-hoc elements, without a physical understanding of the system and the adequacy of the modelled processes being necessary (Hartmann 1996). Therefore, the question for the validation and verification of simulation arises (e.g. Roache 1997; Winsberg 1999; Oberkampf & Trucano 2002), especially in cases where empirical data is not easily available.

15.2.3.1 *Models in astrophysics*

Besides economics and climate science, astrophysics belongs to the group of subjects, the objects of which cannot be reduced in their complexity by means of experiments. Accordingly, the role of models and simulations is central and phenomenological laws, in the sense of Cartwright (1983), prevail over fundamental laws. Also, the developmental time scales of cosmic phenomena are typically so large that observations of these evolutions based on only one evolving object is impossible for a human being. The accessible cosmic sample of objects in various evolutionary states is therefore to be connected within a consistent evolutionary model with the aid of simulations.

Models always rely on idealisations, simplifications, and assumptions on the modelled object. Therefore the question of the reliability and validity of the results obtained by models and simulations is central. In Astrophysics, unlike climate science and economics, it can be raised largely independent of political and public interest. As the results of astrophysical simulations cannot be tested experimentally, the only possible empirical test is a comparison with observations, which often can only yield a relatively weak criterion of adequacy, because exact quantitative agreement between simulation and observation is only to be expected in exceptional cases. Alternatively, different simulations can be compared among each other, and a simulation can be tested for inner consistency and physical correctness.

Astrophysical modelling and simulation has been subject of the modelling discussion in several contexts. Graßhoff (1998) reconstructed a collective and international modelling process using the example of the 1987 discovered microquasar SS433, comprising a longstanding sequence of model-

7 These steps are: 1. identify the theory that describes the phenomena, 2. specify a class of parameter values, boundary values, and initial conditions, 3. construct a computational model and discretize the equations, 4. choose modelling assumptions, 5. interpret the data.

modifications, data generation and investigation of theoretical implications. Although the participants of this modelling process typically only take part for a limited time and often only understand partial aspects of the whole model, the model building according to Grasshoff is governed by a consensus with respect to explanatory schemes, data evaluation and model construction guidelines. These agreements create a self-organising collective of researchers, even though there is great diversity within the collective with respect to present knowledge, used instrumentation, and the understanding of the overall model.

Bailer-Jones (2000) also studied the modelling of a cosmic phenomenon, specifically the modelling of extended extra-galactic radio sources. She describes the split-up of the model of a phenomenon into partial sub-models, which are easier to handle, but need to be theoretically and empirically consistent if embedded into an overall model. As an important aspect for the recreation of the unity of various sub-models she identifies the visualisation of the phenomenon. Scientific creativity appears accordingly to be efficiently channelled by this division of work and is promoted by visualisation.

Winsberg (2001) presented the simulation of the convective properties of a red giant as an example, which is particularly difficult to model because the fluid properties on small scales exert a strong influence on the fluid properties on large scales. In order to address this problem several modelling assumptions and ad-hoc terms are necessary. Winsberg uses this example to derive characteristic properties of simulations: They lead from the theory down to its application; they are utilized in cases for which only sparse empirical data exist with respect to the modelled phenomenon and therefore the simulations have to be justified internally; finally, they do not solely rest on theoretical knowledge, but also on experience and implicit knowledge. Accordingly simulations cannot be understood by means of the semantic or the syntactic modelling concept, but have to be seen as representations of real systems, mediating between the theory and the world.

Ruphy (2007) extended the discussion of the epistemology of simulation by focusing on the path-dependency and plasticity of simulation. As examples she instanced cosmological simulations and simulations of the Milky Way. She stressed that many simulations are theoretically not well constrained: there are many possible paths of modelling opened by the necessary choices between different sub-models. This yields a potential or also actual plurality of models that all claim to model the same cosmic phenomenon. Typically, different models are incompatible, but empirically adequate to a similar degree. This situation creates a problem if it is possible to adjust the models to new empirical data by increasing their complexity while keeping their previous modelling contents. This occurs in situations where no testing of the ingoing sub-models is possible. In such a situation it becomes impossible to infer an understanding of the real world from the models just on the basis of their empirical adequacy. This, according to Ruphy, "embarassing" situation of a permanent incompatible model-pluralism is, in her opinion, not being appropriately addressed in the public discussion and should initiate a debate of the redeemed goals of respective simulations.

Furthermore, there are several publications in the social sciences dealing with astrophysical modelling practices. Roundtree (2010), for example, analysed the rhetoric of an astrophysical modelling paper in its evolution from the very first drafts until its final publication. Her main interest concerns the rhetorical treatment and justification of modelling assumptions, ad-hoc factors and inherent modelling uncertainties. She observes that the majority of explanatory and assessing rhetorical considerations present in earlier versions do not appear in the final publication anymore. Instead, a

linearized narrative of the modelling evolution is being told. The sociologist Sundberg (Sundberg 2010) concerned herself with the socially valid standards for the assessment of simulations within the astrophysical community. As probing standards she firstly identifies internal tests, such as a thorough understanding of the numerical results based on the source code. Secondly, she describes external tests based on a comparison with observational data. These tests, however, are often confronted with a lack of empirical data in astrophysics. Furthermore, in the case of idealized simulations, which deliberately neglect relevant factors in order to focus on the understanding of individual processes, such an external validation merely makes sense. According to Sundberg it is nevertheless required by the community. Another option for the validation of simulations is the comparison of different simulations among each other and the definition of common standards and benchmarks. Using the example of astrophysics, Sundberg (2011) investigates the social dynamics present as part of such a standardisation of "good" models.

This summary of the modelling discussion based on examples from astrophysics might have shown that even within astrophysics the current modelling practice is highly heterogeneous, depending on the evolutionary stage of the astrophysical sub-discipline and the availability of observational data. Simulations of extragalactic objects confronted with large uncertainties of ingoing theories and severe empirical constraints seem to struggle with different problems from those of the simulations of cosmic phenomena that can be observed within our Galaxy with high spatial resolution using different information channels. It is important to note that models also play an important role within astronomical data generation and reduction. For instance, the recording of data using a single dish radio telescope requires a model of the mechanical and optical properties of the telescope mirror in different positions in order to determine the exact pointing position. For the calibration of data with respect to influences of atmospheric influences a model of the Earth's atmosphere is needed. Flux calibration presupposes models of the planets used in the calibrating observations. As in many complex scientific disciplines, astrophysics is subject to a "hybrid" situation, where a clear distinction between empirical data and model-based interpretation is becoming more and more difficult. This situation might challenge elements of the modelling discussion as lead so far (e.g. Morrison 2009).

Moreover, newly commissioned or planned instruments, such as the ALMA interferometer, bring about a tremendous improvement of the empirical observational basis, while at the same time the need for easy to use, standardized models is growing. Thereby, questions for the verification, validation and standardisation of simulations gain additional importance, emphasized by a common differentiation of labour between modellers and model-users.

15.2.3.2 *Shock models*

The shock model I have used and revised in my thesis has been developed within the research groups of D. R. Flower and G. Pineau des Forêts since the 1980s (Flower et al. 1985). The basic MHD model (see Sect. 4.2) got expanded to calculate C-type, J-type, and approximated non-stationary shocks with an ever-growing body of physical details. Thus, the evolution of this model might bear some similarity to the model Graßhoff (1998) describes, where modellers entered the details of the shock code at various depths, for various periods of time and with various intentions.

The simulation[8] is fluid-based: it solves for the continuous fluid variables of the gas- and dust-fluids at each point in the shock. The most severe simplification of the model is its one-dimensional geometry. At the same time, it includes a very complex chemistry and treats the relevant micro-physics up to a high level of detail. Experience, however, seems to show that this latter aspect carries more weight for the match between modelling results and observations of shocks in dense clouds than an accurate simulation of the three-dimensional geometry. It is interesting to note that this makes the shock model a kind of hybrid case with respect to the frequently found distinction between idealized and realistic models (e.g. Sundberg 2010). The neglect of features that are considered to be of major importance to the phenomenon (as its multi-dimensional character) is typical for idealized models which are primarily used to acquire an understanding of the modelled processes, while the model's intended use in the interpretation of astronomical observations is characteristic of realistic models.

My modelling study as presented in Chapter 5 added two more physical effects to the shock model: the shattering of dust grains and the vaporization of SiO from grain cores. These effects, however, had already been implemented into the model before by Guillet et al. (2011), although in a very different way, i.e. using a multi-fluid approach. The difference between the two models of Guillet et al. (2011) and Anderl et al. (2013) can most clearly be understood with regard to their individual purposes. The multi-fluid model was developed in order to understand the influence of grain-grain processing on shocks. In the following I will refer to this kind of model as "investigative model". Accordingly, its main results were of a theoretical kind: it revealed the complex, non-linear interplay between the grain dynamics and -physics and the shock characteristics. Because the character of that interplay was unknown before, it was important for that model to be as realistic as possible with respect to grain properties, -dynamics, and grain charging. However, that high degree of detailedness in dust modelling leads to a large increase in computation time that competes with a different, important purpose of simulation other than the understanding of the modelled processes: the prediction of observations, which in turn was the main purpose of my modelling study. The change of intended purpose between mine and the multi-fluid model brings along a different modelling style: it is not bottom-up anymore (from the physical principles up to the resulting effects) but top-down: the resulting effects were parametrized, such that the detailed, underlying physics is not computed anymore. The corresponding loss of physical information results in a remarkable saving in computing time that allowed for the coupling with a detailed description of molecular line radiation transport. I will refer to this kind of model as "ad-hoc model", following Winsberg (1999).

With respect to verification and validation[9], the different model purposes will distinguish themselves. In both cases, a validation in terms of a comparison with observational data is very limited due to the geometrical restrictions of the model. For the "investigative model", validation and verification will instead be evaluated in terms of physical plausibility of the outputs. Although the model

8 It might be worth noting that, other than the typical examples in the philosophy of simulation, the shock model computes a stationary state of the shock, therefore the partial time derivatives are set to zero, while the integration variable is the spatial variable z. Even in the case of approximated non-stationary shocks the derived shock profile is only a snap-shot of that shock at a certain age. So far and in the following I do not make a further distinction between the simulation and its underlying model and use these terms interchangeable.

9 "*Verification* is said to be the process of determining whether the output of the simulation approximates the true solutions to the differential equations of the original model. *Validation*, on the other hand, is said to be the process of determining whether the chosen model is a good enough representation of the real-world system for the purpose of the simulation." Winsberg (2013), p. 20.

results are not compared with actual observations, the ingoing physics is well-known and corresponding tests can be conducted. For instance, it can be checked whether known behaviour of the system for simple cases of application can be reproduced. Furthermore, uncertainties can be determined and the robustness of the models with respect to ingoing parameters and assumptions can be tested. The "ad-hoc model", in contrast, can not be checked with respect to the underlying physical theory, but has to be compared with the complex "investigative model" that it aims at approximating to. In our case, this test constituted the first part of our project, where the overall shock model was chosen to be exactly the same as the shock model that was coupled with the multi-fluid approach for the dust-processing. Our criterion for the quality of our approximation was then an agreement of both models with respect to the modelling outputs that were expected to be relevant for our purpose of observational predictions. With that procedure, of course, all uncertainties and limitations are inherited from the investigative model, in addition to new uncertainties arising from the approximative nature of the ad-hoc model. A similar constellation of an investigative model being followed by an ad-hoc model can be found in the case of non-stationary shock models, where the fully time-dependent equations were only solved in the first case, while the ad-hoc model approximates non-stationary shocks by means of combining truncated, stationary C- and J-type shocks (see Subsec. 1.3.1).

Based on this, it seems important to distinguish different kinds of ad-hoc models in astrophysics: there are theory-driven and observation-driven ad-hoc models. The latter case was, for instance, described by Ruphy (2007), where complex simulations are adapted to new observational constraints by introducing additional parameters or other ad-hoc adjustments. Validation in this case is performed in its original meaning of a real-world comparison. Theory-driven ad-hoc models, in contrast, follow more complex models that have explored the effects of certain physical effects. Accordingly, the validation of theory-driven ad-hoc models occurs only in a wider sense, with respect to a more accurate model of the real-world phenomenon (an "investigative model"). It is interesting to note that this situation can be related to the alleged similarity between simulation data and experimental data – The validation of theory-driven ad-hoc models works with simulation data just like the validation of observation-driven models works with experimental data. Still, the epistemology of both model types is quite different. While the justification in one case is eventually made based on physical understanding, the justification in the other case is based on the similarity of model-outputs with properties of the modelled phenomenon.

15.2.4 *Data in science*

In 1962 Patrick Suppes initiated the speaking of "data models", by pointing at a hierarchy of models that link the raw data with the theory. The relationship between a data model and the underlying data is, according to Suppes, given by a detailed statistical theory of the "goodness of the fit". The semantic concept of models of theories (see Subsect. 15.2.3) is thereby extended in its application towards models of experiments and models of data. Harris (2003) has illustrated this concept of data models by using planet observations as an example, where bad observations are dismissed and the remaining data points smoothed, such that the final plotted path of the planet would constitute a data model: on the one hand it is similar to the original data, on the other hand it is also different. At the same time, the concept of data models acknowledges the fact that there are different ways to model

data. Harris dissociates himself from the concept of unprocessed "raw data" because "the process of data acquisition cannot be separated from the process of data manipulation" (Harris 2003, p. 1512). Even for the simplest instruments it is necessary for the scientist to possess certain learned skills to properly read the data.

The scientific treatment of data and their relation to the underlying theory was also discussed by Bogen & Woodward (1988). In their article "Saving the Phenomena" they introduce the distinction between data and phenomena, which, according to them, had not attracted proper attention until then. Therein, they distance themselves from the position held in logical positivism, according to which theories explain and predict facts about observables. In fact, Bogen and Woodward claim that data cannot be systematically explained or predicted because their actual values are influenced by a wide range of factors that are not part of the phenomenon under consideration. Therefore, data can only yield evidence for the existence of phenomena, which are themselves not directly observed. The temperature readings in the experimental determination of the melting point of lead, for instance, will show a statistical scatter. Further assumptions about the nature of this scatter (e.g. having a normal distribution) are necessary in order to arrive at a statement on the melting point of lead (as the phenomenon being predicted by theory) from the measured values. Furthermore, the distinction between data and phenomena becomes clearer with respect to their different context-sensitivities. While data very much depend on the characteristics of the particular experiment and cannot be understood without corresponding information, phenomena occur in many different contexts and situations. Their existence only depends on a limited number of causal factors, therefore they exhibit stable, repeatable characteristics.

With their article Bogen and Woodward acknowledged the experimental practice, specifically the practice of data analysis and data selection, which had been neglected within the theory-dominated discussions of the philosophy of science. Since then, a new branch within the philosophy of science has emerged: the philosophy of scientific experiment. An important topic in this philosophical subdiscipline is the reliability of experimental data (e.g. Hacking 1983; Collins 1985; Franklin 1986; Galison 1987; Mayo 1996; Staley 1999). The strategies for the prevention of errors and the extraction of "patterns" that yield the properties of the underlying phenomena thereby constitute an epistemology of the experiment. Bogen and Woodward have however been criticized that it is by no means unambiguous which features of the data to extract as reliable evidence of phenomena (e.g. McAllister 1997). There might be different patterns in the data, and the choice between them introduces an element of interpretation.

Therefore, different social and historical contexts might yield different strategies of data processing (or different "data models", Harris 2003) and thus may argue against the possibility of an ahistorically valid, experimental knowledge. To what extend this might be the case has been controversially discussed (Hacking 1981; Pickering 1984; Collins 1985; Galison 1987; Ackermann 1990; Hacking 1992b; Franklin 1994; Galison 1997). Moreover, different roles were studied, which experiments adopt within scientific practice. In addition to philosophically established roles in the context of the-

ory testing, the autonomous role of experiments independent of theory ("a life of their own[10]") was stressed.

15.2.4.1 *Astrophysical data*

Apparently, an epistemological analysis of data generation has so far not thoroughly been conducted from a philosophical perspective within modern astrophysics. In contrast, the social sciences are home to a broad discussion on topics such as data-access, databases, and increasing data intensity of scientific cooperations. This discussion also refers to examples from astrophysics (e.g Collins 1998; Wynholds et al. 2012; Sands et al. 2012). A philosophical investigation of data generation, -selection and -reduction within astronomy appears particularly interesting, as astrophysicists like to stress their status as passive observers: they only gather information that can be received from the universe (see Subsect. 15.1.1).

In fact, modern observational methods require much more manipulation and interaction than the classic picture of the astronomer looking through his or her telescope might suggest. Even before the actual raw data is generated, many decisions have to be made, which depend on the observer's intention with respect to the usage of the data. Furthermore, the calibration of the telescope, the calibration of the data regarding the atmosphere's influence and the calibration of the used receiver are very complex processes, which rely on assumptions and models. After the user has received the data, he or she is confronted with various tasks: sorting out bad data, data calibration, searching for systematic errors and, if present, correcting for them and finally visualising the data so that a scientific interpretation is possible. Depending on the observational technique and instrumentation used, this process of data reduction can become extremely complex.

One extreme case in that respect is given by the method of interferometry (not used in this thesis), where observations of several telescopes are pairwise combined in order to simulate one large telescope with a diameter corresponding to the maximum distance between a pair of telescopes. This technique relies on the measurement of Fourier components of the source distribution in the sky, so that the intensity distribution needs to be determined by means of a Fourier transformation. At the same time, information on the source is lost due to an insufficient coverage of the surface of the simulated large telescope. The central step within the data reduction therefore cannot aim at a reconstruction of the real source distribution, but rather at the detection of a plausible distribution, which is compatible with the real distribution of the source. This problem might serve as an example of a situation where several "patterns" can be found within the data, and additional assumptions are needed to choose an appropriate "data model".

In any case, with respect to the complexity of data generation and processing there seems to be no obvious difference between astronomy and experimental sciences. Harwit 1981 therefore might offer a too simplified account for the practice of astronomical observation if he does not consider the whole chain of activities related to data processing. If he did, however, his finite phase space of possible observations would experience a tremendous extension, and it might no longer be true that

10 "Over a decade ago I wrote that experiments have a life of their own. I intended partly to convey the fact, that experiments are organic, develop, change, and yet retain a certain long-term development, which makes us talk about repeating and replicating experiments [. . .]. I think of experiments as having a life: maturing, evolving, adapting, being not only recycled but also, quite literally, being retooled." Hacking (1992a), p. 307.

the case of astronomy is so much easier to analyse than experimental disciplines. It is interesting to note that this fact is even acknowledged by Ian Hacking, although in Hacking (1989) he so firmly stresses the difference between astronomy and the experimental sciences:

> "It is sometimes said that in astronomy we do not experiment; we can only observe. It is true that we cannot interfere very much in the distant reaches of space, but the skills employed by Penzias and Wilson [S.A.: the discoverers of the cosmic microwave background] were identical to those used by laboratory experimenters." (Hacking 1983, p. 160).

The more complex the process of data selection and analysis becomes, the more the processing of data also relies on experience. Accordingly, instructions on astronomical data reduction are not found in textbooks and often only briefly in documentations of the respective software packages. The practice of data reduction is rather transferred in schools or workshops or directly among colleagues. This practice contains strong elements of what M. Polanyi described as "tacit knowledge", distinguished from explicit knowledge (Polanyi 1958; Collins 2010)[11]. The existence of tacit knowledge can become a problem if it causes a loss of information with respect to data-genesis and the context of data processing when data gets transferred. Within modern astrophysical practice, which works increasingly based on the division of labour and is directed towards a multiple use of data, the question arises how databases and corresponding data formats can be organised as to prevent a negative impact on the meaningfulness of the data.

These questions are for instance currently discussed in the context of the establishment of the so-called "Virtual Astronomical Observatory" (VAO). This VAO aims at assembling data archives and services as well as data exploration and analysis tools. The vision behind that endeavour is summarized on the VAO homepage:

> "Today so much data is being collected that astronomers cannot see or understand everyone else's data as well as their own. The VAO will let astronomers easily search for data, from all instruments at all wavelengths of the electromagnetic spectrum, that will help them to understand the universe."

The underlying idea is that anyone in the world with a decent internet connection is enabled to perform astronomical science. The epistemic consequences of such a complete decoupling of scientific data interpretation from the process of data generation and processing would constitute an interesting problem for the philosophical discussion of astrophysical research.

So in summary, compared to experimental scientific disciplines that are organized within large international projects, it becomes questionable to what extent the observational aspect, the impossibility of an interaction with the object of research, really bears epistemic relevance. A similar argument was already made in Subsect. 15.2.1. Instead, it might seem that astrophysics is becoming increasingly concerned with similar epistemological problems to those already now found in to particle physics.

11 At this point it may become apparent that Shapere's (Shapere 1982) generalisation of the concept of observation falls short when it comes to data processing. The fact that "tacit knowledge" becomes relevant may show that astronomical observations include steps that cannot be conducted by machines just as well as by humans.

15.2.4.2 *Shock data*

Although in this thesis the used data was generated by the relatively simple technique of single dish observations, there was still significant data processing applied (briefly described in Sect. 8.3). From the "raw" data, as received from the telescope, up to and including the data as we present them in our papers many "data models" had been created in intermediate steps. The operations and transformations applied to the data were carefully minuted in notebooks and stored in script files to assure repeatability. But, following the discussions on the reliability of data (e.g. Franklin 1986; Mayo 1996) one could still ask: why do we believe in our observations? Could it be the case that we have misinterpreted artefacts as valid results? In this context Hacking (1983) stressed the important role of possible intervention with the object under study. This is not a possibility in astronomy. We nevertheless believe in our results. On what basis do we do so?

I was not present myself during the recording of the data, which means I had to trust the accuracy of the data up to the point when I received them. However, Rolf Güsten, the observer in charge, is a co-author and could always be consulted if there were questions with respect to the data generation and quality. The following strategies were used to assure the reliability of our data (we here refer to the more detailed study of W44):

- "Independent confirmation": We compared our observations with observations already performed towards W44 E and F. In particular, for CO (3–2) similar observations had been conducted before (Frail & Mitchell 1998), where the maps showed the same spatial emission as our maps. Furthermore, the spectra of CO (3–2) could be compared to existing spectra in CO (2–1) and CO (3–2) (Frail & Mitchell 1998; Reach & Rho 2000; Reach et al. 2005). These spectra confirmed the observed line shapes. The similarity of maps and spectra in all our observed transitions encouraged us to transfer this confirmation from CO (3–2) to the other observed transitions.

- "Consistency with previous observations": Knowledge about the source as presented in previous studies was used to judge the plausibility of the data, e.g. information on source velocities, geometry, and emission in other wavelength regimes.

- "Internal consistency of the data cube": We could switch between the two different data-representations of velocity integrated emission maps and spectra. Thereby we could, for example, exclude the possibility of spectral features being only local artefacts and decide on possible physical origins based on the spatial distribution.

- "Physical plausibility": We could use physical background knowledge on CO. For instance, on these grounds it became obvious that there was a problem with the data in CO (4–3) because this line was more deeply absorbed in its line centre than CO (3–2) – a situation that physically does not make sense because it would hint at a population inversion in the absorbing material. Examination of the reference position, which is used to calibrate the data, revealed that this reference position suffered from emission in CO (4–3). Therefore the deep absorption was identified as an artefact caused by an error in the data taking.

- "Robustness of data processing": The robustness of the data processing procedure was checked: the processing was redone (by the same person but partly also by different persons) and com-

pared with previous results, the order of some of the steps of the processing was changed, and ingoing parameters were varied.

Based on these strategies, we assert that our belief in the observational results is reasonable. Furthermore, we had great confidence in the instruments we used, either because they have reliably been operated for a while (like the APEX telescope) or because we trust the people and their experience with respect to the instruments who have conducted the observations (like for the SOFIA telescope).

Except for internal consistency and robustness of the data processing, all the strategies rely on existing knowledge shared by the community. One might therefore be concerned that these strategies are endangered of being influenced by social and historical elements. Given that something totally unexpected would be observed, would we take it for an artefact because it does not match the theoretical expectations? This is the point where a thorough knowledge of the observing technique becomes important. As, for example, in the case of our absorbed CO (4–3) spectra the interpreting astronomer needs to know about possible reasons for such a deep absorption to perform an "elimination of plausible sources of error and alternative explanations of the result (the Sherlock Holmes strategy)" (Franklin 2012). This strategy, however, is only possible if a) the alternative explanations are known and b) the necessary information to check them is accessible. If the processes of data generation and data interpretation become more and more separated and if raw data and intermediate stages of processed data are not stored (as complete storage is often impossible in big data archives), it might become increasingly difficult to disentangle valid results and artefacts.

BIBLIOGRAPHY

Abdo, A. A., Ackermann, M., Ajello, M., et al. 2010, ApJ, 718, 348

Abdo, A. A., Ackermann, M., Ajello, M., et al. 2010, Science, 327, 1103

Achinstein, P. 1968, Concepts of Science (Baltimore, Johns Hopkins Press)

Ackermann, M., Ajello, M., Allafort, A., et al. 2013, Science, 339, 807

Ackermann, R. 1990, PSA: Proceedings of the Biennial Meeting of the Philosophy of Science Association, 451

Adelmann, R., Frercks, J., Heßler, M., & Hennig, J. 2009, Datenbilder - Zur digitalen Bildpraxis in den Naturwissenschaften (Transcript Verlag)

Aharonian, F., Akhperjanian, A. G., Bazer-Bachi, A. R., et al. 2008, A&A, 481, 401

Anderl, S., Guillet, V., Pineau des Forêts, G., & Flower, D. R. 2013, A&A, 556, A69

Andersen, M., Rho, J., Reach, W. T., Hewitt, J. W., & Bernard, J. P. 2011, ApJ, 742, 7

Arikawa, Y., Tatematsu, K., Sekimoto, Y., & Takahashi, T. 1999, PASJ, 51, L7

Axford, W. I., Leer, E., & Skadron, G. 1977, in International Cosmic Ray Conference, Vol. 11, International Cosmic Ray Conference, 132

Bachiller, R., Martin-Pintado, J., & Fuente, A. 1991, A&A, 243, L21

Bailer-Jones, D. M. 2000, Sud. Hist. Phil. Mod. Phys., 31, 49

Bailer-Jones, D. M. 2002, Perspectives on Science, 10, 275

Barlow, M. J. 1978, MNRAS, 183, 367

Biermann, P. & Harwit, M. 1980, ApJ, 241, L105

Blandford, R. & Eichler, D. 1987, Physics Reports, 154, 1

Blandford, R. D. & Cowie, L. L. 1982, ApJ, 260, 625

Bogen, J. 2013, in The Stanford Encyclopedia of Philosophy, spring 2013 edn., ed. E. N. Zalta

Bogen, J. & Woodward, J. 1988, Philosophical Review, 97, 303

Borkowski, K. J. & Dwek, E. 1995, ApJ, 454, 254

Braithwaite, R. B. 1953, Scientific Explanation (Cambridge University Press)

Brand, P. W. J. L., Toner, M. P., Geballe, T. R., & Webster, A. S. 1989, MNRAS, 237, 1009

Cabrit, S., Codella, C., Gueth, F., & Gusdorf, A. 2012, A&A, 548, L2

Cabrit, S., Codella, C., Gueth, F., et al. 2007, A&A, 468, L29

Cardelli, J. A., Clayton, G. C., & Mathis, J. S. 1989, ApJ, 345, 245

Carnap, R. 1939, Foundations of Logic and Mathematics (The University of Chicago Press)

Carroll, B. W. & Ostlie, D. A. 2006, An Introduction to Modern Astrophysics (Addison-Wesley)

Cartwright, N. 1983, How the laws of physics lie (Oxford University Press Inc., New York)

Castelletti, G., Dubner, G., Brogan, C., & Kassim, N. E. 2007, A&A, 471, 537

Caswell, J. L., Murray, J. D., Roger, R. S., Cole, D. J., & Cooke, D. J. 1975, A&A, 45, 239

Cesarsky, D., Cox, P., Pineau des Forêts, G., et al. 1999, A&A, 348, 945

Chernoff, D. F. 1987, ApJ, 312, 143

Cheung, A. C., Rank, D. M., Townes, C. H., Thornton, D. D., & Welch, W. J. 1968, Phys. Rev. Lett., 21, 1701

Chevalier, R. A. 1999, ApJ, 511, 798

Chieze, J.-P., Pineau des Forêts, G., & Flower, D. R. 1998, MNRAS, 295, 672

Chokshi, A., Tielens, A. G. G. M., & Hollenbach, D. 1993, ApJ, 407, 806

Claussen, M. J., Frail, D. A., Goss, W. M., & Gaume, R. A. 1997, ApJ, 489, 143

Claussen, M. J., Goss, W. M., Frail, D. A., & Desai, K. 1999, ApJ, 522, 349

Collins, H. 1985, Changing Order. Replication and Induction in Scientific Practice (The University of Chicago Press)

Collins, H. 1998, American Journal of Sociology, 104, 293

Collins, H. 2010, Tacit and Explicit Knowledge (The University of Chicago Press)

Cox, D. P. 2005, ARA&A, 43, 337

Cox, D. P., Shelton, R. L., Maciejewski, W., et al. 1999, ApJ, 524, 179

Cox, D. P. & Smith, B. W. 1974, ApJ, 189, L105

Crutcher, R. M. 1999, ApJ, 520, 706

Crutcher, R. M. 2012, ARA&A, 50, 29

da Costa, N. C. A. & French, S. 2003, Science and Partial Truth : A Unitary Approach to Models and Scientific Reasoning (Oxford University Press)

Dalgarno, A., Yan, M., & Liu, W. 1999, ApJS, 125, 237

Davis, C. J., Froebrich, D., Stanke, T., et al. 2009, A&A, 496, 153

Denoyer, L. K. 1983, ApJ, 264, 141

Dickel, J. R., Dickel, H. R., & Crutcher, R. M. 1976, PASP, 88, 840

Douven, I. 2011, in The Stanford Encyclopedia of Philosophy, spring 2011 edn., ed. E. N. Zalta

Downes, S. M. 1992, PSA: Proceedings of the Biennial Meeting of the Philosophy of Science Association, 1992, 142

Draine, B. T. 1980, ApJ, 241, 1021

Draine, B. T. 1986, MNRAS, 220, 133

Draine, B. T. 2009, in Astronomical Society of the Pacific Conference Series, Vol. 414, Cosmic Dust - Near and Far, ed. T. Henning, E. Grün, & J. Steinacker, 453

Draine, B. T. 2010, Physics of the Interstellar and Intergalactic Medium, Princeton Series in Astrophysics, 1st edn. (Princeton University Press)

Draine, B. T. & McKee, C. F. 1993, ARA&A, 31, 373

Draine, B. T., Roberge, W. G., & Dalgarno, A. 1983, ApJ, 264, 485

Draine, B. T. & Salpeter, E. E. 1979, ApJ, 231, 77

Draine, B. T. & Sutin, B. 1987, ApJ, 320, 803

Edge, D. O., Shakeshaft, J. R., McAdam, W. B., Baldwin, J. E., & Archer, S. 1959, MmRAS, 68, 37

Einstein, A. 1954, Physics and Reality (New York, Crown), in 'Ideas and Options', trans. Sonja Bargmann

Elfhag, T., Booth, R. S., Hoeglund, B., Johansson, L. E. B., & Sandqvist, A. 1996, A&AS, 115, 439

Elitzur, M. 1976, ApJ, 203, 124

Esposito, J. A., Hunter, S. D., Kanbach, G., & Sreekumar, P. 1996, ApJ, 461, 820

Fazio, G. G., Hora, J. L., Allen, L. E., et al. 2004, ApJS, 154, 10

Ferland, G. J., Fabian, A. C., Hatch, N. A., et al. 2008, MNRAS, 386, L72

Field, G. B., Goldsmith, D. W., & Habing, H. J. 1969, ApJ, 155, L149

Fitzpatrick, E. L. 1999, PASP, 111, 63

Flower, D. R., Bourlot, J. L., Pineau des Forêts, G., & Cabrit, S. 2003, MNRAS, 341, 70

Flower, D. R. & Gusdorf, A. 2009, MNRAS, 395, 234

Flower, D. R. & Pineau des Forêts, G. 2003, MNRAS, 343, 390, (FPdF03)

Flower, D. R. & Pineau des Forêts, G. 2010, MNRAS, 406, 1745, (FPdF10)

Flower, D. R. & Pineau des Forêts, G. 2012, MNRAS, 421, 2786

Flower, D. R., Pineau des Forêts, G., & Hartquist, T. W. 1985, MNRAS, 216, 775

Flower, D. R., Pineau des Forêts, G., & Hartquist, T. W. 1986, MNRAS, 218, 729

Flower, D. R., Pineau des Forêts, G., & Rabli, D. 2010, MNRAS, 409, 29

Fortov, V. E., Ivlev, A. V., Khrapak, S. A., Khrapak, A. G., & Morfill, G. E. 2005, Phys. Rep., 421, 1

Fragile, P. C., Anninos, P., Gustafson, K., & Murray, S. D. 2005, ApJ, 619, 327

Frail, D. A., Giacani, E. B., Goss, W. M., & Dubner, G. 1996, ApJ, 464, L165

Frail, D. A., Goss, W. M., & Slysh, V. I. 1994, ApJ, 424, L111

Frail, D. A., Kulkarni, S. R., & Vasisht, G. 1993, Nature, 365, 136

Frail, D. A. & Mitchell, G. F. 1998, ApJ, 508, 690

Franklin, A. 1986, The Neglect of Experiment (Cambridge University Press)

Franklin, A. 1994, Studies in History and Philosophy of Science Part A, 25, 463

Franklin, A. 2012, in The Stanford Encyclopedia of Philosophy, winter 2012 edn., ed. E. N. Zalta

Frigg, R. 2006, Theoria, 21, 49

Galison, P. L. 1987, How experiments end (The University of Chicago Press)

Galison, P. L. 1997, Image and Logic (The University of Chicago Press)

Giacani, E. B., Dubner, G. M., Kassim, N. E., et al. 1997, AJ, 113, 1379

Giannini, T., McCoey, C., Caratti o Garatti, A., et al. 2004, A&A, 419, 999

Gibbard, A. & Varian, H. R. 1978, Journal of Philosophy, 75, 664

Giuliani, A., Cardillo, M., Tavani, M., et al. 2011, ApJ, 742, L30

Giuliani, A., Tavani, M., Bulgarelli, A., et al. 2010, A&A, 516, L11

Graßhoff, G. 1998, Philosophia naturalis, 35, 161

Green, D. A. 1989, MNRAS, 238, 737

Groenewold, H. J. 1960, Synthese, 12, 222

Guan, X., Stutzki, J., Graf, U. U., et al. 2012, A&A, 542, L4

Gueth, F., Guilloteau, S., & Bachiller, R. 1998, A&A, 333, 287

Guillet, V. 2008, PhD thesis, Ecole Doctorale d'Astrophysique Spatiale

Guillet, V., Jones, A., & Pineau des Forêts, G. 2008, in COSPAR Meeting, Vol. 37, 37th COSPAR Scientific Assembly, 1110

Guillet, V., Jones, A., & Pineau des Forêts, G. 2009, in EAS Publications Series, Vol. 35, EAS Publications Series, ed. F. Boulanger, C. Joblin, A. Jones, & S. Madden, 219

Guillet, V., Jones, A. P., & Pineau des Forêts, G. 2009, A&A, 497, 145, (Paper II)

Guillet, V., Pineau des Forêts, G., & Jones, A. P. 2007, A&A, 476, 263, (Paper I)

Guillet, V., Pineau des Forêts, G., & Jones, A. P. 2011, A&A, 527, 123, (Paper III)

Gusdorf, A., Anderl, S., Güsten, R., et al. 2012, A&A, 542, L19

Gusdorf, A., Cabrit, S., Flower, D. R., & Pineau des Forêts, G. 2008a, A&A, 482, 809

Gusdorf, A., Giannini, T., Flower, D. R., et al. 2011, A&A, 532, A53

Gusdorf, A., Pineau des Forêts, G., Cabrit, S., & Flower, D. R. 2008b, A&A, 490, 695

Gustafsson, M., Ravkilde, T., Kristensen, L. E., et al. 2010, A&A, 513, A5

Güsten, R., Baryshev, A., Bell, A., et al. 2008, in Society of Photo-Optical Instrumentation Engineers (SPIE) Conference Series, Vol. 7020

Güsten, R., Nyman, L. Å., Schilke, P., et al. 2006, A&A, 454, L13

Habart, E., Abergel, A., Boulanger, F., et al. 2011, A&A, 527, A122

Hacking, I. 1981, Pacific Philosophical Quarterly, 63, 305

Hacking, I. 1983, Representing and Intervening. Introductory Topics in the Philosophy of Natural Science. (Cambridge University Press)

Hacking, I. 1989, Philosophy of Science, 56, 555

Hacking, I. 1992a, PSA: Proceedings of the Biennial Meeting of the Philosophy of Science Association, 1992, 302

Hacking, I. 1992b, Science as Practice and Culture, 63, 29

Harris, T. 2003, Philosophy of Science, 70, 1508

Harrus, I. M., Hughes, J. P., & Helfand, D. J. 1996, ApJ, 464, L161

Hartmann, S. 1995, in Theories and Models in Scientific Processes (Amsterdam: Rodopi), 49

Hartmann, S. 1996, in Modelling and Simulation in the Social Sciences from the Philosophy of Science Point of View (Kluwer: Dordrecht), 77

Hartmann, S. 1999, in Models as Mediators (Cambridge University Press), 326

Harwit, M. 1981, Cosmic Discovery: The Search, Scope, and Heritage of Astronomy (MIT Press)

Hentschel, K. & Wittmann, A. D., eds. 2000, The Role of Visual Representations in Astronomy: History and Research Practice (Acta Historica Astronomiae, Verlag Harri Deutsch)

Hewitt, J. W., Yusef-Zadeh, F., & Wardle, M. 2009, ApJ, 706, L270

Heyminck, S., Graf, U. U., Güsten, R., et al. 2012, A&A, 542, L1

Heyminck, S., Kasemann, C., Güsten, R., de Lange, G., & Graf, U. U. 2006, A&A, 454, L21

Hirashita, H. 2010, MNRAS, 407, L49

Ho, P. T. P. & Townes, C. H. 1983, ARA&A, 21, 239

Hoeppe, G. 2012, Anthropological Quarterly, 85, 1141

Hoffman, I. M., Goss, W. M., Brogan, C. L., & Claussen, M. J. 2005, ApJ, 627, 803

Hoffman, I. M., Goss, W. M., Brogan, C. L., & Claussen, M. J. 2005, ApJ, 620, 257

Hollenbach, D. & McKee, C. F. 1979, ApJS, 41, 555

Hollenbach, D. & McKee, C. F. 1989, ApJ, 342, 306

Houck, J. R., Roellig, T. L., van Cleve, J., et al. 2004, ApJS, 154, 18

Hoyningen-Huene, P. 1995, Wissenschaftsforschung - Probleme und Perspektiven, Klausurtagung 1994 des Schweizerischen Wissenschaftsrates. Forschungspolitik, 20, 17

Humphreys, P. 2004, Synthese, 169, 615

Ivlev, A. V., Lazarian, A., Tsytovich, V. N., et al. 2010, ApJ, 723, 612

Jaschek, C. 1989, Data in Astronomy (Cambridge University Press)

Jones, A. P., Tielens, A. G. G. M., & Hollenbach, D. J. 1996, ApJ, 469, 740

Jones, A. P., Tielens, A. G. G. M., Hollenbach, D. J., & McKee, C. F. 1994, ApJ, 433, 797

Jones, L. R., Smith, A., & Angelini, L. 1993, MNRAS, 265, 631

Kasemann, C., Güsten, R., Heyminck, S., et al. 2006, in Society of Photo-Optical Instrumentation Engineers (SPIE) Conference Series, Vol. 6275, 19

Kawasaki, M., Ozaki, M., Nagase, F., Inoue, H., & Petre, R. 2005, ApJ, 631, 935

Keller, E. F. 2000, Philosophy of Science, 67, 86

Klein, B., Hochgürtel, S., Krämer, I., et al. 2012, A&A, 542, L3

Klein, B., Philipp, S. D., Krämer, I., et al. 2006, A&A, 454, L29

Knapp, G. R. & Kerr, F. J. 1974, A&A, 33, 463

Knuuttila, T. & Merz, M. 2009, Scientific Understanding: Philosophical Perspectives, 146

Koo, B.-C. & Heiles, C. 1995, ApJ, 442, 679

Kramer, C., Buchbender, C., Xilouris, E. M., et al. 2010, A&A, 518, L67

Kristensen, L. E. 2007, PhD thesis, LERMA (Observatoire de Paris-Meudon), LAMAP (Université de Cergy-Pontoise)

Kristensen, L. E., Ravkilde, T. L., Pineau des Forêts, G., et al. 2008, A&A, 477, 203

Krymskii, G. F. 1977, Akademiia Nauk SSSR Doklady, 234, 1306

Kuhn, T. S. 1962, The Structure of Scientific Revolutions (The University of Chicago Press)

Kundu, M. R. & Velusamy, T. 1972, A&A, 20, 237

Kutner, M. L. 1954, Astronomy: A Physical Perspective, 2nd edn. (Cambridge University Press)

Landau, L. D. & Lifshitz, E. 1987, Fluid Mechanics, Volume 6 (Course of Theoretical Physics), 2nd edn. (Butterworth-Heinemann)

Langer, W. D. & Penzias, A. A. 1993, ApJ, 408, 539

Le Bourlot, J., Pineau des Forêts, G., Flower, D. R., & Cabrit, S. 2002, MNRAS, 332, 985

Le Picard, S. D., Canosa, A., Pineau des Forêts, G., Rebrion-Rowe, C., & Rowe, B. R. 2001, A&A, 372, 1064

Lequeux, J. 2005, The Interstellar Medium (Springer-Verlag Berlin Heidelberg)

Lesaffre, P., Chièze, J.-P., Cabrit, S., & Pineau des Forêts, G. 2004a, A&A, 427, 147

Lesaffre, P., Chièze, J.-P., Cabrit, S., & Pineau des Forêts, G. 2004b, A&A, 427, 157

Li, A. & Draine, B. T. 2001, ApJ, 554, 778

Liffman, K. & Clayton, D. D. 1989, ApJ, 340, 853

Lockett, P., Gauthier, E., & Elitzur, M. 1999, ApJ, 511, 235

Longair, M. S., Stewart, J. M., & Williams, P. M. 1986, QJRAS, 27, 153

Lynch, M. & Edgerton, S. Y. 1988, in: G. Fyfe and J. Law (eds.), Picturing Power: Visual Depiction and Social Relations, 30, 184

Lynch, M. E. & Woolgar, S., eds. 1990, Representation in Scientific Practice (The MIT Press)

Maciejewski, W., Murphy, E. M., Lockman, F. J., & Savage, B. D. 1996, ApJ, 469, 238

Maier, D., Barbier, A., Lazareff, B., & Schuster, K. F. 2005, in Sixteenth International Symposium on Space Terahertz Technology, 428

Martin-Pintado, J., Bachiller, R., & Fuente, A. 1992, A&A, 254, 315

Mathis, J. S., Rumpl, W., & Nordsieck, K. H. 1977, ApJ, 217, 425

May, P. W., Pineau des Forêts, G., Flower, D. R., et al. 2000, MNRAS, 318, 809

Mayo, D. G. 1996, Error and the growth of experimental knowledge (The University of Chicago Press)

McAllister, J. W. 1997, Erkenntnis, 47, 217

McKee, C. F. & Cowie, L. L. 1975, ApJ, 195, 715

McKee, C. F. & Cowie, L. L. 1977, ApJ, 215, 213

McKee, C. F. & Hollenbach, D. J. 1980, ARA&A, 18, 219

McKee, C. F., Hollenbach, D. J., Seab, G. C., & Tielens, A. G. G. M. 1987, ApJ, 318, 674

McKee, C. F. & Ostriker, J. P. 1977, ApJ, 218, 148

McMullin, E. 1968, Logic, Methodology and Philosophy of Science III: Proceedings of the Third International Congress for Logic, Methodology and Philosophy of Science, 385

Meijerink, R., Kristensen, L. E., Weiß, A., et al. 2013, ApJ, 762, L16

Michelle, S. 2010, Techné, 14, 252

Mills, B. Y., Slee, O. B., & Hill, E. R. 1958, AuJPh, 11, 360

Morrison, M. 2009, Philosophical Studies, 143, 33

Morrison, M. & Morgan, M. 1999, Models as Mediators (Cambridge University Press)

Morton, A. 1993, British Journal for the Philosophy of Science, 44, 659

Muders, D., Hafok, H., Wyrowski, F., et al. 2006, A&A, 454, L25

Mullan, D. J. 1971, MNRAS, 153, 145

Musgrave, A. 1981, Kyklos, 34, 377

Nagahara, H. & Ozawa, K. 1996, GeCoA, 60, 1445

Neufeld, D. A., Hollenbach, D. J., Kaufman, M. J., et al. 2007, ApJ, 664, 890, N07

Nisini, B., Codella, C., Giannini, T., et al. 2007, A&A, 462, 163

Nissen, H. D., Gustafsson, M., Lemaire, J. L., et al. 2007, A&A, 466, 949

Oberkampf, W. L. & Trucano, T. G. 2002, Progress in Aerospace Sciences, 38, 209

O'Donnell, J. E. & Mathis, J. S. 1997, ApJ, 479, 806

Oster, L. 1973, Modern Astronomy (San Francisco: Holden-Day)

Paron, S., Ortega, M. E., Rubio, M., & Dubner, G. 2009, A&A, 498, 445

Petre, R., Kuntz, K. D., & Shelton, R. L. 2002, ApJ, 579, 404

Pickering, A. 1984, Constructing Quarks (The University of Chicago Press)

Pilipp, W. & Hartquist, T. W. 1994, MNRAS, 267, 801

Pineau des Forêts, G., Flower, D. R., Hartquist, T. W., & Dalgarno, A. 1986, MNRAS, 220, 801

Planck Collaboration. 2011, A&A, 536, 24

Polanyi, M. 1958, Personal Knowledge: Towards a Post-Critical Philosophy (The University of Chicago Press)

Portides, D. P. 2005, Philosophy of Science, 72, 1287

Radhakrishnan, V., Goss, W. M., Murray, J. D., & Brooks, J. W. 1972, ApJS, 24, 49

Raymond, J. C., Hester, J. J., Cox, D., et al. 1988, ApJ, 324, 869

Reach, W. T. & Rho, J. 1996, A&A, 315, L277

Reach, W. T. & Rho, J. 2000, ApJ, 544, 843

Reach, W. T., Rho, J., & Jarrett, T. H. 2005, ApJ, 618, 297

Redhead, M. 1980, British Journal for the Philosophy of Science, 31, 145

Rho, J. & Petre, R. 1998, ApJ, 503, L167

Rho, J., Petre, R., Schlegel, E. M., & Hester, J. J. 1994, ApJ, 430, 757

Rieke, G. H. & Lebofsky, M. J. 1985, ApJ, 288, 618

Risacher, C., Vassilev, V., Monje, R., et al. 2006, A&A, 454, L17

Roache, P. J. 1997, Annual Review of Fluid Mechanics, 29, 123

Rohrlich, F. 1990, PSA: Proceedings of the Biennial Meeting of the Philosophy of Science Association, 507

Rosenblueth, A. & Wiener, N. 1945, Philosophy of Science, 12, 316

Roundtree, A. K. 2010, Journal of Science Communication, 9, A02

Ruphy, S. 2007, unpublished

Sands, A., Borgman, C. L., Wynholds, L., & Traweek, S. 2012, Proceedings of the American Society for Information Science and Technology, 49, 1

Sano, H., Sato, J., Horachi, H., et al. 2010, ApJ, 724, 59

Scheuer, P. A. G. 1963, The Observatory, 83, 56

Schickore, J. 1999, Journal for General Philosophy of Science, 30, 273

Schilke, P., Walmsley, C. M., Pineau des Forêts, G., & Flower, D. R. 1997, A&A, 321, 293

Scoville, N. Z., Yun, M. S., Sanders, D. B., Clemens, D. P., & Waller, W. H. 1987, ApJS, 63, 821

Seab, C. G. & Shull, J. M. 1983, ApJ, 275, 652

Sedov, L. I. 1993, Similarity and Dimensional Methods in Mechanics, 10th edn. (CRC Press)

Seta, M., Hasegawa, T., Dame, T. M., et al. 1998, ApJ, 505, 286

Seta, M., Hasegawa, T., Sakamoto, S., et al. 2004, AJ, 127, 1098

Shapere, D. 1982, Philosophy of Science, 49, 485

Shapere, D. 1993, Philosophy of Science, 60, 134

Shelton, R. L., Cox, D. P., Maciejewski, W., et al. 1999, ApJ, 524, 192

Slavin, J. D., Jones, A. P., & Tielens, A. G. G. M. 2004, ApJ, 614, 796

Smith, A., Jones, L. R., Watson, M. G., et al. 1985, MNRAS, 217, 99

Smith, M. D. & Brand, P. W. J. L. 1990, MNRAS, 245, 108

Smith, M. D., Khanzadyan, T., & Davis, C. J. 2003, MNRAS, 339, 524

Snell, R. L., Hollenbach, D., Howe, J. E., et al. 2005, ApJ, 620, 758

Spector, M. 1965, British Journal for the Philosophy of Science, 16, 121

Stahler, S. W. & Palla, F. 2004, The Formation of Stars (WILEY-VCH Verlag GmbH & Co. KGaA Weinheim)

Staley, K. W. 1999, Perspectives on Science, 7, 196

Sundberg, M. 2010, Studies in History and Philosophy of Science Part B, 41, 273

Sundberg, M. 2011, Social Studies of Science, 41, 107

Suppes, P. 1960, Synthese, 12, 287

Suppes, P. 1962, Logic, Methodology, and Philosophy of Science: Proceedings of the 1960 International Congress, 252

Surdej, J. 1977, A&A, 60, 303

Szymkowiak, A. E. 1980, In: Type I supernovae; Proceedings of the Texas Workshop, 32

Tafalla, M. & Bachiller, R. 1995, ApJ, 443, L37

Tammann, G. A., Loeffler, W., & Schroeder, A. 1994, ApJS, 92, 487

Taylor, J. H. & Cordes, J. M. 1993, ApJ, 411, 674

Tielens, A. G. G. M. 2005, The Physics and Chemistry of the Interstellar Medium (Cambridge University Press)

Tielens, A. G. G. M., McKee, C. F., Seab, C. G., & Hollenbach, D. J. 1994, ApJ, 431, 321

Timmermann, R. 1996, ApJ, 456, 631

Timmermann, R. 1998, ApJ, 498, 246

Tucker, J. R. & Feldman, M. J. 1985, Rev. Mod. Phys., 57, 1055

van Dishoeck, E. F., Jansen, D. J., & Phillips, T. G. 1993, A&A, 279, 541

Van Loo, S., Ashmore, I., Caselli, P., Falle, S. A. E. G., & Hartquist, T. W. 2009, MNRAS, 395, 319

Van Loo, S., Ashmore, I., Caselli, P., Falle, S. A. E. G., & Hartquist, T. W. 2012, MNRAS, 428, 381

Velázquez, P. F., Dubner, G. M., Goss, W. M., & Green, A. J. 2002, AJ, 124, 2145

Velusamy, T. 1988, in IAU Colloq. 101: Supernova Remnants and the Interstellar Medium, ed. R. S. Roger & T. L. Landecker, 265

Wang, J., Davis, A. M., Clayton, R. N., & Hashimoto, A. 1999, GeCoA, 63, 953

Wardle, M. & Draine, B. T. 1987, ApJ, 321, 321

Watson, M. G., Willingale, R., Pye, J. P., et al. 1983, IN: Supernova remnants and their X-ray emission; Proceedings of the Symposium, 101, 273

Weiler, K. W. & Sramek, R. A. 1988, ARA&A, 26, 295

Weingartner, J. C. & Draine, B. T. 2001, ApJ, 548, 296

Werner, M. W., Roellig, T. L., Low, F. J., et al. 2004, ApJS, 154, 1

Westerhout, G. 1958, Bulletin of the Astronomical Institutes of the Netherlands, 14, 215

White, R. L. & Long, K. S. 1991, ApJ, 373, 543

Wilgenbus, D., Cabrit, S., Pineau des Forêts, G., & Flower, D. R. 2000, A&A, 356, 1010

Winsberg, E. 1999, Science in Context, 12, 275

Winsberg, E. 2001, Proceedings of the Philosophy of Science Association, 2001, S442

Winsberg, E. 2003, Philosophy of Science, 70, 105

Winsberg, E. 2013, in The Stanford Encyclopedia of Philosophy, summer 2013 edn., ed. E. N. Zalta

Wolszczan, Cordes, J. M., & Dewey, R. J. 1991, ApJ, 372, L99

Woltjer, L. 1972, ARA&A, 10, 129

Wootten, A. 1981, ApJ, 245, 105

Wootten, H. A. 1977, ApJ, 216, 440

Wynholds, L. A., Wallis, J. C., Borgman, C. L., Sands, A., & Traweek, S. 2012, Proceedings of the 12th ACM/IEEE-CS joint conference on Digital Libraries, 19

Xilouris, E. M., Tabatabaei, F. S., Boquien, M., et al. 2012, A&A, 543, A74

Yang, B., Stancil, P. C., Balakrishnan, N., & Forrey, R. C. 2010, ApJ, 718, 1062

Young, E. T., Becklin, E. E., Marcum, P. M., et al. 2012, ApJ, 749, L17

Yuan, Y. & Neufeld, D. A. 2011, ApJ, 726, 76, Y11

Zijlstra, A. A., Rodriguez, J., & Wallander, A. 1995, The Messenger, 81, 23

ACKNOWLEDGEMENTS

You see, Momo,' he [Beppo Roadsweeper] told her one day, 'it's like this. Sometimes, when you've a very long street ahead of you, you think how terribly long it is and feel sure you'll never get it swept.' He gazed silently into space before continuing. 'And then you start to hurry,' he went on. 'You work faster and faster, and every time you look up there seems to be just as much left to sweep as before, and you try even harder, and you panic, and in the end you're out of breath and have to stop - and still the street stretches away in front of you. That's not the way to do it.' He pondered a while. Then he said, 'You must never think of the whole street at once, understand? You must only concentrate on the next step, the next breath, the next stroke of the broom, and the next, and the next. Nothing else.' Again he paused for thought before adding, 'That way you enjoy your work, which is important, because then you make a good job of it. And that's how it ought to be.' There was another long silence. At last he went on, 'And all at once, before you know it, you find you've swept the whole street clean, bit by bit. What's more, you aren't out of breath.' He nodded to himself. 'That's important, too,' he concluded.

Michael Ende 1973

Doing astronomical research is quite an abstract activity. Depending on their individual backgrounds, people associate a variety of things with that: from "something like being unemployed" via "seeking for the theory of everything" to "romantically watching the stars at night". So finally, here is the solution in the form of a book that contains the results of my work of the recent years. Indeed, I have been working during that time. I haven't found the theory of everything, though. But I have learnt a lot and had a very intensive time.

Therefore, I would like to thank all the people who have helped me and supported me during this period. In particular, I would like to thank my supervisor, Frank Bertoldi, who strongly encouraged me to acquire a very broad knowledge of different phenomena, models, and types of data, and who also promoted my philosophical side projects. His support reached well beyond his duties as a supervisor. I am very much indebted to Guillaume Pineau des Forêts and Vincent Guillet who inducted me into the art of shock modelling, received me in great hospitality in Paris many times, and supported me in many different ways. I would also like to thank David R. Flower, who provided the computational resources for the grid calculations of our LVG shock models at Durham University and crucially helped with the fine-tuning of our study on grain-grain processing. Moreover, I have to thank Peter Schilke who initiated the contact with Guillaume and Vincent and who encouraged me to visit them as soon as possible. Furthermore, I would like to thank Antoine Gusdorf for most pleasant teamwork and many important discussions, as well as Rolf Güsten, who let me take part in the interpretation of SOFIA and APEX data and agreed with my lead in the study on W44. In the very beginning of my doctoral studies, Ralf Timmermann kindly provided me with his numerical shock

model, which helped me to gain first insight into the modelling of C-type shocks. Although I did not use this code for actual science, I would like to thank Ralf for his support.

I also have to thank Christina Stein-Schmitz who has taken care of all the important institutional matters in a perfect way and who always had a sympathetic ear for all possible kinds of problems. Moreover, the infrastructures of the IMPRS for Astronomy and Astrophysics, the BCGS of Physics and Astronomy, and of the SFB 956 created a very inspiring environment for my research and offered various opportunities to broaden my expertise on many different levels. Within the BCGS, Jürgen Stutzki has supported me as a mentor, while Bérengère Parise gave valuable advice as a member of my IMPRS thesis committee.

For the opportunity to present parts of my philosophical work, I would like to thank the research collaboration "Untersuchung des Denkstils astrophysikalischer Forschung" (primarily based at the TU Berlin), in particular Friedrich Steinle, the research collaboration "Epistemology of the Large Hadron Collider" (based at the University of Wuppertal), and Norbert Wermes who invited me to the "Teilchenseminar des Physikalischen Instituts". Furthermore, I would like to thank Martin Harwit, Margaret Morrison, Allan Franklin, and Andreas Bartels for very helpful discussions and correspondence.

Although my private activities in science journalism were not directly related to my research, they made me rediscover the beauty of science and helped me through difficult phases. Therefore, also the Frankfurter Allgemeine Zeitung played a part in contributing to the success of my thesis. Finally, Marcus Albrecht und Ute Feldmann gave important comments on the final version of this thesis and helped me to detect many typos.

Schließlich möchte ich mich ganz besonders bei meinem Partner, Claudio Roller, und meiner Familie bedanken. Sie haben als "Beppo Straßenkehrer" manches Mal die Prioritäten zurecht gerückt und meinen Blick von der gesamten Straße zurück auf den nächsten Schritt gelenkt. Ohne ihre Unterstützung würde es diese Arbeit daher mit Sicherheit nicht geben.